Improving pure enantiomer provision by coupling chromatography with enzymatic racemization

Dissertation
zur Erlangung des akademischen Grades

Doktoringenieurin
(Dr.-Ing.)

von M.Sc. Isabel Harriehausen
geb. am 28. November 1992 in Hannover

genehmigt durch die Fakultät für Verfahrens- und Systemtechnik
der Otto-von-Guericke-Universität Magdeburg

Promotionskommission:	apl. Prof. Dr. rer. nat. Heike Lorenz (Vorsitz)
	Prof. Dr.-Ing. Andreas Seidel-Morgenstern (Gutachter)
	Prof. Dr. rer. nat. Jan von Langermann (Gutachter)
	Prof. Yoshiaki Kawajiri, Ph. D. (Gutachter)

Promotionskolloquium am 12. Januar 2024

Abstract

Enantiomers are pairs of chemical compounds that are mirror images of each other. Due to their stereoisomerism, they take on fundamentally different roles in biological systems. The development of efficient stereoselective production processes is therefore of great industrial importance. One approach is the chiral separation of a racemic mixture (1:1 mixture of both enantiomers) in combination with a partial or total racemization of the unwanted enantiomer and a consecutive recycling of the resulting mixture.

In this work, the approach of coupling a continuous "Simulated Moving Bed" (SMB) chromatography apparatus with enzymatic racemization in a fixed bed reactor was investigated with simulations and in an experimental setup. The challenges of finding suitable coupling conditions, as well as optimising the operating parameters of both processes, were investigated using two case studies: The production of a) *S*- or *R*-mandelic acid with an immobilised mandelate racemase and b) *L*- or *D*-methionine with an immobilised amino acid racemase. For this purpose, both systems were characterised experimentally and modelled mathematically by means of the thermodynamic and kinetic parameters. Simulation studies carried out on this basis illustrate the advantages of the coupled system. Not only can the process yield be increased from 50 % to over 99 %, but the productivity of the chromatography step can also be increased. Reason for this is that the recycling of the unwanted enantiomer eliminates the usual trade-off between productivity and yield.

Furthermore, the efficiency of the fermentation and purification of the amino acid racemase was enhanced. As a result, the material costs for the production of the immobilized amino acid racemase for the reactor could be reduced by 80 %.

Based on the simulation studies conducted and the racemase cost estimates, operating conditions for efficient production were identified and a laboratory plant was designed, constructed and used for validation studies. In a final run, it was operated for two days and produced *D*-methionine with a purity of 99 % and equally high yield during steady-state operation.

Kurzfassung

Enantiomere sind Paare chemischer Verbindungen, die Spiegelbilder voneinander sind. Aufgrund dieser Stereoisomerie spielen sie fundamental unterschiedliche Rollen in biologischen Systemen. Die Entwicklung effizienter stereoselektiver Produktionsprozesse ist daher von großer industrieller Bedeutung. Ein Ansatz ist die chirale Trennung eines Racemats (1:1-Mischung eines Enantiomerenpaars) in Kombination mit einer Weiterverwendung des unerwünschten Enantiomers durch dessen partielle oder vollständige Racemisierung und anschließender Rückführung des Gemisches.

In dieser Arbeit wurde die Verschaltung der kontinuierlichen Chromatographiemethode "Simulated Moving Bed" (SMB) zur Enantiomerentrennung mit enzymatischer Racemisierung durch Racemasen in einem Festbettreaktor untersucht. Die Herausforderungen, geeignete Kopplungsbedingungen zu identifizieren sowie die Betriebsparameter beider Prozesse zu optimieren, wurde anhand von zwei Fallstudien untersucht: Die Produktion von a) *S*- oder *R*-Mandelsäure mit einer immobilisierten Mandelsäureracemase und b) *L*- oder *D*-Methionin mit einer immobilisierten Aminosäureracemase. Dafür wurden die Teilschritte beider Fallstudien experimentell charakterisiert und mathematisch modelliert. Die darauf aufbauenden Simulationsstudien verdeutlichen die Vorteile des gekoppelten Systems. Zum einen steigt die Prozessausbeute von 50 % auf über 99 %, zum anderen kann die Produktivität des Chromatographieschritts erhöht werden. Grund hierfür ist, dass Prozessausbeute und Produktivität der Trennung durch den Rückführungsschritt des Gegenenantiomers entkoppelt werden.

Darüber hinaus konnten im Rahmen dieser Arbeit die Materialkosten für die Produktion der Aminosäureracemase durch Effizienzsteigerung bei der Fermentation und Optimierung des Aufreinigungsprozesses um 80 % gesenkt werden.

Basierend auf den Simulationsergebnissen und den Kostenabschätzungen der Racemase, wurden Betriebsbedingungen für eine effiziente Produktion identifiziert. Anhand der Betriebsbedingungen wurde eine Laboranlage ausgelegt, aufgebaut und für diverse Validierungsexperimente genutzt. In einem abschließenden Lauf wurde sie für zwei Tage betrieben und produzierte *D*-Methionin mit einer Reinheit von 99 % und ebenso hoher Ausbeute im kontinuierlichen Betrieb.

Collaborations and Research Publications

This Ph.D. project was embedded in a research project on intensification of chiral resolution processes for the provision of pure enantiomers within the group for *Physical and Chemical Foundations of Process Engineering research* (PCF) at the *Max Planck Institute (MPI) for Dynamics of Complex Technical Systems Magdeburg*.

Prior work on the establishment of the conditions for the chromatographic separation of mandelic acid enantiomers and the characterization of the mandelate racemase has been done by Katarzyna Wrzosek (*MPI Magdeburg*). Within this Ph.D. project, the separation was parameterized and modelled in single and multi column modes. The initial work of characterization of the free amino acid racemase has been done by Kerstin Würges (*Institute of Biotechnology, Jülich*) and Katerina Petrusevska (*MPI Magdeburg*). Thiane Carneiro (*MPI Magdeburg*) continued their work by optimizing the immobilization of the racemase. Subsequent to this, the activity and stability of the racemase was characterized by the author of this thesis and the protocol for the production of the racemase was improved.

The miniscale-plant for coupling chromatographic separation with enzymatic racemization was designed and set up within this Ph.D. project. The HPLC on-site analytic system, exploited for the monitoring of the plant, was developed by Ju-Weon Lee (*MPI Magdeburg*). Furthermore, the amino acid racemase produced within the scope of this thesis was integrated into a process of temperature cycling induced deracemization by Kritsada Intaraboonrod (*Vidyasirimedhi Institute of Science and Technology, Thailand*) and a process with continuous crystallization by Jonathan Gänsch (*MPI Magdeburg*, not published yet).

Some of the research results have already been published in the following journal articles:

As first author:

I. Harriehausen, K. Wrzosek, H. Lorenz, and A. Seidel-Morgenstern. "Assessment of process configurations to combine enantioselective chromatography with enzymatic

racemization." In *Adsorption* 26 (2020), pp. 1199-1213.
Ref. [157] - The results are discussed in Chapter 5.

I. Harriehausen, J. Bollmann, T. Carneiro, K. Bettenbrock, and A. Seidel-Morgenstern. "Characterization of an Immobilized Amino Acid Racemase for Potential Application in Enantioselective Chromatographic Resolution Processes." In *Catalysts* 11.6 (2021), p. 726.
Ref. [149] - The results are discussed in Chapter 4.

As co-author:

K. Wrzosek, I. Harriehausen, and A. Seidel-Morgenstern. "Combination of enantioselective preparative chromatography and racemization: experimental demonstration and model-based process optimization." In *Organic Process Research & Development* 22.12 (2018), pp. 1761-1771.
Ref. [158] - The contribution of the author of this thesis to this publication was the experimental determination of the adsorption isotherm parameters, the modelling of the coupled process and the writing of the associated parts of the paper. Some of the results are discussed in Section 5.1.

K. Intaraboonrod, I. Harriehausen, T. Carneiro, A. Seidel-Morgenstern, H. Lorenz, and A. E. Flood. "Temperature cycling induced deracemization of *DL*-asparagine monohydrate with immobilized amino acid racemase." In *Crystal Growth & Design* 21.1 (2020): pp. 306-313.
Ref. [150] - The contribution of the author of this thesis to this publication was the provision of the amino acid racemase and the proof reading. The results are not discussed within the scope of this document.

Glossary

General abbreviations

Symbol	Description
3Z/4Z	Three/four zone
AAR	Amino acid racemase
B-1/B-2/B-3	Batch 1, 2, 3
BV	Bed volume
CE	Crude extract
CS	Case study
CSP	Chiral stationary phase
D	Lat.: *D*exter = right
E_1/E_2	Enantiomer 1/2
E. coli	*Escherichia coli*
E. coli BL21 (DE3)	common *E. coli* strain for high-level protein expression
ee	Enantiomeric excess
E. C.	Enzyme class
EFBR	Enzymatic fixed bed reactor
FB	Fed batch
HETP	Height of an equivalent theoretical plate
His-Tag	Polyhistidin-Tag for protein purification
HPLC	High performance liquid chromatography
IMAC	Immobilized metal ion affinity chromatography
KPI	Key performance indicators
L	lat.: *L*aevus = left
MM	Michaelis Menten
MMK	Michaelis Menten kinetic
ModiCon	Modulated feed concentration
MPI	Max Planck Institute
Ni-Seph. 6 FF	Ni Separose 6 Fast Flow
OA	On-site analytic
OD	Optical density
ODE	Ordinary differential equation
OF	Objective function
PC	Preparative chromatography
PCF	Physical and Chemical Foundations of Process Engineering research

Symbol	Description
PDE	Partial differential equation
Pierce H. C. Ni-IMAC	Pierce High Capacity Ni-IMAC
P. putida	*Pseudomonas putida*
P. putida KT2440	Naturally stress resistant *P. putida* strain
R	Lat.: *R*ectus = right
RI	Refractive index
RT	Room temperature
S	Lat.: *S*inister = left
SDS-PAGE	Sodium dodecyl sulfate polyacrylamide gel electrophoresis
SMB	Simulated moving bed
TMB	True moving bed
UV/VIS	Ultraviolet and visible light
VLE	Vapor-liquid-equilibrium

Abbreviations for chemical compounds and molecules

Symbol	Description
2xTY media	Bacteria growth medium with twice the amount of tryptone and yeast
Arg	Arginine
Asn	Asparagine
Co	Cobalt
Cu	Copper
EtOH	Ethanol
E2080	Ethanol water mixture with a ratio of 20:80
E4060	Ethanol water mixture with a ratio of 40:60
Gln	glutamine
H_2O	Water
HEPES	4-(2-hydroxyethyl)-1-piperazineethanesulfonic acid
IPTG	Isopropyl beta-D-1-thiogalactopyranoside
LB-medium	Luria-Bertani broth: standard growth medium for bacteria
MA	Mandelic acid
MeOH	Methanol
M2080	Methanol water mixture with a ratio of 20:80
Met	Methionine
NaCl	sodium chloride
Ni	Nickel
PLP	Pyridoxal phosphate
Ser	Serine
T	Trypton
Y	Yeast

Notation

Symbols

Symbol	Description	Unit
A	Absorption signal	AU
b_i	Coefficient of the Langmuir isotherm of component i	L/g
$b_{\mathrm{I},i}/b_{\mathrm{II},i}$	Coefficients of the bi-Langmuir isotherm of component i	L/g
$b_{1,i}$ /$b_{2,i}$	Coefficients of the quadratic isotherm of component i	L/g
CV	Column volumes	-
c_i	Concentration of component i in a liquid phase	g/L
c_{tot}	Concentration of the sum of two components 1 and 2	g/L
D_{app}	Apparent dispersion	m/s^2
D_{carrier}	Carrier dosage	g/L
d_{p}	Particle diameter	m
F_{c}	Phase ratio	-
HETP	Height of an equivalent theoretical plate	-
H	Henry coefficient	-
k_{deact}	Deactivation coefficient	-
L_{c}	Column length	m
L_{reactor}	Reactor length	m
m_{z}	Flow rate ratio of zone z	-
$\dot{m}_i$	Through put	g/d
K_{M}	Michaelis coefficient	mM
N	Number of components	-
N_{col}	Number of columns	-
N_{P}	Number of theoretical plates	-
Pr_i	Productivity of component i	g/L/d
$\mathrm{Pr}_{i,\mathrm{CSP}}$	Productivity of component i	g/L/d
$\mathrm{Pr}_{i,\mathrm{wt}}$	Productivity of component i	g/g/d
Pu_i	Purity of a component i	%
Δp	Pressure drop	bar
q_i	Loading of component i onto the stationary phase	g/L
q_{s}	Saturation capacity for Langmuir-isotherms	g/L
$q_{\mathrm{I},i}$ / $q_{\mathrm{II},i}$	Saturation capacity at the first/second binding site of component i for bi-Langmuir-isotherm	g/L

Symbol	Description	Unit
r	Reaction rate	U/g
r_0	Initial reaction rate	U/g
$r_{\max}$	Maximum reaction rate	U/g
SC_i	Solvent consumption	g/L
t	Time variable	min
t_0	Dead time of the column	min
t_R	Residence time of a compound in a column or reactor	min
t_plant	Extra-column dead time of the plant	min
Δt_shift	Time interval between two consecutive shifts	min
$\Delta t_\mathrm{i,cyc}$	Cycle time of component i	min
u_int	Interstitial velocity of liquid phase	m/s
u_s	Velocity of solid phase	m/s
V	Volume of a column, reactor or tank	L
V_c	Column volume	L
V_cell	Single cell volume	L
V_plant	Dead volume of a plant	L
V_reactor	Reactor volume	L
V_solid	Volume of stationary phase in a column	L
V_void	Void column volume	L
$\dot{V}$	Flow rate	L/min
$\dot{V}_\mathrm{ext}$	Inlet and outlet flow rate of liquid phase	L/day
$\dot{V}_\mathrm{s}$	Flow rate of solid phase	mL/min
$\dot{V}_\mathrm{z}$	Flow rate of liquid phase in zone z	L/day
x	Space variable	m
Y	Process yield	%
t	Time variable	min
X_i	Conversion rate	%
z	Space variable	m

Greek Symbols

Symbol	Description	Unit
α_c	Separation factor of a chromatographic process	-
δ_c	Density	g/L
ε_t	Total porosity of column or reactor	-
ε_b	External (interstitial) porosity of column or reactor	-
μ	Microbial growth rate	h^{-1}
ν_i	Stoichiometric coefficient	-
τ	Residence time in a reactor	min

Subscripts

Symbol	Description	Range
1, 2	Enantiomer 1/2	
280nm	Absorption signal at 280nm	
650nm	Absorption signal at 650nm	
I, II, III, IV	Section of the SMB or TMB process	
i	Component i	1,2
B	Liquid bottom fraction	
CSP	Chiral stationary phase	
D	Desorbent	
D0	Fresh desorbent	
dist	Distomer	
E	Extract port	
enz	Enzyme	
extr	Extract of a SMB or TMB process	
feed	Feed for a SMB or TMB process	
feed,0	Fresh feed	
rac	Racemase	
raff	Raffinate of a SMB or TMB process	
rec	Recycled stream	
S	Solvent removal unit	
tank	Tank within plant	
tot	Total amount or sum of all components	
P	Plate number	
p	Particle	
wb	Wet biomass	
z	Zone number	I,...,IV

Contents

1 Introduction

> *An expert is a person who has made all the mistakes that can be made in a very narrow field.*
>
> **— Niels Bohr**
> (Physicist, philosopher and promoter of scientific research)

The production of pure enantiomers is crucial for the provision of pharmaceutical ingredients and in the food and agrochemical industries [1, 2, 3, 4, 5]. Even though chiral synthesis by fermentation is well established, e.g. for the production of essential amino acids, this pathway is not always applicable or favorable. An unselective synthesis with a subsequent separation and recycling of the chiral counterpart (also called distomer or by-product enantiomer), is therefore an attractive alternative approach. One way of achieving chiral separation is enantioselective chromatography [6, 7]. In this work, theoretical and practical aspects of integrating enzymatic racemization into chiral chromatographic separation processes for yield maximization are studied and compared for two case studies.

In the next section, stereochemistry and its role in living organisms is explained. Chiral separation methods are briefly introduced and the motivation for coupling chromatographic resolution with enzymatic racemization is given. Afterwards, a summary of prior work and current challenges is given, before the main objectives of this work are stated and the structure of this thesis is provided.

1.1 Stereochemistry and pure enantiomer provision

In a symmetric environment, enantiomers are two molecules with identical physicochemical properties. They only differ in their optical activity due to their distinctive spatial arrangement of being non-super-imposable mirror images of one another. This property is called *chirality* from the Greek word $\chi\epsilon\iota\rho$, which is translated to "hand" (Fig. 1.1). The two forms can be referred to as stereoisomers or enantiomers.

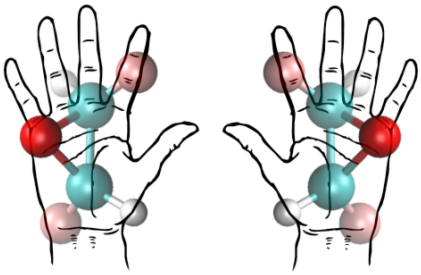

Fig. 1.1: Enantiomers are chiral pairs of molecules with identical properties, except for being mirror images of one another and therefore rotating plane-polarized light in opposite directions [8].

Solutions with only one enantiomer are considered enantiopure, while an equimolar mixture of both enantiomers is called a racemate.

In biological systems the two enantiomers become more distinctive, since nature is made from chiral building blocks and thus stereoselective [9]. As a result two mirror images of the same molecule can play fundamentally different roles in organisms. The two forms of the molecule can be labelled with two systems. The *D*-/*L*-system of Emil Fischer is predominantly used for carbohydrates and amino acids. It is based on a plane projection of the molecule and the position of the substituent with the highest priority determines the name of the enantiomer [10]. The nomenclature originates from the Latin word ***L**aevus* = left, and ***D**exter* = right. Other enantiomers are usually labeled with the Cahn-Ingold-Prelog convention. Here, the enantiomers are determined by the spatial arrangement of the substituents attached to their chiral center and are then referred to as the *R*- or *S*-enantiomer, from **R**ectus and **S**inister [11, 12].

Prominent enantiomers in our every-day life are e.g. *D*- and *L*-amino acids or -sugars. While our proteins are made entirely from *L*-amino acids, our metabolism runs on *D*-sugars. Other enantiomers are pharmaceutical ingredients like the anaesthetic agent *S*-ketamine or sedative *R*-thaliodomide. Their chiral counterparts, can have no function at all or completely different and harmful functions, like the teratogenic effect of *S*-thaliodomide [13]. Especially due to the Contergan- or Thaliodomide scandal, in the 1960 regulatory authorities became aware of this issue. They reacted to it by passing laws like the "Drug Efficacy Amendment in the U.S. (1962) and the "Directive 65/65/EEC" (1965), which was the first European pharmaceutical directive. These laws stipulate that the efficacy and safety of new drugs, including the separate testing of both enantiomers, must be proven. As a consequence, the amount of new enantiopure drugs continuously increased [14] and nowadays almost all chiral drugs enter the market in their enantiopure form [15].

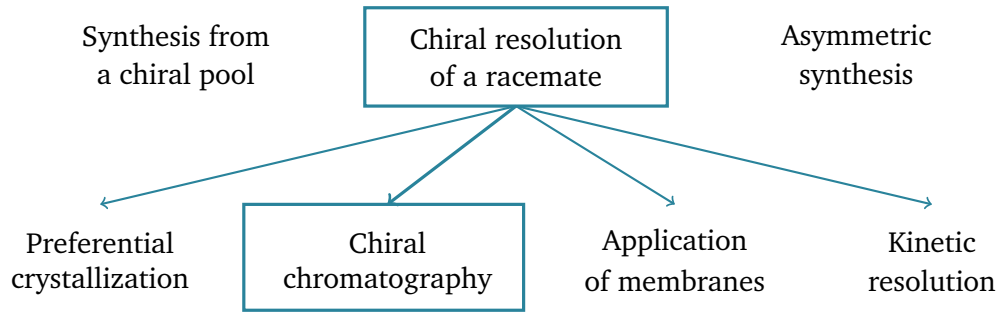

Fig. 1.2: Important methods for pure enantiomer provision focusing on the chiral resolution of a racemate.

Enantiopure compounds can be obtained with different approaches: synthesis from a chiral pool, asymmetric synthesis, or racemic synthesis with consecutive chiral resolution (Fig. 1.2). Asymmetric synthesis or stereoselective synthesis, traditionally exploits enzyme cascades and whole-cell catalysis. But there are also other approaches using chiral Lewis acids [16] or small molecules like the amino acid proline [17]. The latter was rewarded with the Nobel Prize in Chemistry to Benjamin List and David W. C. MacMillan "for the development of asymmetric organocatalysis" in 2021 [18]. Despite theses recent developments, racemic synthesis is more attractive for some systems, due to the option of simple chemical synthesis of the racemic mixture, followed by a chiral resolution step. Good examples are the productions of *D*-amino acids, which are crucial in biomedical applications for e.g. the production of bioactive *D*-peptides, but are unattainable by fermentation [19, 20].

Due to the virtually identical physical properties of enantiomers, the chiral resolution of the racemate is a challenging task. Thus, different separation methods have been developed. Among them are preferential crystallization, chiral chromatography, kinetic resolution and membrane-based approaches [3, 6, 21, 22, 23]. Kinetic resolution (first proposed by Marckwald and McKenzie in 1899 [24]) and the application of membranes [25] are not yet available for broad applications. The first has the disadvantage of needing suitable reaction partners and even then only being able to provide one of the two enantiomers whereas the latter still suffers from being generally less enantioselective [26]. Thus, in the following only the differences between crystallization and chiral chromatography are briefly discussed.

For conglomerate forming systems, preferential crystallization is in general more productive and relatively inexpensive, compared to chiral chromatography. However, only 5-10 % of all substances are conglomerate forming systems [7] and crystallization of racemic compound forming systems always requires an enantiomerically enriched solution. Chiral chromatography on the other hand, is the more versatile

technique. Due to a wide spectrum of commercially available chiral stationary phases and compatible fluid mobile phase, it enables a separation of the majority of racemates with comparably small effort in the method development [3, 27, 28, 29, 30]. Yet, the high costs of chiral stationary phases, demand an efficient design of the chromatographic systems for their optimal exploitation [31].

1.2 Coupling chiral chromatography with racemization: prior work and current challenges

Independent of the chosen resolution method, chiral resolution of a racemate is limited to 50 % yield. An attractive option to overcome the loss of 50 % of the initial material is a recycling of the distomer (here B) by incorporation of a racemization step into the process [32, 33, 34, 35, 36, 37] (Fig. 1.3). Such coupled processes have the potential to reduce waste and increase the yield up to 100 % while enhancing the process productivity. Furthermore, due to the unselectivity of racemization, the process can be designed to produce either enantiomer. Thus, also e.g. *D*-amino acids, which can not be obtained with standard fermentation methods, could be provided with high yield.

A summary of racemization methods, which can be used for this coupled concept, were already given by Ebbers et al. in 1997 [38]. Despite these early prospects, only in 2007 racemization was first used for the production of pure enantiomers with dynamic kinetic resolution and simulated moving bed (SMB) chromatography [39]. At the Max-Planck-Institute (MPI) for Dynamic of Complex Technical Systems in Magdeburg in the group "Physical and Chemical Foundations of Process Engineering"

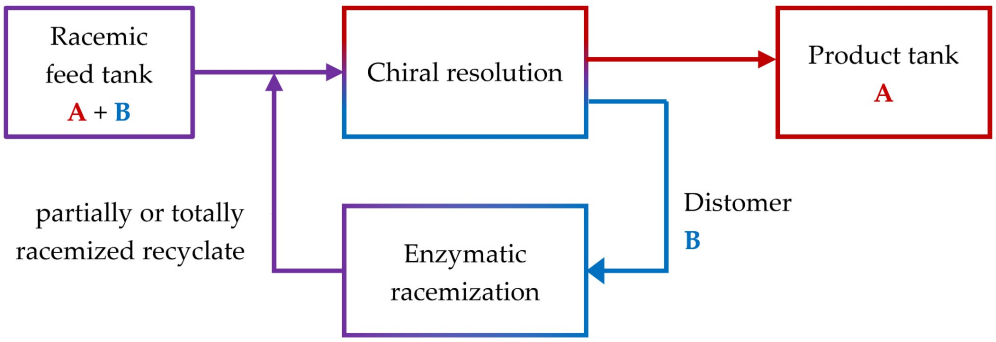

Fig. 1.3: Integration of chiral resolution with enzymatic racemization for the production of target enantiomer (here A) and recycling of the distomer (here B).

the research on this topic started in 2008 within the scope of the EU funded project INTENANT with the goal of studying "Integrated synthesis and purification of single enantiomers" [40]. The outcome of this joint work of ten European collaborators were simulation studies and experimental implementations of integrated setups combining chiral chromatography, preferential crystallization and chemical or enzymatic racemization [41, 6]. Following these successes, the research on chiral resolution methods and racemization was continued. While preferential crystallization was pushed forward in the EU funded "COntinuous REsolution" project, chromatographic resolution was studied with the *R-/S*-mandelic acid system and two racemases were successfully immobilized [42, 43]. A more detailed summary of the current state of the art and the research done at the MPI in Magdeburg can be found in Sec. 2.3.2.

In the present work, the research on integrated setups and suitable racemases was continued and three follow-up challenges were tackled. The first one was a continuation of the work on the recently immobilized amino acid racemase (AAR). Its production needed to be improved and it needed to be characterized under suitable coupling conditions with chiral resolution methods. Furthermore, operating parameters of chromatographic separation needed to be optimized for a coupled setup. Based on these results the coupled process was compared for two case studies and finally implemented in a continuously operating plant.

1.3 Outline and main results of the thesis

Based on the above mentioned challenges, three main objectives were defined:

- OBJ 1: Enhancing the attractiveness of enzymatic racemization: Efficient production, characterization and exploitation of an immobilized AAR.
- OBJ 2: Quantitative evaluation of simulated moving bed chromatography as a stand-alone unit and in an integrated setup.
- OBJ 3: Design, implementation, and operation of an integrated setup combining chiral chromatographic separation and enzymatic racemization.

The second objective was studied with the two chiral model systems *R-/S*-mandelic acid (MA) with a mandelate racemase and *D-/L*-methionine (Met) with an AAR. The first and third objective focused on the second model system. In combination, these three objectives allow insights into the potential of enantioselective chromatography and enzymatic racemization individually and in an integrated setup.

Chapter 2 provides background information and theoretical fundamentals about racemization in a fixed bed reactor and chromatographic separation using simulated moving bed chromatography. This includes the mass balances of chromatographic columns and assumptions regarding the jointly quantified racemization and recycling steps. Also, this chapter provides a short summary of approaches to increase the efficiency of chromatographic separations by optimizing the separation itself or by coupling it with other process units.

Chapter 3 introduces the two case studies used for the investigation of the coupled process. Furthermore, it describes the applied methods and materials and presents the final process setup used for the model validation.

The key findings regarding above listed objectives can be found in the following three result chapters. The first objective of increasing the attractiveness of an immobilized AAR was split into two sections. In the first part of **Chapter 4** the approach and results of optimizing the production of the AAR regarding productivity, costs and time are elaborated. Afterwards, the reaction kinetics of the immobilized amino acid racemase under coupling conditions with enantioseparation processes is presented for different amino acids and varying process conditions like solvent composition and temperature. Furthermore, the stability of the immobilized enzyme is shown, as well as suitable operating conditions and their respective productivities are proposed. This work is a continuation of the work of Thiane Carneiro on this racemase and was done in close collaboration with the lab of Katja Bettenbrock.

The second objective is a qualitative comparison of different chromatography configurations regarding their suitability for coupling with racemization. **Chapter 5** presents the simulation results comparing the application of conventional SMB chromatography with the opportunities of using SMB chromatography in an integrated setup for both case studies. The simulation studies are then used for the design of a SMB chromatography unit separating *D*-/*L*-Met.

In **Chapter 6** the third objective is covered: Based on the key findings presented in Chapters 4 and 5, a coupled process was experimentally implemented. In the mini-plant, a recycling loop was added to the SMB chromatography unit for recycling of the distomer by enzymatic racemization and distillative solvent removal. The productivity and robustness of the coupled setup was studied with different settings and the trade-off between process simplicity and productivity was discussed.

Finally, **Chapter 7** summarizes the most relevant findings of this work and gives an outlook on future research directions.

2 Principles and theoretical foundations of the individual unit operations and the coupled processes

Predictions based on approximations and numerical simulations can considerably reduce material and time needed for process analysis and optimization. For a proper process characterization, mathematical models should be defined and parameterized for all process units. Based on experimentally determined parameters and suitable models, numerical simulations can provide efficient process analysis and optimization. In the following all relevant material and energy balances are introduced along with equations quantifying the thermodynamic equilibria or reaction kinetics. The models were chosen detailed enough to include all relevant parameters and yet simple enough to allow fast calculation times.

In this chapter, first, fundamental equations for chromatography and relevant process modes are explained. Next, racemization, the concept of enzyme immobilization and the essential equations for the quantification of an enzymatic fixed bed reactor are given. Finally, existing processes combining chromatography and racemization are presented and engineering parameters for process evaluation and design aspects are proposed.

2.1 Fundamentals of chromatographic separation of a binary mixture

Chromatography is a powerful method for the separation and purification of almost any material. It was invented by the Russian scientist Mikhail Tsvett in 1903. He separated leaf pigments based on their different adsorption strength on a column filled with calcium carbonate and named his method "chromatography", originating from the greek words chroma (engl.: color) and graphein (engl.: to write). After him,

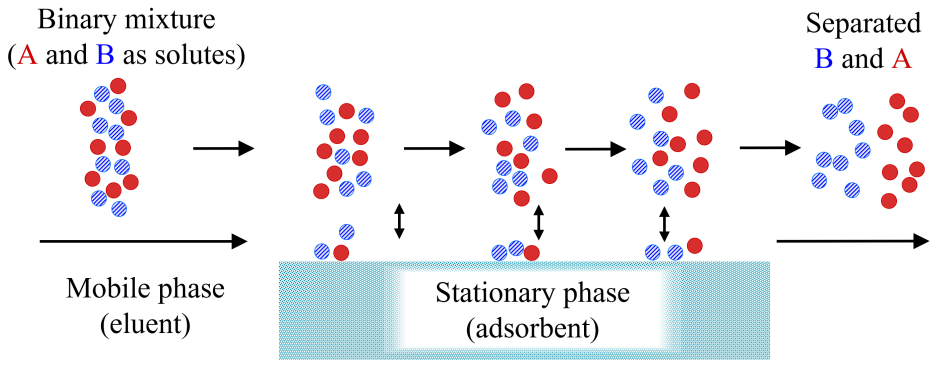

Fig. 2.1: Adsorption of a binary system in a mobile phase onto a stationary phase.

chromatography was forgotten for some time and then rediscovered in the 1930s [44]. In the following 20 years, thin-layer chromatography was developed [45] and in the 60s early high performance liquid chromatography (HPLC) systems were built and commercialized [46]. Since then the methods, equipment and stationary phases have continuously improved, which decreased the required time for a separation from hours to less than a minute [44].

Nowadays, HPLC systems can be found in almost every lab for analysis and quality control purposes. Furthermore, even though chromatography is often avoided for being comparably expensive, there are some chromatography-dominated industrial applications. Reason for this are its often unique ability to provide energy-efficient solutions for many ancient and current challenges of mankind like the purification of water, solvent recovery and exhaust gas treatment. The pharmaceutical industry for example often requires chromatography for the purification of monoclonal antibodies or vaccine production [47]. Even the small antigen-tests that everybody is familiar with these days, are based on thin-layer chromatography.

2.1.1 Principles of chromatography

The concept of chromatography is the separation of a homogeneous molecular mixture based on its interactions with two phases (Fig. 2.1). One phase is a mobile liquid or gas, which is the solvent and acts as a carrier for the mixture. It transports the mixture through or along the stationary phase, which can be a solid or immiscible fluid and acts as the adsorbent. When both phases are chosen correctly, based on their thermodynamic equilibrium, the mixture is separated by component-specific enrichment of the molecules in the two phases. Depending on the type of interactions and properties of the phases, different types of chromatography can be

distinguished. The relevant types for this work were enantioselective and affinity chromatography:

Enantioselective chromatography requires porous silica particles with attached chiral polymers and monomers with chiral centers. They achieve chiral recognition by forming steric three-point interactions, which vary between the two enantiomers or stereoisomers, leading to different retention times in the stationary phase. The chiral separation media can be classed into three groups: macromolecular, macrocylic and low-molecular mass selectors. A detailed overview about them was provided by Lämmerhofer et al. (2010) [27].

Affinity chromatography is based on highly specific macromolecular binding interactions between the target molecule, which is often a protein or antibody, and the binding partner or ligand on the stationary phase. In contrast to standard liquid chromatography, the affinity chromatography forms strong bonds between the target and the adsorbent. The stationary phase is often a polymer like agarose, which is then chemically modified to form stable covalent bonds with the ligand. In this work immobilized metal ion affinity chromatography (IMAC) is used for the purification of an enzyme, the amino acid racemase, with a polyhistidine-tag. This tag consists of at least six histidine residues at the amino- or carboxy-terminus of the amino acid sequence of the enzyme and is an artificial modification of the protein. It increases its affinity for the metal chelate adsorbent (stationary phase), due to histidines ability to form coordinate bonds with metal ions in the adsorbent [48, 49]. Affinity chromatography normally consists of an equilibration step, the sample load, a washing step to remove unbound material and an elution step in which the target molecule is collected. This method is used for the enzyme purification in this work.

2.1.2 Basics of adsorption equilibria

In order to describe the specific, and for the separation essential adsorption equilibria $q_i(c_1, ..., c_N)$, different adsorption isotherm models can be used. In this work three models are required to describe the model systems. They are presented in Fig. 2.2 along with their distinctive ad- and desorption behavior.

The simplest form is the linear adsorption isotherms:

$$q_i = H_i \cdot c_i \qquad\qquad i = [1, N] \tag{2.1}$$

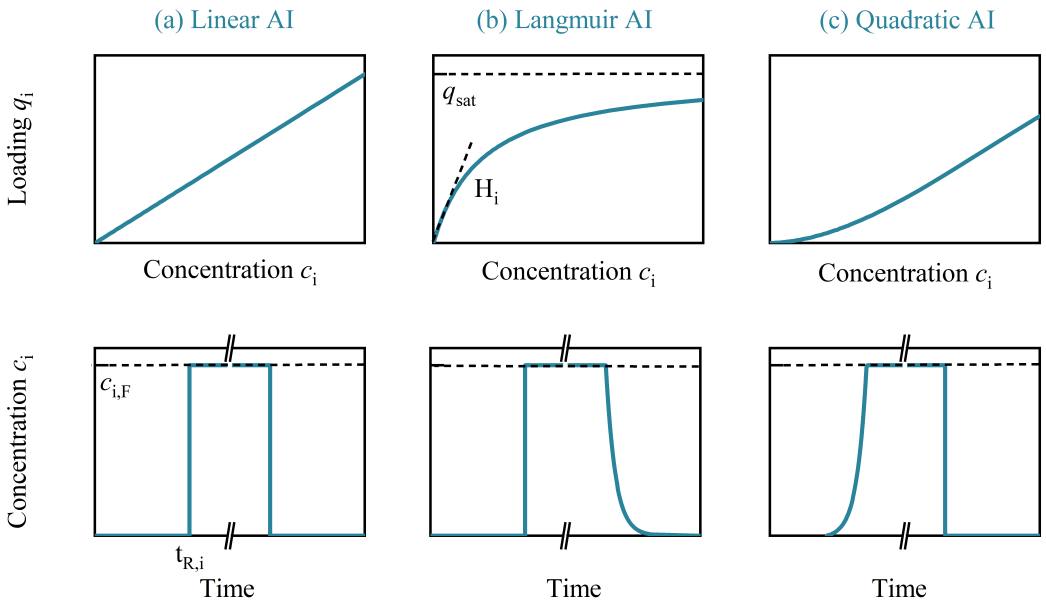

Fig. 2.2: Three common adsorption isotherms (linear, Langmuir, and quadratic adsorption isotherm) and their characteristic adsorption and desorption behaviour shown beneath each adsorption isotherm.

Once higher concentrations are reached, nonlinear models are required to describe the adsorption process. Often the loading on the adsorber diverges towards its saturation capacity, q_s. The adsorption can then be described with the Langmuir adsorption isotherm with the adsorption isotherm coefficient b_i:

$$q_i = H_i \frac{c_i}{1 + b_i \cdot c_i} = q_s \frac{c_i \cdot b_i}{1 + b_i \cdot c_i} \qquad i = [1, N] \tag{2.2}$$

This model is able to provide at least a rough approach to describe the adsorption behaviour of many components. It assumes energetically equal adsorption sites, which can only adsorb one solute molecule at once forming only single layers. Also it can not describe lateral interference between adsorbed molecules. If one of these criteria is not fulfilled, the model needs to be expanded by additional terms or another model needs to be chosen. One option providing an additional parameter is the quadratic isotherm model:

$$q_i = q_s \frac{c_i \cdot (b_{1,i} + 2 \cdot b_{2,i} \cdot c_i)}{1 + b_{1,i} \cdot c_i + b_{2,i} \cdot c_i^2} \qquad i = [1, N] \tag{2.3}$$

It can be used for describing the equilibria of compounds with a fronting behaviour, also referred to as anti-Langmuir. Here, $b_{i,1}$ and $b_{i,2}$ are quantifying adsorption isotherm coefficients. An other option is the bi-Langmuir isotherm [50], which takes

the adsorption of the component on two independent adsorption sites I and II with individual maximal adsorption capacities $q_{s,I}$ and $q_{s,II}$:

$$q_i = \frac{H_{I,i} \cdot c_i}{1 + b_{I,i} \cdot c_i} + \frac{H_{II,i} \cdot c_i}{1 + b_{II,i} \cdot c_i} = q_{s,I} \frac{c_i \cdot b_{I,i}}{1 + b_{I,i} \cdot c_i} + q_{s,II} \frac{c_i \cdot b_{II,i}}{1 + b_{II,i} \cdot c_i} \qquad i = [1, N] \tag{2.4}$$

An overview of other common adsorption isotherms can be found in detailed in Schmidt-Traub (2020) [51].

All above mentioned adsorption isotherms describe the adsorption behavior of a single component *i*. In the presence of multiple adsorbing molecules in the mobile phase, the molecule species influence the adsorption behavior of one another. Thus, the adsorption of these mixtures need to be described with multi-component adsorption isotherms. While the linear model (Eq. (2.1)) can not take competitive effects into account, the Langmuir (Eq. (2.2)) and bi-Langmuir (Eq. (2.4)) model can be expanded to the multi-Langmuir (Eq. (2.5)) and multi-bi-Langmuir (Eq. (2.6)) model. In this form they describe the adsorption behaviour of a component *i* in the presence of all N components (i = [1,N]):

$$q_i = \frac{H_i \cdot c_i}{1 + \sum_{i=1}^{N} b_i \cdot c_i} = \frac{q_s \cdot b_i \cdot c_i}{1 + \sum_{i=1}^{N} b_i \cdot c_i} \tag{2.5}$$

$$q_i = \frac{H_{I,i} \cdot c_i}{1 + \sum_{i=1}^{N} b_{I,i} \cdot c_i} + \frac{H_{II,i} \cdot c_i}{1 + \sum_{i=1}^{N} b_{II,i} \cdot c_i} = \frac{q_{s,I} \cdot b_{I,i} \cdot c_i}{1 + \sum_{i=1}^{N} b_{I,i} \cdot c_i} + \frac{q_{s,II} \cdot b_{II,i} \cdot c_i}{1 + \sum_{i=1}^{N} b_{II,i} \cdot c_i} \tag{2.6}$$

The adsorption of binary chiral mixtures on chiral stationary phases is often characterized by two kinds of adsorptions: an unselective, achiral adsorption, which is similar for both components and a selective, chiral binding site with individual adsorption strength for the two enantiomers [52, 53]. These assumptions simplify Eq. (2.7) to:

$$q_i = \frac{q_I \cdot b_I \cdot c_i}{1 + b_I \cdot (c_1 + c_2)} + \frac{q_{II} \cdot b_{i,II} \cdot c_i}{1 + b_{1,II} \cdot c_1 + b_{2,II} \cdot c_2} \qquad i = [1, 2] \tag{2.7}$$

2.1.3 Concept and mass balance of single column chromatography

In this section chromatographic separation of a mixture with one column and pulse injections is presented. It can be implemented with a simple process design and is a reliable method for first or quick solutions to new separation challenges. The corresponding setup is shown in Fig. 2.3 and can be applied for (a) analytical and (b) preparative purposes. In both cases the eluent is pumped through a column, packed with stationary phase. With a selection valve small or large pulses of the

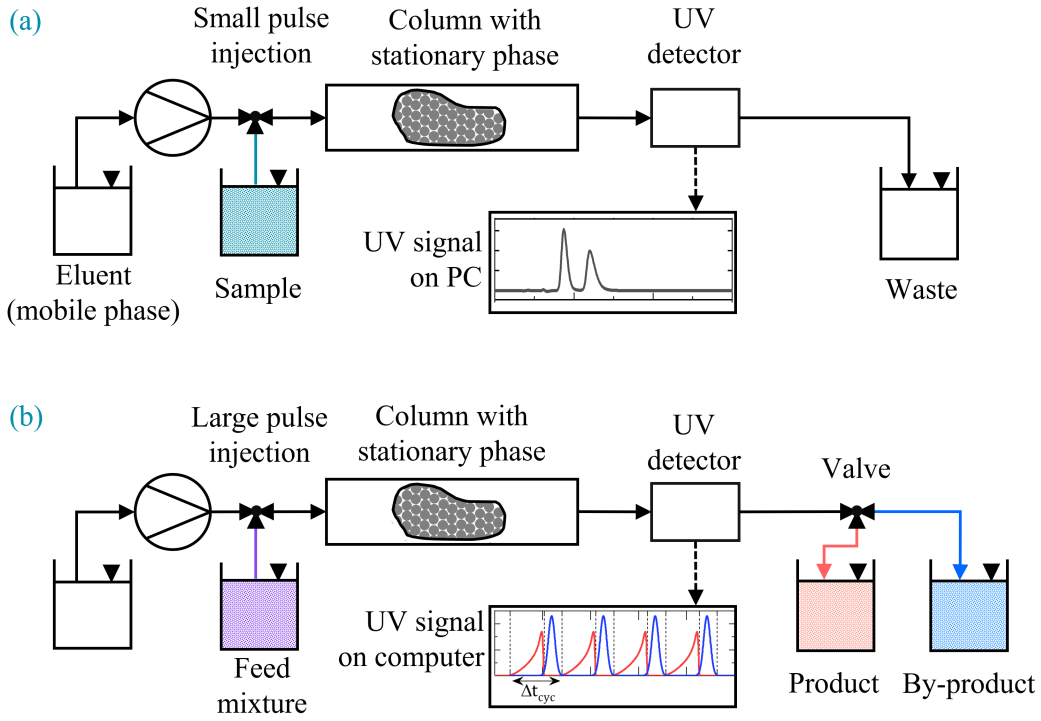

Fig. 2.3: Single column chromatography for (a) analytical purposes and (b) preparative separation of a binary mixture. The concentrated mixture is injected as a pulse and transported in the eluent through the column. Due to the different adsorption strength on the stationary phase in the column, the components elute at different times and can be send to different tanks via a valve.

mixture are injected and then carried within the mobile phase through the column. At the column outlet the eluting profile can be detected with e.g. an UV detector. In analytical applications the elute is afterwards discarded or for preparative purposes fractionated to collect the purified components. In case of stationary phases of small particles and a liquid mobile phase, this technique is called HPLC. Its analytical applications are designed for rapid qualitative or quantitative analysis, requiring only 0.1-2 μL of a sample. Usually small samples of 0.1-1.0 μL are injected and base line separation is desired. For preparative application larger pulses of high concentrations are injected within short time intervals to increase the productivity of the process. While the first application was used in this work multiple times, in the following the focus is set on the latter one.

When designing a chromatographic separation, various design and operating parameters needs to be chosen. Despite some of them forming independencies, like the choice of stationary and mobile phase or the flow rate and the column dimension, many degrees of freedom exist. To obtain optimal results, the set of parameters needs to be chosen carefully. Approaches to compare different parameter sets are

given in Sec. 2.1.4. Each parameter set results in characteristic physical and chemical parameters, which can be used to model the separation process. While some parameters, like dispersion effects, can be estimated a priori, others like the resulting adsorption behaviour can still not be predicted with sufficient certainty. Thus, they needed to be determined for each chromatographic process.

Chromatographic processes can be described with models of varying complexity. The ideal model is the fundamental version, based on the mass balance for a component i and the equilibrium theory. Thus, it only considers convection and adsorption equilibria:

$$\frac{\partial c_i}{\partial t} + F\frac{\partial q_i(c_1, \ldots, c_\mathrm{N})}{\partial t} + u_\mathrm{int}\frac{\partial c_i}{\partial x} = 0 \tag{2.8}$$

Here, c_i is the concentration and $q_i = f(c_1, \ldots, c_\mathrm{N})$ is the loading of the component $i = 1, ..., N$ where N is the number of components. Furthermore, the time and space variables are noted as t and x, respectively, and u_int is the interstitial linear velocity. The phase ratio, F, of the column is defined in Eq. (2.9) by the total porosity, ε_t, of the stationary phase as a ratio of the solid and void phase.

$$F = \frac{1 - \varepsilon_\mathrm{t}}{\varepsilon_\mathrm{t}} \tag{2.9}$$

This model can be expanded by above mentioned model parameters describing dispersion, mass transfer, adsorption or kinetic effects. Even though the general rate model includes all mentioned aspects and is therefore the most accurate model, for most process understanding and modeling tasks, not all aspects are relevant and can sometimes be lumped. Often a simple dispersion model, assuming a homogeneous column and input profile, non compressible liquids and negligible axial diffusion, can be sufficient [51]:

$$\frac{\partial c_i}{\partial t} + F\frac{\partial q_i(c_{1\ldots\mathrm{N}})}{\partial t} + u_\mathrm{int}\frac{\partial c_i}{\partial x} = D_\mathrm{app}\frac{\partial^2 c_i}{\partial x^2} \tag{2.10}$$

The apparent dispersion, D_app, lumps contributions of e.g. axial dispersion and mass transfer resistances.

2.1.4 Model parameter estimation and chromatography specific performance indicators

For the modeling or evaluation of a chromatographic separation, certain key performance indicators and model parameters need to be determined. Since general process

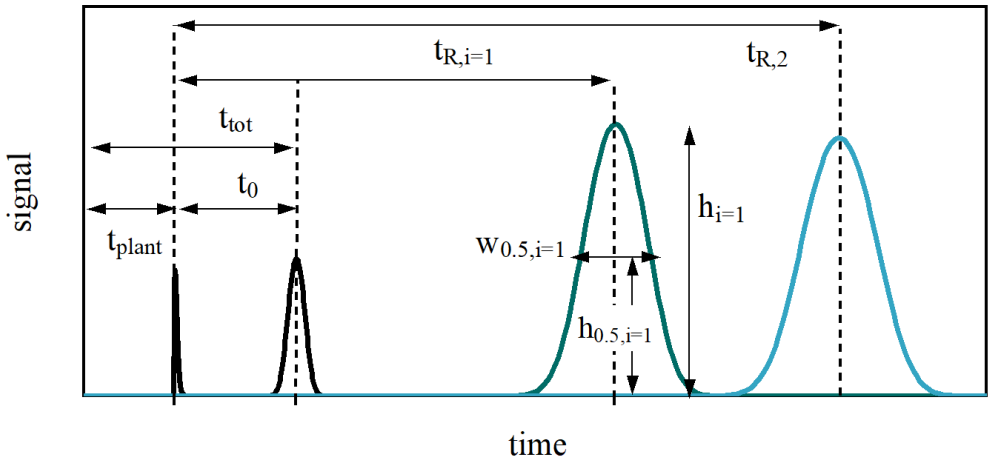

Fig. 2.4: Chromatogram with peaks of a non-retained tracer molecule without a column (t_{plant}), with a column (t_{tot}) and for two retained two components 1 and 2. The retention times $t_{R,1}$ and $t_{R,2}$ are the retention times of the components in the column. The peak width at 50 % of the height of the peak i ($w_{0.5,\,i}$) is used for the determination of the HETP for component i.

performance indicators will be introduced in Sec. 2.4, here only the plate number, the capacity factor and the resolution are discussed. Afterwards, the adsorption isotherm determination methods used in this work are presented.

Performance indicators for the efficiency of a separation

The success of a chromatographic separation can be measured by different criteria, which directly effect the productivity of the separation process. Key factors are the plate number, the selectivity and the resolution. The definitions below are explained using Fig. 2.4.

Columns are packed with porous material. The void volume of a column, V_0, is the sum of the volumes in the pores and between the adsorbent beads. For a given flow rate $\dot{V}$ the residence time of a non-retained component in the column is t_0:

$$t_0 = V_0/\dot{V} \tag{2.11}$$

In Eq. (2.12) total porosity, ε_t, is the ratio of void volume, V_0, of the total column volume V_c:

$$\varepsilon_t = V_0/V_c \tag{2.12}$$

The plant volume, V_{plant}, includes all capillaries, valves and in some case pumps inside of the chromatographic system, between the sample injection point and the

detector or collection tank. The corresponding residence time of a compound in a plant is t_{plant} in analogy to Eq. (2.11):

$$t_{\mathrm{plant}} = V_{\mathrm{plant}}/\dot{V} \tag{2.13}$$

In a given chromatographic system, the sum of the plant volume and the dead volume will be the total void volume, V_{tot}:

$$V_{\mathrm{tot}} = V_{\mathrm{plant}} + V_0 \qquad \text{or} \qquad t_{\mathrm{tot}} = t_{\mathrm{plant}} + t_0 \tag{2.14}$$

The stronger a migrating component gets adsorbed on the stationary phase, the longer its retention time, $t_{\mathrm{R},i=1}$, will be delayed. In a binary system where component 2 is adsorbed stronger than component 1, it holds:

$$t_0 < t_{\mathrm{R},1} < t_{\mathrm{R},2} \tag{2.15}$$

Based on the retention times, $t_{\mathrm{R},i}$, of very small pulse injections, the Henry coefficients or retention factors can be estimated. The capacity or retention factor, k_i', describes the amount of one component in the stationary phase, compared to its amount in the mobile phase. It can be estimated experimentally with:

$$k_i' = \frac{t_{\mathrm{R},i} - t_0}{t_0} \tag{2.16}$$

Henry coefficients, H_i, are the slopes of the adsorption isotherms, as seen in Fig. 2.2:

$$H_i = \frac{\varepsilon_{\mathrm{t}}}{1-\varepsilon_{\mathrm{t}}} \frac{t_{\mathrm{R},i} - t_0}{t_0} \tag{2.17}$$

Both parameters will always depend on the estimated dead time of a non-retained column. Since these times are difficult to obtain for e.g. chiral phases, the capacity factor as well as the resulting selectivity should only carefully be used outside the experimental setup, in which they were determined.

The plate number, N_{P}, is the number of equilibrium stages and directly correlates to kinetic effects. A high plate number is desired to minimize band broadening. In case of normally distributed peaks, N_{col} can be estimated accurately by assuming the first normalized moment of a peak, μ_{i}, being equivalent to the retention time $t_{\mathrm{R,i}}$, and N_{P} being correlated to the width of the peak at half of its maximum height $w_{0.5,i}$:

$$\mu_{t,i} \simeq t_{\mathrm{R},i} \tag{2.18}$$

$$N_{\mathrm{P},i} \simeq 5.54 \cdot \left(\frac{t_{\mathrm{R},i}}{w_{0.5,i}} \right)^2 \tag{2.19}$$

For a better comparison of different columns, the plate number, N_{col}, can also be expressed as the height of a theoretical plate (HETP) of a chromatographic column with the length L_{c}:

$$\mathrm{HETP}_i = \frac{L}{N_{\mathrm{P},i}} \tag{2.20}$$

Both parameters are a function of the flow rate through the column.

Another criterion for the quality of a separation is the selectivity α_c. It describes the distribution of two components between the stationary and mobile phase and can be estimated from the Henry coefficients (Eq. (2.17)):

$$\alpha_c = \frac{H_2}{H_1} = \frac{k_2'}{k_1'} = \frac{t_{\mathrm{R},2} - t_0}{t_{\mathrm{R},1} - t_0} \tag{2.21}$$

2.1.5 Adsorption isotherm determination

Adsorption isotherms characterize the driving force for transport of the solutes between the mobile and stationary phase at a constant temperature (Sec. 2.1.2). They dominantly influence the chromatograms by determining retention time and shape of the propagating fronts. Depending on the available amount and purity of the solutes, as well as the goal of the chromatographic separation process, different adsorption isotherm determination methods can be used.

Small pulse injections for the determination of Henry coefficients is a simple method and sufficient to describe the adsorption behavior of components with linear adsorption behavior. This often only holds true for small concentrations, but can be sufficient for analytical applications. The Henry coefficient, H_i, (Eq. (2.17)) is determined from the retention time of very small pulse injections of the components and a non-retained tracer molecule (see Fig. 2.4):

Analysis of adsorption and desorption fronts of large pulse injections is a simulation-based peak-fitting method, which requires only small amounts of the components and a standard HPLC system, as well as computing power. For this method elution profiles $\bar{c}_{\mathrm{exp},i,j}$, with $j = 1, n_p$ as the running index of the injected pulses of varying size of either the pure component or a mixture with i components, are measured. Then simulated elution profiles $\bar{c}_{\mathrm{model},i,j}$ are fitted to the experimental data. For the generation of the simulated profile e.g. the dispersion model (Eq. (2.10)) and a suitable adsorption isotherm models (Eqs. (2.2)-(2.5)) are used. In the model

the known operating parameters are fixed and the adsorption isotherm parameters are to be optimized to match the experimentally obtained profile. This can be done by finding the minima of an objective function OF, which e.g. is based on the least square method, considering the difference between the theoretical and measured concentration profiles (Eq. (2.22)). An algorithm like *fminsearch* on MATLAB can then be used to numerically find the solution with the best fitting adsorption isotherm parameters:

$$OF = f\left(\sum_{j=1}^{n_p}(\bar{c}_{\mathrm{exp},j} - \bar{c}_{\mathrm{model},j})^2\right) \quad \rightarrow \min \quad \text{for } j = 1 \ldots n_p \tag{2.22}$$

In order to increase the impact of low concentration, also the relative error can be minimized:

$$OF = f\left(\sum_{i=1}^{n_p}\left(\frac{\bar{c}_{exp,i,j} - \bar{c}_{\mathrm{model},i,j}}{\bar{c}_{exp,i,j}}\right)^2\right) \quad \rightarrow \min \quad \text{for } j = 1, \ldots, n_p \tag{2.23}$$

Frontal Analysis exploits equilibrium theory for adsorption isotherm prediction of single and multi-component mixtures with N components. For this method, step changes of the feed concentration are applied and the resulting breakthrough curve's at the column outlet are analyzed. Each adsorption front starts with an initial concentration $\bar{c}_{k=\mathrm{I}}$ and contains one breakthrough time $t^*_{\mathrm{R},i}$ of each component i and $(N-1)$ intermediate plateaus $\bar{c}_k$ with $k = 2, N$ before reaching the new feed concentration $\bar{c}_{\mathrm{Feed}}$. When assuming an adsorption equilibrium, the ideal chromatography model (Eq. (2.8)), can be rearranged to directly connect the above mentioned breakthrough curves features to the respective loading $q_i(c_i)$:

$$q_{\mathrm{Feed},i}(\bar{c}_{\mathrm{Feed}}) = q_{I,i}(\bar{c}_{\mathrm{I}}) + \frac{(t^*_{\mathrm{R},i} - t_0)(c_{\mathrm{Feed,i}} - c_{\mathrm{I},i})}{F \cdot t_0} \tag{2.24}$$

with

$$t^*_{\mathrm{R},i} = \frac{\sum_{k=1}^{N}\left(t^k_{\mathrm{R}}(c_i^{k+1} - c_i^k)\right)}{c_{\mathrm{Feed},i} - c_{\mathrm{I},i}};\ i = 1, N \tag{2.25}$$

In general, a successive step-wise increase of the feed concentration is required to obtain sufficient data points $q_i(\bar{c})$ for the entire shape of the adsorption isotherm. The resulting points can then be fitted to a suitable adsorption isotherm. A more detailed explanation of this method is given in Lisec et al. 2001 [54].

A special case of non-linear adsorption isotherms are Langmuir adsorption isotherms. Here, the adsorption parameters can be obtained for single and multi-component mixtures from a single breakthrough experiment. The solution for a binary mixture can be found in Seidel-Morgenstern 2020 [55] and the solution for a ternary mixture as well as a more detailed derivation of Eq. (2.25) can be found in the App. C.1.

Perturbation method is performed similar to frontal analysis and analysis perturbations caused by small pulses of lower or higher concentration on plateau concentrations. The retention time of these pulses provide information about the local total derivatives of the adsorption isotherm dq_i/dc_i:

$$\left.\frac{dq}{dc}\right|_{c^*} = \left(\frac{t_\mathrm{R}(c^*)}{t_0} - 1\right)/F \tag{2.26}$$

The partial derivatives $\partial q_i/\partial c_i$ of adsorption isotherms can then be fitted to the data points to find a suitable match and parameter set.

The later applied derivatives of the Langmuir and bi-Langmuir adsorption isotherm are as follows:

$$\frac{dq_i}{dc_i} = \frac{H_i}{(1 + b_i \cdot c_i)^2} = \frac{q_\mathrm{s} \cdot b_i}{(1 + b_i \cdot c_i)^2} \qquad i = [1, N] \tag{2.27}$$

$$\frac{dq_i}{dc_i} = \frac{H_{i,1}}{(1 + b_{i,1} \cdot c_i)^2} + \frac{H_{i,2}}{(1 + b_{i,2} \cdot c_i)^2} \qquad i = [1, N] \tag{2.28}$$

Compared to the analysis of large pulse injection, this method has the advantage of taking memory effects of high concentrations on the stationary phase into account. This can be important for continuous chromatography modes, where some columns are long-time exposed to high concentrations.

2.1.6 Simulation of chromatographic adsorption

For a modeling of the chromatographic separation in a column, the partial differential equation (PDE) (Eq. (2.10)) needs to be solved with the correct initial and boundary conditions. This can be done with existing standard PDE-solvers, but requires high computational effort because of the second order diffusion term. A simple and fast alternative is an algorithm proposed by Kremser et al. (1930) [56]. This elegant algorithms has small computational effort but can only be applied for linear adsorption models.

More general, yet rapid approaches are the method of lines, which is a discretization of the PDE in space [57, 58], or the Rouchon algorithm, a finite-difference method with a full discretization in time and space [59, 60, 61]. Both approaches were used in this work and are described below. The operation results in a numerical error, which is proportional to the second derivative. When chosing a spacial grid with N_P sections, equivalent with the HETP (Eq. (2.20)), the numerical error can be used to model the apparent dispersion coefficient:

$$D_\mathrm{app} = \frac{u_\mathrm{int} \cdot \mathrm{HETP}}{2} = \frac{u_\mathrm{int} \cdot L_\mathrm{c}}{2N_\mathrm{P}} \tag{2.29}$$

In the following both methods are explained for a binary system, which requires the transformation of a system of two PDEs, both following the ideal chromatographic model (Eq. (2.8)). Since the loading of both components on the stationary phase, q_i, are a function of both concentrations $\bar{c} := (c_1, c_2)$, the differential, $\partial q_i(\bar{c})/\partial t$, needs to be considered as

$$\frac{\partial q_i(c_1, c_2)}{\partial t} = \sum_j^2 \frac{\partial q_i(c_1, c_2)}{\partial c_j} \frac{\partial c_j}{\partial t} \qquad i = 1, 2 \tag{2.30}$$

Including Eq. (2.30) into Eq. (2.8) results in:

$$\frac{\partial c_i}{\partial t} \left(1 + F \cdot \left(\frac{\partial q_i(c_1, c_2)}{\partial c_j} \frac{\partial c_j}{\partial t} \right)_{i=1,2} \right)^{-1} = -u_\mathrm{int} \cdot \frac{\partial c_i}{\partial z} \qquad i = 1, 2 \tag{2.31}$$

This linear system of the time derivatives of the concentrations c_1 and c_2 can then be reformulated in an explicit form. For the method of lines, Eq. (2.31) is discretized in space. When applying a backward difference quotient, matching the grid size Δz with the HETP from Eq. (2.20)

$$\Delta z = \frac{L_c}{N_\mathrm{P}} \tag{2.32}$$

and converting the interstitial velocity u_int into a flow rate $\dot{V}_z$

$$u_\mathrm{int} = \frac{\dot{V}_\mathrm{z} \cdot L_\mathrm{c}}{V_\mathrm{c} \cdot \varepsilon_\mathrm{t}} \tag{2.33}$$

the following ordinary differential equation (ODE) system in time is obtained:

$$\frac{\partial c_{i,n}}{\partial t} \left(1 + F \sum_j^2 \left(\frac{\partial q_i(c_{1,n}, c_{2,n})}{\partial c_n} \frac{\partial c_j}{\partial t} \right) \right) = -\frac{u_\mathrm{int}}{\Delta z} (c_{i,n} - c_{i,n-1}) \qquad i = 1, 2 \tag{2.34}$$

Here, n is the running variable in space with $n = 1, ..., N_\mathrm{P}$.

An further simplified approach is followed with the algorithm proposed by Rouchon et al. [59], which exploits another finite difference to approximate the time derivative and converts the ODE system (Eq. (2.34)) into a system of linear equations. An application of the finite difference algorithm on (Eq. (2.8)) forward in space and backwards in time results in the following explicit discretization:

$$\bar{c}|_{n+1}^{m} = \bar{c}|_{n}^{m} - \frac{\Delta z}{u_{\text{int}}\Delta t}\left[\bar{c}|_{n}^{m} - \bar{c}|_{n}^{m-1} + F\left(\bar{q}|_{n}^{m} - \bar{q}|_{n}^{m-1}\right)\right] \tag{2.35}$$

The solution of this system of linear equations can provide a rather accurate approximation for the solution of Eq. (2.10), if the grid sizes in space and time are adjusted correctly. While index n is again chosen to match N_{P} and thus Δz = HETP, the grid size in time (Δz) needs to fulfill the Courant-Friedrichs-Lewy stability condition, which evaluates the initial isotherm slope [62]:

$$a_c = \frac{u_{\text{int}}}{1 + F \cdot H}\,\frac{\Delta t}{\Delta z} \geq 1 \tag{2.36}$$

For two enantiomers with similar migration speed, the courant number, a_c, is limited to $2 \leq a_c \leq 10$ and the time step size is defined as

$$\Delta t = \frac{2\,\overline{HETP}}{u_{\text{int}}} = \frac{2\,\overline{t_{R,i}}}{\overline{N_p}} \tag{2.37}$$

and

$$\Delta z = \frac{\overline{HETP}}{a_c - 1} \tag{2.38}$$

with the averaged values of the HETP ($\overline{HETP}$), the residence time $\overline{t_{R,i}}$ and the plate number $\overline{N_{\text{P}}}$.

In a next step, proper initial and boundary conditions need to be defined, and discretized according to the chosen method. In case of fully regenerated columns, the initial condition is independent of the chosen chromatographic mode:

$$c_i(t = 0, x) = 0 \tag{2.39}$$

The boundary condition

$$c_i(t, x = 0) = c_{\text{in}}(t) \tag{2.40}$$

on the other hand depends on the chromatographic system and will be explained for true and simulated moving bed chromatography in Sec. 2.1.7.

Additional information about this discretization method can be found in Zahn 2010 or Nowak et al. 2012 [63, 64].

2.1.7 Multi-column simulated moving bed chromatography: Concept and model

Single column chromatography can be designed and implemented relatively easily, but often suffers from high eluent consumption and inefficient exploitation of the stationary phase. Thus, chromatography modes involving multiple columns and countercurrent flow have been developed, which result in greater productivity, yield and concentration. While various approaches can be found in literature (some of them are introduced later on in Sec. 2.3.1), in this section the most common form, the SMB chromatography, is introduced. It was initially proposed by Broughton and Gerhold in 1961 for large-scale separations in the petrochemical and food processing industries [65]. Its popularity increased in the 90s, when SMB was tested for many other applications [66, 67, 68, 69]. The application of SMB for the separation of enantiomers was first tested by Francotte and Richert in 1997 [70].

Concept of SMB chromatography

In classical four zone closed-loop (4Z-SMB) chromatography each zone consists of one or more fixed columns, which are connected to periodically switching inlet and outlet ports. The ports move in the same direction as the fluid stream and therefore simulate a counter current true moving bed (TMB) process (Fig. 2.5). The flow in each zone varies to match its specific task [65]. The zones II and III perform the separation of the binary system by carrying the less retained enantiomer to the raffinate port and the more retained enantiomer to the extract port. The first zone regenerates the stationary phase and the fourth zone regenerates the eluent. In the following section the traditional SMB process is described. Further variations, which have been developed by numerous research groups and the industry to further optimize the concept, are discussed later on in Sec. 2.3.

In SMB chromatography the feed is introduced continuously onto the first column between the second and third zone and all other columns are fed with the outlets of the prior column:

$$c_{\mathrm{in,SMB}}(t) = \begin{cases} c_{i,\mathrm{III}}(t, x = 0) = c_{i,\mathrm{F}} \\ c_{i,z}(t, x = 0) = c_{i,z-\mathrm{I}}(t, x = L_{\mathrm{c}}) \end{cases} \tag{2.41}$$

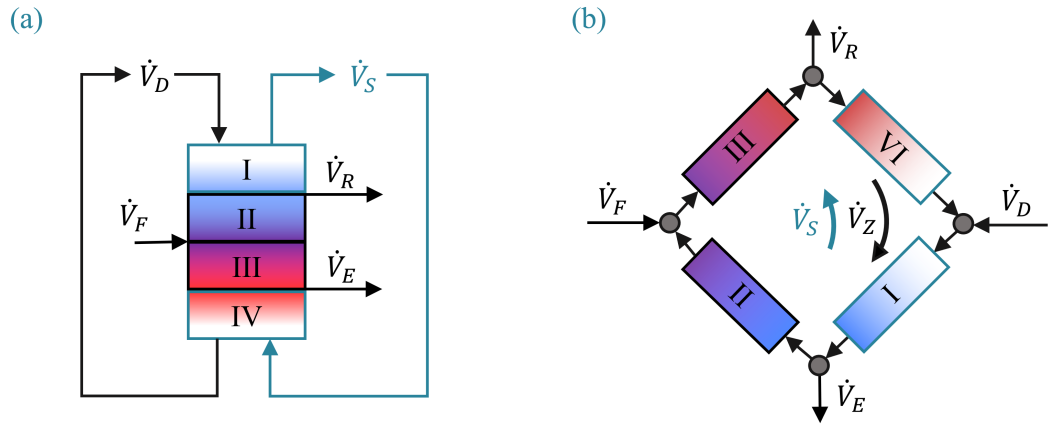

Fig. 2.5: Scheme of a conventional (a) TMB and (b) SMB process with four zones.

Mass balances and design of true moving bed processes

A well established approach to estimate the SMB performance is the TMB model [65, 71]. Here, the standard chromatography mass balance equation (Eq. (2.10)) is expanded by a term quantifying counter-current movement of the stationary phase:

$$\frac{\partial c_i}{\partial t} + F \cdot \frac{\partial q_i(c_1, \ldots, c_N)}{\partial t} + u_{\text{int}} \frac{\partial c_i}{\partial x} - F \cdot u_s \frac{\partial q_i(c_1, \ldots, c_N)}{\partial x} = 0 \tag{2.42}$$

In a TMB unit the volumetric flow rates $\dot{V}_z$ in each zone (z = I,...,IV) are connected with the external flow rates for desorbent, extract, feed and raffinate, respectively:

$$\dot{V}_{\text{ext}} = [-\dot{V}_{\text{desorb}}, \dot{V}_{\text{extr}}, -\dot{V}_{\text{feed}}, \dot{V}_{\text{raff}}] \tag{2.43}$$

It holds that:

$$\dot{V}_{\text{I}} = \dot{V}_{\text{desorb}} + \dot{V}_{\text{IV}} \tag{2.44}$$

$$\dot{V}_{\text{II}} = \dot{V}_{\text{I}} - \dot{V}_{\text{extr}} \tag{2.45}$$

$$\dot{V}_{\text{III}} = \dot{V}_{\text{II}} + \dot{V}_{\text{feed}} \tag{2.46}$$

$$\dot{V}_{\text{IV}} = \dot{V}_{\text{III}} + \dot{V}_{\text{raff}} \tag{2.47}$$

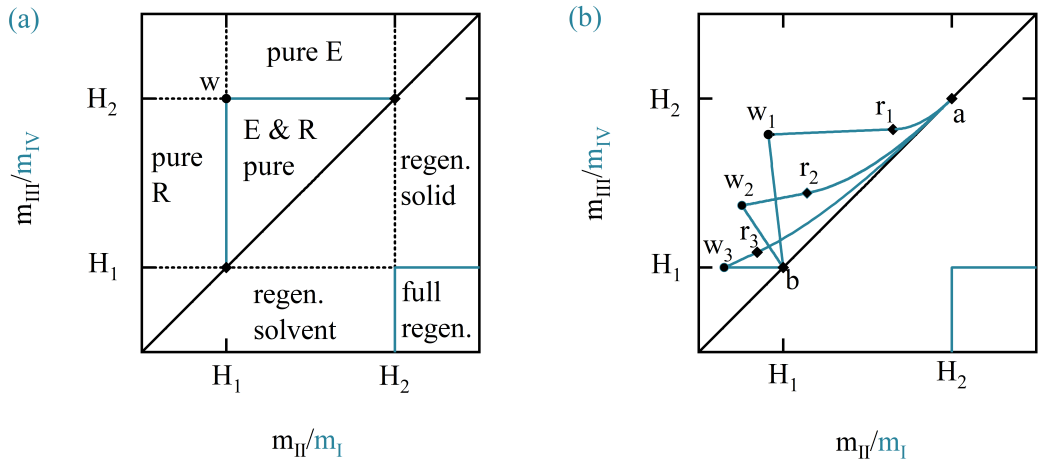

Fig. 2.6: Overview of separation regions for (a) linear adsorption isotherms and (b) Langmuir adsorption isotherms and three increasing feed concentrations: pure components at the raffinate (R) and extract (E) can only be obtained if m_{II} and m_{III} are within the triangle of the points (H_1,H_1), w and (H_2,H_2).

To generate enantiopure solutions at the raffinate and extract port, the flow rates in each zone need to be properly set. They can be described in a normalized form as dimensionless flow rate ratios m_z:

$$m_z = \frac{\dot{V}_z^{TMB}}{\dot{V}_s^{TMB}} \tag{2.48}$$

with $\dot{V}_s$ being the volumetric flow rate of the solid phase. By exploiting the equilibrium theory of chromatography, regions for the flow rates can be derived, which allows a successful binary separation and a regeneration of the stationary and mobile phases [72]. For linear isotherms it holds that:

$$H_1 < m_{II} < m_{III} < H_2 \tag{2.49}$$

$$m_I > H_2 \tag{2.50}$$

$$m_{IV} < H_1 \tag{2.51}$$

The region for linear isotherms in which both enantiomers elute with 100 % purity is triangular and plotted in the m_{II}-m_{III}-plane, as shown in Fig. 2.6 (a). In the vertex, w, of this triangle the difference between the flow rate ratios is the highest and is therefore the location of the theoretical productivity optimum. The blue rectangle in the right corners mark the region of full regeneration of zone I and IV for m_I and m_{IV}. If m_{II} and m_{III} are outside the triangles one or both outlets are contaminated with the other component.

When only one enantiomer is targeted, the constraint on the distomer becomes obsolete, which reduces Eq. (2.49) to Eq. (2.52)) if the purity constraint regarding the raffinate is removed and to Eq. (2.53) if the constraint on the extract is removed.

$$m_{\mathrm{II}} < m_{\mathrm{III}} < H_2 \tag{2.52}$$

$$H_1 < m_{\mathrm{II}} < m_{\mathrm{III}} \tag{2.53}$$

Eq. (2.52) opens the triangle towards the area "pure R" while Eq. (2.53) opens it towards the area "pure E" With the constraint in Eq. (2.51), the solvent can be regenerated in the last zone to reduce its consumption. In a closed-loop SMB operation, a removal of this zone would cause a contamination of the extract. In a 3Z open-loop operation, the zone is omitted in trade-off for a higher dilution of the raffinate stream and higher solvent consumption. The 3Z-system can then be described by Eq. (2.50) and (2.52) or (2.53).

When operating in regions of non-linear adsorption, the triangle in Fig. 2.6 (a) becomes distorted [73]. For Langmuir adsorption isotherms the shape of the triangle can be described by a set of equations, defining the points w and r and their connecting lines, which result in the triangle shown in Fig. 2.6 (b). The equation set was derived by Mazzotti et al. (1997) from the mass balances and boundary conditions of all zones and the equilibrium theory. The approach as well as all relevant equations can be found in the above mentioned paper [74] and are listed in App. C.3. For systems obeying other adsorption isotherm models no analogous analytical solutions exists and the separation regimes can not be determined numerically.

Modeling and simulation of SMB chromatography

TMB and SMB processes are comparable, if the conversion of the solid and liquid phase movement in a TMB are described by the shifting times and the liquid phase movement of a SMB process. The solid flow is simulated by a shifting of the columns in the direction of the flow:

$$\dot{V}_s = \frac{1 - \varepsilon_{\mathrm{t}}}{\Delta t_{\mathrm{shift}}} \cdot V_{\mathrm{c}} \tag{2.54}$$

Here, $\Delta t_{\mathrm{shift}}$ is the time interval between two shifts. A full cycle is completed once a column has reached its initial position again after being on each column position, which equals the time of N_c shifts:

$$\Delta t_{\mathrm{cycle}} = N_{\mathrm{c}} \cdot \Delta t_{\mathrm{shift}} \tag{2.55}$$

For the conversion of the liquid flow in a TMB, the column movement and the dead volumes need to be considered as well:

$$\dot{V}_{\mathrm{z}}^{\mathrm{TMB}} = \dot{V}_{\mathrm{z}}^{\mathrm{SMB}} - \frac{\varepsilon_{\mathrm{t}} \cdot V_{\mathrm{c}}}{\Delta t_{\mathrm{shift}}} - \frac{V_{\mathrm{plant}}}{N_{\mathrm{col}} \cdot \Delta t_{\mathrm{shift}}} \tag{2.56}$$

By using Eq. (2.55) and Eq. (2.56), with Eq. (2.48) the time interval between two shifts $\Delta t_{\mathrm{shift}}$ can be estimated:

$$\Delta t_{\mathrm{shift}} = \left(m_z + \frac{1}{F} + \frac{V_{\mathrm{plant}}}{N_{\mathrm{col}} \cdot (1 - \varepsilon_{\mathrm{t}}) \cdot V_{\mathrm{c}}} \right) \cdot \frac{(1 - \varepsilon_{\mathrm{t}}) \cdot V_{\mathrm{c}}}{\dot{V}_{\mathrm{z}}^{\mathrm{SMB}}} \tag{2.57}$$

For the simulation of SMB chromatographic processes the mass balance equation Eq. (2.42) can again be solved with the method of lines. The discretization can be done analogous to the discretization of the single column mass balance (see Eq. (2.8) and Eq. (2.34)).

Of particular interest is the steady state solution of the TMB process which forms, after spacial discretization, a large system of nonlinear algebraic equations [75]. It is a well established procedure to solve the dynamic equations until the final steady state, which is the operating state of interest, is reached. This approach was also used for all other units considered in the overall process schemes.

The external streams through the two inlets and outlets are considered with

$$\dot{V}_z = \left\{ \dot{V}_{\mathrm{I}},\, \dot{V}_{\mathrm{II}},\, \dot{V}_{\mathrm{III}},\, \dot{V}_{\mathrm{IV}} \right\} \tag{2.58}$$

$$\dot{V}_{ext} = \left\{ -\dot{V}_{\mathrm{feed}},\, \dot{V}_{\mathrm{raff}},\, -\dot{V}_{\mathrm{desorb}},\, \dot{V}_{\mathrm{extr}} \right\} \tag{2.59}$$

$$\bar{\mathbf{c}}_{ext} = \left\{ \bar{c}_{\mathrm{feed}},\, \bar{c}_{\mathrm{raff}},\, \bar{c}_{\mathrm{desorb}},\, \bar{c}_{\mathrm{extr}} \right\} \tag{2.60}$$

resulting in

$$\frac{\partial \bar{c}}{\partial t} = \left(\mathit{I\!I} + F \cdot \frac{D\bar{\mathbf{q}}(\bar{c}_n)}{D\bar{c}_n} \right)^{-1} \left[-u_{\mathrm{int}} \cdot \frac{\partial \bar{c}}{\partial z} - u_{\mathrm{ext}} \cdot \frac{\partial \bar{c}_{\mathrm{ext}}}{\partial z} + F \cdot u_s \cdot \frac{\partial \bar{q}}{\partial z} \right] \tag{2.61}$$

and together with a discretization backwards in time, the final ODE system with $n = 1, \ldots, N_{\mathrm{P}}$, is obtained:

$$\left. \frac{\partial \bar{c}}{\partial t} \right|_n = \frac{1}{V_{\mathrm{cell}} \cdot \varepsilon_t} \left(\mathit{I\!I} + F \left. \frac{D\bar{\mathbf{q}}(\bar{c})}{D\bar{c}} \right|_n \right)^{-1} \left[-\dot{V}_z(\bar{c}_n - \bar{c}_{n-1}) - \dot{V}_{\mathrm{ext}} \bar{c}_{\mathrm{ext}} + \dot{V}_s(\bar{q}_{n+1} - \bar{q}_n) \right] \tag{2.62}$$

With this model, the dynamic behaviour of SMB processes with any adsorption isotherm can be studied to design and optimize SMB plants. For other applications, with linear or Langmuir adsorption isotherms, which only require knowledge about the steady state, faster approaches can be chosen. One option, which can be used in case of linear adsorption isotherms, is the recursion technique suggested by Kremser [75, 56]. A second option, in case of linear or Langmuir adsorption isotherms is e.g. a short-cut method proposed by Kaspereit et al. (2016) [76].

2.2 Fundamentals of enzymatic racemization and enzyme immobilization

Application of enzymes as bio-catalysts is an environmentally friendly alternative to conventional, and often toxic, catalysts. The large variety of enzymes in nature and the progress in enzyme engineering offers new opportunities in reaction engineering. To increase the enzyme stability, it is expedient to immobilize them. With the right resin, the immobilization is not worsening the enzymes activity and significantly improves their reusability. Enzymatic racemization can be used to convert the distomer (by-product) into the targeted enantiomer. In this section the fundamentals of enzymatic racemization and heterogeneous catalysis is summarized. Furthermore recent developments in enzyme immobilization are presented.

2.2.1 Racemases

Racemization is the irreversible interconversion of an enantiopure or enantiomerically enriched solution into its racemic mixture as shown in Fig. 2.8 (b). Enzymes which catalyze this conversion are racemases and belong to the group of isomerases. While being unfavorable in stand-alone operations, racemases are increasingly gaining attention in their role of recycling the unwanted enantiomer in chiral resolution processes. By racemizing the unwanted enantiomer, they can increase the theoretical process yield of resolution process to up to 100 %. Furthermore, due to their non-selectivity, they can be exploited for the provision of both enantiomers.

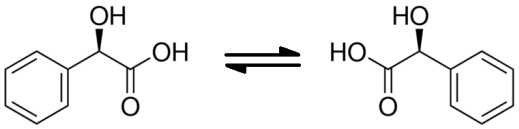

Fig. 2.7: Racemization of *R*-MA (left) to *S*-MA (right).

For consistency, in the following section the by-product enantiomer (E_2) is considered to be in excess and therefore the substrate and the target enantiomer (E_1) is the product.

In the past, various racemases from different bacterial strains have been extracted and characterized. Important for this work are prior studies on AAR and mandelate racemase. The AARs have already been studied since 1954 [77, 78, 79] and by genome engineering the racemic activity of a decarboxylase was increased by a factor of 30 [80]. The functions and mechanisms of AARs have been studied by Yoshimura in 2003 [81] and their stability and activity was enhanced by Strauss et al. (2000) [82].

Racemases play a key role in dynamic kinetic resolution, the provision of pure enantiomers from a racemate. They can either be combined with a second, irreversible reaction, which is solely or dominantly consuming the target enantiomer [83, 23] or with a chiral resolution step like chiral chromatography or preferential crystallization (Sec. 2.3.2). The discovery, purification and characterization steps needed for the racemases exploited in this work are introduced in Sec. 3.2.2 and Sec. 3.2.1.

2.2.2 Enzyme immobilization

A traditional approach for enzyme catalyzed continuous reaction process, exploits membrane reactors, with ultra-filtration membranes, that keep the enzymes within the reactor while letting the substrates pass [84]. This homogeneous reaction has successfully been applied by Fuereder et al. 2016 [37] and others in combination with chiral resolution methods.

However, the stability of free, soluble enzyme is often limited to hours or days and a reusability is not given. A more promising approach, which is already used in classical reaction engineering, is heterogeneous bio-catalysis. It is achieved by immobilization of the enzyme to a support. This fixation simplifies the enzyme recovery and its separation from the products. Furthermore, the stability can increase [85] and continuously stirred tank reactors can be replaced with more effective reactor configurations, like tubular fixed bed reactors. These advantages significantly lower the cost of biocatalysis and enhance its attractiveness for industrial applications [86, 87, 88, 89].

Enzyme immobilization can be achieved by cross-linking, entrapment, encapsulation or binding to a solid support [88]. The latter one is the most common one and can be done by irreversible (covalent coupling) or reversible (ionic, affinity or hydrophobic

adsorption) bindings onto carriers. These carriers are usually macroporous beads (d_p = 100-300 μm) of resins like methacrylate or epoxy-agarose [90, 91].

Despite over two decades of studying enzyme immobilization, the effect of materials on the activity loss of enzymes is still not fully understood. Thus, experimental work is required to find the most suitable carrier for a given enzyme and reaction environment [92]. The search of suitable carriers for the enzymes exploited in this work has been done by Wrzosek et al. 2014 for the mandelate racemase [42] and by Carneiro et al. 2020 for the AAR [43]. The enzymes exploited in this work were fixed by multi-point covalent bindings.

2.2.3 Racemization kinetics

The kinetics of a free racemase can be described by a reversible Michaelis-Menten (MM) approach [93]. This approach assumes a two-step reaction in which one enantiomer and the enzyme (Enz) form a substrate-enzyme-complex, which is followed by a conversion of the bound enantiomer:

$$Enz + E_2 \underset{k_{-1}}{\overset{k_1}{\rightleftharpoons}} Enz\ E_2 \xrightarrow{k_2} Enz + E_1 \tag{2.63}$$

Summarizing both steps into one results in the following MM rate expression:

$$r_0 = \frac{(r_{\text{max},2}/K_{\text{M},2})c_2 - (r_{\text{max1}}/K_{\text{M},1})c_1}{1 + (c_2/K_{\text{M},2}) + (c_1/K_{\text{M},1})} \tag{2.64}$$

Hereby, c_2 and c_1 are the by-product and target enantiomer concentrations, respectively. The initial rate of depleting the excess of the by-product enantiomer due to the initial racemization reaction r_0 has the unit U/mg of enzyme or U/g of wet carrier in case of immobilized enzymes. One unit U equals the amount of 1 μmol converted substrate in 1 min. The maximum reaction rates, $r_{\text{max},i}$, and the Michaelis coefficients, $K_{\text{M},i}$ (i = [1,2]), are the temperature dependent MM coefficients. A typical MM-plot is given in Fig. 2.8(a) with its characteristic parameters.

Often the reaction rates and thus the MM coefficients for both enantiomers are similar and Eq. (2.65) can be simplified:

$$r_0 = r_{\text{max}} \frac{c_2 - c_1}{K_{\text{M}} + c_{2,0} + c_{1,0}} = r_{\text{max}} \frac{c_2 - c_1}{K_{\text{M}} + c_{\text{tot}}} \tag{2.65}$$

with the constant overall concentration $c_{\text{tot}} = c_1 + c_2$. An analogous description holds if the target, E_1, and by-product enantiomer, E_2, are switched. A typical reaction

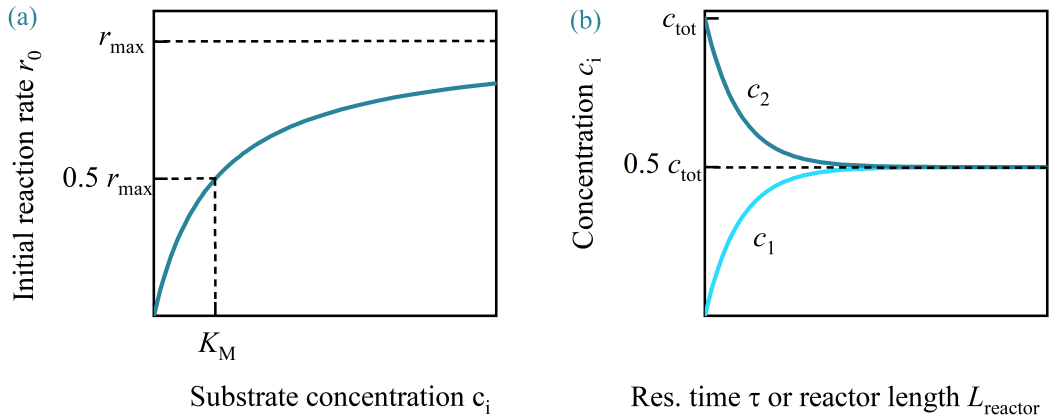

Fig. 2.8: Enzyme kinetics: (a) Reaction rate following MM kinetics, (b) Concentration changes of both enantiomers over retention time or reactor length.

rate following the MM kinetic is shown in Fig. 2.8 (a) along with the trend of the concentration profile of the two enantiomers. Here, E_2 is converted into E_1 over the residence time in a continuous stirred tank reactor or the reactor length of an plug flow tubular reactor until both reach their final concentration of 0.5 x c_{tot} (Fig. 2.8 (b)).

Both MM coefficients are temperature dependent. For the maximum racemization rate, the dependency can be described using a classical Arrhenius approach with Eq. (2.66) a pre-exponential factor A, an activation energy E_A, and the universal gas constant R:

$$r_{\max}(T) = A \cdot \exp\left(-\frac{E_A}{RT}\right) \tag{2.66}$$

$$K_M(T) = A_0 + A_1 \exp\left(-T/A_2\right) \tag{2.67}$$

The temperature effect on the coefficient K_M can be well described empirically with Eq. (2.67) with the three parameters A_0, A_1, and A_2.

When operating catalysts over a longer time (days or weeks), typically deactivation needs to be taken into account in rate models. For immobilized enzymes, the deactivation can be caused by various factors, for instance, protein denaturation, fouling, poisoning, or breaking of the covalent linkage to the resin.

A simple expression capable to describe drops in rates over the time of operation is:

$$r(t) = \exp(-k_{\text{deact}}(t - t_0)) \cdot r_0(t = 0) \tag{2.68}$$

where r_0 is the initial reaction rate at $t = t_0$, valid for the fresh enzyme, and the activity loss is described empirically by an exponential decay function using a

deactivation rate constant k_{deact}. The final racemization rate expression including possible enzyme deactivation is:

$$r(c_1, c_2, t) = \exp(-k_{\text{deact}}(t - t_0)) \cdot \frac{(c_2 - c_1)}{K_{\text{M}} + c_{\text{tot}}} \tag{2.69}$$

2.2.4 Racemization in an enzymatic fixed-bed reactor

The racemases applied in this work were immobilized and packed in a tubular fixed-bed reactor (EFBR). Therefore, their activity was characterized in this reactor configuration. Neglecting axial and radial dispersion and assuming ideal plug-flow reactor conditions, in analogy to Eq. (2.8), the mass balance of both enantiomers can be summarized to:

$$\frac{\partial c_i}{\partial t} = -u_{\text{int}} \cdot \frac{\partial c_i}{\partial z} + \nu_i D_{\text{carrier}} \cdot r(t) \qquad i = 1, 2 \tag{2.70}$$

where z is the spacial coordinate, u_{int} is the fluid phase velocity, $\nu_i = [+1, -1]$ is the stoichiometric coefficient of the specific enantiomer, r is the racemization rate Eq. (2.65) and D_{carrier} is the carrier dosage (Eq. (2.71)). It is the relative amount of enzyme m_{carrier} in a reactor with the volume V_{R} and the porosity ε_{t}:

$$D_{\text{carrier}} = \frac{m_{\text{carrier}}}{\varepsilon_{\text{t}} V_{\text{reactor}}} \tag{2.71}$$

The ratio of the amount of enzyme, m_{enz}, determined from the concentration of the free enzyme c_{enz} in the initial solution of a volume, V_{enz}, and the amount of carrier is the specific load q_{enz}:

$$q_{\text{enz}} = \frac{m_{\text{enz}}}{m_{\text{carrier}}} = \frac{c_{\text{enz}} V_{\text{enz}}}{m_{\text{carrier}}} \tag{2.72}$$

An important parameter to evaluate the extent of the reaction is the residence time, τ:

$$\tau = \frac{\varepsilon_{\text{t}} V_{\text{reactor}}}{\dot{V}} = \frac{L_{\text{reactor}}}{u_{\text{int}}} \tag{2.73}$$

which can be introduced into the mass balance using the reactor length, L_{reactor}.

The concentration of the enantiomers at the reactor outlet, for defined initial concentrations $c_{1,0}$ and $c_{2,0}$, are the key factors to evaluate the degree of racemization. They can be obtained by assuming steady state conditions and applying the expression for the initial reaction rate, an integration of the balance equation Eq. (2.70). This leads to the following analytical solution:

$$c_i(\tau) = \frac{1}{2}\left(c_{\text{tot}} + (c_{2,0} - c_{1,0}) \exp\left(-2\nu_i \tau D_{\text{carrier}} \frac{r_{\max}}{K_{\text{M}} + c_{\text{tot}}}\right)\right) \tag{2.74}$$

The resulting concentration profile over time or reactor length is shown in Fig. 2.8.

2.3 Methods for improvement of chiral chromatographic processes

Chiral chromatographic resolution is a comparably expensive method. Thus, optimizing the production processes is crucial, which can be approached in various ways. The most straight forward approach is the development of more efficient single and multi-column modes. However, this method, while increasing productivity, will never increase the yield beyond 50 %. To overcome this limitation the chiral separation needs to be integrated into a coupled process with racemization and recycling of the unwanted enantiomer. The most promising findings on chromatographic modes and coupling options are presented below.

The downside of the resulting complex process configurations is that they are often accompanied with a reduced process robustness. Thus, even though the racemization kinetics of the by-product absorbs some process fluctuations, the overall process becomes more fragile. To counteract, a process monitoring can ensure a continuous quality control. Furthermore, to maintain or improve the performance, a fast online-monitoring allows for active process control by adjustment of operation variables during the running process. This is optimization method is discussed in the last section of this chapter.

2.3.1 State of research on optimization of chromatographic processes

The development of new chromatographic separation processes often starts with batch column optimization. By applying the common strategies like adjusting the eluent, flow-rates, injection profile, cut times and different recycling-strategies, the productivity and solvent consumption of a given system can be improved [94, 95, 96, 97, 98]. However, as explained in Sec. 2.1.7, exploiting multi-column processes and especially SMB processes often increases productivity while lowering eluent consumption. In the past 60 years, the impact of various design parameters was tested and improved modification of the conventional SMB process have been invented, validated and compared [99, 100, 101, 102]. In this section the two relevant advanced operating strategies for the separation of binary mixtures are

explained in the following. Many further asymmetric operating options, like Varicol, PowerFeed, ModiCon or Intermittent SMB [103, 104, 105, 106], can be found in literature. Yet, it should be kept in mind that, even though all of them can improve process performance, the choice of the optimal process configuration and parameter setting depends on the given separation challenge [107].

Number of columns: One of the most obvious adaptions is the optimization of the number of columns per zone. The minimum requirement for a traditional SMB process is one column per zone. With increasing number of columns per zone, the SMB performance converges towards the one of the TMB process and thus towards a better separation. However, on the other hand the integration of each additional column increases the investment costs. As a consequence, many traditional processes are operated in an 2-2-2-2 scheme with two columns per zone or in more recently a 1-2-2-1 scheme with only one column in the the two regeneration zones.

Three zone SMB (3Z-SMB) While the above listed variations all incorporated at least four columns, there are also approaches for 3Z-SMB configurations. In the most straight forward variation, the fourth zone is simply omitted and the SMB process is operated in an open-loop configuration. This way the column number can be reduced without compromising throughput or product purity in exchange for an increased solvent consumption. This is an attractive approach for systems with an expensive stationary phase and a relatively cheap mobile phase [108, 109].

The latest 3Z-variation was proposed by Tangpromphan (2018), in which multi-position valves are used to lower the above mentioned solvent consumption in comparison to a standard 3Z-SMB and reduce the number of required pumps while maintaining high purities [110].

2.3.2 Concept of coupling units for process intensification

While many optimization approaches focus on the improvement of the stand-alone unit, processes must also be studied in an integrated system. This also holds true for the SMB chromatography process. No matter how well it is optimized, it always needs to be considered as a simple piece of a more complex system, like Blehaut and Nicoud stated in 1998 [111]. Chromatography is a purification method and therefore often used in the downstream process for the purification of difficult targets from e.g. a multi-component feed like a fermentation broth or the outlet

stream of a reactor. If the purified target is the final product, the target stream can be further purified and processed by e.g. a crystallization unit [33]. For overall process optimization, also the eluent should be recovered and the waste fraction should be further processed. In this work, the feed stream is simplified to be a pure racemic mixture and the emphasis is on the recovery of the distomer in the waste fraction. An overview of prior approaches to couple chromatography with a reactor for byproduct recycling, is given below.

General coupling of separation and reaction processes

Integration of chromatographic separation with reaction steps was already discussed by e.g. Hashimoto et al. (1983) [112] and used to increase yield and productivity for producing a targeted sugar. Based on this idea, a number of approaches involving combinations of separation and reaction types for enrichment of high and low value products of different purities were studied, e.g. in the group of Panke at ETH Zurich and Schmidt-Traub [113, 114, 115, 35]. The process configurations investigated had different degrees of integration and complexity. A proof-of-concept for coupling of a continuously operated reactor and SMB chromatography for the production of *D*-Psicose has been done by Wagner et al. (2012) [116]. A more complex system was studied theoretically and experimentally by Lee et al. (2014) [117].

Dynamic kinetic resolution by coupling chiral chromatography with (enzymatic) racemization

One prominent specification of the general coupling of chromatographic separation and reaction is its application for kinetic dynamic resolution. A first introduction into the potential of this approach and relevant work done in the project "Integrated synthesis and purification of single enantiomers" (INTENANT) was given in Sec. 1.2. In this project lots of conceptual work on the process coupling and experimental implementations has been done in the groups of Seidel-Morgenstern and Kaspereit [36, 118]. Furthermore, the process was applied to an industrial application for 2',6'-pipecoloxylidide in Langermann et al. (2012) [34]. A table of relevant works in this field can be found in App. D.1.2. However, most projects focused on chiral chromatography in combination with chemical catalysts. The advantage of enzymes as biocatalysts has already been highlighted in Sec. 2.2. The downside of their optimal operation under mild process conditions is, that most enzymes are not stable in organic solvents, which are used for many chiral separations. Thus, a challenge is to find a compatible chiral stationary phase and a suitable solvent system.

The advantages and costs of integrating an amino acid racemase as crude extract in an enzymatic membrane reactor into a coupled process was investigated by Fuereder et al. (2016) for the production of methionine enantiomers. However, as mentioned in Sec. 2.2, the soluble enzyme quickly looses its stability and could only be operated in the range of a few days and with significant activity loss.

Enzyme immobilization is a powerful approach to minimize this activity loss. In the past years different racemases have successfully been immobilized [119, 120]. Two successful racemase immobilization protocols have also been established in the PCF group at the MPI in Magdeburg: an mandelate racemase (Sec. 3.2.1) and an amino acid racemase (Sec. 3.2.2) were immobilized onto carriers [42, 43]. Now the enzyme can be used in its immobilized form as an EFBR. A first approach of coupling an immobilized EFBR with chiral chromatography was done by Wrzosek et al. by establishing a method for the separation of *R-/S*-MA under coupling conditions [42]. The most recent approach was published last year and proposes a precise short-cut model for the sizing of the process units of a coupled setup [121, 122].

Additional integration of a solvent removal unit

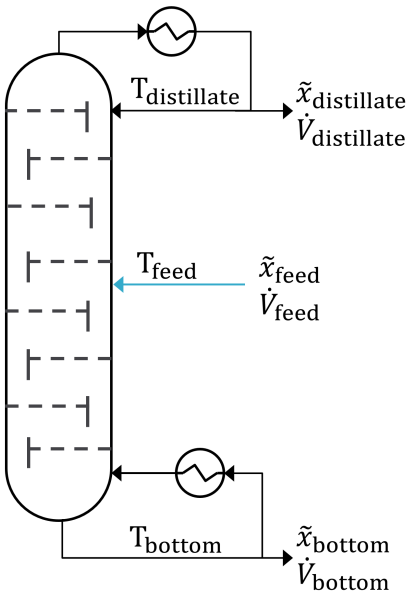

Fig. 2.9: Simple rectification column for the separation of a binary mixture.

There are two obvious solutions to avoid a dilution of the feed tank by the recycling stream: Either the fresh feed, which is mixed with the recycled fraction, is highly concentrated to maintain the initial feed concentration or the concentration of the recycled fraction needs to be increase to match the feed tank concentration. The first option is the easier one. Yet, it is only practical if the recycled stream is significantly smaller than the feed stream and the feed concentration is far below the solubility limit. If this is not the case, a concentration of the recycling fraction is inevitable.

The concentration can again be achieved in two ways: A previous coupling approach used membrane separation to concentrate the recycling stream [118].

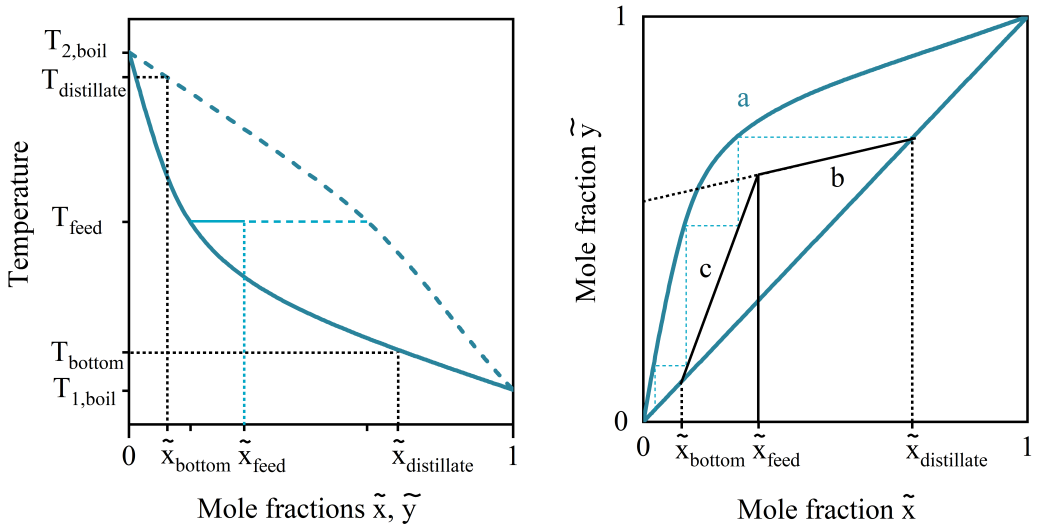

Fig. 2.10: Design of a rectification column based on (a) VLE-diagram and (b) McCabe-Thiele for given feed, bottoms and distallation mole fractions and temperatures.

Nanofiltration is an energy efficient concentration option, but it comes with the drawback of membrane fouling and contaminated permeate, which can contaminate the desorbent tank separation. A more common alternative is the evaporation of the solvent. When using evaporation for concentration of an alcoholic solvent, it has the additional advantage of removing especially the alcohol from the solution. This is favorable when using alcohol-sensitive enzymatic racemization since the alcohol fraction in the recycling stream can be reduced, before the stream enters the racemization unit.

For the separation of mixtures with a separation factor $\alpha < 10$, the evaporation can be realized with a rectification column, as shown in Fig. 2.9, with constant pressure and sufficient theoretical plates. Like in chromatography, the theoretical plates define the separation efficiency. In distillation, the alcohol fraction in the bottom, $\tilde{x}_{\text{bottom}}$, and distillate, $\tilde{x}_{\text{distillate}}$, of the rectification column can directly be controlled by their temperatures, T_{bottom} and $T_{\text{distillate}}$, respectively. Their direct correlation can be displayed in a T-x-y-diagram. In the T-x-y-diagram in Fig. 2.10 (a) the dew and bubble point curves are shown along with the resulting vapor-liquid-equilibrium of a feed of mole fraction $\tilde{x}_{\text{feed}}$ and T_{feed}. Based on the vapor-liquid-equilibrium (VLE) data, a McCabe-Thiele diagram (Fig. 2.10(b)) can be obtained. For given mole fractions of the two solvents, e.g. ethanol/water or methanol/water, in the feed, $\tilde{x}_{\text{feed}}$, in the column head, $\tilde{x}_{\text{distillate}}$, and bottom, $\tilde{x}_{\text{bottom}}$, all relevant temperatures and the number of required trays can be derived. The theory behind the diagram is not directly part of this work and therefore summarized in the App. D.1.

2.3.3 On-site process monitoring and control

Even though the above mentioned optimization approaches are great methods for process intensification and improvement, all of them increase the process complexity. Also, the trade-off of productivity and purity often leads to very narrow operation window. Therefore, small changes within the process, like a shifting feed composition, performance loss of the separating and reaction unit or inconsistent pumps, can threaten the adherence of e.g. purity specifications. While detailed process models can help with the prediction of some deviations, it is difficult to cover all aspects. Therefore, monitoring of the process is crucial for maintaining the desired product quality of complex systems and quick interventions in case of disturbances or deviations.

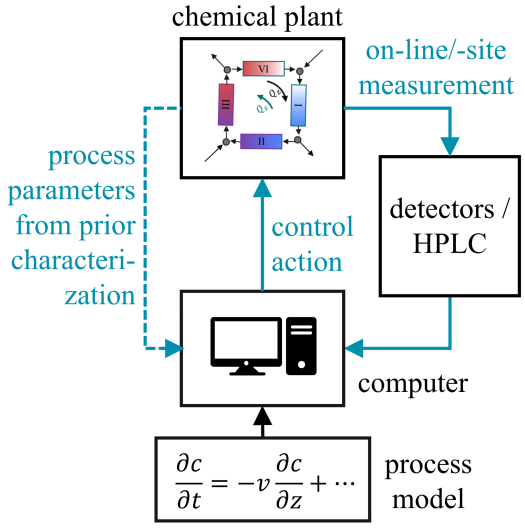

Fig. 2.11: Concept of on-site monitoring and control.

The second advantage of monitoring systems is that they reduce the detail of information which is required to run a process in the first place. Even without detailed process characteristics, a new process can be run and then optimized on-site, based on the provided monitoring information. This shortens the time for new process developments and allows the usage of rudimentary, underlaying models. The complexity of the models and optimization algorithm are limited by the given computation time of the system until a new set of parameters needs to be provided to the process control system. Promising approaches for automated control of SMB systems have been presented by Lee et al. (2018) and Kawajiri (2021) [123, 124, 107].

Foundation of a good control system is a monitoring system which can provide precise and reliable data from the right point in the process at the right time or time span. Furthermore, the monitoring system should neither remove too much sample or material from the process nor add unnecessary dead volume. A simple solution for the monitoring of chiral separation systems is therefore a combination of an UV-detector and a polarimeter [125]. However, while they provide instant and constant information about the process without removing material, their information

is often of less value. Reason for this is that signal can be unreliable due to baseline shift and a lack of base line separation.

A more complex, but also more reliable option is therefore an on-site HPLC system. When correctly designed and installed, it provides information of higher value [126]. However, its application is more complex, since it requires the optimization of the sample separation on the analytical column in the HPLC and an automated analysis of the resulting elution profiles.

2.4 Process evaluation and design aspects

In an integrated process, the effectiveness of the individual units and the overall process need to be considered. In this section performance indicators are introduced to later on compare different chromatographic processes for chiral separation in batch and TMB/SMB mode as well as for an evaluation of coupled systems, including by-product recycling by racemization.

While some performance indicators are only needed for either separation or reaction processes, others are identical or should be tailored to each unit. Universal information, which are also relevant for the process coupling, are the entering and eluting masses of all components i with $i = [1, 2]$ for a given unit in (quasi) steady-state during a specific time interval $\Delta t_{\mathrm{cycle}}$ within a cycle k:

$$m_{\mathrm{i,in}} = \int_{\mathrm{t_k}}^{\mathrm{t_k}+\Delta t_{\mathrm{cycle}}} (c_{\mathrm{i,in}} \cdot \dot{V}_{\mathrm{in}})\, dt \tag{2.75}$$

$$m_{i,\mathrm{out}} = \int_{\mathrm{t_k}}^{\mathrm{t_k}+\Delta t_{\mathrm{cycle}}} (c_{\mathrm{i,out}} \cdot \dot{V}_{\mathrm{out}})\, dt \tag{2.76}$$

Here, $\dot{V}_{\mathrm{in}}$ and $\dot{V}_{\mathrm{out}}$ are the component stream in and out of the unit, which are often assumed to be constant. The concentrations of component i, $c_{i,\mathrm{in}}$ and $c_{i,\mathrm{out}}$, are integrated over the time interval of the smallest repeating unit. This interval will be specified in the following sections for TMB and SMB chromatography and an EFBR. By dividing any mass collected during a time interval, m_i, by the aforesaid time, the corresponding mass flux is obtained:

$$\dot{m}_i = \frac{m_i}{\Delta t_{\mathrm{cycle}}} \tag{2.77}$$

Due to the binary nature of the system, the total mass flux is the sum of both eluting compounds:

$$\dot{m}_{\mathrm{tot}} = \dot{m}_1 + \dot{m}_2 \tag{2.78}$$

Also, both, the separation and the racemization unit, allow the targeting of either one of the enantiomers. Thus, in the following both options of targeting the less retained component (target = 1) and targeting the stronger retained component (target = 2) will be considered.

2.4.1 Evaluation of chromatographic processes

For batch and true or simulated bed chromatography different definitions of the mass flux at the inlet and outlet are required. Here, the differences are explained before general performance indicators are defined.

Mass flux in TMB and SMB chromatographic systems

In conventional TMB and SMB chromatography the feed is continuously injected between zone II and III:

$$m_{\mathrm{i,in}} = c_{\mathrm{i,feed}} \cdot \dot{V}_{\mathrm{feed}} \tag{2.79}$$

The outlet stream is not split into two time intervals but into two simultaneously eluting streams containing the raffinate $\dot{V}_{\mathrm{raff}}$ and extract $\dot{V}_{\mathrm{extr}}$ (see Sec. 2.1.7). When targeting the less retained enantiomer the average target and total masses flux are defined as

$$m_{\mathrm{tot}} = \int_{t_{\mathrm{k}}}^{t_{\mathrm{k}}+\Delta t_{\mathrm{shift}}} (\dot{V}_{\mathrm{raff}} \cdot (c_{1,\mathrm{raff}} + c_{2,\mathrm{raff}}))dt \tag{2.80}$$

$$m_{\mathrm{target}} = m_1 = \int_{t_{\mathrm{k}}}^{t_{\mathrm{k}}+\Delta t_{\mathrm{shift}}} (\dot{V}_{\mathrm{raff}} \cdot c_{1,\mathrm{raff}})dt \tag{2.81}$$

with $\Delta t_{\mathrm{shift}}$ being the time between two column shifts. Analogously, the target mass flux of the stronger retained enantiomer is defined as

$$m_{\mathrm{tot}} = \int_{t_{\mathrm{k}}}^{t_{\mathrm{k}}+\Delta t_{\mathrm{shift}}} (\dot{V}_{\mathrm{extr}} \cdot (c_{1,\mathrm{extr}} + c_{2,\mathrm{extr}}))dt \tag{2.82}$$

$$m_{\mathrm{target}} = m_2 = \int_{t_{\mathrm{k}}}^{t_{\mathrm{k}}+\Delta t_{\mathrm{shift}}} (\dot{V}_{\mathrm{extr}} \cdot c_{2,\mathrm{extr}})dt \tag{2.83}$$

accordingly. The associated mass fluxes are obtained by dividing the masses by the time between two shifts (Eq. (2.77)).

Key performance indicators of chromatographic systems

For the evaluation of chromatographic systems, often purity (Pu_i) requirements for the target compound are given and defined as the amount of target substance in the total collected mass (Eq. (2.78)):

$$\mathrm{Pu}_{\mathrm{target}} = \frac{\dot{m}_{\mathrm{target}}}{\dot{m}_{\mathrm{tot}}} \cdot 100\% \tag{2.84}$$

Purity requirements are often in a range of 98-99 %, but can also go up to >99.99 % for pharmaceutical applications In this work a purity of 99.0-99.5 % was targeted. The distomer purity was no criteria for optimization, as it was recycled and therefore only effected the productivity by indirectly reducing the intrinsic feed (Eq. (2.81)-(2.83)).

As representative parameters for economic efficiency, productivity and solvent consumption were chosen. The productivity, $\mathrm{Pr}_{\mathrm{target}}$, is given in terms of collected mass flux per total column volume

$$V_{\mathrm{tot}} = N_{\mathrm{col}} \cdot V_{\mathrm{c}} \tag{2.85}$$

or the volume

$$V_{\mathrm{CSP}} = N_{\mathrm{col}} \cdot V_{\mathrm{c}} \cdot (1 - \varepsilon_{\mathrm{t}}) \tag{2.86}$$

or the mass

$$m_{\mathrm{CSP}} = N_{\mathrm{col}} \cdot V_{c} \cdot (1 - \varepsilon_{\mathrm{e}}) \cdot \delta_{\mathrm{c}} \tag{2.87}$$

of chiral stationary phase (CSP) of the chromatographic system, as the latter is a decisive factor in the process economy:

$$\mathrm{Pr}_{\mathrm{target}} = \frac{\dot{m}_{\mathrm{target}}}{V_{\mathrm{CSP}}} \tag{2.88}$$

$$\mathrm{Pr}_{\mathrm{target,CSP}} = \frac{\dot{m}_{\mathrm{target}}}{V_{\mathrm{CSP}}} \tag{2.89}$$

$$\mathrm{Pr}_{\mathrm{target,wt}} = \frac{\dot{m}_{\mathrm{target}}}{m_{\mathrm{CSP}}} \tag{2.90}$$

Here, N_{col} is the number of columns applied and ε_e is the external or interstitial porosity between the particles, for which roughly $\varepsilon_e = 0.37$ can be assumed [127]. Unfortunately, often neither the porosity nor the mass of the stationary phases are provided by the manufacturer. For this work the porosity will be determined experimentally, while the density was assumed from the typical density of silica gels ($\delta_{\mathrm{c}} = 2.2$ g/cm^3).

The solvent consumption, $\mathrm{SC}_{\mathrm{target}}$, is the ratio of the required fresh desorbent and the mass flux at the target outlet.

$$\mathrm{SC}_{\mathrm{target}} = \frac{\dot{V}_{\mathrm{eluent}}}{\dot{m}_{\mathrm{target}}} \tag{2.91}$$

In case of SMB chromatography not only the desorbent stream, but also the eluent in the feed stream need to be considered:

$$\mathrm{SC}_{\mathrm{target}} = \frac{\dot{V}_{\mathrm{desorbent}} + \dot{V}_{\mathrm{feed}}}{\dot{m}_{\mathrm{target}}} \tag{2.92}$$

Main benefit of the process integration investigated here is the enhanced overall yield, $\mathrm{Y}_{\mathrm{target}}$, which is defined in Eq. (2.93). While the yield can theoretically reach 100 %, a possible incomplete recovery of the substance in the solvent removal unit leads to lower values. In this case yield can be determined with Eq. (2.93).

$$\mathrm{Y}_{\mathrm{target}} = \frac{\dot{m}_{\mathrm{target}}}{m_{\mathrm{tot,in}}} \tag{2.93}$$

Pressure drop

One important parameter when designing chromatographic systems is the pressure drop. The Ergun-equation is a good approximation for pressure drop estimation in packed beds [128]:

$$\Delta p = 150 \frac{(1-\varepsilon_e)^2 \cdot u_{\mathrm{int}} \cdot H \cdot \eta}{\varepsilon_e^3 \cdot d_p^2} \tag{2.94}$$

with $\varepsilon_e = 0.37$ [127]. The interstitial velocity u_{int} can also be expressed as a function of the flow rate $\dot{V}_z$ through a column z:

$$u_{\mathrm{int}} = \frac{4 \cdot \dot{V}_{\mathrm{z}}}{\pi \cdot D^2} \tag{2.95}$$

Furthermore, H and D are the height and inner diameter of the column and d_p is the particle diameter.

In case of multiple columns, like in SMB chromatography, the pressure drop through all columns must be added up and, in case of N identical columns, can be expressed as a function of the flow rates:

$$\sum_{z=1}^{N} \Delta p = \frac{150 \cdot 4 \cdot (1-\varepsilon_e)^2 \cdot H \cdot \eta}{\varepsilon_e^3 \cdot d_p^2 \cdot \pi \cdot D^2} \cdot \sum_{z=1}^{N} \dot{V}_z \tag{2.96}$$

2.4.2 Evaluation of a racemization reactor

Contrary to chiral resolution, the enzyme reactor is evaluated by the conversion $X_2(\tau)$ of the unwanted enantiomer in excess, e.g. E_2 into enantiomer E_1 at the column outlet:

$$X_2(\tau) = 2\frac{c_{2,0} - c_2(\tau)}{2\,c_{2,0} - c_{\mathrm{tot}}} \tag{2.97}$$

The maximal obtainable conversion of 100 % is achieved, if both enantiomers have the same concentration $c_1 = c_2$. Exploiting the expression for the concentration at the reactor outlet (Eq. (2.74)), the conversion at the reactor outlet can be predicted:

$$X_2(\tau) = 1 - \exp\left(2\nu_i \tau D_{\mathrm{carrier}} \frac{r_{\max}}{K_{\mathrm{M}} + c_{\mathrm{tot}}}\right) \tag{2.98}$$

Rearranging this equation for τ, results in

$$\tau(X_{2,\mathrm{out}}) = -\ln(1 - X_{2,\mathrm{out}}) \frac{K_{\mathrm{M}} + c_{\mathrm{tot}}}{2\,D_{\mathrm{carrier}}\,r_{\max}} \tag{2.99}$$

which can be used along with Eq. (2.73) to design the reactor size to reach a required outlet conversion $X_{2,\mathrm{out}}$.

However, for designing a reactor in a coupled setup, the more relevant parameter is the enantiomeric excess of a component i ($\mathrm{ee_i}$)

$$\mathrm{ee}_2 = \frac{c_2 - c_1(\tau)}{c_{\mathrm{tot}}} \tag{2.100}$$

which can be rearranged similar to Eq. (2.98) to determine the enantiomeric excess at the reactor outlet:

$$\mathrm{ee}_2(\tau) = \frac{c_{2,0} - c_{1,0}}{c_{\mathrm{tot}}} \exp\left(2\nu_i \tau D_{\mathrm{carrier}} \frac{r_{\max}}{K_{\mathrm{M}} + c_{\mathrm{tot}}}\right) \tag{2.101}$$

or the required retention time to obtain a desired $\mathrm{ee}_{2,\mathrm{out}}$:

$$\tau(\mathrm{ee}_{2,\mathrm{out}}) = \frac{K_{\mathrm{M}} + c_{\mathrm{tot}}}{2\nu_i D_{\mathrm{carrier}}\,r_{\max}} \ln\left(\frac{\mathrm{ee}_2 c_{\mathrm{tot}}}{c_{2,0} - c_{1,0}}\right) \tag{2.102}$$

For a given volumetric feed flow rate and inlet concentrations, the required amount of carrier to obtain a certain enantiomeric excess can be estimated:

$$m_{\mathrm{carrier}} = \dot{V}\,\frac{K_{\mathrm{M}} + c_{\mathrm{tot}}}{2\,\nu_i\,r_{\max}} \ln\left(\frac{\mathrm{ee}_2\,c_{\mathrm{tot}}}{c_{2,0} - c_{1,0}}\right) \tag{2.103}$$

Analogous to the productivity of a chromatographic system, the productivity of an EFBR can be expressed by the amount of converted enantiomer E_2 per time and the amount of carrier:

$$\mathrm{Pr}(X_{2,\mathrm{out}}) = \frac{0.5 X_{2,\mathrm{out}} (c_{2,0} - c_{1,0})}{D_{\mathrm{carrier}} \tau(X_{2,\mathrm{out}})} \tag{2.104}$$

2.4.3 Evaluation of a coupled setup

In an integrated setup of chromatographic separation and racemization of the by-product enantiomer some KPIs like productivity, yield and solvent consumption need to be reevaluated.

Due to the recycling of the by-product enantiomer, the only outlet of the coupled system is through the target stream. Hence, the only difference from a 100 % yield is the contamination of the target stream by the by-product. The yield of the coupled setup is therefore equal to the target purity (Eq. (2.84)):

$$\mathrm{Y}_{\mathrm{target,coupled}} = \mathrm{Pu}_{\mathrm{target}} \tag{2.105}$$

In case of recycling of the by-product enantiomer, and the respective stream, the solvent consumption is reduced to the amount of solvent in the target stream into the product tank:

$$\mathrm{SC}_{\mathrm{target}} = \frac{\dot{V}_{\mathrm{target}}}{\dot{m}_{\mathrm{target}}} \tag{2.106}$$

3 Material and methods

In this work the coupled system was studied for two case studies: *DL*-Met and *RS*-MA. For both systems an immobilized racemase was available to study the process intensification for the provision of pure enantiomers with optimal yield. The two model systems are small molecules with distinct characteristics and can each be racemized with a highly active racemase.

Methods of enzyme preparation were mainly developed by Thiane Carneiro, Kasia Wrozek and the group of Katja Bettenbrock. The setup for the characterization of the immobilized AAR in an EFBR and the stability tests are presented, which have been developed within the scope of the master thesis of Jonas Bollmann. The setup of the plant was realized with the help and experience of Ju Weon Lee as well as the electrical and mechanical workshops of our institute.

3.1 Model compounds for two case studies

Two model compounds are introduced, which are used in two case studies (CS). More details about their purity and suppliers as well as information about the solvents used in this work, can be found in App. A.

3.1.1 Case study I: *RS*-mandelic acid

MA belongs to the group of alpha-hydroxy acids, which are carboxylic acids with a substituted hydroxyl group on the alpha carbon and are best known for their applications in the cosmetic industry. But they are also key intermediates in the synthesis of pharmaceuticals and fine chemicals [129]. MA can serve as a model system to present this class of chemical compounds. The Fig. 3.1 and 3.2 show the chemical structure of both enantiomers and Tab. 3.1 summarizes its most important properties.

The *R*-enantiomer of MA is a versatile intermediate for chiral pharmaceuticals and a resolving agent in chiral resolution processes [130]. Hence, it is produced

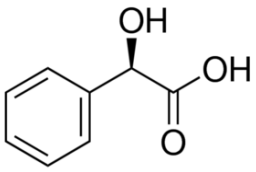

Fig. 3.1: *R*-mandelic acid (*R*-MA)

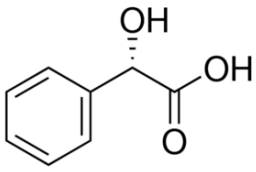

Fig. 3.2: *S*-mandelic acid (*S*-MA)

in a scale of about several hundred metric tons per year [131]. Because of this high demand for enantiopure *R*-MA, a variety of methods were developed for the production of this hydroxic acid and its chiral precursors. Often metal-based complexes, organic catalysts or enzymes as biocatalysts were used for an asymmetric synthesis [131]. The alternative is non-selective production with a subsequent enantioselective separation step.

Tab. 3.1: Chemical properties of *R*-/*S*-MA

Properties	
Formula	$C_8H_8O_3$
Molecular weight of MA	152.15 g mol^{-1}
Appearance	white crystalline powder
Solubility in water	1.587 g L^{-1}

3.1.2 Case study II: *DL*-methionine

Methionine (Met) is an α-amino acid and the *L*-form is one of the essential amino acid for humans and a precursor molecule for some other amino acids. The molecular structure of both enantiomers is given in Fig. 3.3 and Fig. 3.4. Due to its necessity for the metabolism of humans and many other species, Met production is relevant in the life science industry. Since the publication of its first isolation 100 years ago in 1923 by Mueller [132] methods for a racemic production have continuously been improved [133]. Today about 1 million annual tons [134] *DL*-Met are produced. Most of it is produced by chemical synthesis from methyl mercaptan, acrolein and hydrogen cyanide [135]. Chiral pure *L*-Met can be obtained by enzymatic conversion or fermentation [136, 137].

A biosynthetic production of Met from aspartate is possible [138], yet more expensive due to its requirement of enzymes. An overview of the properties of *DL*-Met is given

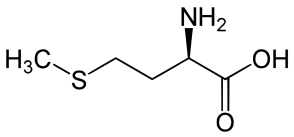

Fig. 3.3: *D*-methionine (*D*-Met)

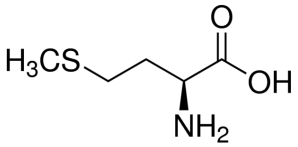

Fig. 3.4: *L*-methionine (*L*-Met)

Tab. 3.2: Chemical properties of *DL*-Met

Properties	
Formula	$C_5H_{11}NO_2S$
Molecular weight: methionine	149.21 g mol^{-1}
Appearance	white crystals
Std. enthalpy of formation	-789.4 kJ mol^{-1}
Solubility*: *DL*-Met at 20 °C and 30 °C	2.8 wt% and 3.5 wt%
Solubility*: *L*-Met at 20 °C and 30 °C	5.0 wt% and 5.9 wt%
Isoelectric point	pH 5.74

*[142]

in Tab. 3.2. Detailed solubility data can be found in Poleske et al. (2009) [139]. The separation of *DL*-Met on Chirobiotic TAG phases (Astec) in 35/65 MeOH and 5 mM NH_4Ac has been studied by Fuereder et al. 2014 [140] and on Chirobiotic T phases (Astec) using EtOH/H_2O by Petrusevska et al. (2006) [141].

3.2 Racemases and immobilization supports

According to the nomenclature committee of the International Union of Biochemistry and Molecular Biology, racemases belong to the enzyme class (E. C.) 5. In this work a mandelate racemase and an amino acid racemase are exploited. Both have been immobilized for increased stability and re-usability.

3.2.1 Case study : Mandelate racemase (E.C. 5.1.2.2) from *Pseudomonas putida*

The mandelate racemase E.C. 5.1.2.2 from *P. putida* catalyses the racemization of both enantiomers of mandelic acid. It was first described by Hegemann in 1970

[143]. Since then, its activity and production process was improved [144, 145]. Around fifty years later, an immobilization protocol for the racemase was established by Wrzosek et al. 2016 [42]. The racemase was immobilized on the carrier "Eupergit CM", a microporous, epoxy-activated acrylic support by multipoint covalent binding between the epoxy groups on the acrylic polymer and functional groups of the protein. Its kinetic parameters of the immobilized enzyme are given in Tab. 3.3.

Tab. 3.3: Kinetic parameters for Eq. (2.63) describing the catalytic activity of the immobilized mandelate racemase on "Eupergit CM" in an aqueous solution with 20 mM HEPES, 3.3 mM $MgCl_2$ pH 6.8 and 20 % MeOH [42].

Parameter	Symbol	Value	Unit
Michaelis-Menten coefficient	K_M	8.59	mM
max. reaction rate	r_{max}	169.5	$U/g_{carrier}$
Dosage	$D_{carrier}$	1512	$g_{carrier}/L$

3.2.2 Case study II: Amino acid racemase (E.C. 5.1.1.10) from *Pseudomonas putida KT2440*

The amino acid racemase (AAR, 45 kDa, pI = 7.03) used in this work is naturally expressed in *Pseudomonas putida* KT2440 DSM 6125 [146]. It was first purified and characterized by Lim et al. in 1993 [79] and patented ten years later because of its low substrate specificity by Ikeda et al. [147]. It catalyzes the conversion of the excess enantiomers using a pyridoxal-5'-phosphate (PLP)-dependent mechanism [81]. For its utilization, the DNA-sequence for the racemase was cloned into *Escherichia coli* Rosetta2 (DE3) by Wuerges et al. (2009) [148]. After fermentation, the racemase was purified on a sepharose column and tested regarding its activity for methionine and asparagine. The broad substrate specificity was confirmed by Radkov et al. (2013). Besides converting asparagine and methionine (Met), they also demonstrated its activity for seven other chiral amino acids: lysine, arginine, glutamine, alanine, serine, leucine and histidine. Yet, the enzymatic activity differs for each amino acid [149].

The AAR was immobilized on the carrier Lifetech ECR 8309F (Lifetech^{TM}, pore size 600-1200 A, 150-300 μm, stable pH range: 3-10), which is an amino-activated support with ethylene spacer. Immobilization occurs by forming a covalent bond between the aldehyde and the amino groups of the enzyme, after a pre-activation of the carrier with glutaraldehyde.

3.3 Experimental procedures for the characterization of the racemase

The protocols for the fermentation and purification have been developed and improved in the past decade in Research Center Jülich by the group of Stephan Lütz and in the MPI in Magdeburg by the PCF group and the lab of Katja Bettenbrock. In the following, the established batch fermentation method is briefly introduced. Next the new and improved fed-batch fermentation, developed for this work in collaboration with Katja Bettenbrock and Andrea Schütze, is presented. The next section describes the small scale purification method, developed by Thiane Carneiro and Claudia Bednarz, which was used for the characterization of the immobilized AAR, followed by a method for the purification of larger amounts of the AAR with IMAC slurries. The latter method has been developed together with Stefanie Oberländer. Both, the fed-batch fermentation and the large scale purification were the focus of the master thesis of Louise Witzlack. The immobilization protocol in the last part of this section has been optimized by Thiane Carneiro from the PCF group at the MPI Magdeburg.

3.3.1 Amino acid racemase fermentation

The AAR was produced by over expression in *E. coli* BL21 (DE3) by batch and fed-batch fermentations. The main difference between the preexisting batch protocol and the implemented fed-batch protocol was the higher starting optical density (OD), the continuous glucose feed, the increased Isopropyl β-D-1-thiogalactopyranoside (IPTG) concentration and the increase of the fermentation time from 9-10 to 22 h. These changes led to an increase from 9 to 230 mg_{AAR}/L_{ferm}. Detailed information about the different fermentation methods and media are given in App. B.2.

3.3.2 Amino acid racemase purification

Before the protein purification the cells were disrupted by high-pressure homogenization (EmulsiFlex-C5, Avestin Inc.), followed by centrifugation (25 000 g, 4 °C, 25 min, Sartorius Sigma 3K30) and a filtration. The co-factor PLP was added to a final concentration of 100 μM [150]. The resulting crude extract (CE) was then purified in small and large scale procedures. All analysis methods applied during the purification steps are summarized in Sec. 3.3.5.

Purification with a pre-packed "HisTrap FF crude" column

The packed column "HisTrap FF crude 5 mL" (GE Healthcare) was used for small scale purification in an Äkta system (Purifier 25, GE Healthcare, 4 °C). Due to a binding capacity of the HisTrap FF crude of around 20 mg/mL, with each run about 100 mg AAR can be purified with each purification. The protocol with all buffers is given in App. B.1. Afterwards, the concentration of the purified AAR, c_{AAR} in the relevant fractions was determined with "NanoDrop UV/VIS" (UV/VIS = ultraviolet and visible light) spectrophotometry and used to map the elution profile obtained from the Äkta-system. The elution profile during the elution step showed two dominant peaks and sometimes a small intermediate peak. The first peak contained inactive racemase. Thus, only the fractions containing the second peak were collected.

Purification with gravity-flow columns and different IMAC slurries

For the application of the immobilized AAR in larger scale applications and for the coupling with the fluidized bed preferential crystallizer of Jonathan Gänsch (*PCF group at the MPI Magdeburg*), large quantities of AAR need to be purified. For this purpose different resins were compared with respect to their capacity and ability to purify the AAR with a high yield and purity. Therefore, seven IMACs were tested in a 1-mL- and 5-mL-scale and different loading volumes. Their properties, according to the manufacturers, are summarized in Tab. 3.4. The main difference to the purification with the pre-packed column was the incubation time of 1 h during which the cell extract and the resin slurries were mixed at 4 °C. Afterwards, the mixture was filled into the gravity-flow columns and flushed with the washing and elution buffers, as shown in Fig. B.5. The detailed protocol can be found in App. B.3.

3.3.3 Immobilization

All pure fractions were combined and after a buffer exchange and concentration, they were covalently immobilized onto the carrier ECR 8309F (Purolite) to a final loading of 35-37 $mg_{AAR}/g_{carrier}$. After an incubation time of 18 h, the immobilized AAR was filtrated with a crucible filter (Schott) and then stored at 4 °C. More detailed information are given in [43].

Tab. 3.4: Comparison of available slurries with their by the manufacturer claimed properties and the resulting hypothetical amount of enzyme, which could be purified with it.

Name of resin	Company	Capacity mg/mL*	Re-usability -	Tot. enz. mg/mL*	Appl.
Ni Sepharose 6 Fast Flow	VWR	40	5	200	P
HisPur Ni-NTA SF Agarose	Fisher	≤ 70	≤ 25**	≤ 1500	P
Pierce High C. Ni-IMAC	Fisher	≤ 60	≤ 10***	≤ 600	P
Chromalite MIDA/Co	Purolite	?	?	?	P&I
Chromalite MIDA/Ni	Purolite	?	?	?	P&I
Chromalite MIDA/Cu	Purolite	?	?	?	P&I

P = purification only; P&I purification and simultaneous immobilization;
Fisher = Fisher Scientific
* unit of capacity and total amount of enzyme: mg/mL = mg_{enz}/mL_{slurry}
** for their prove only six of their 25 runs were done with the purification from a lysate.
*** an attached picture showed visible decline of capacity already in the 8th run.

3.3.4 Packing of the enzymatic fixed bed reactor

For characterization of the EFBR, 56 mg loaded carrier and 25 mg of glass wool, to fill the remaining column volume, were packed in a BenchMark Microbore column (Omnifit Labware). For the packing, a 5 mL pipette tip was fixed to the upper part of the column (see Fig. 3.5) Next, the column and the tip were filled with water. Then, the slurry was transferred with a pipette into the funnel and the resin sank into the column. The remaining empty space in the column was filled with glass wool. For a compression of the freshly packed the bed, it was connected to the HPLC and the flow rate through the column was gradually increase until a pressure of 80 bar was reached. Relevant column parameters are given in Tab. 3.5.

3.3.5 Methods for the quantification of racemase in samples

Three different analysis methods were used for qualitative and quantitative analysis of the concentration of AAR in samples:

Sodium dodecyl sulfate polyacrylamide gel electrophoresis (SDS-PAGE) is an electrophoresis method which separates proteins based on their mass [151]. When applied along with a calibration standard, the presence of the AAR, which has a size

Fig. 3.5: Setup for the packing of AAR in a 25x3 mm BenchMark Microbore column.

Fig. 3.6: packed EFBR in comparison to a 150x10 mm Chirob T column used for SMB chromatography

Tab. 3.5: Properties of the EFBR used for characterization (see Fig. 3.6)

Property	Symbol	Size	Unit
Column height	L_c	25	mm
Bed height	L_{reactor}	13 ± 0.5	mm
Column diameter	d_R	3	mm
Bed volume	V_R	0.092 ± 0.004	mL
Mass of carrier	m_{carrier}	56 ± 2	mg
Loading	q_{AAR}	B-1: 37	$mg_{AAR}/g_{carrier}$
		B-2 & B-3: 35	$mg_{AAR}/g_{carrier}$
Porosity	ε_t	0.83 ± 0.05	-
Dosage	D_{carrier}	732 ± 25	mg_{AAR}/mL

of 45 kDA, in a given sample can be confirmed. This qualitative method can be used for CEs and purified fractions.

NanoDrop-assay for AAR concentration Protein concentration can be determined with NanoDrop UV/VIS spectrophotometry at 280 nm. Since it requires an individual calibration of each protein, it was only used to analyze purified samples. The calibration coefficient depends on the absorption properties of all amino acids of the protein and can e.g. be calculated on https://www.novoprolabs.com/tools/protein-

extinction-coefficient-calculation. With the adsorption coefficient of the AAR, k_{AAR} = 0.787, the AAR concentration is obtained with:

$$c_{\mathrm{AAR}} = k_{\mathrm{AAR}} \cdot A_{280} \tag{3.1}$$

Polarimeter-assay for free AAR activity The activity of the free enzyme was determined with a modification of the assay described by Carneiro [43]. Here, the substrate was a 20 g/L *L*-Met solution. Small samples of solutions with free AAR (1-10 μL) were injected into the substrate solution. The mixture was injected into a polarimetric cell (Modular Circular Polarimeter (MCP) 500, Anton Paar) and the racemization was monitored as a function of the decreasing optical rotation at 365 nm.

3.3.6 Setup for the characterization of immobilized racemase in an enzymatic fixed bed reactor

All experiments were carried out by connecting the packed EFBR to a HPLC system (Agilent Technologies 1200 and 1260). The activity was tested for substrate concentrations in the range of 10-40 g/L and with solvents containing alcohols or phosphate buffers. For each inlet substrate solution four to six residence times, τ, were investigated by a stepwise, randomized change of the flow rate in the range of 0.5-3.7 mL/min (p ≥ 80 bar). The highest investigated concentration was decreased for later experiments to avoid crystallization in the tubing at the EFBR outlet [139]. The degree of conversion at the reactor outlet was monitored online with a "PDR-chiral Advanced Laser Polarimeter" (PDR-Separations LLC), which was connected to the HPLC-System. Once steady state was reached, a sample was drawn for each flow rate. The samples were analyzed in duplicate using HPLC (see Tab. 3.9). The ratio of the peaks correlated directly to the ratio of the two enantiomers and thus the conversion rate.

The initial reaction rates were determined by fitting the data points of each substrate concentration to Eq. (2.98). Then the estimated retention time for a conversion rate of 20 % (τ(X=0.2)) was extracted from the fit and used to obtain the initial reaction rate:

$$r_0 = \frac{X_L c_{L,0}}{\tau(X_L = 0.1)\, D_{\mathrm{carrier}}} \tag{3.2}$$

A non-linear fit was then used to estimate the corresponding MM parameters (Eq. (2.63)). The conditions under which the AAR was studied, are listed in Tab. 3.6.

Tab. 3.6: Properties of the enzymatic fixed-bed reactors used for characterization. All solutions have been prepared with Milli Q water (Millipore Q-Pod MilliQ).

Operating parameter	Range
Flow rate	0.5-3.7 mL/min
Temperature	10-30 °C
pH range	6-8
Buffer and salt	20 mM NaH_2PO_4/Na_2HPO_4 + 20 mM NaCl (see App. B.1).
EtOH or MeOH	0-10 vol%

It is worth mentioning, that in other work the conversion rate chosen for the initial reaction rate was sometimes only 10 %, which of course would have led to higher initial reaction rates. However, since the reaction rate could not be measured at lower conversion rates, the conversion rate of $X = 0.2$ was chosen in this work. More detailed information and a graphical explanation are provided in App. B.7.

3.3.7 Setup for stability test of the racemase under storage and operating conditions

The stability of the enzyme under operating conditions was tested by exposing an EFBR at room temperature to a constant flow of 1.0 mL/min water and later on 95/5 H_2O/EtOH over a time of 10-60 days. Every 1-3 days, the remaining activity of the EFBR was tested by measuring the conversion rate of 10 g/L *L*-Met after a residence time of $\tau = 1.8$ and 4.5 s (which corresponds to flow rates of 1.0 and 2.5 mL/min) with the method described in Sec. 3.3.6.

3.4 Experimental procedures for the characterization of enantioselective chromatography

Chromatography was studied for two purposes: fast and reliable analytics and productive preparative applications with high purity. The later one had been studied

as single column chromatography and with SMB chromatography. In the following the applied experimental procedures are explained. Unless stated otherwise, the experiments were performed on an 1260 HPLC system with a diode array detector (both from Agilent, Palo Alto, USA). The used devices and their specifications are listed in App. A. All solutions have been prepared with Milli Q water (Millipore Q-Pod MilliQ).

3.4.1 Applied chiral chromatographic columns

In this work the chiral stationary phase (CSP) *Astec Chirobiotic T* from Merck KGaA (Darmstadt) was used in different column and particle sizes. The CSP is a spherical silica gel with a pore size of 100 Å with covalently bound Teicoplanin, which is a macrocyclic glycopeptide with 23 chiral centers. The centers surround four cavities and provide a large selectivity for plenty amino acids, peptides and amines. Furthermore, compared to other commercially available phases, it does not require organic solvents, but can operate with aqueous eluents at moderate pH values. According to the supplier a void volume of about 70 % can be assumed [152]. The smallest Chirobiotic T column was used for the on-site analytics (Column OA-a) of the SMB chromatography system with CS-I, the middle one for the initial characterization of the adsorption behavior of CS-I and CS-II (Column OA-b) and the large columns were used for the preparative chromatography (PC) applications for CS-I with large pulse injections (Column PC-I) and for the experiments with CSII and in the SMB (Column PC-II). Further characteristics of this stationary phase and the used column sizes are summarized in Tab. 3.7.

Tab. 3.7: characteristics of the Astec Chirobiotic T chiral HPLC-column (Supelco, Merck KGaA, Damstadt)

Characteristic	**Column**			
	OA-a	**OA-b**	**PC-I**	**PC-II**
Column length [mm]	100	250	150	150
Column diameter [mm]	2.1	4.6	10	10
Particle size [μm]	5	5	15	5
Max. operating pressure [bar]	110	170	110	110
Maximal pressure [bar]	241			
Temperature stability [°C]	0 - 45			
pH-range [-]	3,8 - 6,8			

3.4.2 Characterization of adsorption behaviour

A brief study of the impact of solvents on the resolution of a mixture on a given column can best be done by studying the elution profile of small pulse injections in the tested solvents. Once suitable solvents are selected, sufficient knowledge about the plant dead volumes and the column porosity are required for an accurate characterization of the adsorption behavior. Finally, the adsorption isotherms can be determined. In this work, primarily the peak-fitting method and the perturbation method were used (see Sec. 2.1.5). The case specific methods are explained below.

Determination of plant dead volume and column porosity

The plant volume, V_{plant}, can be measured, if the columns are removed from the chromatographic system and a small pulse is injected. The time after which the pulse elutes or creates an absorption profile in the detector correlates to the dead volume (see Eq. (2.13)). Based on the plant volume, the dead volume, V_0, of a column and its internal porosity can be determined. Therefore, the column is build installed in the chromatographic system and a non-retained, pore-penetrating tracer substance is injected. For chiral stationary phases, which interact with almost any molecule, such a substance is difficult to find. Thus, small injections of different alcohols were tested to verify the by the supplier proposed 70 % void volume. From the measured residence time, t_{R}, the column void volume and porosity can be calculated with Eqs. (2.11)-(2.13).

Small pulse injections for Henry coefficient and plate number estimation

In this work, small pulse injections (see. Sec. 2.1.5) were used in a solvent screening for CS-II. The solvents were evaluated based on the Henry coefficients (Eq. (2.17)) and the separation efficiency (Eq. (2.21)) of *D-/L*-Met on the Chirobiotic T stationary phase. Different solvent systems were tested for the operation of the SMB plant and the development of a rapid online analysis. For these purposes the impact of temperature, EtOH and MeOH on the resolution were studied with small pulse injections of 0.1-5 μL of 1-20 g/L *D-/L*-Met onto the column OA-b (see Tab. 3.7). The plate numbers and HETP were studied in the required flow rate of each column. All tested operating conditions are given in Tab. 3.8.

Tab. 3.8: Operating conditions with varying solvent conditions, temperatures and flow rates for studying the resolution of *D*-/*L*-Met on the Chirobiotic T columns from Tab. 3.7.

Operating conditions	Range
Flow rate	0.2-3.0 mL/min
Temperature	10-20 °C
EtOH or MeOH in H_2O	0-50 vol%

Adsorption isotherm determination from large pulse injections

The pulse injection method was used for the adsorption isotherm parameter estimation of CS-I. Therefore, pulses with volumes of 5-100 μL with 20 g/L *R*-, *S*- and *R*-/*S*-MA were injected onto the Chirobiotic T column PC-I (see Tab. 3.7) with an eluent with 20 mM HEPES, 3.3 mM $MgCl_2$ in 20/80 MeOH/H_2O (M2080) at pH 6.8. The elution profiles were then used as in Eq. (2.22) with the method elaborated in Sec. 2.1.5 for the adsorption isotherm parameter estimation.

Adsorption isotherm determination with the perturbation method

The adsorption isotherm parameters of CS-II (*D*-/*L*-Met) were measured with the perturbation method in M2080 and 20/80 EtOH/H_2O (E2080) with 2.5, 5, 7.5 and 10 g/L *D*- and *L*-Met as well as in 40/60 EtOH (E4060) up to 5 g/L *D*- and *L*-Met. Once each plateau was reached and the absorption signal of the UV-detector was constant, small 1 μL pulses of deviating concentrations were injected onto the loaded column. The evaluation of the retention times of the resulting small peaks was done by calculation of the local total derivatives with Eq. (2.26) and fitting the data points to the derivatives of the respective isotherm functions.

3.4.3 Analytical chromatography methods

A reliable analysis of *D*-/*L*-Met samples was required for the characterization of the EFBR (Sec. 3.3.6), the SMB process (Sec. 3.5.1) and the monitoring of the mini-scale plant (Sec. 3.5).

Off-line analysis of *DL*-Met samples and other amino acids

For the analysis of the enzymatic activity of the EFBR and an off-site analysis of SMB samples, the concentration of *D*- and *L*-Met was obtained from calibration data and the elution profiles of pulse injections of the samples with a flow rate of 1 mL/min at 215-220 nm. Furthermore, separation conditions for the other amino acids arginine (Arg), asparagine (Asn), glutamine (Gln) and, serine (Ser), were required for the analysis of the racemization samples of the experiments presented in Sec. 4.2. All methods are summarized in Tab. 3.9.

Tab. 3.9: Separation conditions of the tested amino acid (AA) for the analysis of the racemization samples.

DL-AA	Column	Eluent	Temp. °C	Wavelength nm
Arg	Chirob. T [1]	20 mM AAc [3], pH 4.1: MeOH (50:50)	23	205
Asn	Chirex [2]	Perchloric acid, pH 1	4	210
Gln	Chirob. T [1]	0.1 mM NaH_2PO_4:H_2O (60:40)	25	220
Met	Chirob. T [1]	MeOH:H_2O (60:40)	25	220
Ser	Chirob. T [1]	EtOH:H_2O (70:30)	20	210

[1] Chirobiotic T, 250 mm x 4.6 mm (OA-b), 5 μm, [2] Pheomenex, 250 mm x 4.6 mm, 5 μm, [3] Ammonium acetate

On-site analysis of *DL*-Met samples

For the rapid on-site analysis (OA) of the samples from the mini-scale plant, the separation of *D-/L*-Met was optimized on the OA-a column (100x2.1 mm, Tab. 3.7) to analyze samples with an injection volume of V_{inj} = 0.1 μL in under 2 min. With the conditions in Tab. 3.10 an almost perfect baseline separation can be acchieved. The addition of formic acid improves the peak sharpening.

Tab. 3.10: OA conditions for analysis of *DL*-Met samples.

	Column	Eluent	Temp. °C	Wavelength nm
Met	Chirob. T [1]	800:200:0.2 EtOH:H_2O:FA [2]	25	205

[1] Chirobiotic T, 100x2.1 mm (OA-a), 5 μm, [2] FA = Formic Acid

3.5 Mini-scale plant coupling simulated moving bed chromatography with fixed bed enzymatic racemization

The mini-plant consists of three of the units, which have been presented above: an SMB chromatography unit (Fig. 3.7) for the separation of the chiral compounds, an evaporation unit (Fig. 3.9) to concentrate the recycling stream and reduce its alcohol content, and an enzymatic fixed bed reactor (Tab. 3.5) for the racemization of the unwanted enantiomer in the recycling stream. In this section, first the design and operation of the units is presented before the integrated setup introduced.

3.5.1 Design and operation of the simulated moving bed chromatography unit

The SMB unit used in this work is a Knauer SMB Pilot Unit "CSEP C9". The flow scheme of the SMB unit is shown in Fig. 3.7. It can be operated with 4, 8, and 16 columns and is operated with four columns in this case. The plant volume was estimated by measuring the length of all capillaries and adding 1.0 mL per pump. Since only four of the six available Chirobiotic T columns (150x10 mm, PC-I; Tab. 3.7) were needed, all columns were tested in an Agilent 1200 HPLC unit and their porosities and Henry coefficients for *D*- and *L*-Met were compared. The four most similar columns were then used for the operation of the SMB unit.

In combination with a maximum pressure limit of the system of first 60 bar and later on 80 bar, the column could only be operated for 20/80 EtOH/H_2O up to 0.9-1.0 mL/min and for 20/80 MeOH/H_2O up to a flow rate of 1.5-1.7 mL/min in zone I. Up to this flow rate the four pumps were tested individually and all tohether and their accurate pumping could be confirmed with an acceptable error margin of 2 %. The calibration process has been described in detail in the Bachelor Thesis of Xenia Becker (2021) [153].

Based on the adsorption isotherm parameters of CS-II and the triangle theory (see. Sec. 2.1.7) multiple experiments were performed to validate the prior determined parameters of the SMB-unit and the adsorption parameters. Useful start-up and operating instructions are given in App. D.3.

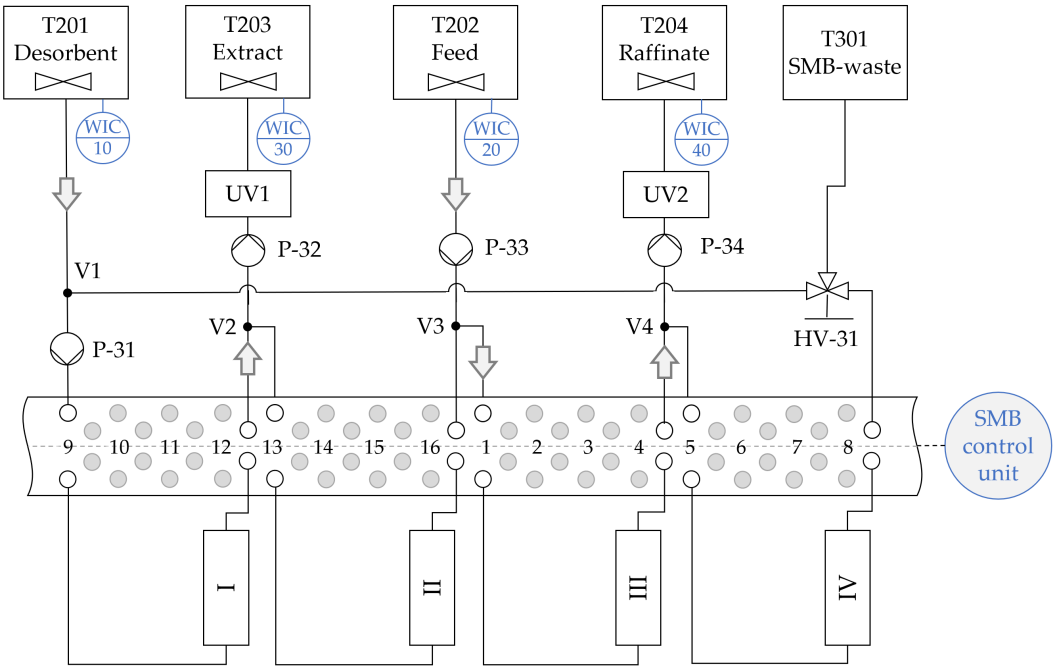

Fig. 3.7: Flow scheme of the 4Z-SMB-unit with one internal pump in Zone I (P-31), and three external pumps which provide feed (P-33), and remove the extract (P-32) and raffinate (P-34).

3.5.2 Design and operation of the evaporation unit

In order to reach a quasi-steady-state of the coupled process (see Fig. 1.3), the recycling stream needs to be concentrated before being fed back to the feed tank. Furthermore, the MeOH/EtOH (up to 20 vol% EtOH or MeOH in H_2O) needs to be removed before the recycling stream enters the EFBR. Thus, the goal of the evaporation unit was twofold: concentration of the racemic mixture and reduction of the alcohol content in the recyclate.

Design of the evaporation unit

Based on the Wilson-model and the set of equations and parameters given in the App. D.1, the vapor-liquid-equilibrium (VLE)-diagrams for EtOH/H_2O and MeOH/H_2O were plotted. The concentration of the liquid feed (F) varries in the range of 1-3 g/L depending on whether the extract or raffinate outlet is recycled and the exact operating conditions of the SMB. To increase the recyclate back to the feed concentration of the SMB chromatography unit of 20 g/L *DL*-Met, 30-90 % of the

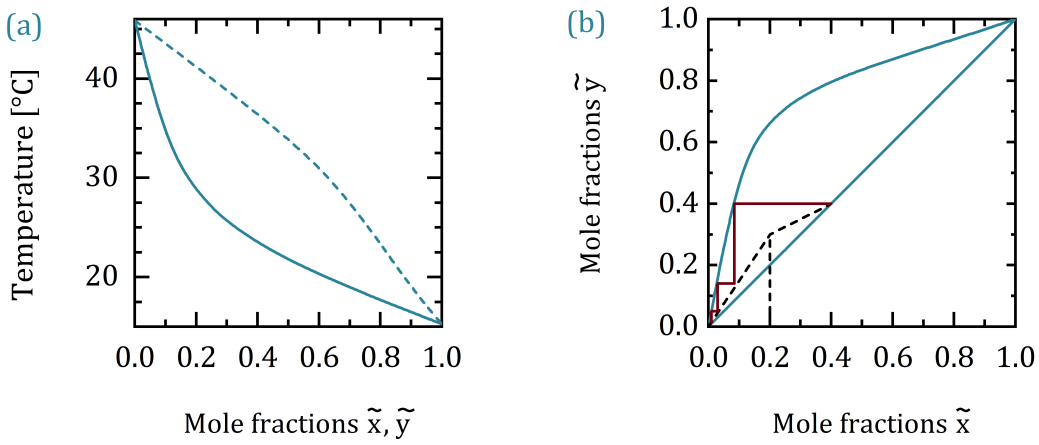

Fig. 3.8: (a) T-x- and T-y-diagram for MeOH in H_2O at 100 mbar(a); (b) VLE-diagram.

liquid need to be evaporated. While this requires sufficient head intake, it can be achieved in a one step evaporation.

However, the stripping and rectification lines in the VLE-diagram in Fig. 3.8(b) show that the reduction of the alcohol content of the liquid bottom fraction (B) from 20 % to less than 5 % more than one separation step is required. Thus, a small rectification column was necessary. Even though this column might not be relevant for all sections, it ensures that the following EFBR will less likely be exposed to high alcohol concentrations. Also, since the rectification could be done in one step, the feed had to enter at the top of the rectification column.

Installation and operation of the evaporation unit

The flow scheme of the installed evaporation system is shown in Fig. 3.9. It includes a small rectification column (3x15 cm, hollow glass beads), a double walled stirred tank reactor for the collection of the bottoms liquid, a distillate tank and two total condenser. The system is operated at 100-300 mbar(a), which are controlled by a vacuum pump (PC 3001 VARIO select). All other pumps are mzr-2921X1 from "HNP Microsysteme GmbH", Schwerin. The liquid feed from the SMB distomer outlet is entering at the head of the rectification column. The vapor is condensed in the first total condenser to the distillate tank where it can be collected, pumped to the desorbent tank of the SMB process or be used as a re-flux to cool the head of the rectification column. The temperature at the head is adjusted to match the desired mole fraction for the required concentration as shown for 40 vol% MeOH in Fig. 3.8. The second condenser was installed to prevent vapor reaching the vacuum pump.

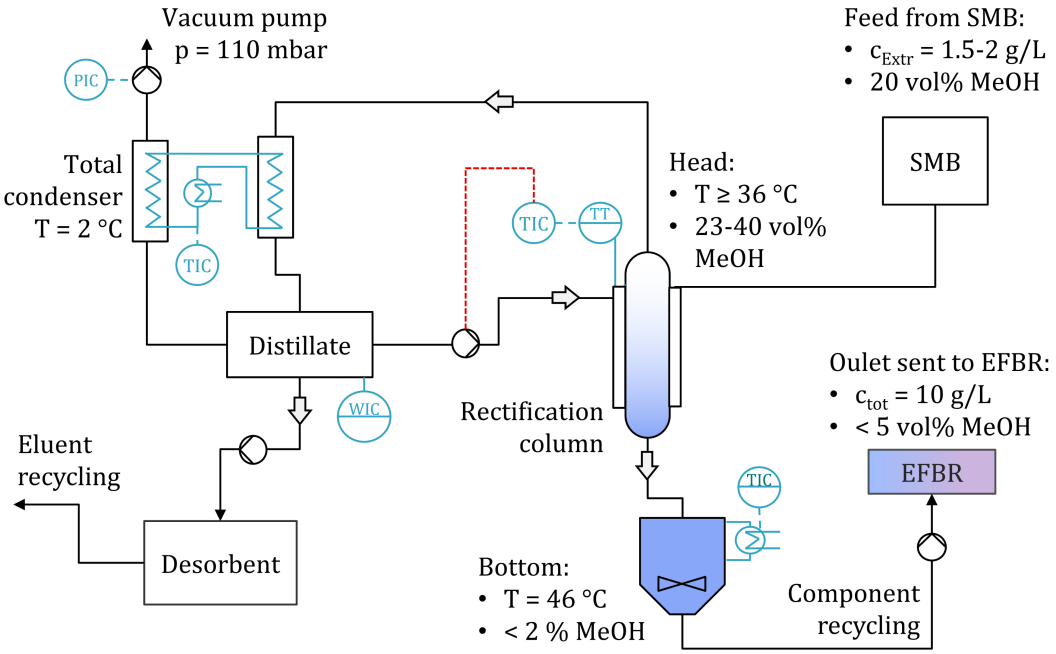

Fig. 3.9: Assembled evaporation system for the concentration of the distomer stream of the SMB process and simultaneous alcohol removal before the bottoms product is transported to the EFBR.

The liquid at the bottom of the rectification column (bottoms product) is almost free from alcohol and concentrated. Since its temperature is close to the evaporation temperature of water, the reactor outlet was realized at the lowest point in the reactor and the pump was placed even lower to avoid evaporation in the capillaries.

The plant was first operated with EtOH/H_2O-mixtures at 100-300 mbar(a) to study the system, before moving to MeOH/H_2O and then *DL*-Met in 20/80-MeOH/H_2O and finally the outlet of the SMB process with a pressure of 110-120 mbar(a). During the process the alcohol fraction in the collected samples was analyzed with a Densitometer (Mettler Toledo DM40) and the *DL*-Met concentration was analyzed with HPLC (Sec. 3.4.3).

One crucial adaptation to the initial setting was to change the fittings of all connections at the evaporation outlets from the stainless steel fittings provided by HNP to one-way-fittings, of the type "check valve outlet assembly, 1/4-28, (Perfluor), 1pc/PAK" (Upchurch Scientific). The allowed a reliable pump performance and adjustment of the flow rates. More explanations are given in App. D.3.

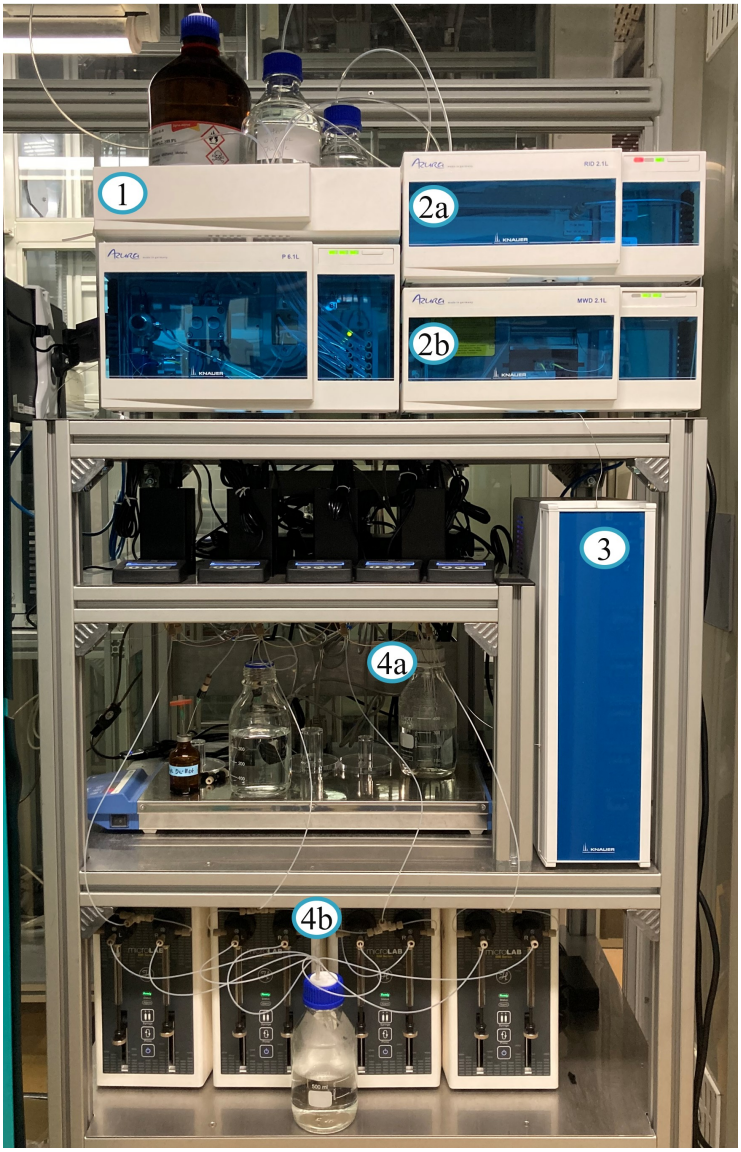

Fig. 3.10: Setup of the OA unit with a quarternary pump (1), an RI- (2a) and an UV/VIS-detector (2b) and a column oven (3) from Knauer and two kind of sampling options (4a) and (4b).

3.5.3 Design and operation of the on-site analytic system

In order to ensure a stable operation of the mini-plant and see the effect of disturbances on the process, a rapid on-site analysis (OA) is necessary. This OA-system (Fig. 3.10) was designed and build by Ju Weon Lee. It includes a quarternary pump (1), an RI- (2a) and an UV/VIS-detector (2b) and a column oven (3) from Knauer and two kind of sampling options: a six-port-valve for up to six connections for by-pass-samples and four syringe pumps for measurement of averaged concentrations

from small buffer tanks. The software of the system is based on LabView and is integrated into the LabView user interface of the SMB system. There it displays the determined concentration of the samples over time.

For its application with the mini-scale plant two syringe pumps and two by-pass-connections are used and connected to the mini-plant as shown in Fig. 3.11. The concentrations at the extract and raffinate ports of the SMB unit follow a saw-tooth profile. In order to obtain information about the average concentration of a cycle, a part of the outlet flows of the SMB unit is sent via a by-pass to two small HPLC-vials with a volume of about 1.8 mL in which the flow is mixed. The flow of the by-passes is controlled by the syringe pumps, which continuously pumped the collected samples through six-way-valve back to the plant. The other two by-pass sample connections are directly after the evaporation unit and after the EFBR. Here the concentrations are no longer periodically changing and the entire flow can be directed through the six-port-valves. During the time of one SMB cycle samples of all four sample points are taken by consecutive switches of the six-way-valves, each sending 0.5 μL sample onto the analytical column.

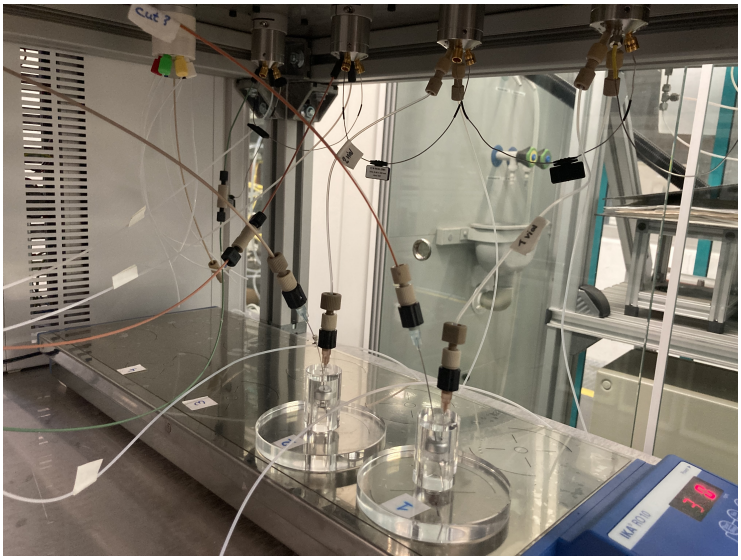

Fig. 3.11: Wiring of the tubes connecting the OA with the mini-plant.

The sample were injected onto a Chirobiotic T column OA-a (Tab. 3.7), which was heated in the column oven to 30 °C. The eluent was 800:200:0.2 EtOH:H_2O:Formic Acid and the HPLC system was operated with a flow rate of 0.5 mL/min. The system injected four samples within each SMB cycle and evaluated the elution profiles (exemplary shown in Fig. 3.12) by integrating the profiles between preliminary fixed time points and conversion based on individual quadratic calibration curves for each of the four samples.

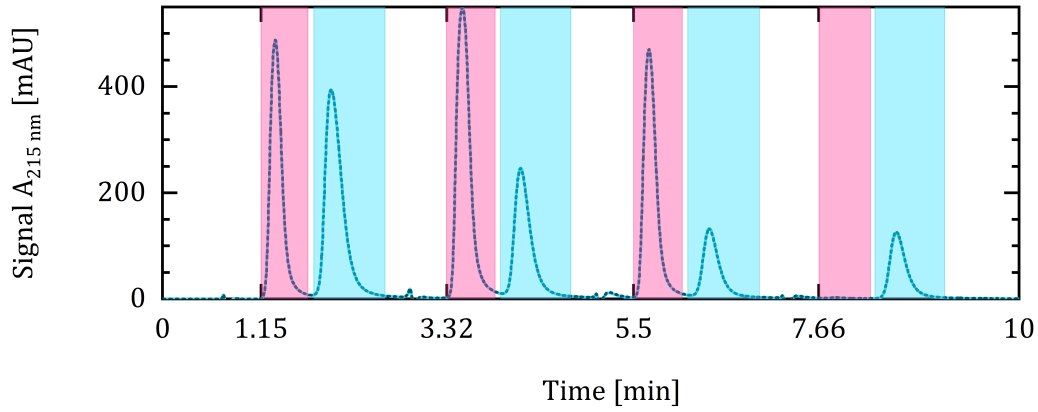

Fig. 3.12: Exemplary elution profile of the OA-unit with pink and blue areas in which the profile is integrated for *L*- and *D*-Met, respectively.

3.5.4 Combination of chromatographic separation and racemization in the plant

After characterization of the chiral chromatographic separation, the enzymatic racemization and the evaporation as single units, they were finally combined in an integrated setup. The resulting mini-plant was designed, implemented and characterized and the production of pure enantiomers was studied for different settings. All units are connected with capillaries and pumps of type mzr-2921X1 from HNP Microsysteme. The mini-plant is shown in Figure 3.13. A detailed flow-scheme and a list of all components are given in App. D.3. The plant was assembled in the Technikum of the MPI Magdeburg and requires two process control systems. The SMB unit is controlled with an interface based on LabView while the rest of the plant is controlled with the Siemens process control system "WinCC" (Siemens), provided by the electrical workshop of the MPI Magdeburg.

The experiments coupling continuous chromatographic separation with enzymatic racemization were carried out in the designed SMB-EFBR-plant. Detailed operating instructions and the manual are provided in the App. D.3.

Fig. 3.13: SMB-EFBR-plant. Top: Distillate tank, rectification column, feed and desorbent tank; middle: evaporation tank, EFBR (OA in the back), product tank, SMB unit; bottom: thermostats and evaporation pump.

4 Characterization and production of an immobilized amino acid racemase

A key element for increasing the yield of pure enantiomer provision from a racemate is the recycling of the unwanted enantiomer (distomer). Racemases can perform this recycling by catalyzing the conversion from either enantiomer towards the racemate. Enzymatic catalysts can outperform traditional chemical catalysts due to their adaptability by enzyme engineering, non-toxicity, and mild reaction conditions. Yet, their production is comparably expensive and should be considered in the optimization of the entire process. Immobilization of enzymes onto a carrier can increase their reusability, lifespan and along with it its productivity.

In the first part of this chapter the racemization kinetics of the immobilized amino acid racemase (AAR) in an enzymatic fixed bed reactor (EFBR) were characterized. The kinetics were studied under varying solvent conditions and regarding its stability and storability. In the last part of this chapter the promising results of improving the fermentation and purification process are presented along with a brief cost estimation. The work done for this chapter profited from assistance by Andrea Schütze, Stefanie Oberländer and Claudia Bednarz and from the experience of Thiane Carneiro. The work presented in Sec. 4.1, 4.2 and 4.3 can also be found in Harriehausen et al. (2021) [154] and the Master theses of Jonas Bollmann. The experiments from Sec. 4.4 were done within the scope of the Master thesis of Louise Witzlack. An application of the immobilized AAR with preferential crystallization can be found in Intaraboonrod et al. (2020) [155].

4.1 Activity of free and immobilized racemase from different fermentations for *D*- and *L*-methionine

Unless mentioned otherwise, the AAR characterized in the following sections has been produced with four batches (B-1, B-2, B-3 and FB-6). The first three batches have been produced with the batch-protocol (B-1, B-2, B-3, Sec. 3.3.1), the fourth

batch was the improved fed-batch-fermentation (FB-6, Sec. 4.4). The first two batches have been used for the characterization of the racemase and the experiments presented in the following three sections. The activities of the immobilized third and fourth batch were only measured under standard conditions to study the robustness of the AAR production process. Afterwards, the immobilized carrier was used for experiments in the mini-plant.

4.1.1 Comparison of the activity of the free and immobilized racemase

Before the immobilization of batch B-2, B-3, and FB-6, the activity of the purified free AAR for *L*-Met was measured with 20 g/L *L*-methionine (Met) at 30 °C with enzyme dosages of 1-2 mg/L using the method described in Sec. 3.3.5. Within the first 3 min an average initial activity for *L*-Met was measured. The results are listed in Tab. 4.1.

Afterwards, B-1 was immobilized with $q_{\mathrm{AAR}} = 37\ \mathrm{mg_{AAR}/g_{carrier}}$ and the other three batches with 35 $\mathrm{mg_{AAR}/g_{carrier}}$. The activity of the immobilized racemase was tested with the same substrate concentration in an EFBR as described in Sec. 3.3.6 but with different dosages and temperatures (Tab. 4.1). For the immobilized enzyme the dosage was 732 mg/mL and thus 600-700-fold higher than the dosage of the free enzyme. The initial activity of B-1 at 30 °C was 48 $\mathrm{U/mg_{AAR}}$ and, thus, almost 3-times lower than the free AAR.

Several reasons for the observed difference in activities are possible. One explanation for a lower activity of immobilized AAR is its decreased flexibility due to its binding to the carrier. Also, the binding pocket for the substrate could be partially blocked by the resin. Another reason could be that the AAR partially decayed during the immobilization step, which was performed for 18 h at room temperature. In addition, the accessibility of the immobilized enzyme in deeper pores might be limited. The dependency of the pore size on the overall activity had already been shown by Carneiro [43]. Furthermore, the moisture content in the carrier resin might fluctuate, which adds uncertainty about the density and dosage of the carrier. Probably many of these aspects accumulated and caused this lower activity. However, a deeper understanding of the deactivation rate would require a range of further experiments, which are out of the scope of this work.

Tab. 4.1: Experimental data of the enzyme activity for free and immobilized AAR on "ECF 8309F" (Purolite, 56 $mg_{carrier}$ filled in the EFBR). All reactions were performed with a feed solutions of 20 g/L of *L*-Met.

Batch		Loading q_{AAR} $mg_{AAR}/g_{carrier}$	Dosage $D_{carrier}$ mg_{AAR}/mL	Volume $V_{reactor}$ mL	Temp. T °C	React. rate r^* U/mg_{AAR}
B-1	immob.	37	27.100	0.092	30	48
B-2	free	-	0.039	3.000	30	139
	immob.	35	25.600	0.092	20	29.8
B-3	free	-	.....	3.000	30	139
	immob.	35	25.600	0.092	20	30.0
FB-6	free	-	...	3.000	30	340
	immob.	35	25.600	0.092	20	30.0

4.1.2 Reproducibility of the racemase kinetics with different fermentation batches

In order to compare the kinetics of the different batches, the EFBR was packed with resin from each batch and tested with different *L*-Met concentrations at 20 °C in pure water. The initial reaction rates were determined based on the time needed to reach 20 % conversion. The respective methods are summarized in Sec. 3.3.6. In Fig. 4.1 (a) the initial reaction rates of batch B-1 and B-2 are given for 67, 134, 201 mM and in case of B-1 for 268 mM *L*-Met in pure water. This corresponds to 10, 20, 30 and 40 g/L *L*-Met. For batch B-2 the experiments have been repeated three times with freshly packed beds. The green symbols represent the values of three individual columns with carrier from B-2, which were packed within a time span of three weeks and an average was taken.

Based on the initial reaction rates for the tested substrate concentrations, kinetic parameters were estimated with respect to the amount of racemase in the bed. The resulting MM kinetics were added to the experimental data points in Fig. 4.1 as black and gray lines for B-1 and B-2, respectively and the estimated parameters were listed in (Tab. 4.2). For B-3 and FB-6 only one concentration was measured. For B-3 it perfectly matched with B-2 and the measured activity from FB-6 was even higher with > 300 U/mg_{AAR}, even though the activity of the immobilized enzyme was 30 U/mg_{AAR} and therefore matching the activites of the AAR from batch fermentations.

According to the fit, batch B-2 has a 26 % lower r^*_{max} than batch B-1. On the other hand, the Michaelis constant of B-2 is 28 % lower than that of B-1. These

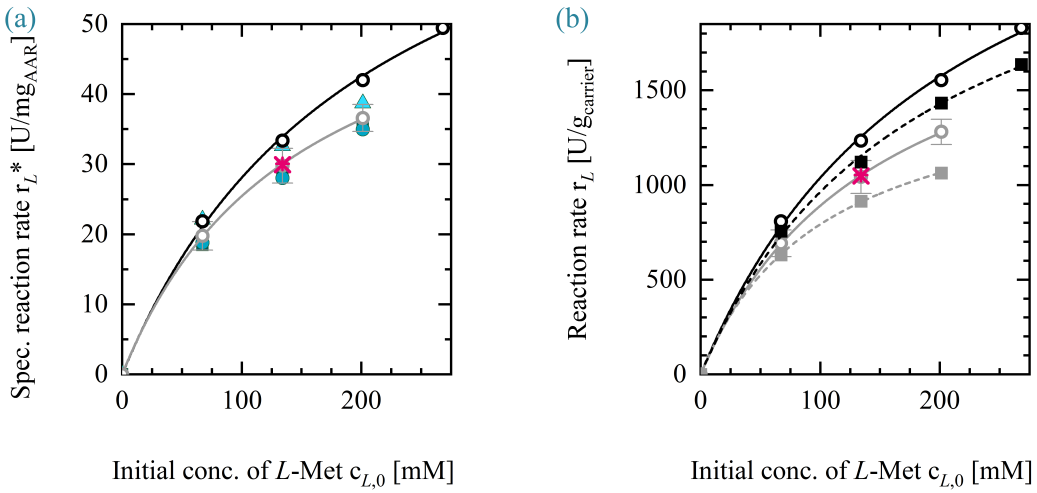

Fig. 4.1: Initial reaction rates of immobilized AAR from all batches for *L*- and *D*-Met in pure water at 20 °C with respect to the amount of (a) AAR and (b) immobilization carrier. *L*-Met: B-1: ○ ━; B-2: three packed beds on day 1 (▲), day 9 (●) and day 24 (■) and their average ● ━; B-3: ×; FB-6: +. *D*-Met (only in (b)): B-1: ○ ╍; B-2: ○ ╍.

contradictory results can be explained by the gradient of the reaction rate, which remains steep until the solubility limit of Met. This makes an accurate parameter estimation of r^*_{max} difficult. Therefore, a more reliable comparison between the two sets of kinetic parameters is the ratio r^*_{max}/K_M. Here, the difference of the two batches is only 2 %, but the ratio of B-1 is lower than B-2. Thus, we chose to compare the initial activities at each initial substrate concentration. Also, the activity of B-1 is 14 ± 2 % higher than the one of B-2. The reason for the activity difference between the batches is partly due to their different loadings. When comparing the activity with respect to the amount of enzyme, the difference between the batches decreases to 11 ± 2 % and the difference in their r^*_{max}/K_M drops to 2 %.

The remaining difference can result from variances in the bacterial fermentation and purification processes. As shown in Sec. 4.3, the cell lysate contains active and inactive racemase of varying amounts due to a variety within the cells of different batches, fermentation conditions, or variations in the harvest and purification steps. Since the active and inactive fractions can not be completely separated during the purification step, the AAR fraction used for immobilization will contain different amounts of active AAR. Thus, B-2 might have been produced with more inactive AAR or some AAR lost its activity due to denaturation during the processing steps, lowering the average concentration. However, with respect to the number of factors, which can contribute to different activities, the overall kinetics of batch B-1 and B-2 are remarkably similar.

Tab. 4.2: Kinetic parameters for Eq. (2.63) describing the catalytic activity of the batches B-1 and B-2 for *D*- and *L*-Met in pure water.

	Met	K_M mM	r^*_{max} U/mg_{AAR}	r_{max} $U/g_{carrier}$	r^*_{max}/K_M $U/mM/mg_{AAR}$	r_{max}/K_M $U/mM/g_{carrier}$
B-1	*L*	211 ± 22	87 ± 5	3236 ± 181	0.41	15.3
B-2	*L*	151 ± 7	64 ± 2	2235 ± 54	0.42	14.8
B-1	*D*	186 ± 19	75 ± 4	2757 ± 140	0.40	14.8
B-2	*D*	104 ± 3	46 ± 1	1617 ± 20	0.44	15.5

For a later design of an EFBR, the kinetics of the AAR with respect to the amount of carrier are more relevant. Thus, the initial reaction rates were also used to estimate the kinetics for B-1 and B-2 with respect to the amount of required carrier (Tab. 4.2). In Fig. 4.1 (b) the reaction rate in $U/g_{carrier}$ of B-1 (black), the averaged B-2 (gray) and the two data points for B-3 (×) and FB-6 (+) were plotted. Furthermore, the activity of the AAR for *D*-Met was tested. The initial reaction rates of AAR from B-1 and B-2 were determined for 10-30 g/L *D*-Met and added to Fig. 4.1(b) (▬ ▬). The resulting MM kinetics were added to Tab. 4.2.

In a direct comparison between the initial reaction rates at different concentrations, the AAR activity for *D*-Met is about 10 % lower than for *L*-Met. This is reflected by the maximal reaction rate, r_{max} estimations, which are 16 % smaller for B-1-*D*-Met compared with B-1-*L*-Met and, even more drastically, 38 % smaller for B-2-*D*-Met compared with B-2-*L*-Met. Only the activity at the lowest concentration of 10 g/L is similar for both enantiomers. This affects the estimated values of K_M for *D*-Met (186 mM and 104 mM for AAR batches B-1 and B-2, respectively), which are lower in comparison with those calculated for *L*-Met (211 and 151 mM for AAR batches B-1 and B-2, respectively). However, owing to the contrary trends of r_{max} and K_M, the ratio r_{max}/K_M is almost identical for *D*- and *L*-Met, even when comparing the two batches.

4.2 Characterization of the immobilized racemase

In the previous section the general activity of the free and immobilized AAR was compared and the reproducibility of the activity with different batches was confirmed. Next, the operating window of the AAR was tested at different pH, temperature, and alcohol concentrations. Unless stated otherwise, all reaction rates were measured at 20 °C.

4.2.1 Influence of temperature, alcohol and pH-value for *D*-/*L*-methionine

Based on the studies of Würges et al. 2009 [148], the characteristics of the AAR were studied for *L*-Met in a phosphate buffered system (Sec. 4.2). The impact of temperature on the reaction rates is displayed in Fig. 4.2 (a) and (b) and the resulting MM-kinetic parameters are summarized in Tab. 4.4. The results showed a clear temperature dependence. In coherence with the van 't Hoff law, the reaction rate doubles when increasing the reaction temperature from 10 °C to 20 °C, and triples when it is increased to 30 °C. This is also represented by the increasing ratios r_{max}/K_M from 7.92 to 16.5 and 23.5 U/mM/$g_{carrier}$. The temperature dependency was described with Eqs. (2.66)-(2.67) and the resulting parameters are summarized in Tab. 4.3. It should be mentioned that, in contrast to operation at 10 °C and 20 °C, an activity drop was observed after two days of operation at 30 °C.

Tab. 4.3: Parameters of Eqs. (2.66) and (2.67) modelling the temperature dependence of the Michaelis–Menten (MM) coefficients given in Tab. 4.4.

$r_{max}(T)$		$K_M(T)$		
A [U/$g_{carrier}$]	E_A[kJ/mol]	A_0 [mM]	A_1 [mM]	A_2 [mM]
$2.72 \cdot 10^6$	16.6	150.6	$3.7 \cdot 10^{18}$	7.5

In Sec. 5.1.3 it will be shown that the separation of *D*-/*L*-Met by chromatography benefits from the addition of organic solvents like MeOH or EtOH to the aqueous eluent. Therefore, the AAR was tested with 5 vol% and 10 vol% MeOH and EtOH. Here, 10 vol% MeOH was tested with AAR from batch B-1, whereas the other three conditions were tested with AAR from batch B-2. The resulting reaction rates are displayed in Fig. 4.4 (c). Owing to the different activity values in pure water, the reaction rates were normalized to the maximal reaction rates of the corresponding rate in pure water. Fig. 4.4 (d) shows the normalized reaction rates. It can be seen that the presence of 5 vol% only had a small effect on the reaction rates. However, when increasing the organic solvent fraction to 10 vol %, the reaction rate decreases by 17 % for methanol and 29 % for EtOH.

The impact of pH is displayed in Fig. 4.3 (a) and (b). In a phosphate-buffered system, the AAR performs best in a range of pH 7–8, while the reaction rate decreases at pH 6. However, the activity of the AAR in an unbuffered *L*-Met solution is similar to the one at pH 7–8, even though 30 g/L *L*-Met in water has pH 5.8. This would indicate that the phosphate buffer or NaCl might have a negative effect on the

Tab. 4.4: Kinetic parameters for Eq. (2.63) describing the catalytic activity for different reaction temperatures, alcoholic solvents and pH.

	Buffer Y/N[1]	pH -	T °C	EtOH vol%	MeOH vol%	K_M mM	r_{max} $\frac{U}{g_{carrier}}$	r_{max}/K_M $\frac{U}{mMg_{carrier}}$
B-1	N	5.8	20	0	0	211 ± 22	3236 ± 190	15.30
B-1	Y	7	10	0	0	300 ± 56	2376 ± 270	7.92
B-1	Y	7	20	0	0	190 ± 22	3140 ± 200	16.50
B-1	Y	7	30	0	0	161 ± 37	3775 ± 400	23.50
B-2	Y	7	20	5	0	162 ± 65	2114 ± 466	14.20
B-2	Y	7	20	10	0	158 ± 7	1637 ± 39	14.20
B-2	Y	7	20	0	5	161 ± 45	2238 ± 344	14.20
B-1	Y	7	20	0	10	210 ± 32	2667 ± 240	14.20
B-1	Y	6	20	0	0	402 ± 165	3599 ± 980	8.95
B-1	Y	8	20	0	0	250 ± 30	3553 ± 240	14.20

[1] Y= Yes, N= No, buffered eluent: 20 mM NaH_2PO_4/Na_2HPO_4, [2] EtOH or MeOH, [3] for 30 g/L *L*-Met

reaction rate. Similar negative effects have been reported for other enzymes [150]. For this reason more experiments with different buffer and salt concentrations were performed and presented in Fig. 4.3 (c) and (d). These screenings showed no definite trends regarding positive nor negative effects of the buffer and salt. More experiments might clarify the trends, but the work on this topic was stopped, since the most important message, the AAR works well in pure water, was already proven (see Fig. 4.1).

4.2.2 Kinetics of racemization for *D*-methionine and other amino acids

The enzyme was also tested for other *L*-amino acid substrates with an initial concentration of 134 mM at 20 °C and flow rates between 4.0 mL/min and 0.1 mL/min. The measured conversion rates at the different retention times are shown in Fig. 4.4. The racemization conversion obtained with the AAR was normalized for each amino acid in comparison with the activity for *L*-Met. The activity at a conversion rate of 20 % normalized to the rate for *L*-Met is presented in Fig. 4.4. The activity for *L*-Arg and *L*-Lys exceeded that of *L*-Met by 22 % and 107 %, respectively, while the other amino acids had a lower racemization rate. *L*-Asn showed the lowest activity, with only 10 % compared with *L*-Met. However, it needs to be mentioned that the activities for *L*-Lys and *L*-Arg were measured in a solution where the pH was decreased to pH 7.5

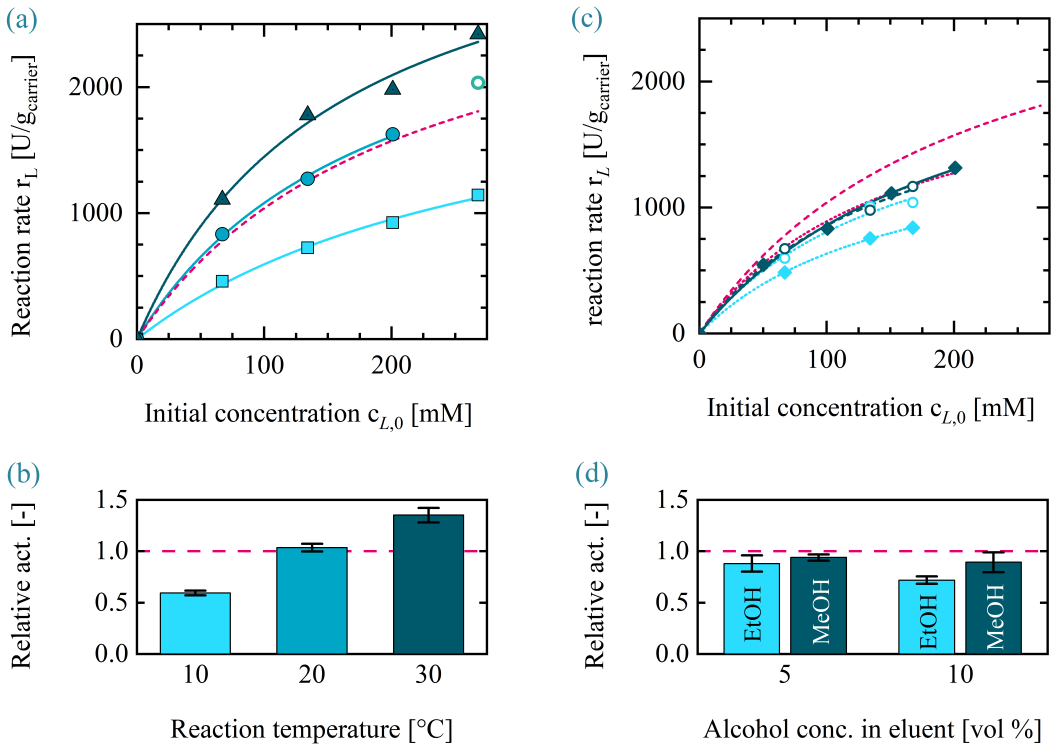

Fig. 4.2: (a) Initial reaction rates of *L*-Met at pH 7 at three reaction temperatures (10 °C: ■; 20 °C: ●; 30 °C: ▲), outlier: r($c_{L,0}$ = 286 mM, 20 °C) (○). (b) Relative activity in dependence of reaction temperature. (c) Initial reaction rates of *L*-Met at 20 °C and pH 7 in 5 and 10 vol% EtOH (○, ◆) and 5 and 10 vol% MeOH (○, ◆). (d) Relative activity in dependence of vol%-alcohol. Reference: activity in pure water from B-1 – – and B-2 ···.

with 1 M HCl (hydrogen cloride). An operation in a pure aqueous solution was not possible as the AAR was instantly deactivated after being exposed to aqueous solutions of 134 mM Lys and Arg, which had a pH > 10. Even though the exact relation between the activity for different amino acid varies, they are comparable to the results presented by [149] for the free AAR. The results obtained confirm the wide application range of the immobilized AAR.

4.2.3 Stability under storage and operating conditions

For testing the storage stability of the AAR, an EFBR was packed with B-1 shortly after the immobilization procedure and its activity was measured. Then the packed reactor was stored at 4 °C for almost six months, before tested again. The resulting initial activities are shown in the Fig. B.11. The AAR still had circa 78 % of its initial activity left.

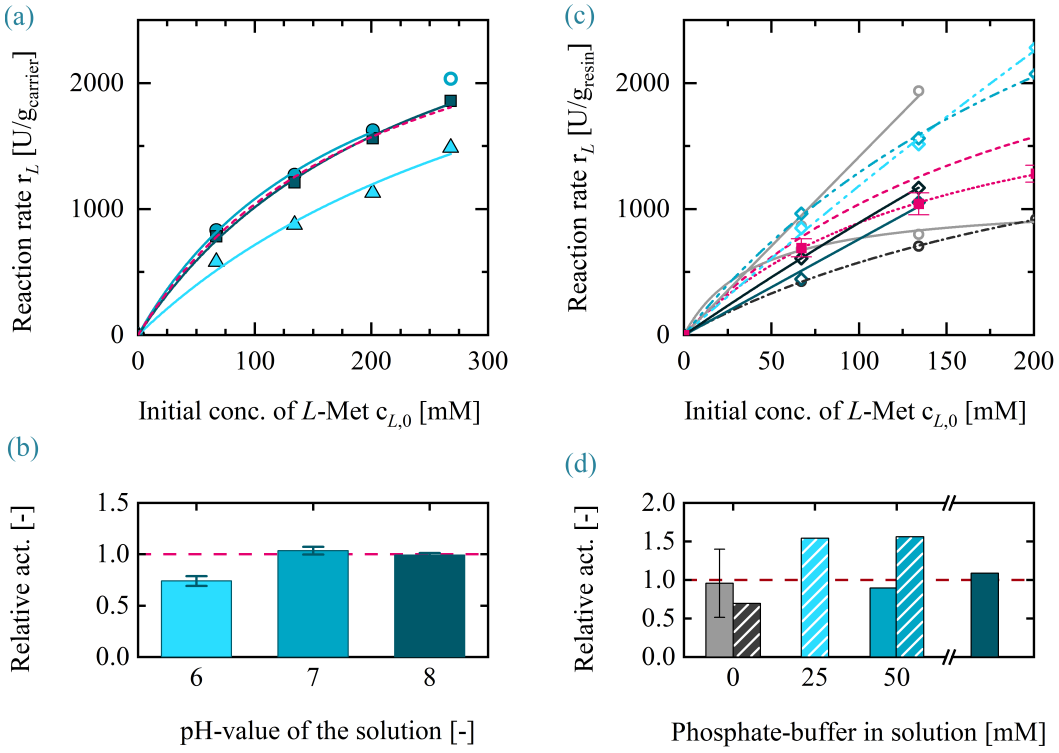

Fig. 4.3: (a) Reaction rates for different pH values of the solution (pH 6: ▲; pH 7: ●; pH 8: ■) for *L*-Met. (b) Relative activity in dependence of the pH value. (c) Reaction rates in different NaCl (20 mM —, 50 mM - -) and phosphate buffer (0 mM ○, 25 mM ◇, 50 mM ◇, 100 mM ◇) concentrations. (d) Relative activity of NaCl (20 mM (solid), 50 mM (dashed)) and phosphate buffer (0 mM ■, 25 mM ■, 50 mM ■, 100 mM ■). Reference: activity in pure water from B-1 – – and B-2 ····.

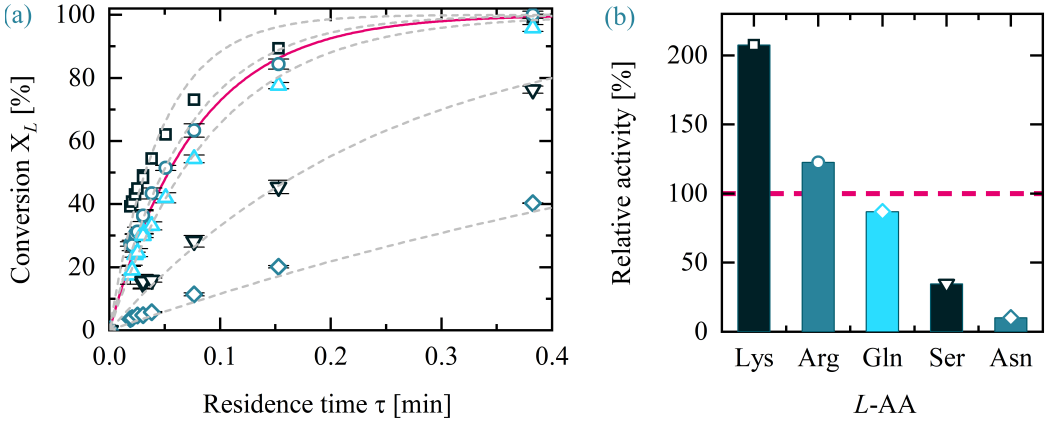

Fig. 4.4: (a) Conversion rates and (b) relative activity for different *L*-AAs with a concentration of 134 mM in comparison to *L*-Met (—): *L*-Lys (□), *L*-Arg (○), *L*-Gln (△), L-Ser (▽), *L*-Asn (◇).

For an indication of the AAR performance under operating conditions, the stability of AAR in continuous flow was tested in the setup described in Sec. 3.3.7 at room

temperature (RT). The experiment was repeated three times with fresh AAR and increasing duration of the testing period (11, 17 and 59 days).

In the third run, the solvent was switched on day 32 from pure water to 5 vol% EtOH. In Fig. 4.5 the measured conversion rates of *L*-Met and the relative activity loss over time is shown. After an initial drop in the first 24 h, the AAR lost about 3.5 % of its initial activity per week under continuous flow of pure water, resulting in a deactivation constant of k_{deact} = 7.8x10^{-3} day^{-1} (Eq. (2.69)) and a remaining activity of 76 % after 32 days. When switching to 5 vol% EtOH the activity dropped by 4 %, but in the following 42 days the average activity decline remained almost the same as before (k_{deact} = 8.2x10^{-3} day^{-1}, Eq. (2.69)). Furthermore, after two weeks the measured activity for the highest flow rate (2.5 mL/min) started to drop faster than for 1 mL/min. One explanation is that some fouling could have occurred, which might have blocked pores of the carrier.

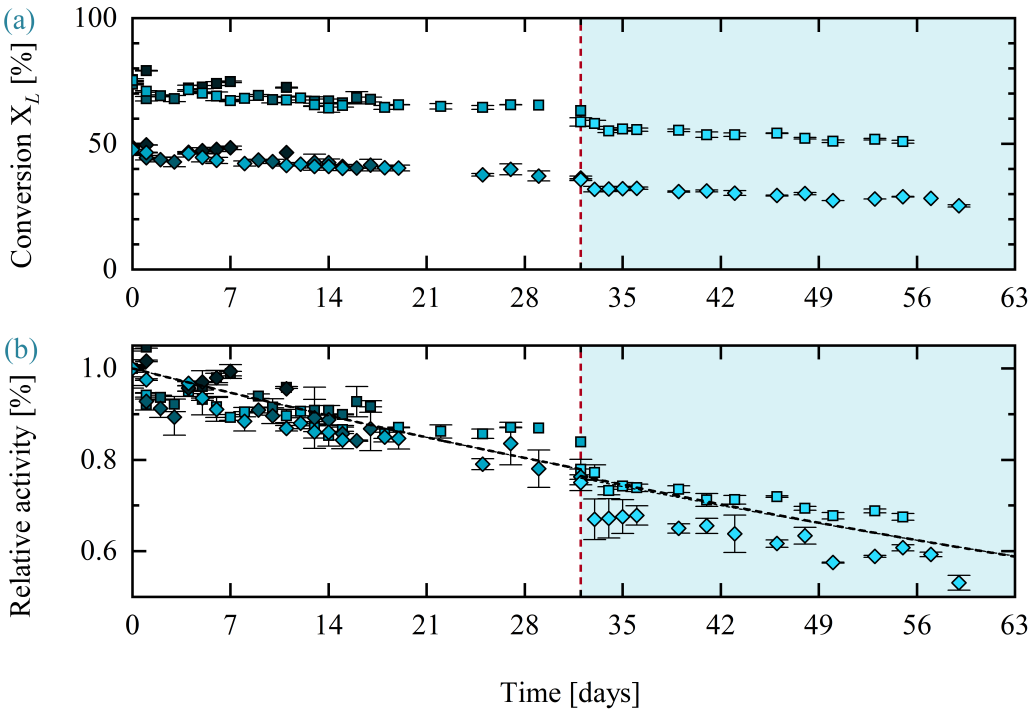

Fig. 4.5: Activity decline of the AAR in an EFBR at room temperature with a constant throughput of 1 mL/min water. The experiment was repeated three times (Run 1: 11 days (■, ◆), run 2: 17 days (■, ◆); run 3: 59 days (■, ◆)). For run 3, 5 vol% EtOH were added to the eluent from day 32 on. The activity was measured with 10 g/L *L*-Met pumped through the column with a residence time of 0.076 min (1 mL/min, ■,) and 0.03 min (2.5 mL/min, ◆) and the conversions were determined at the column outlet.

This experiment adds additional stability data to the observations made by Carneiro et al. 2020 [43], where the AAR was operating for two days at 40 °C, and Würges

et al. 2009 [148], where the free AAR lost 90 % of its activity at 35 °C within less than seven days. The observed stability of the AAR encourages the application of the AAR in continuous production processes. Assuming that the setup used in our stability test would be used in a continuous production process with a flow rate of 1 mL/min, the substrate would elute with an average conversion of $X_L = 0.35$. It can be estimated that under this condition the productivity would be approximately $Pr = 90\ g_{D\text{-Met}}/g_{carrier}/day$. The results of additional experiments on the stability of the AAR in alcoholic solvents and 30 °C is presented in App. B.9.

4.3 Dimensioning of the reactor based on operating conditions and required productivity

Based on the reaction kinetics of the immobilized AAR for pure Met, its stability and suitable operating conditions of a coupled process are discussed. Afterwards, the productivity of the EFBR was estimated for different settings with chromatographic separation.

4.3.1 Operating conditions for the enzymatic fixed bed reactor

The results from Sec. 4.2 showed that a reaction temperature of 20 °C is a suitable operating temperature by being sufficiently high for fast conversion rates and low enough for stable long term operations. Later on, in contrast to the eluent composition, the reaction temperature can easily be increased during the run. Correct temperature adjustment based on the estimated temperature dependencies of the AAR in Tab. 4.3 could then be used to compensate the deactivation. This way a constant enantiomeric excess at the reactor outlet, and constant product quality can be achieved. However, this action will further increase the deactivation rate of the racemase.

Furthermore, the AAR performs sufficiently well in 5 vol% MeOH or EtOH. A further increase of the alcohol fraction to 10 vol% negatively impacts the reaction kinetics. This indicates that the operating solvent in case of applying the EFBR within a process combination including enantioselective chromatography should have preferably an alcohol fraction below 10 vol% and if possible, as low as 5 vol%.

The results indicate that the AAR is highly active in buffered systems with 20 mM NaH_2PO_4/Na_2HPO_4 at pH 7-8 and unbuffered pure Met solutions show similar

stabilities in both systems. Therefore, while working with Met, an unbuffered system with pure water can be used. This simplifies production steps and eluent recovery while minimizing the eluent costs. However, when working with basic AAs and thus solutions with pH >10, the pH of the amino acid solutions should first be lowered to pH 7.5.

4.3.2 Productivity of operating an enzymatic fixed bed reactor with immobilized racemase

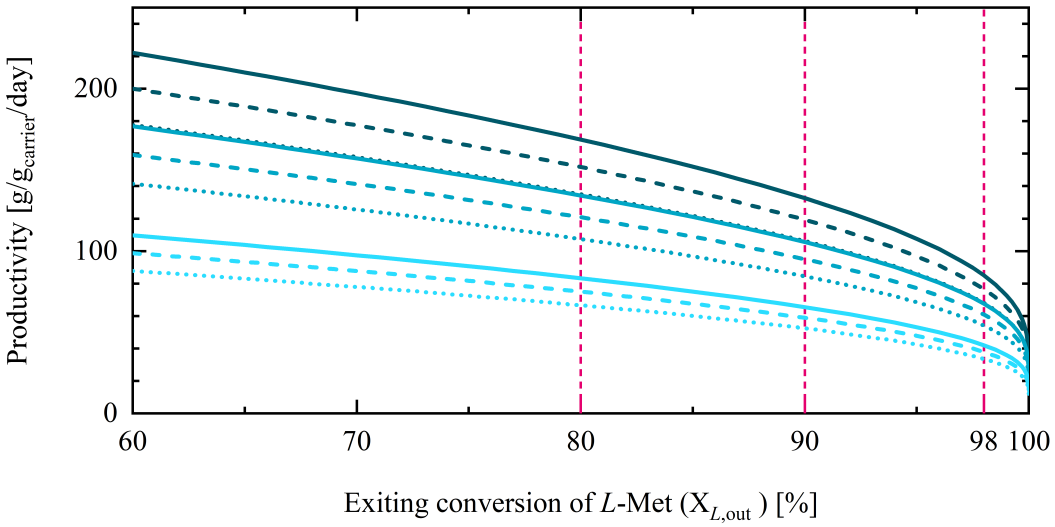

Fig. 4.6: Productivity $Pr_{D\text{-Met}}$ of racemization reaction with the AAR for different total concentrations c_{tot}: 30 g/L (▬), 20 g/L (▬), 10 g/L (▬)) and varying initial (entering) enantiomeric excess at the EFBR inlet $ee_{L,0}$ (80 % (▪▪▪), 90 % (▬ ▬), 100 % (▬)) as a function of the conversion exiting the reactor $X_{L,out}$.

Like for many processes, targeting productivity or purity leads to opposite trends. When measuring process purity as the remaining enantiomeric excess of the counter enantiomer at the exiting port, the latter one symbolizes a key parameter for this trade-off. Since the enantiomeric excess is also the main driving force of the AAR, this parameter should be taken into consideration during the process design and is thus further evaluated below. Based on the kinetic data from batch B-1 in pure water (Tab. 4.2) and the carrier dosage (Tab. 3.5), the productivity of a fresh EFBR was simulated. Its productivity is shown in Fig. 4.6 for different scenarios. In the following we want to discuss the different options of a total concentration of c_{tot} = 20 g/L. When targeting a moderate conversion rate of X_L = 90 % for an inlet stream of $c_{L,0}$ = 20 g/L (100 %$ee_{L,0}$), the reactor reaches a productivity of $Pr_{D\text{-Met}}$ = 106 $g_{D\text{-Met}}/g_{carrier}$/day.

The productivity of the EFBR is proportional to the remaining enantiomeric excess at the outlet and there is a loss in productivity when the by-product stream is contaminated with the product enantiomer. With increasing extent of conversion at the column exit, the influence of the concentration is lowered in comparison to the impact of the outlet conversion. Also, in comparison to a pure by-product stream, a contamination with the target enantiomer of e.g. $c_{D,0}$ = 2 g/L ($c_{L,0}$ = 18 g/L, 80 %ee_L) at the inlet stream only reduces the productivity by 20 %. In contrast, to increase the conversion of a reactor with 100 %$ee_{L,0}$ from e.g. X_L = 90 % to 99.8 % results in a productivity drop of 59 % from Pr = 106 $g_{D\text{-Met}}/g_{carrier}$/day to 43 $g_{D\text{-Met}}/g_{carrier}$/day. This shows that the productivity of the EFBR benefits more from relaxed conversion requirements at its outlet than from higher enantiomeric excess of the by-product at the inlet of the EFBR. Yet, in a stand-alone process, a remaining enantiomeric excess lowers the process yield. However, when integrating the EFBR into a coupled process with a feedback loop, the overall process yield is no longer lowered by incomplete conversion at the reactor outlet.

4.4 Improvement of the racemase fermentation and purification

The previous section showed the great productivity and stability of the AAR. However, like for most enzymes, high up- and downstream costs are still an exclusion criterion for many larger scale applications. Different aspects can be tackled to lower these costs. One aspect is genome engineering to improve the AAR gene expression, which has already been done to enhance the AAR production (see Sec. 3.2.2, [148]). Also the immobilization process has already been studied [43]. The remaining steps needing an improvement were the fermentation and purification of the AAR, which were therefore tackled in this work to lower the costs of the racemization step.

4.4.1 Fermentation: From batch to fed-batch mode

In the publication from Würges et al. (2009), a 22-L-fed-batch fermentation was performed with a harvested wet-biomass of about 34 g/L. From the wet-biomass 0.23 mg/g pure lyophilizate were obtained, which is a yield of about 8 mg pure lyophilizate per liter fermentation broth. With the established batch fermentation mode performed by Carneiro et al. 2020, 5-6 g/L wet-biomass (wb) with 2.5-3.0 mg_{AAR}/g_{wb} could be produced. This results in a yield of already 14 mg_{AAR}

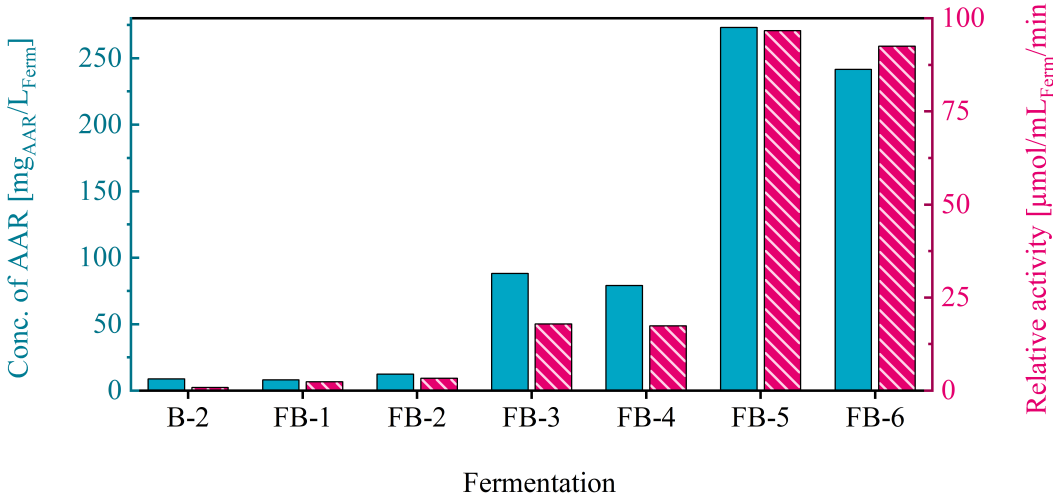

Fig. 4.7: Comparison of the effectiveness of the different fermentation approaches by measuring the amount of active AAR by: (a) the relative activity obtained of the purified AAR with respect to the ferm. volume (■) and amount of AAR obtained per ferm. volume (■).

per liter fermentation broth. However, since the purification method of the two fermentations are not comparable, it is difficult to say whether the fermentation or the purification had the biggest influence on the productivity and which parameters are the most favorable. Thus, different fermentation conditions were tested and compared regarding their amount of obtained active AAR. In Tab. 4.5 the results from the six most relevant fed-batches are compared to each other and with respect to the results for batch B-2, which had been produce with the old standard batch protocol (App. B.2). Due to the lack of time and resources the protocols of FB-1 to FB-4 were each only performed once with an initial reactor volume of $V_{ferm,0} = 12$ L and the first three fermentations were only performed with in a small bio reactor with $V_{ferm,0} = 0.5$ L. Only FB-5 and FB-6 were produced with the same settings to check the reproducibility.

The success of the fermentations were measured by the amount of AAR purified per fermentation volume and its activity (shown in Tab. 4.5 and Fig. 4.7). The purification of the batches was done with a pre-packed HisTrap FF crude column, as described in Sec. 3.3.2. Afterwards, the fractions with active AAR were collected and their concentration and activity were determined with the "NanoDrop-assay" and "Polarimeter-assay" described in Sec. 3.3.5. Therefore, the concentrations of AAR discussed in the following are always referring to the amount of AAR, which could be purified from the wet-biomass. This excludes AAR, which was present in its soluble form.

Tab. 4.5: Harvested AAR under varying (fed-)batch conditions.

Attribute	B-2	FB-1	FB-2	FB-3	FB-4	FB-5	FB-6
Medium	LB	LB	LB	LB	2xTY	LB	LB
Gluc. start [g/L]	10	20	20	20	20	20	20
Gluc. feed [g_{Glu}/h/$L_{ferm,0}$]	-	1.5	1.5	1.5	0.15	1.5	1.5
$V_{ferm,\ 0}$ [L]	12	0.50	0.50	0.50	12.0	10.0	12.0
$V_{harvest}$ [L]	12	0.65	0.80	0.74	14.8	12.5	14.4
Stirring rate [rpm]	250	500	500	500	300	300	300
Gassing [L_{air}/min/$L_{ferm,0}$]	0.7	2-3	2-3	2-3	0.8	1.0	1.0
Anti foam	no	no	P810	P810	P810	P810	P810
IPTG [mM]	1.0	0.1	0.1	1.0	1.0	1.0	1.0
Ind. Temp. [°C]	22	27	27	22	22	22	22
pH-reg. (to pH 7)	no	1x	yes	yes	yes	yes	yes
Ferm. time [h]	6-7	25	25	25	25	22	22
cell density [g_{wb}/L_{ferm}]	5.4	6.4	15	11.0	32	15	14
AAR fraction [mg_{AAR}/g_{wb}]	2.6	1.3	0.8	8.0	2.5	18	17
AAR yield [mg_{AAR}/L_{ferm}]	14	8	14	88	79	273	242
r_{AAR}/V_{ferm} [U/mL]	2.7	2.4	3.3	18	17	97	93

B = Batch, FB = Fed-batch, 1x = once manually, P810 = Pluronic 810

The fermentation results show how the production of biomass and AAR could be influenced by multiple factors. The first three factors tested were the glucose concentration in the media (from 10 g/L to 20 g/L), the induction temperature (from 22 °C to 27 °C) and the IPTG-concentration (from 1.0 mM to 0.1 mM IPTG). Further differences between FB-1 and FB-2 are that in FB-1 the pH was only adjusted once after 22 h with 1 M NaOH, while a pH-control was installed for FB-2 and all following fermentations. Furthermore, from FB-2 on, 40 μL/L_{ferm} "Pluronic 8100" (BASF), a nonionic surfactant, was added to counteract the foam formation[1]. In comparison to B-2, the amount of harvested wet-biomass did increase from 5.4 to 6.4 and 14.7 in FB-1 and FB-2, respectively. However, along with it the amount of AAR, which could be purified from the wet-biomass decreased and inclusion bodies could be seen under the microscope. As a result, B-2 and FB-2 reach similar yields of 13.9 and 14.4 mg_{AAR}/L_{ferm} and FB-1, which was performed with neither pH control nor surfactant against foam, had a yield of about 60 % compared to B-2.

Closer to their optimal growth temperature of 37 °C and with less IPTG, the cells could grow faster, reaching higher cell densities (measured as optical density at

[1] In a fermentation not shown here, the surfactant "Struktol J647" was tested. Once it was added, the pO_2 dropped to zero and the OD in the reactor started to decrease. The harvested wet-biomass was of a much darker color than usual and had a sulphurous-like smell.

a wavelength of 650 nm (OD_{650nm})) and produced more biomass. These results indicate a correlation between high growth rates and the aggregation of AAR into inclusion bodies. Inclusion bodies are aggregates of bio-macromolecules, mostly proteins, and are generally expressed from foreign genes without proper modifications or folding. They seem to occur, when the equilibrium of protein folding, aggregation and degradation is unbalanced and is associated with many factors including the host cell metabolism [156, 157]. While it is possible to recover enzymes from inclusion bodies by *in vitro* refolding [158, 159], this process is not yet established for our system. The simpler approach was to slow down the growth of the *E. coli*, by reducing the induction temperature back to 22 °C. At this reduced growth rate the host could "focus" its protein-folding machinery back to the AAR.

In the next fed-batch fermentation FB-3, the induction temperature and IPTG-concentration were set back to the setting of the batch protocol. Compared to FB-3 only around 75 % of the biomass was formed, but the amount of AAR increase by a magnitude from 0.84 to 8.0 mg_{AAR}/g_{wb}. This resulted in 88.1 mg_{AAR}/L_{ferm}, which was over six times more than in B-2 and FB-2. These results confirmed our hypothesis regarding the formation of inclusion bodies. At this lower temperature less biomass was formed, but along with it the AAR remained in its soluble form and could be harvested after cell disruption from the cell lsyate. As a result, more AAR could be recovered from the biomass. Despite this success, the cell density in all fermentations stopped at an OD_{650nm} of around 8.5 after 22-24 h, even though *E. coli* can reach much higher cell densities. This indicated that further growth was inhibited by either a depletion of a nutrient or the increasing level of a toxic side product. The monitored parameters of Ferm. 3, 5, 6 and 7 are shown in Fig. B.1.

Next, the fed-batch protocol of FB-3 was upscaled from a 0.5 L (Infors Unit 1) to a 12 L fermenter (B. Braun Biotech International GmBH) with starting volumes of 10 and 12 L. A consequence was a different reactor geometry, lower stirring rate and less aeration (max. 10 L/min). In this fermenter the standard LB ampicillin-media with the usual feed of 1.5 $g_{Glu}/h/L_{ferm,0}$ (FB-5 and FB-6) and the 2xTY ampicillin-media with a feed of 0.15 $g_{Glu}/h/L_{ferm,0}$ (FB-4) were tested. The two media differ in their concentration of trypton (T) and yeast (Y). In comparison to the LB-media, in 2xTY-media, the trypton concentration is doubled from 5 g/L to 10 g/L and the yeast concentration is increased from 10 g/L to 16 g/L. It is therefore nutrient-rich and should benefit the growth.

Despite only 10 % of the usual glucose feed rate, FB-4 with a 2xTY-media had a faster cell growth and an OD_{650nm} = 8.5 was reached after 22 h. Afterwards, the cell density started to decrease again and the cells were harvested after 25 h at an

OD_{650nm} = 16.9 (data not shown). This led to a harvest of almost 32 g_{wb}/L_{ferm}. Similar to FB-1 and FB-2 the fast cell growth correlated with the formation of inclusion bodies and the overall yield was only as high as for FB-3. The fermentations FB-5 and FB-6 had a slower growth rate, but still reached a higher cell density (OD_{650nm} = 10-11) and therefore yielded 14 g_{wb}/L_{ferm}. From the biomass around 18 mg_{AAR}/g_{wb} could be obtained, which is more than double compared to FB-3. The combination of more wet-biomass and higher AAR fraction increased the yield by a factor of 2.7-3.0 to an overall yield of around 240-270 mg_{AAR}/L_{ferm}.

A comparison of FB-4 with FB-5 and FB-6 showed that the 2xTY-media was not beneficial for the AAR production and could also not prolong the cell growth. Therefore, the LB-media seems to be more suitable for the production of AAR. The higher yields in FB-5 and FB-6 compared to FB-3 must result from the before listed differences of the two fermentors. The most probable reasons were the lower stirring rate or the lower gassing with less turbulence.

It can be summarized that by switching from batch to a fed-batch fermentation with sufficient glucose feed, pH-reguation and a fermentation time of 22 h, the fermentation protocol could be drastically improved: The AAR fraction within the cells was increased by the 7-fold from 2.6 to 18 mg_{AAR}/g_{wb} and the AAR yield could be increased more than 17 fold from 14 to 240-270 mg_{AAR}/L_{ferm}.

4.4.2 First attempt of upscaling the fed-batch-fermentation

For the application of the immobilized AAR in a larger scale plant and for its coupling with the fluidized bed preferential crystallizer of Jonathan Gänsch (*MPI Magdeburg*), large quantities of immobilized AAR are required.

Therefore, a service provider was hired to perform a 500-L-fed-batch-fermentation based on the optimized protocol of the previous section. Due to the larger scale, some adaptations to the protocol from App. B.3 were necessary. For the media, the products "Amberferm 7020" and "Tastone 900-A" (Sensient Technologies, USA) were used instead of "Bacto Yeast extract" and "Typtone" (Gibco, Life Technologies Corporation, USA). The second pre-culture was performed in a bioreactor with a cultivation time of 8 instead of 16 h. Furthermore, the pre-culture was not centrifuged, but the entire broth was used for the inoculation. The OD_{650nm} trend over time is shown in Fig. 4.8 along with the OD_{650nm}'s of the fermentations in our lab.

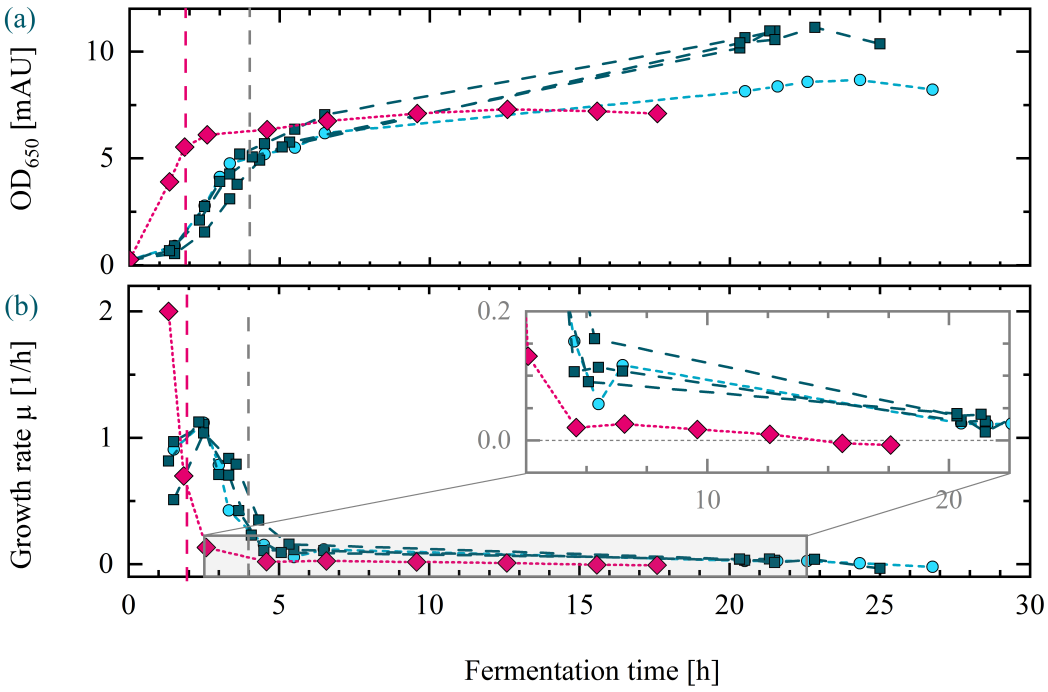

Fig. 4.8: OD_{650nm} and growth rate of the 500-L-Fed-Batch fermentation (◆) in comparison to the 0.5-L fed-batch fermentation FB-3 (●) and the 10-L-fermentations FB-5, FB-6 and FB-7 (■) performed in our lab. The dashed lines present the approximate time of the induction with IPTG.

In contrast to our fermentations, an OD_{650nm} = 6 was reached after two hours and the growth rate started at μ(t = 1.3 h) = 2 h^{-1} before decreasing within the third hour to only μ(t = 2.6 h) = 0.13 h^{-1}. In comparison, the OD of our fermentations rose slower during the first three hours and the maximum growth rate of μ(t ≈ 2-4 h) = 0.9-1.3 h^{-1} was reached after 2-4 hours and lasted longer. Due to the faster growth rate, the service provider already started the induction with IPTG and the feeding after two hours, which is only half of the time our fermentations stayed in normal growth batch mode. Furthermore, the fermentation was already stopped after seventeen hours, since the OD stagnated after about 9 hours and then started to decrease.

The monitored parameters of this large scale fermentation are shown in Fig. B.2. All aspects considered, the trends look similar. Differences were the steeper rise of the OD, resulting in an earlier temperature drop for the induction. The aeration rate was only about 25 % compared to our fermentations, yet the pO_2-level was comparable to our fermentations. The slow rise of the pO_2 might correlate with the declining growth rate.

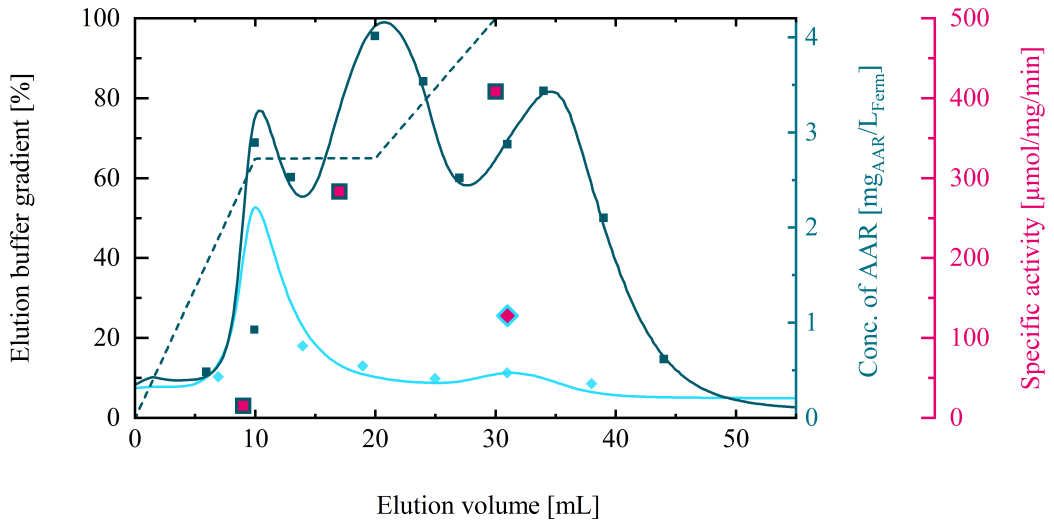

Fig. 4.9: Elution profile of the His-Tag-purification: concentration of the eluting proteins, specific activity of the AAR and the applied elution buffer gradient. The profile in light blue is a typical profile obtained from the fermentations in our lab (■) in comparison to the elution profile from the 500-L-ferm (◆).

The harvested broth yielded 6.49 kg of the very "dry" cell paste. During the washing of the cells a lysis occurred, resulting in a loss of the cell paste and a final mass of 5.87 kg wet biomass. In comparison to our light brown wet biomass, the cell paste from the toller was of a much darker color and had a sour smell.

For analyzing the amount of active AAR obtained from the 500 L, the standard purification method (see Sec. 3.3.2) was used. The elution profiles are shown in Fig. 4.9. The resulting elution profile again looked very different than the usual profiles, since the characteristic peak around 25-40 mL of the active AAR was barely detectable.

The collected fraction of the first peak had no significant activity and the very small second peak had active AAR but resulted in only 0.15 mg_{AAR}/g_{wb} and thus 1.7 mg_{AAR}/L_{ferm}. Since we obtained on average 230-240 mg_{AAR}/L_{ferm} in FB-5 and FB-6, this would mean that we produced 2.3 g free AAR in our 10 L fermentation, while the 500 L fermentation only contained 0.85 g soluble AAR. Hence the total delivery cost of the AAR, including labor cost and overhead expenses, was over 21.300 €/g_{AAR}.

A SDS-PAE of the biomass (Fig. B.3) showed that the AAR was indeed produced but probably trapped in inclusion bodies, like we had observed in FB-2 and FB-4. Therefore, the cell disruption method was not sufficient to extract the AAR. There are methods and kits recommended to obtain enzyme from inclusion bodies, which

were recommended to us by the toller ("Pierce™ Protein Refolding Kit" from Thermo Fisher Scientific or "QuickFold™ Protein Refolding Kit & Buffers" from Athenas). This was outside the scope of this project but should be considered in future work.

4.4.3 Affinity chromatography: Improved purification

The bottleneck of the purification of the active AAR from the wet biomass of the existing method described in Sec. 3.3.2 was the 5 mL HisTrap FF crude column, pre-packed with the resin "Ni-Sepharose 6 Fast Flow". Only around 60-90 mg active AAR were purified with each run. This equals a productivity of 12-17 mg_{AAR}/mL_{resin}. In order to improve the purification, the selectivity and capacity of six resins was tested for the his-tag-purification step and the protocol itself was optimized for the most promising candidate.

Comparison of different resins for the his-tag-purification step

Some of the resins were only available as slurries. Therefore, all of them were tested with the slurry method described in Sec. 3.3.2 in a 1-mL-scale. Similar to the previous section the quality of the purification was measured by the amount of protein, which is expected to be AAR and the activity of the captured fractions. Since the applied protein concentration determination method can neither differentiate between AAR and other proteins with natural occurrence of histidine nor between active and inactive AAR, the determined activity is the more relevant information.

All tests with different resins in this section were performed with material from FB-4 for which a mass fraction of 2.5 mg_{AAR}/g_{wb}. This ratio was determined by purification of 6.76 g of FB-4 with the established method with a pre-packed column, for which 16.9 mg_{AAR} active AAR were collected. It was then used to assume the amount of loaded AAR as follows:

$$m_{\mathrm{AAR,load}} = 2.5\,\mathrm{mg_{AAR}}/\mathrm{g_{wb}} \cdot m_{\mathrm{wb}} \tag{4.1}$$

Based on Eq. (4.1), the resins from Tab. 3.4 "Ni-Sepharose 6 Fast Flow" ("Ni-Seph. 6 FF"), "HisPur Ni-NTA SF Agarose" ("HisPur Ni-NTA") and "Pierce High Capacity Ni-IMAC" ("Pierce H. C. Ni-IMAC") and the three "Chromalite MIDA" with cobalt (Co), nickel (Ni) and copper (Cu) were tested. All were loaded with 13 and 31 mg_{AAR}/mL_{resin} and the promising candidates were also loaded with 41 and 61 mg_{AAR}/mL_{resin}. The amount of AAR collected in the eluting fractions and their

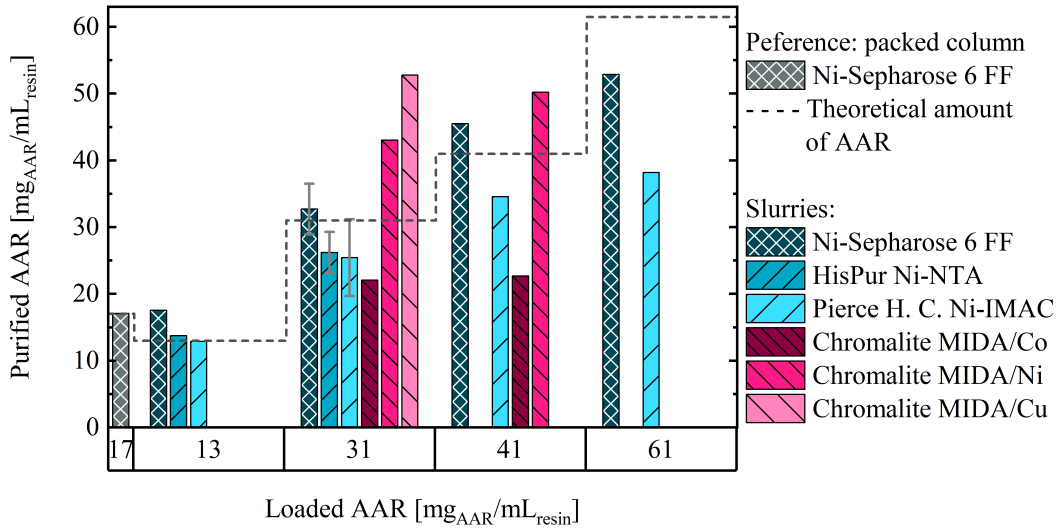

Fig. 4.10: Collected mass of AAR or protein from the purification with 1 mL of different resins with the slurry method described in Sec. 3.3.2.

activity is shown in Fig. 4.10 and Fig. 4.11. At this point, it should be emphasized again that the amount of AAR was quantified from a calibration of the absorption signal at 280 nm of all fraction containing the active AAR, as shown in Fig. B.7. It can therefore be assumed out that the fractions with active AAR also contained inactive AAR and other proteins, which were then also counted as active AAR.

For a theoretical load of 13 mg_{AAR}/mL_{resin} the three tested resins purified around 13 mg_{AAR}/mL_{resin} and the activity of the collected fractions from all samples were close to the expected 580 μmol/min/g_{wb}. For 31 mg_{AAR}/mL_{resin} the differences between the materials became more significant. Of the first three resins the "Ni-Seph. 6 FF" material captured 33 mg_{AAR}, followed by the "HisPur Ni-NTA" and "Pierce H. C. Ni-IMAC" with 26 and 25 mg_{AAR}, respectively. Also, the activity of "Ni-Seph. 6 FF" and "Pierce H. C. Ni-IMAC" are again close to 580 μmol/min/g_{wm}. The activity of the sample from "HisPur Ni-NTA" however dropped to 446 μmol/min/g_{wb}, which is only around 75 % of the expected activity. Therefore, only "Ni-Seph. 6 FF" and "Pierce H. C. Ni-IMAC" were tested for higher loadings. Up to 41 mg_{AAR}/mL_{resin} "Ni-Seph. 6 FF" collects more AAR than expected and reaches the expected activity. Only for 61 mg_{AAR}/mL_{resin} the collected AAR drops to 53 mg_{AAR}/mL_{resin} and the activity to 485 μmol/min/g_{wb}. For "Pierce H. C. Ni-IMAC" the effect is even stronger: Already for 41 mg_{AAR}/mL_{resin} the activity drops to 515 μmol/min/g_{wb} and at 61 mg_{AAR}/mL_{resin} to 394 μmol/min/g_{wb}.

Despite reaching similar activities, with the slurry method more protein was captured than with the column method. The main reason for this is the lower resolution of

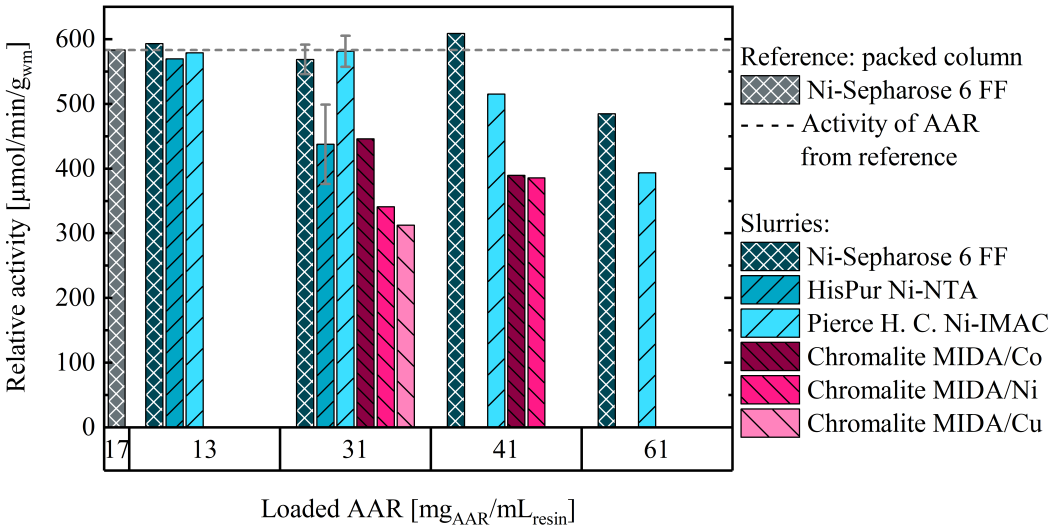

Fig. 4.11: Activity with respect to the amount of applied wet mass of collected AAR from the purification with 1 mL of different resins with the slurry method described in Sec. 3.3.2.

the elution fractions, due to the collection of rather large eluting fractions. This made it more difficult to separate the inactive and active AAR fractions (shown in Fig. B.7). Therefore, in the following, the results were evaluated with a focus on the relative activity of the samples. In contradiction to the claimed capacities by the manufacturers, the capacities of the IMACs "HisPur Ni-NTA" and "Pierce H. C. Ni-IMAC" of 60 and 70 mg/mL could therefore not be confirmed for the capture of AAR from the cell lysate. With "HisPur Ni-NTA" already 25 % AAR were lost at 31 mg$_{AAR}$/mL$_{resin}$ and with "Pierce H. C. Ni-IMAC" ≈12 % were lost at 41 mg$_{AAR}$/mL$_{resin}$. For "Ni-Seph. 6 FF" the suppliers claim of 40 mg/mL was accurate and could be confirmed. These results conclude that when using the "Ni-Seph. 6 FF" resin, which had already been used in the old protocol, the productivity of the purification process can at least be increased from 12-17 to 40 mg$_{AAR}$/mL$_{resin}$ without loss of AAR. Loss of AAR (≈15 %) could only be observed for 61 mg$_{AAR}$/mL$_{resin}$.

The "Chromalite MIDA" resins all performed weaker than the "Ni-Seph. 6 FF" and "Pierce H. C. Ni-IMAC". For 31 mg$_{AAR}$/mL$_{resin}$ the resin with copper bound around 150 % of the expected amount of AAR and simultaneously the collected fractions had only around 50 % of the expected activity. The nickel-resin collected less protein and had a slightly higher total activity than the copper-form, even though it collected more protein with less activity than the other Nickel resins. The cobalt-resin captured only around 70 % of the expected AAR, but the overall activity was still the highest compared to the other two metals ions. For 41 mg$_{AAR}$/mL$_{resin}$ the nickel-resin collected 50 mg$_{AAR}$/mL$_{resin}$, which is more than twice as much protein as

the cobalt-resin bound, but both ended up with the same activity of round 60-70 % of the expected activity. The observed trends in selectivities and binding capacities match with the information from the manufacturer.

The results for the "Chromalite MIDA" resins emphasise the importance of focusing on the activity rather than the determined AAR concentration. The copper and nickel resins both allowed a significant amount of unspecific bindings. The relative activity was therefore the best indicator to evaluate the resins. Furthermore, despite reaching lower activities and therefore binding less active AAR, the "Chromalite MIDA/Co" from Purolite could become an interesting alternative to the "Ni-Seph. 6 FF" resin. In comparison to the other three resins, the Chromalite resins not only can be used for purification, but simultaneously can replace the current immobilization resin ECR8309F (Purolite). This would significantly shorten the production protocol to obtain immobilized AAR by eliminating the elution step and the requirement of another immobilization and could decrease the production costs. However, it was not tested yet, whether the AAR reaches the same activity and stability as on the ECR8309F, even though promising results have been shown for other enzymes [160]. Therefore, in the following the purification method with "Ni-Seph. 6 FF" resin is improved with a targeted loading capacity of 40 mg_{AAR}/mL_{resin}.

Improvement of the protocol with Ni-Sepharose 6 FF resin

Even though the shape of the elution profile of AAR from the pre-packed "Ni-Seph. 6 FF" columns varied between the different fermentations, always at least two of three characteristic peaks occurred. The material for this section was obtained from a fed-batch fermentation (FB-5b), which was performed similar to FB-5 but was not listed above and had an AAR concentration of around 15.5 mg_{AAR}/g_{wb}, according to the standard purification protocol.

The profile from a purification of FB-5b in Fig. 4.12 shows all three peaks. Their elution profile were detected with an UV/VIS detector at 650 nm and then calibrated by measuring the concentration of some fractions. The first peak reaches its maximum after 9-13 mL and can be found in all purifications. The second and third peak usually elute at around 18-22 mL and 34-37 mL, respectively. However, sometimes the second peak was really small or did not show and in rare cases, especially when purifying old batches, the third peak did not occur.

The specific activity of fractions from all three peaks was measured. The first peak (shaded in blue) contains no active AAR, while the other two (shaded in pink) contain active AAR. The activity of the AAR continuously increases and reaches its

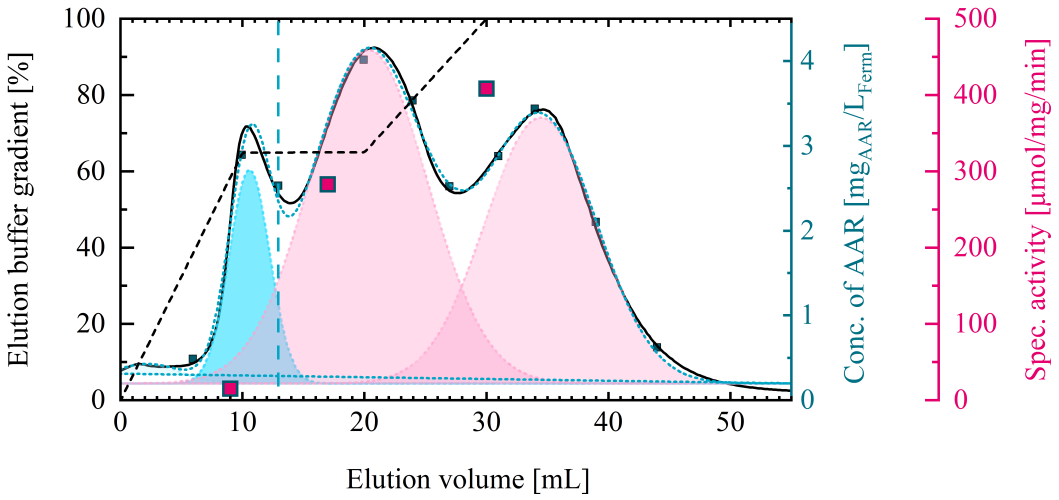

Fig. 4.12: Peak analysis of a typical elution profile of FB-5 along with activity tests of the three fractions 9, 17 and 30 (■): the elution profile shows three main peaks. The blue one shows no activity, while the two pink ones contain active AAR.

maximum at the end of the third peak (data not shown here). While the first peak could result from inactive AAR and other proteins, the occurrence of two active peaks indicates the presence of two AAR-forms. The amount of PLP (co-factor) added to the cell lysate before the immobilization, had no significant impact the elution profile. Another possible explanation would be the appearance of oligomers of the AAR [161]. Even though the activity of the second peak is higher, both fractions are sufficiently active. Therefore, a cut is made between the first and second peak and only the two rear are pooled for immobilization.

The goal was therefore to reduce the amount of inactive material in order to increase the capacity for active AAR and to separate the inactive peak from the active peaks. The latter was tackled by testing different imidazole gradients. The current protocol included an intermediate plateau at 65 % elution buffer, which equals 195 mM imidazole. The peak analysis however shows that active AAR already starts to elude at approximately 150 mM. Therefore, a lower intermediate plateau of 120 mM was tested. The resulting elution profiles from both plateaus and the measured activity of the relevant peaks are shown in Fig. 4.13. The collected AAR from the active fractions and their relative activity is plotted in Fig. 4.14. The run with an intermediate plateau at 40 % (120 mM) showed a clear separation of the active and inactive fraction and even managed to merge the second and third peak. Despite collecting less mass than with the standard protocol, the relativity of the collected AAR was 10 % higher, indicating that the fraction contained more and purer active AAR.

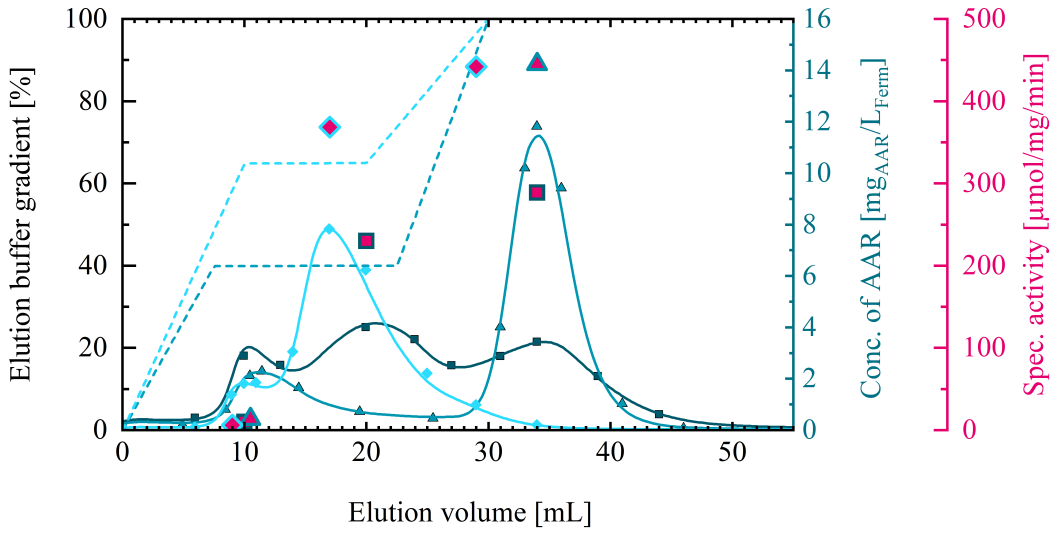

Fig. 4.13: Effect of the elution buffer gradient on the separation of the active and inactive AAR fraction: (a) 65-%-plateau, 0 % imidazole in lysis buffer -■- ■, (b) 40-%-plateau, 0 % imidazole in lysis buffer -▲-▲ and (c) 65-%-plateau, 4 % imidazole in lysis buffer -◆-◆. The dashed lines represent the imidazole concentration in % from 0 to 300 mM, the solid line is the calibrated absorption signal $A_{280\ nm}$ in g/L while the solid points present individual concentration measurements. The relative activity is plotted with pink centers.

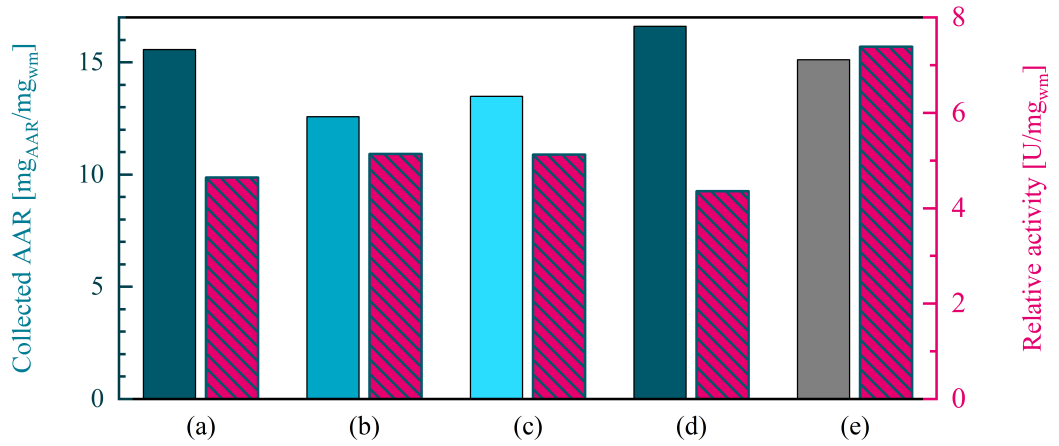

Fig. 4.14: Comparison of the standard method (a) with 1 mL/min flow through a pre-packed column, an imidazole concentration at the intermediate plateau of 65 % = 195 mM, 0 % imidazole in the lysis buffer, and a load of 20 mg_{AAR}/g_{resin} in comparison to (b) a plateau at 40 % elution buffer, (c) 4 % imidazole in the lysis buffer, (d) a load of 34 mg_{AAR}/g_{resin} and (e) again a load of 34 mg_{AAR}/g_{resin} and 1 h incubation of the crude extract before elution.

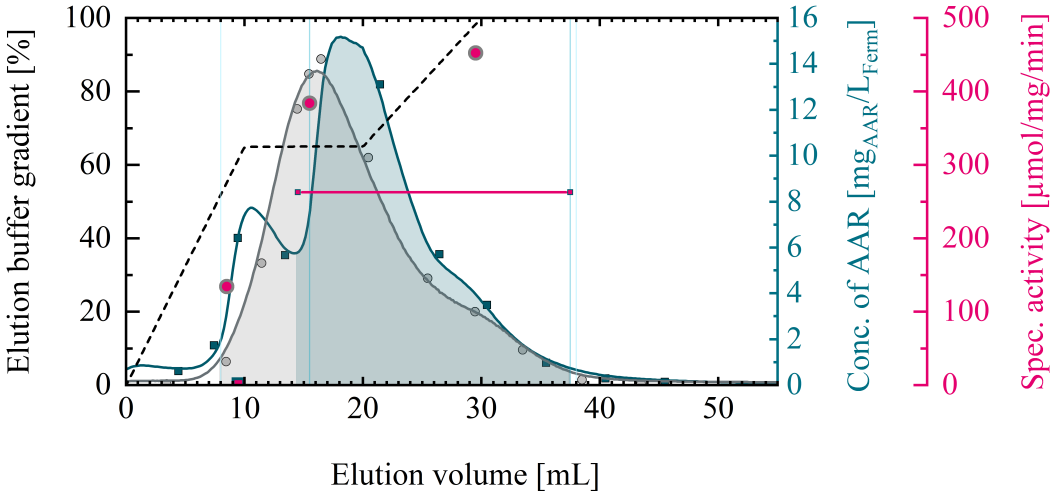

Fig. 4.15: Elution profiles and activity of the two different incubation methods (a) during the flow through the column -■- — (average activity of entire fraction) or (b) 1 h incubation with the slurry method, before the loaded resin is packed into a column. Both beds were loaded with 40 mg$_{AAR}$/mL$_{resin}$ -●-●.

These results show that, at least the largest portion of active AAR will not elute below 120 mM. Thus, next the effect of 12 mM imidazole in the lysis buffer was tested. The elution profiles of a purification with 12 mM imidazole are also shown in Fig. 4.14 and in Fig. B.4, starting with the washing step. For the profile with imidazole, the characteristic peak around 50 mL before the start of the elution is much smaller, indicating less unspecific binding. This is confirmed in the overview in Fig. 4.14. Again, less protein is collected, but the activity obtained per amount of protein is 10 % higher. The earlier elution of the main peak might have been caused by the presence of imidazole during the lysis process, but did not seem to impact the activity.

Finally, the column was also loaded with 40 mg$_{AAR}$/mL$_{resin}$ and the effect of the flow of the crude extract through the column at 1 mL/min in comparison to an 1 h incubation and sub-sequential packing of the loaded material, was compared. The resulting elution profiles are shown in Fig 4.15 and the collected amount of AAR and its activity is again plotted in Fig 4.13. The longer incubation with the slurry method allows the solution to reach an equilibrium state, favoring the specific his-tag-bindings of the active AAR. Therefore, more active AAR is bound to the resin and can elute. This trend confirms the advantages of the slurry method or at least the benefit of a longer contact time of the AAR with the resin.

Concentration and buffer change

The existing immobilization protocol included a step for the concentration of the AAR solution after the purification, followed by a buffer exchange step in order to remove the imidazole. According to Purolite, imidazole should not hinder the immobilization of AAR onto ECR8309F. Therefore, the activity of immobilized AAR with and without concentration and buffer exchange was tested.

The resulting activities are shown in Fig. B.8 and show an activity loss of about 10 % when immobilizing the AAR without prior concentration or buffer exchange. In case the long time activity of the immobilized AAR can be proven to be as good as with the buffer exchange, it is recommended to remove the steps from the protocol for cost reduction.

Concluding recommendations and outlook for small and large scale AAR production

Based on the results in this section, the above described fed-batch fermentation protocol of FB-5 and FB-6 is recommended. With this protocol, the productivity can be increased in comparison to the existing protocol by a factor of 17 to a yield of 240-270 mg_{AAR}/L_{ferm}.

The purification was improved by increasing the load from 12-17 to 40 mg/mL, improving the imidazole gradient and applying the slurry method. The resin was not changed, since it showed the highest capacity in comparison to the tested alternatives. If small amounts of AAR are required, it is recommended to use the pre-packed column, disrupt the wet biomass in lysis buffer with 12 mM imidazole and load the column with 40 mg_{AAR}/mL_{resin} ($\approx$ 18 mg_{AAR}/g_{wb}). After the washing step and an elution gradient of 1 BV 0-40 %, 2 BV 40 % and 1 BV 40-100 % elution buffer is recommended. With this method around 180-200 mg AAR with a concentration of 7.8-8 g/L and an activity of $\approx$ 385 U/mg_{AAR} can be obtained with one purification with a "HisTrap FF crude 5 mL".

For larger scale purifications the slurry method should be preferred. It can be upscaled easily and in contrast to the flow through method with the pre-packed column the load time will not increase. Again, around 36-40 mg_{AAR}/mL resin can be purified with an activity of $>$ 450 U/mg_{AAR}. Afterwards, the material can be reused at least four more times, before its binding capacity decreases. Thus, a productivity of at least 180-200 mg_{AAR}/mL_{resin} can be achieved.

With the improved protocols, the new material cost for the production of immobilized AAR is estimated to be 200 €/g_{AAR} with respect to the amount of AAR and 7 €/$g_{carrier}$ with respect to the resin, which is immobilized with 35 $mg_{AAR}/g_{carrier}$ (see App. B.6). Therefore, the material costs were reduced by 80 %.

4.5 Conclusions regarding the amino acid racemase kinetics and production process

The application of racemases to improve enantioselective separation processes is still an overlooked option. In this work, the wide applicability and high stability of an immobilized amino acid racemase (AAR) is shown. For the characterization, the AAR was immobilized on the carrier "ECF 8309F" (Purolite) with a loading of 35 $mg_{AAR}/g_{carrier}$. The immobilized racemase was then packed as an enzymatic fixed bed reactor (EFBR) and studied regarding its activity for racemizing *L*- and *D*-methionine (Met). The highest activity at 20 °C was achieved in a solvent with 20 mM phosphate buffer at pH 7 and 8 as well as in an unbuffered eluent of pure water and Met at pH 5.8. While 5 vol% had no significant effect on the activity, an addition of 10 vol% alcohol resulted in an activity loss of 20-30 %. Furthermore, significant AAR activities were confirmed for *L*-lysine and *L*-arginine in a solution of pH 7.5 and for *L*-glutamine, *L*-serine and *L*-asparagine in 100 % water.

An encouraging result for further application of enzymatic fixed-bed reactors (EFBR) as a process intensification tool in coupled processes is the observed high stability of immobilized racemase in comparison to free enzymes. After exposing the EFBR for one month to water with a flow rate of 1 mL/min and at room temperature, the AAR had a remaining activity of 80 %. Therefore, the EFBR is suitable for an integration into an enantio-separation process for a range of different amino acids, if the separation is performed in a water-based non-toxic solvent. By integrating an evaporation step, the coupling with alcohol-containing solvents is also possible. For a given process with a total feed concentration of 20 g/L *DL*-Met, the EFBR can reach productivities of around 120 $g_{D\text{-Met}}/g_{carrier}$/day in case of 90 % enantiomeric excess at the reactor inlet and an exiting conversion of 90 %. It can be finally concluded, that an integration of immobilized AAR into chiral resolution processes has large potential to increase the overall performance of providing enantiopure amino acids. The conceptional findings can be extended to other chiral target molecules and other racemases.

In order to apply the AAR to other enantioselective separation processes, its production process needed to be improved. Within the scope of this work the fermentation medium was improved and the process was changed to a fed-batch fermentation. These changes improved the AAR yield from 14 to over 240 mg_{AAR}/L_{ferm} and improved the ratio of active to not active AAR, resulting in an increase of the relative activity from 2.7 to 93 U/mL_{ferm}. The purification of the AAR was identified as the most expensive part of the down-stream process. By increasing the load of the AAR onto the resin and improving the elution gradient, the productivity of the purification was improved from 17 to 40 mg_{AAR}/mL_{resin} and the overall activity was enhanced. With theses improvements, the required AAR can now be produced in-house with direct materials costs of 200 €/g_{AAR} and 7 €/$g_{carrier}$.

5 Characterization and simulation-based comparison of different chromatographic separations as stand alone units and in an integrated setup

The success of a process not only depends on its setup and on the specific characteristics of the chiral substances but also on the chosen chromatographic system. Batch chromatography with pulse injections and simulated moving bed (SMB) chromatography are two well known chromatography modes. Their advantages and disadvantages for case study I (CS-I) have been studied in Harriehausen et al. 2020 [162]. Therefore, the focus of this chapter is put on the separation with true moving bed (TMB) and SMB chromatography.

When coupling the chiral chromatographic separation with a by-product recycling step, new design aspects need to be considered, since the process yield becomes independent from the distomer purity. This leads to improved operating conditions for the chromatographic process. The TMB processes were modelled and discussed for two case studies to highlight difference between general conclusions and case specific advantages. For the accurate process prediction, a detailed model, incorporating adsorption isotherms as well as a model for the chromatographic column with well estimated model parameters, was set up.

In the first section of this chapter, the column characteristics and adsorption behaviors of both case studies were studied. Afterwards, the operating conditions for multi-column units are explored with TMB models as stand-alone units and in an integrated setup with distomer racemization. Finally, the productivies of the two case studies are compared for different scenarios in an integrated setup.

5.1 Characterization of the chromatographic separation of the racemic mixtures on Chirobiotic T columns

Before optimizing the chromatographic processes of the two model systems, the plant and column characteristics, as well as the adsorption behaviors on the stationary phase Chirobiotic T were characterized. The theory and methods applied in this section were introduced in Sec. 2.1.5 and 3.4.2.

5.1.1 Plant characteristics, column porosities and plate numbers

Based on the dead volume of the used HPLC system and the elution time of non-retained isopropanol or ethanol (EtOH), the dead time, void or pore volume, and porosity of all used Chirobiotic T columns (see Sec. 3.4.1) were estimated with Eqs. (2.11)-(2.14). For the simulation study the height of a theoretical plates (HETP) in the flow rate range of 0.4 - 3.0 mL/min were determined by analyzing small pulse injections of the racemate on the columns (Eq. (2.19), shown for PC-II in Fig. C.5). The results for the main operating flow rate of each column are summarized in Tab. 5.1 and the elution profiles for the determination of the porosities of the preparativ columns PC-I and PC-II are shown in Fig. C.3.

Tab. 5.1: Plant dead volume and column porosities of the columns from Tab. 3.7 [152] for the experiments of both CSs.

Characteristic	**Column**			
	OA-a**	**OA-b**	**PC-I***	**PC-II****
Main operating flow rate, $\dot{V}$ [mL/min]	0.5	0.5	0.5	1.0
Plant dead time, t_{plant} [min]	0.050	0.055	0.099	0.061
Plant dead volume, V_{plant} [mL]	0.050	0.11	0.198	0.061
Column volume, V_{c} [mL]	0.346	4.155	11.78	11.78
Column dead time, t_0 [min]	0.564	3.46	14.52	9.23
Column void volume, V_{void} [mL]	0.232	1.69	7.21	9.23
Column porosity, ε_{t} [-]	0.67	0.72	0.65	0.78
Plate number comp. 1, $N_{\mathrm{P},1}$ [-]	625	-	2.960	14.000
Plate number comp. 2, $N_{\mathrm{P},2}$ [-]	580	-	2.280	11.600
HETP_1 [μm]	110	-	51	11
HETP_2 [μm]	210	-	58	13

* used only for separation of *S-/R*-MA in CS-I

** used only for separation of *D-/L*-Met from CS-II

Tab. 5.2: Estimated adsorption isotherm parameters of *R*-/*S*-MA by peak-fitting, as shown in Fig. 5.1 for the quadratic and linear model (Eqs. (2.1) and (2.3)) on Chirobiotic T material (PC-I) in an eluent with 20 mM HEPES, 3.3 mM $MgCl_2$ in 20/80 MeOH/H_2O at pH 6.8 [163].

α_{RS}	H_R	H_S	$q_{s,S}$	$b_{1,S}$	$b_{2,S}$
-	-	-	g/L	L/g	L^2/g^2
2.4	0.694	0.282	4.7	0.060	0.014

5.1.2 Adsorption behavior of *RS*-mandelic acid

The adsorption equilibria of *R*-/*S*-mandelic acid (MA) on Chirobiotic T material were studied with large pulse injections [163]. In Fig. 5.1 (a) the resulting elution profiles of *R*- and *S*-MA for 10 μL pulses with 20 g/L on the Chirobiotic T column PC-I and an eluent with 20 mM HEPES, 3.3 mM $MgCl_2$ in 20/80 MeOH/H_2O at pH 6.8 are shown (see Sec. 3.4.2).

The peak of the stronger retained *R*-MA indicates an almost linear adsorption behavior within concentration range of the injected and eluted peaks (Fig. 5.1), matching the linear isotherm type (Eq. (2.1)). The peak of the less retained *S*-enantiomer has significant fronting, a characteristic of the rare anti-Langmuir behavior. Therefore, the adsorption behaviour of this enantiomer was fitted to the quadratic adsorption isotherm model (Eq. (2.3)). The parameters of both enantiomers were determined using a peak fitting method based on the least square algorithm (Eq. (2.23)) and are shown in Tab. 5.2. Remaining inconsistencies between predicted and experimental profiles for *R*-MA are a consequence of the limitations of the assumed dispersion equilibrium model, the isotherm model structure and the neglect of competitive adsorption. The consequences of the latter were found to be minor in more extensive simulations including an empirical competitive isotherm model. The differences of the peak maxima between experimental and modeled profiles visible for the peaks belonging to the highest injection concentration, shown in Fig. 5.1 (40 g/L), are also due to approaching of the detection limit of the UV/VIS detector.

5.1.3 Adsorption behaviour of *DL*-methionine

For the design of a process with chromatographic separation and enzymatic racemization, the separation of *D*-/*L*-methionine (Met) was studied with small pulse injections of the racemate on the Chirobiotic T column OA-b (250x4.6 mm) at possible operating conditions as described in Sec. 3.4.2. For a quick evaluation, the

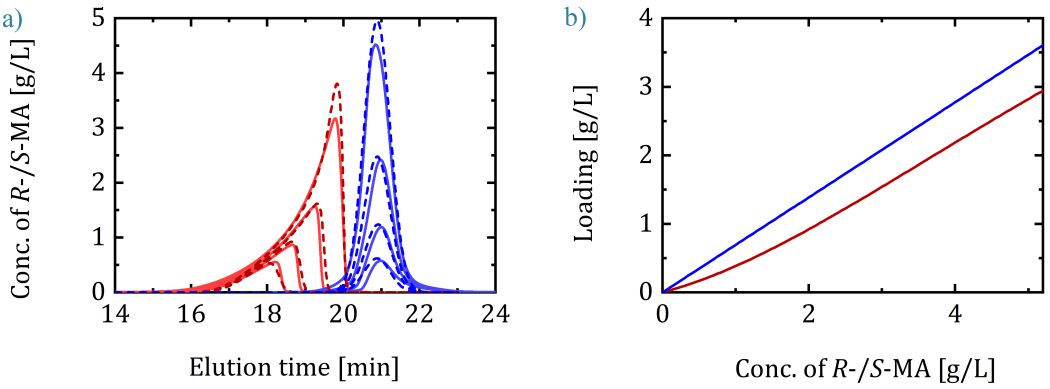

Fig. 5.1: (a) Elution profiles from pulse injections (—) and the corresponding simulated profiles (- -); (b) Adsorption isotherms of *R*- (—) and *S*-MA (—), obtained with the peak-fitting method from the pulse injections.

focus was set on the impact of the operating conditions on the Henry coefficients and the separation factor. In contrast to other parameters, like the flow rate and the operating temperature of the separation, the eluent composition has a direct effect on the racemization rate in a coupled reactor. Therefore, the influence of a phosphate buffer and the fraction of alcohol in the eluent were tested. While the impact of the buffer was rather low (see Fig. C.4), the effect of EtOH and MeOH on the separation factor was significant (Fig. 5.2, [164]).

In Fig. 5.2 (a) and (c) the Henry coefficients (Eq. (2.1)) and the resulting separation factor (Eq. (2.21)) are plotted as a function of the EtOH and MeOH fraction in the aqueous eluent. Increasing fractions of both alcohols have similar effects and in both cases *D*-Met adsorbs stronger on the chiral stationary phase than *L*-Met. The lowest retention time of both enantiomers is reached at 10-20 vol% EtOH and 20 vol% MeOH, which Henry constants of around H_L = 1.1-1.2 and H_D = 1.7 for both, EtOH and MeOH. For alcohol concentrations > 20 vol%, the Henry coefficients increase again with a stronger effect on *D*-Met. This resulted in an overall increase of the separation factor for EtOH and MeOH from α_c = 1.4 without alcohol to α_c = 2.3 for 50 vol% EtOH and 2.1 for 50 vol% MeOH. Detailed experimental data is provided in Tab. C.1. On the other hand, the solubility drops with increasing alcohol fractions and the viscosity peaks at around 25 vol% alcohol (see Fig. 5.2 (b) and (d)). This leads to an increased pressure drop over the column length.

Some conclusions can be drawn from this eluent study: For *DL*-Met and all other amino acids separated on Chirobiotic T columns in the scope of this work (see Tab. 3.9, data not shown), the *L*-form of α-amino acids is less retained than the *D*-form. This trend was confirmed for all native amino acids on chiral stationary

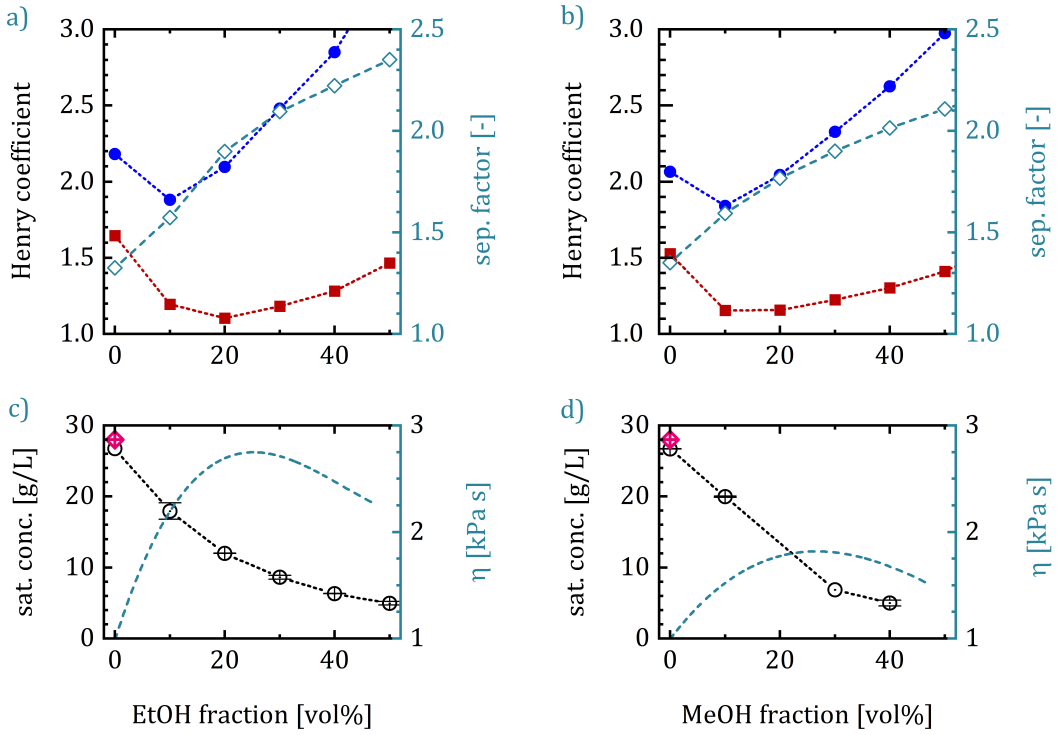

Fig. 5.2: Impact of increasing ethanol and methanol in the eluent on the separation of *D*- (●) and *L*-Met (■) with respect to (a) and (b) the Henry coefficients and the resulting separation factor and (c) and (d) the solubility limit (○) and the viscosity (▬ ▬). The pink crosses mark the solubility limit of pure *D*- and *L*-Met in H_2O according to Binev (2016) [142].

phases with teichoplanin (like the Chirobiotic T) [165] and no conditions were found, under which the elution order could be reversed.

The increasing retention time and thus higher Henry coefficients in higher alcohol concentrations is due to the reduced solubility of the solutes in the alcoholic eluent. This behaviour has been described before for the Chirobiotic T columns for various amino acids in MeOH [29]. For an efficient separation of two enantiomers their separation factor should be sufficiently high and at least $\alpha = 1.5$. For *DL*-Met this separation factor meets the criteria for >10 vol% EtOH and MeOH in the eluent.

In a trade-off between solubility and separation efficiency, eluents with 20 and 40 vol% alcohol were chosen as suitable candidates of a coupled setup. The adsorption behaviour of *D*-/*L*-Met in M2080, E2080 and E4060 was determined with the perturbation method (see Sec. 2.1.5). For the perturbation method, the column PC-I was loaded with 0, 2.5, 5, 7.5 and 10 g/L of the pure enantiomer. Every concentration was applied until the detector signal was stable and the column had reached a new equilibrium state. Then, small pulses with a volume of 1 µL and a

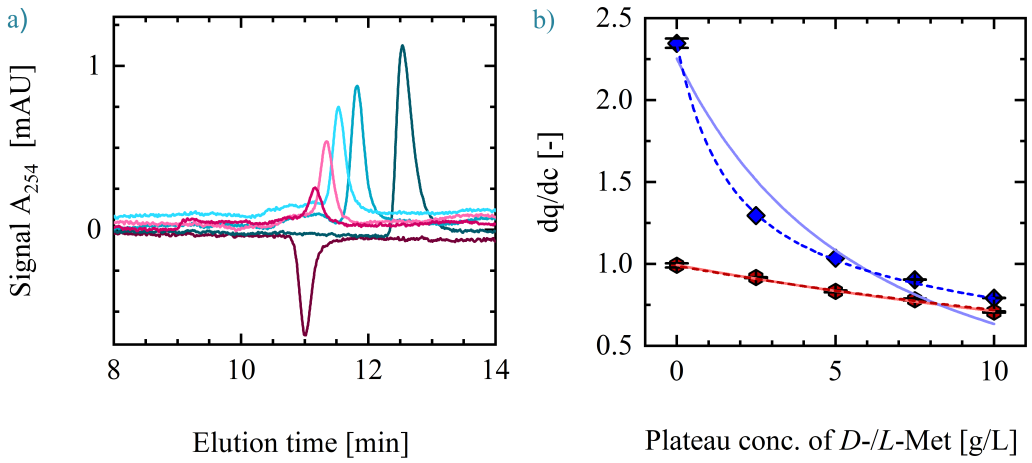

Fig. 5.3: Application of perturbation method: (a) Signal of small pulse injections onto plateaus of 0, 2.5, 5, 7.5 and 10 g/L of *L* or *D*-Met, (b) $\partial q/\partial c$ of *D*- (◆) and *L*-Met (◆) in M2080 and fitted Langmuir (—) and bi-Langmuir (- -) models.

concentrations, which was higher or lower than the plateau, were injected onto the column at a flow rate of 1 mL/min. In Fig. 5.3 (a) the elution profiles of exemplary pulses are shown for each plateau of *D*-Met in M2080. The elution time of the peaks was determined and then converted with Eq. (2.26) into the derivative $\partial q/\partial c$. The resulting points for *D*- and *L*-Met in M2080 are plotted in Fig. 5.3 (b) and can be found in Tab. 5.3. The corresponding figures and tables for the EtOH-water-mixture are shown in App. C.4.

The derivatives $\partial q/\partial c$ (c = 0 g/L) of the perturbation method are the same as the Henry coefficients from the eluent study and should be identical. Yet, e. g. while the initial slopes for M2080 were $H_1 = 1.10$ and $H_2 = 1.75$, the corresponding Henry coefficients measured with the perturbation method were $H_1 = 1.0$ and $H_2 = 2.0$. A similar behaviour could be seen for EtOH-water mixtures and for 40/60 the retention of *D*-Met was even stronger and shifted the H_2 from 2.2 to 3.7. Such a deviation of the retention times is quite common [166] and there are different possible explanations for this discrepancy: The retention peaks for a plateau concentration of 0 g/L was measured with an old Chirobiotic T column (OA-b) with 20 μm particles while the perturbation method was applied to a new semi-preparative column (PC-I) with 5 μm particle size. Therefore, the adsorption behaviour could have been altered in the older column over time, reducing the selectivity. Another explanation could be that the perturbation value was obtained after loading the column over multiple hours with up to 10 g/L Met. Therefore, a new equilibrium state could have been reached, shifting the equilibrium. This also shows the advantage of the perturbation method. In comparison to simple pulse injections it provides more reliable information about the adsorption behaviour in

Tab. 5.3: Experimental data of the perturbation method for the determination of adsorption isotherms of CS-II on PC-I. All experiments were carried out with a flow rate of 1 mL/min and the 1 μL pulses were injected under constant loading conditions. Assumed parameters: $\varepsilon_t = 0.78$, $t_{dead} = 0.07$ min, F = 0.276.

$c_{D\text{-}/L\text{-Met}}$ g/L	$t_{R,L\text{-Met}}$ min	$\partial q/\partial c_{L\text{-Met}}$ -	$t_{R,D\text{-Met}}$ min	$\partial q/\partial c_D$ -
10.0	11.10 ± 0.01	0.714 ± 0.004	11.32 ± 0.02	0.850 ± 1.1E-3
7.5	11.29 ± 0.02	0.790 ± 0.006	11.60 ± 0.01	0.931 ± 0.9E-3
5.0	11.42 ± 0.01	0.840 ± 0.006	11.93 ± 0.02	1.022 ± 2.2E-3
2.5	11.64 ± 0.01	0.924 ± 0.003	12.60 ± 0.01	1.202 ± 0.7E-3
0.0	11.83 ± 0.03	1.00 ± 0.013	15.28 ± 0.2	1.968 ± 23.4E-3

the production process, in which the column material is also exposed to higher concentrations of the feed.

Next, the derivatives of the Langmuir (Eq. (2.2)) and bi-Langmuir (Eq. (2.4)) adsorption isotherms were fitted with a least-square-method similar to Eq. (2.22) and the nonlinear programming solver *fmincon* in MATLAB R2021a to the $\partial q/\partial c$-points in Tab. 5.3. The parameter for the Langmuir model are summarized in Tab. 5.4 for all three eluents. For M2080 the resulting derivatives for *L*- and *D*-Met are plotted as dashed lines in Fig. 5.3. The corresponding figures for the EtOH-water-mixture are shown in Fig. C.7. While the parameters are able to present the derivation of the *L*-Met adsorption behaviour quite well, the fit for *D*-Met is not able to describe the behaviour at low and high concentrations. The Langmuir model assumes a single binding side. However, the steep decrease of the derivative between 0 and 2.5 g/L *D*-Met, which mirrors a high initial slope (here $H_{D\text{-Met}} \approx 2$), followed by a rapid flattening of the adsorption isotherm curve indicates two binding sites: One site with a strong retention behaviour, but low saturation capacity and another one with less retention, but a higher capacity. This behaviour can be described by the bi-Langmuir model.

Tab. 5.4: Estimated adsorption isotherm parameters from the results of the perturbation method in Tab. 5.3 for the Langmuir model with individual saturation capacities.

Eluent	$H_{L\text{-Met}}$ -	$H_{D\text{-Met}}$ -	$q_{s,L\text{-Met}}$ g/L	$b_{L\text{-Met}}$ L/g	$q_{s,D\text{-Met}}$ g/L	$b_{D\text{-Met}}$ L/g
M2080	0.99	2.25	54.9	0.018	25.46	0.089
E2080	1.22	2.27	31.0	0.039	21.18	0.107
E4060	1.10	3.49	17.5	0.063	8.39	0.416

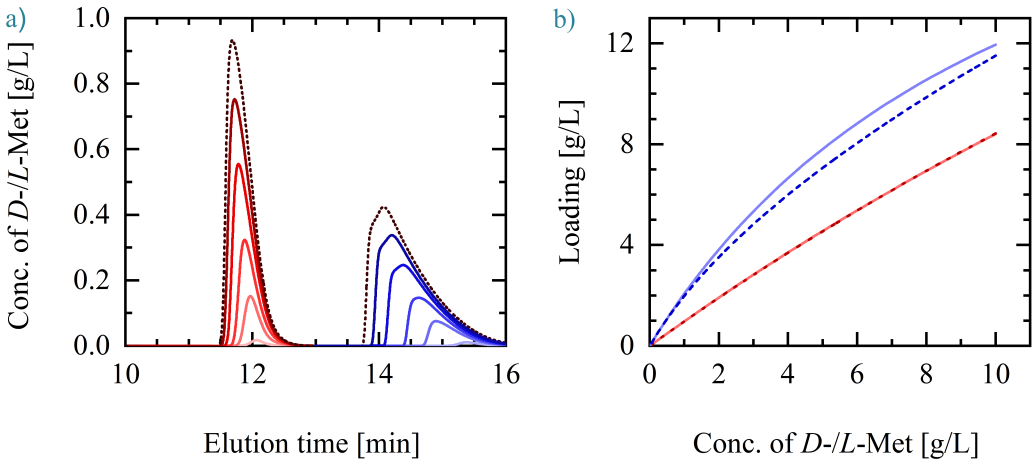

Fig. 5.4: (a) Elution profiles of pulse injections of *D*-Met (—) and *L*-Met (—); (b) Langmuir (—) and bi-Langmuir (– –) adsorption isotherms, determined with the perturbation method for *D*-/*L*- Met in M2080.

The parameter fitting to this model (shown in Tab. C.2) resulted in almost identical parameters $b_{I,L\text{-Met}}$ and $b_{I,D\text{-Met}}$, while the fitted value for $b_{II,L\text{-Met}}$ was much smaller than $b_{II,D\text{-Met}}$. This indicates that the adsorption is characterized by one selective chiral site and one unselective site. Therefore, the data could be fitted to a modification of the bi-Langmuir model, common for chiral systems, presented in Eq. (2.7) [52]. The results of the new fitting are shown in Tab. 5.5.

Tab. 5.5: Estimated adsorption isotherm parameters from the results of the perturbation method in Tab. 5.3 for the bi-Langmuir model for identical saturation capacities and $b_{I,L\text{-Met}} = b_{I,D\text{-Met}} = b_I$.

Eluent	$q_{s,I}$ g/L	b_I L/g	$q_{s,II}$ g/L	$b_{II,L\text{-Met}}$ L/g	$b_{II,D\text{-Met}}$ L/g	$H_{L\text{-Met}}$ -	$H_{D\text{-Met}}$ -
M2080	57.4	0.0172	3.99	0.00	0.339	0.99	2.34
E2080	33.4	0.0363	2.28	0.00	0.579	1.21	2.53
E4060	15.6	0.0689	2.23	0.167	1.18	1.11	3.70

With the chiral bi-Langmuir model both adsorption behaviours can be well described and the estimated Henry-coefficients match with the experimental values of $\partial q_i / \partial c_i$ (c_i = 0 g/L). The first saturation capacity $q_{S,I}$ indicates the large unselective capacity of the chiral column while $q_{s,II}$ presents the capacity of the selective site. Especially for M2080, the coefficient $b_{II,L\text{-Met}}$ is zero, indicating, that the *L*-enantiomer adsorption is not adsorbed on the selective sites, while $b_{II,D\text{-Met}}$ = 0.39 indicates a strong concentration dependent adsorption of *D*-Met. These trends can also be seen in Fig. 5.4 (a) in the elution profiles measured for the eluent M2080 with a flow of 1 mL/min an 1-100 μL injections of 10 g/L *D*- and *L*-Met and the adsorption

isotherms plotted in Fig. 5.4 (b) with the parameters estimated for the Langmuir and bi-Langmuir model.

5.1.4 Evaluation and comparison of adsorption behaviour of the two case studies

Fig. 5.5 (b) shows the single component adsorption isotherms of the MA enantiomers (CS-I) in contrast to the Met enantiomers (CS-II). The zoomed in window shows that despite their similar selectivities of $\alpha_{\text{CS-I}} = \alpha_{\text{CS-II}} = 2.3$, the Henry coefficients for *R*- and *S*-MA of CS-I are much lower than for *D*- and *L*-Met. The low Henry coefficients of CS-I are favorable and will allow a more efficient separation with higher productivities and lower solvent consumptions for low feed concentrations. For higher feed concentrations the entire slope of the isotherms need to be taken into account. The anti-Langmuir behaviour of *S*-MA in combination with the linear adsorption of *R*-MA in the studied concentration range on the other hand is unfavourable for the separation in CS-I. It leads to similar adsorption strength of the two enantiomers, narrowing the operating window. In contrast, for CS-II with Langmuiran adsorption the saturation capacity of the chiral site is high enough for *D-/L*-Met to maintain a sufficient separation. Therefore, even though *RS*-MA has a three times higher solubility than *DL*-Met, the overall productivity of the enantioselective separation at identical feed concentrations will be worse.

5.2 Simulation study: Design of a conventional four zone true moving bed chromatography process

In classical four zone (4Z) close-loop TMB and SMB chromatography each zone has a specific task [65]. The zones II and III perform the separation of the binary system by carrying the less retained enantiomer to the raffinate port and the more retained enantiomer to the extract port. The operating region, in which both enantiomers elute in their pure form at the two ports usually forms a triangle, where one side is a diagonal line through the m_{II}-m_{III}-plane and the two attached corners are defined by the Henry coefficients of the two components: (H_1/H_1) and (H_2/H_2). The shape of the remaining two sides varies in dependence of the adsorption behaviour. The Henry coefficients also influence the required minimal flow rate in zone I for the regeneration of the stationary phase and the maximal flow rate of zone IV for full eluent regeneration.

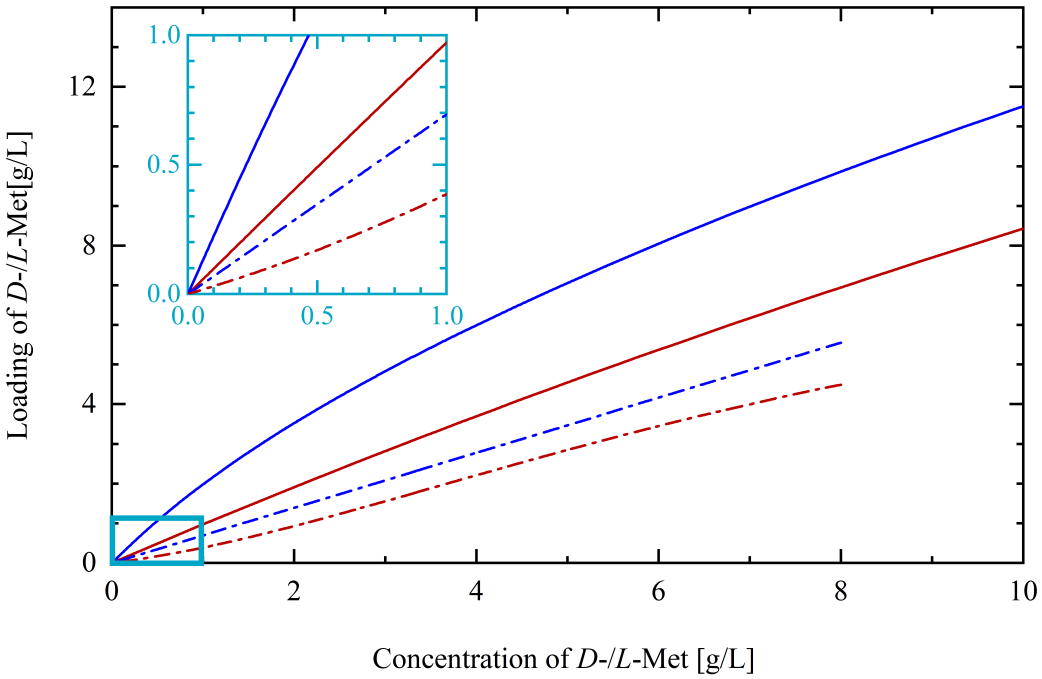

Fig. 5.5: Single adsorption isotherms of both case studies: CS-I (*S*-MA: ▬, *R*- MA: ▬) in 20/80 MeOH/buffer and CS-II (*L*-Met: ▬, *D*-Met: ▬) in 20/80 MeOH/H_2O

The optimal productivity and solvent consumption of a conventional 4Z-TMB unit is achieved when operating the separation zone II and III in the vertex of the triangle and the regeneration zones I and IV in the left corner of the rectangle, with the lowest possible flow rates in zone I and II and the highest possible flow rates in zone III and IV.

Since an actual SMB unit will always perform worse than a TMB unit and possible fluctuations of the systems must be taken into account, the actual operating point must be chosen more conservatively. The following set of equations can serve as an orientation to determine the safety margin β:

$$m_{\mathrm{I,safe}} = m_{\mathrm{I,ideal}} + \frac{m_{\mathrm{I,ideal}} + m_{\mathrm{IV,ideal}}}{2} \cdot \beta \tag{5.1}$$

$$m_{\mathrm{II,safe}} = m_{\mathrm{II,ideal}} + \frac{m_{\mathrm{II,ideal}} + m_{\mathrm{III,ideal}}}{2} \cdot \beta \tag{5.2}$$

$$m_{\mathrm{III,safe}} = m_{\mathrm{III,ideal}} - \frac{m_{\mathrm{II,ideal}} + m_{\mathrm{III,ideal}}}{2} \cdot \beta \tag{5.3}$$

$$m_{\mathrm{IV,safe}} = m_{\mathrm{I,ideal}} - \frac{m_{\mathrm{I,ideal}} + m_{\mathrm{IV,ideal}}}{2} \cdot \beta \tag{5.4}$$

Depending on the amount of columns and operating mode the size of the safety margin can be adjusted.

5.2.1 Case study I: Design, operation and productivity

The CS-I is characterized by the rare anti-Langmuir adsoption behaviour of *S*-MA. Therefore, no explicit solution for the design of the operating region of a separation with TMB chromatography exists. Consequentially, CS-I was studied by simulating the separation of *R*- and *S*-MA in an ideal 4Z-TMB chromatography unit exploiting the method of lines (see Sec. C.2) and the parameter set provided in Tab. 5.6. The solutions of the dynamic model were implemented with Python (Python 3.6, Rossum, CWI, Netherlands). Once the simulation of the dynamic equations had reached a steady state situation at the product outlet, it was terminated and the steady state solutions were used for further analysis.

Tab. 5.6: CS-I: parameter set used for the simulations of the TMB chromatography unit based on parameters from Tab. 5.1 and Tab. 5.2.

Parameter	**Symbol**	**Value**	**Unit**
Fresh feed conc.	$c_{RS,\text{feed}}$	2, 4, 15, 40	[g/L]
Chromatographic separation			
Quadratic isotherm	q_s	4.7	[g/L]
(Eq. (2.3))	b_1	0.060	[g/L]
	b_2	0.014	[g/L]
	H_1	0.282	[g/L]
Linear (Eq. (2.1))	H_i	0.694	[-]
C. plate number	N_p	300	[-]
TMB chromatography			
Total flow rate	$\dot{V}_\text{tot}$	47.8	mL/min
Solid phase flow rate	$\dot{V}_\text{s}$	22-29	[mL/min]

In applying the described scanning procedure to identify the size and shape of the separation region, the single component isotherms of the two enantiomers were used instead of the implicit multi-component adsorption isotherm models, which would have caused large computation times. This was considered to be justified because preliminary equilibrium calculations revealed rather low competition effects for this system.

Fig. 5.6 shows the resulting separation regions of the conventional TMB unit in the m_II-m_III-separation region for three different racemic feed concentrations $c_{RS,\text{F}}$ = 2, 4, 15, and 40 g/L. This region was calculated, fulfilling the requirements of complete regeneration, by choosing sufficiently safe m_I and m_IV-values. In comparison to the corresponding separation regions for linear adsorption behaviour

(Fig. 2.6), the anti-Langmuirian behaviour of *S*-MA leads to a characteristic transformation of the shape of the region. This deformation strength is concentration dependent and the resulting shape of the separation region is oppositely curved to the well-known distortion of the Langmuirian systems [74].

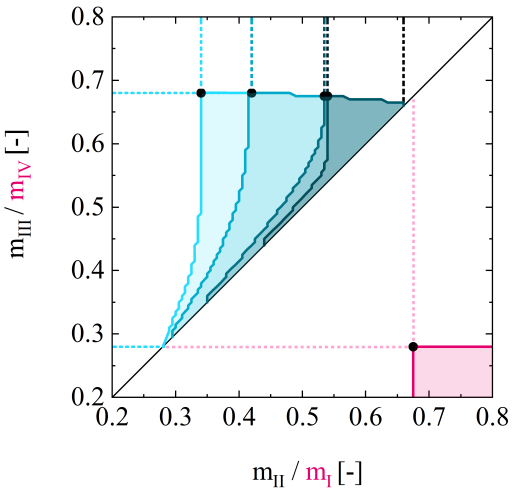

Fig. 5.6: Operating regions for perfect separation of a TMB process described as flow rate ratios in the m_{II}-m_{III}-plane for 2 (—), 4 (—), 15 (—), and 40 (—) g/L *RS*-MA and full regeneration in the m_{I}-m_{IV}-plane (—). The theoretical optimal operating points are marked as black circles in the vertex of the triangles and the upper left corner of the regeneration zone.

Next, the productivities and solvent consumptions with an ideal TMB unit and with reasonable safety margins β= 10 % were determined for the examples presented in Fig. 5.6 and Eqs. (5.1)-(5.4). They are presented in Tab. 5.7. For the highest feed concentration of $c_{RS,F}$ = 40 g/L the operating window was obtained with an extrapolation of the adsorption isotherm data and can therefore be faulty. A more detailed evaluation of the data and a comparison with the results for CS-II can be found in Sec. 5.2.3.

5.2.2 Case study II: Design, operation and productivity

The processing of *DL*-Met, in order to obtain pure *D*- or *L*-Met, was studied based on parameters and conclusions from Sec. 5.1. Even though the adsorption behaviour of *D*-Met is better described with the bi-Langmuir model. The Langmuir model fitted sufficiently for a brief initial scouting. Therefore, the equation set from Mazzotti et al. (1997), summarized in App. C.3, was used for a first comparison of the effect of the three tested eluents 20:80 MeOH:H_2O (M2080), 20:80 EtOH:H_2O (E2080) and 40:60 EtOH:H_2O (E4060) on the operating window of TMB chromatography.

Tab. 5.7: Optimal operating points of an ideal conventional TMB unit for the three options presented in Fig. 5.7 along with the respective productivities and solvent consumptions under the assumption of η = 1.79 kPa·s, Δp_{max} = 80 bar and therefore a total flow rate of 47.8 mL/min.

$c_{DL,feed}$ g/L	i/s* -	m_I -	m_{II} -	m_{III} -	m_{IV} -	$\dot{V}_{feed}$ mL/min	$\dot{m}_{out}$ mg/min	$Pr_{D/L}$ g/L/day	$SC_{D/L}$ L/kg
2	i	0.68	0.34	0.68	0.28	8.23	8.23	251	1162
-"-	s	0.72	0.39	0.63	0.23	5.76	5.76	176	2061
4	i	0.68	0.42	0.68	0.28	6.05	12.09	370	760
-"-	s	0.72	0.48	0.63	0.23	3.49	6.98	213	1635
15	i	0.68	0.54	0.67	0.28	3.09	23.17	708	376
-"-	s	0.72	0.60	0.61	0.23	0.42	3.15	96	3442
40*	i	0.68	0.54	0.67	0.28	2.97	59.45	1817	146
-"-	s	0.72	0.60	0.61	0.23	0.30	5.95	182	1817

*i = ideal system, s = with safety margin of 10 %

In Fig. 5.7 (a) the operating windows for complete enantiomer separation in the m_{II}-m_{III}-plane and complete regeneration in the m_I-m_{IV}-plane are colored for a feed of 10 g/L *DL*-Met for M2080 and E2080 and 5 g/L *DL*-Met for E4060. For the minimal flow rate in zone IV, the settings in the vertex of the separation triangles ($m_{II,opt}/m_{II,opt}$) were used. The dashed lines confine the areas in which only one

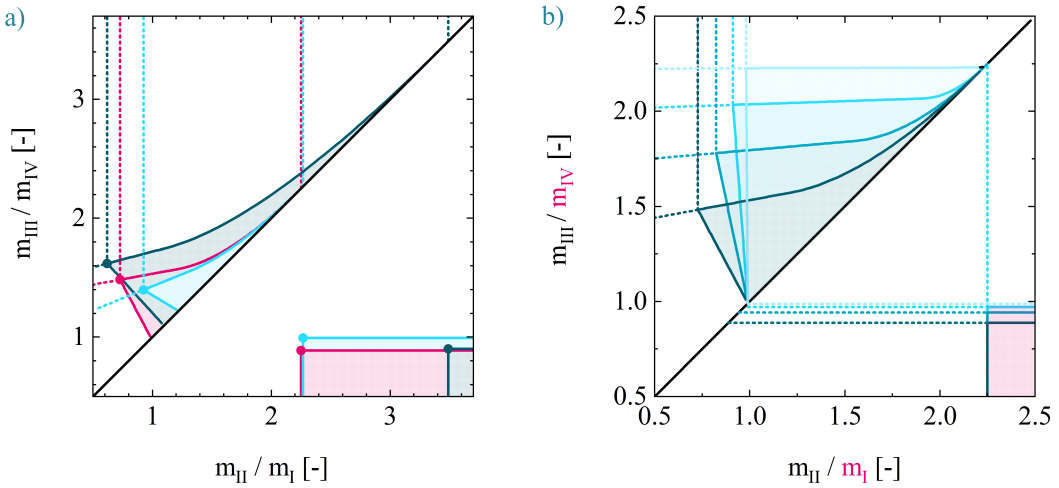

Fig. 5.7: Separation (triangles) and regeneration (rectangles) region for pure *D*-/*L*-Met in TMB for aqueous eluents with EtOH and MeOH. (a) operating region for 10 g/L *DL*-Met in M2080 (—), 10 g/L *DL*-Met in E2080 (—), 5 g/L *DL*-Met in E4060 (—); (b) operating region for 0.2, 2, 5, and 10 g/L *DL*-Met in M2080 (■ → ■).

enantiomer can be collected in its pure form. The area above the triangles are operating for pure extract, while the operating area to the left of the triangles marks the area for pure raffinate. The touching point of the vertical lines with the diagonal is defined by the Henry coefficient of the less retained *L*-Met ($H_{L\text{-Met}}/H_{L\text{-Met}}$). In M2080, *L*-Met is the least retained, enabling lower flow rates in zone II compared to the eluents with EtOH. The Henry coefficient of the stronger adsorbing *D*-Met marks the point where the upper side of the triangle ends on the diagonal ($H_{D\text{-Met}}/H_{D\text{-Met}}$). Due to the increasing Henry coefficient of *D*-Met at higher alcohol concentrations (see Fig. 5.2), the triangle for E4060 ends far higher than for M2080 and E2080. This has the potential to increase the operating window. The most important point however, is the vertex, the point with the greatest distance from the diagonal. Here, the difference between m_{III} and m_{II} is the largest and the dimensionless feed flow rate m_{feed} is therefore the highest. The optimal operation settings for all three eluents are given in Tab. 5.8 for feed concentrations of 5 and 10 g/L *DL*-Met.

In combination with the column parameters, viscosity of the eluent and the maximal pressure drop (Eq. (2.96)), it can be used to estimate the highest possible productivity of an ideal TMB unit. The maximum productivities achievable with four chiral columns of the type PC-I and PC-II under the assumptions of an interstitial porosity of ε_e=0.37 and an overall maximum pressure drop in the columns of 80 bar are given in Tab. 5.9.

Tab. 5.8: Optimal operating points of an ideal conventional TMB unit for the three options presented in Fig. 5.7 and the viscosities η from Fig. 5.2.

Eluent	$c_{DL,feed}$	i/s	m_{I}	m_{II}	m_{III}	m_{IV}	η
M2080	10	i	2.25	0.73	1.48	0.89	1.79
	-"-	s	2.41	0.84	1.37	0.73	1.79
	5	i	2.25	0.82	1.78	0.94	1.79
	-"-	s	2.41	0.95	1.65	0.78	1.79
E2080	10	i	2.27	0.93	1.40	0.99	2.7
	-"-	s	2.66	1.04	1.28	0.83	2.7
	5	i	2.27	1.01	1.69	1.10	2.7
	-"-	s	2.68	1.14	1.55	0.93	2.7
E4060	5	i	3.49	0.62	1.62	0.90	2.48
	-"-	s	4.00	0.73	1.51	0.68	2.48

*i = ideal system, s = with safety margin of 10 %

The Henry coefficients also influence the required minimal flow rate in zone I for the regeneration of the stationary phase and the maximal flow rate of zone IV for full

Tab. 5.9: Maximal achievable productivities with an ideal conventional TMB unit for the cases presented in Fig. 5.7 with the parameter set in Tab. 5.8 and an overall pressure limit of $\Delta p = 80$ bar.

Eluent	$\mathbf{c_{DL,feed}}$ g/L	i/s -	$\dot{V}_{tot}$ mL/min	$\dot{V}_{feed}$ mL/min	$\dot{m}_{out}$ mg/min	$\mathbf{Pr_{D/L}}$ g/L/day	$\mathbf{SC_{D/L}}$ L/kg
Column PC-I: 150x10mm, 20 μm							
M2080	10	i	47.8	6.75	33.7	1031	360
	-"-	s	-"-	4.82	24.1	730	609
	5	i	-"-	7.89	19.7	603	547
	-"-	s	-"-	5.81	14.5	444	909
E2080	10	i	31.7	2.68	13.4	410	539
	-"-	s	-"-	1.41	7.1	216	1256
	5	i	-"-	3.53	8.8	270	693
	-"-	s	-"-	2.18	5.4	166	1420
E4060	5	i	34.5	5.20	13.0	397	1035
	-"-	s	-"-	4.00	10.0	306	1528
Column PC-I: 150x10mm, 5 μm							
M2080	10	i	3.0	0.42	2.11	64.5	360
	-"-	s	-"-	0.30	1.51	46.0	609
	5	i	-"-	0.49	1.23	37.7	547
	-"-	s	-"-	0.36	0.91	27.8	909
E2080	10	i	2.0	0.17	0.84	25.6	539
	-"-	s	-"-	0.09	0.44	13.5	1256
	5	i	-"-	0.22	0.55	16.9	693
	-"-	s	-"-	0.14	0.34	10.4	1420
E4060	5	i	2.2	0.33	0.81	24.8	1035
	-"-	s	-"-	0.25	0.63	19.1	1528

*i = ideal system, s = with safety margin of 10 %

eluent regeneration. The most efficient regeneration is achieved in the left corner of the rectangle, with the lowest possible flow rate in zone I and the highest possible flow rate in zone IV. Here, the solvent consumption, which is the difference m_I-m_{IV}, is the lowest and, when being limited by pressure drop, the highest overall flow rates and therefore productivities can be achieved.

Thus, the weak interaction of *L*-Met for M2080 requires a higher flow rate in zone IV for eluent regeneration. On the other hand the strong adsorption of *D*-Met also increases the flow rate in zone I for full regeneration. In this case, for full regeneration of the stationary phase, the dimensionless flow rate of zone I needs to

be more than 50 % higher than for 20 vol% alcohol. Therefore, even though the viscosity and thus the pressure drop at 40 vol% EtOH are lower than at 20 vol%, when aiming for full regeneration in zone I, the highest possible flow rates in zone II and III of an SMB unit would be lower for 40 vol% EtOH than for 20 vol%.

An even bigger impact factor on the overall productivity is the particle size of the chiral stationary phase. As shown in Tab. 5.9 a reduction of the particle size from 20 μm to 5 μm reduces the overall flow rate and hence the achievable productivity by the 16-fold, due to the much higher pressure drop caused by the 5 μm particles. Unfortunately, by the time the SMB was build, the larger particles were no longer available and columns with a particle size of only 5 μm had to be used. Therefore, the maximal achievable productivity with an ideal, conventional 4Z-SMB system with a 10 g/L *DL*-Met feed can not exceed 65 g/L/day.

5.2.3 Comparison of the productivities of both case studies

In Fig. 5.8 (a) the solvent consumptions and corresponding productivities of the two CS are compared under ideal and realistic conditions. For a feed concentration of 2 g/L racemate, both CS reach similar productivities and solvent consumptions. With increasing feed concentrations, the productivities of CS-II becomes larger than the one of CS-I. Yet, due to the higher solubility, productivities of up to 1.8 kg/L/day are estimated for a feed of 40g/L *RS*-MA, while a maximum of only 1.03 kg/L/day can be reached at the highest possible feed concentration of 10 g/L *DL*-Met in M2080.

When applying a safety margin of 10 % on the operating point, the trend changes drastically, as shown in Fig. 5.8 (b). For both systems the productivity decreases and the solvent consumption increases. However, while the maximal productivity of CS-II only drops to 0.73 kg/L/day, the maximum productivity for CS-I is reached at a feed concentration of 15 g/L and decreases to 0.21 kg/L/day. So even though in the ideal case the productivity is 60 % lower when operating in a distance of 10 % from the ideal operating point, the productivity of CS-II is 250 % higher than for CS-I. The reason for the loss in productivity of CS-II is the overall small operating window, as shown in Fig. 5.9 (a). When applying the safety margin with respect to the flow rate ratios $m_{II,opt}$ and $m_{II,opt}$, the new operating point moves much closer to the diagonal than for CS-II, thus reducing the feed flow rate.

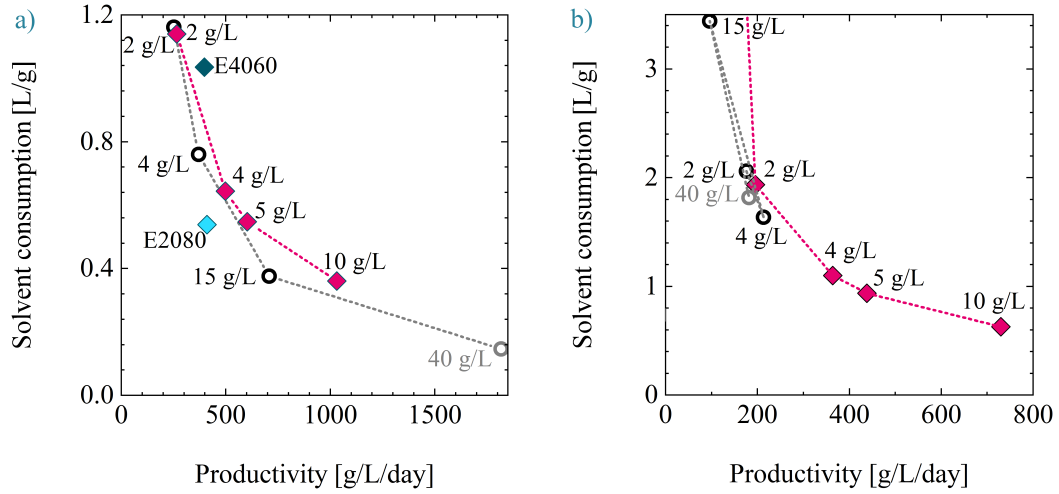

Fig. 5.8: Achievable productivities and solvent consumptions with an ideal, conventional 4Z-TMB unit with Chirobiotic T 150x10 mm, 20 μm columns (PC-I) for both case studies from Tab. 5.7 and Tab. 5.9 with (a) and without (b) safety margins. CS-I: feed of 2-40 gL/ *DL*-Met in 20/80 MeOH/buffer (○); CS-II: feed of 10 g/L *DL*-Met in M2080 (◆), 2-10 g/L *DL*-Met in E2080 (◆), 5 g/L *DL*-Met in E4060 (◆).

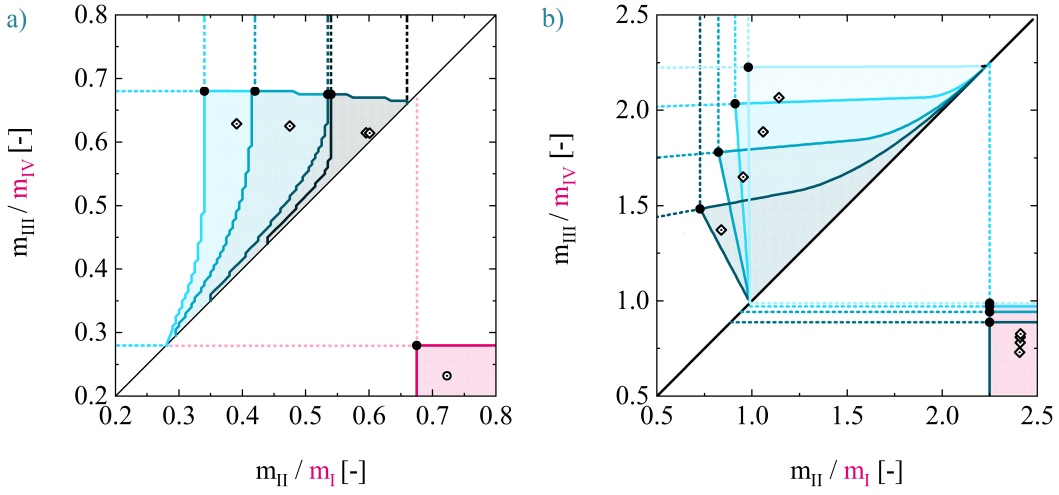

Fig. 5.9: Operating point of an ideal system (○) and with safety margins (◇) in the m_{II}-m_{III}- and m_{I}-m_{IV}-plane for the TMB process of (a) CS-I with 2 (▬), 4 (▬), 15 (▬), and 40 (▬) g/L *RS*-MA and (b) CS-II with 0.2, 2, 5, and 10 g/L *DL*-Met in M2080 (■ → ■).

5.3 Simulation study: Advantage of coupling true moving bed chromatography with an enzymatic fixed bed reactor

In the following the process of pure enantiomer provision by coupling TMB or SMB chromatography with by-product recycling was simulated, evaluated and its advantages were highlighted.

5.3.1 General considerations for process coupling

A process configuration with racemization and recycling of the distomer stream brings two advantages. The distomer racemization increases the overall yield, because the target compound eluting at the wrong port is recycled and the recycling of the by-product stream loosens some operating constraints. This results in new degrees of freedom for the operation of the SMB unit and expands the operating windows for the production of the targeted enantiomer into the operating space for pure raffinate or pure extract as shown in Fig. 2.6. Hence, depending on the target compound, the flow rate in zone II can be lowered for the collection of the less retained compound at the raffinate port or the flow in zone III can be increased for the collection of the stronger retained compound at the extract port. In any case, the feed flow rate $\dot{V}_{\mathrm{F}} = \dot{V}_{\mathrm{III}} - \dot{V}_{\mathrm{II}}$ can be increased to obtain a higher throughput (Eq. (2.87)) compared to conventional operation.

Furthermore, an alternative three zone (3Z) TMB chromatography unit could be applied, in which the fourth zone is omitted. When operating it in an open-loop configuration, the column number can be reduced without compromising throughput or product purity in exchange for an increased solvent consumption. This is an attractive approach for systems with an expensive stationary phase and the option of concentrating the recyclate and product stream with a cheaper method.

While the process coupling and by-product recycling is lifting some constraints, new constraints arise. Both units need to operate with a compatible eluent and the dilution of the by-product stream needs to be compensated. The EFBR requires an aqueous solvent at moderate pH. The only chiral stationary phase, which was compatible with aqueous solvents and could separate *R*-/*S*-MA and *D*-/*L*-Met, was the Chirobiotic T material. However, even this chiral stationary phase requires an eluent with pH < 6.8. This was solved for CS-I by using an eluent with 20 mM

HEPES, 3.3 mM $MgCl_2$ pH 6.8 and 20 vol% MeOH [42]. The solution for CS-II is discussed in Sec. 6.2.

The second issue is the dilution of the recyclate by the chromatographic unit. In order to maintain a constant feed tank concentration and steady state of the coupled process, three conditions need to be met:

1. The total mass flow of the fresh feed, $\dot{m}_{\mathrm{tot},0}$, needs to be equal to the exiting mass flow of the target enantiomer into the product tank, $\dot{m}_{\mathrm{tot,target}}$:

$$\dot{m}_{\mathrm{tot},0} = \dot{m}_{\mathrm{tot,prod}} \tag{5.5}$$

2. The flow rate into the chromatographic unit, $\dot{V}_{\mathrm{feed}}$, needs to be equal to the sum of the flow rate of the fresh feed, $\dot{V}_{\mathrm{feed},0}$, and the recycling stream, $\dot{V}_{\mathrm{rec}}$:

$$\dot{V}_{\mathrm{feed}} = \dot{V}_{\mathrm{feed},0} + \dot{V}_{\mathrm{rec}} \tag{5.6}$$

3. The mass flow rate into the chromatographic unit, $\dot{m}_{\mathrm{tot,feed}}$, needs to be equal to the sum of the mass flow of the fresh feed, $\dot{m}_{\mathrm{tot},0}$, and the recycling stream, $\dot{m}_{\mathrm{tot,rec}}$:

$$\dot{m}_{\mathrm{tot,feed}} = \dot{m}_{\mathrm{tot},0} + \dot{m}_{\mathrm{tot,rec}} = c_{\mathrm{tot},0} \cdot \dot{V}_0 + c_{\mathrm{tot,rec}} \cdot \dot{V}_{\mathrm{tot,rec}} \tag{5.7}$$

Consequently, the necessary concentration of the recycling fraction, $c_{\mathrm{tot,rec}}$, to maintain a constant total concentration of the feed tank, $c_{\mathrm{tot,feed}}$, depends on the concentration of the fresh inlet, $c_{\mathrm{tot},0}$, which is limited by the solubility limit, $c_{\mathrm{tot,solub}}$:

$$c_{\mathrm{tot,rec}} \geq \frac{\dot{m}_{\mathrm{tot,feed}} - c_{\mathrm{tot,solub}} \cdot (\dot{V}_{\mathrm{feed}} - \dot{V}_{\mathrm{rec}})}{\dot{V}_{\mathrm{rec}}} \tag{5.8}$$

Whenever this constraint is lifted, the dilution must be tackled by concentrating the recycled stream with e.g. membrane filtration or evaporation. For simplification, in the following model a perfect concentration unit is assumed, which increases the concentration of the recyclate to the feed concentration, without affecting any enantiomeric excess. The resulting flow scheme for targeting the extract or raffinate is provided in Fig. 5.10.

Another parameter influencing the productivity of the separation is the composition or the enantiomeric excess (ee in %, Eq. (2.100)) in the feed tank. In case of incomplete racemization, the remaining enantiomeric excess of distomer in the

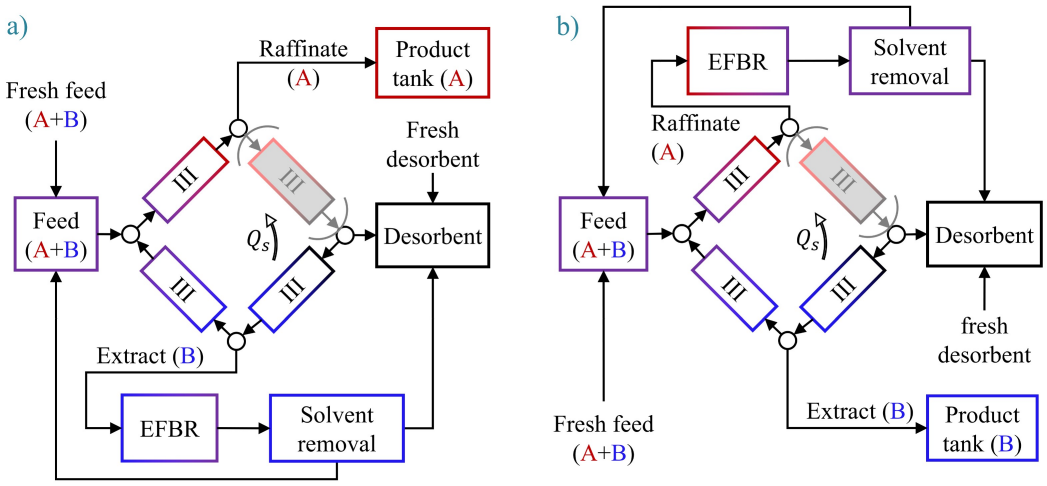

Fig. 5.10: Flow scheme for coupled 3Z-TMB-EFBR processes targeting (a) the raffinate and (b) the extract.

recycled fraction $ee_{\text{dist,rec}}$ will change the composition of the feed tank in a closed-loop arrangement. With each re-injected fraction the composition will gradually shift towards the enantiomer in excess, until a new steady state is reached. The enantiomeric excess of the by-product enantiomer in the feed tank in the steady state ($ee_{\text{dist,feed}}$) is then the ratio between the mass flow of the recyclate ($\dot{m}_{\text{dist,rec}}$, $\dot{m}_{\text{target,rec}}$) and the feed into the SMB unit ($\dot{m}_{\text{dist,feed}}$,$\dot{m}_{\text{target,feed}}$) masses:

$$ee_{\text{dist,feed}} = \frac{\dot{m}_{\text{target,rec}} + \dot{m}_{\text{dist,rec}}}{\dot{m}_{\text{target,feed}} + \dot{m}_{\text{dist,feed}}} \tag{5.9}$$

In the following, the effect of relaxed flow rate constraints on the chromatographic unit and a shift in the feed composition are discussed exemplary for CS-I and CS-II, respectively, before comparing both coupled systems.

5.3.2 Simulated performance of a coupled process for case study I

Based on the preliminary simulations from the previous section, the m_{II}-m_{III}-plane was scanned for a 4Z-TMB, with simulations as described in Sec. 5.2.1, using fixed flow rate ratios with $m_I = 0.8$ close to the theoretical limit of complete regeneration of the solid phase. The choice of the fixed phase ratio $m_{IV} = 0.3$ violates the purity constraint of Eq. (2.51), by slightly exceeding the low Henry coefficient of *S*-MA ($H_1 = 0.282$). This leads to a decrease in purity of *R*-MA under diluted conditions ($Pu_2 = 99.5$ % for $c_{i,\text{feed}} = 2$ g/L). For higher feed concentrations this contamination effect decreases due to the anti-Langmuirian behaviour.

The flow rate ratios were then used to determine the productivities assuming the same pressure drop as in Tab. 5.7. The results are presented in Fig. 5.11 for a feed of 4 and 40 g/L *RS*-MA in color code for targeting *S*-MA in the raffinate or *R*-MA in the extract with 99 % purity. For 4 g/L feed the achievable productivities are 250 g/L_c/day within the triangle of pure extract and raffinate and the small productivity increase outside the triangle in Fig. 5.11 (a) results from lowering m_{II}. For a feed concentration of 40 g/L *RS*-MA, the achievable productivities inside and outside of the triangle vary significantly. The results for a feed of 15 g/L *RS*-MA are presented in Fig. C.8. For each configuration, the operational point with the highest productivity and lowest solvent consumption, within a safety margin of the borders of the separation region, is marked with a star and listed in Tab. 5.10. In particular, for a feed concentration of $c_{RS,\text{feed}} = 40$ g/L, the operating point offering the highest productivity for the production of *S*-MA, shown in Fig. 5.11 (d), shifts towards smaller flow rates in zone II, far left from the separation area of a non-integrated SMB process. This results in an overall productivity for the less retained *S*-MA of > 5 kg/L_c/day, which significantly exceeds the achievable productivity within the triangle of 1.8 kg/L_c/day (Tab. 5.7).

Tab. 5.10: Overview of optimal process performances of CS-I for 99 % target purity. The regeneration flow rate ratios of the TMB unit were fixed to $m_I = 0.8$ and $m_{IV} = 0.3$ for the 4Z-configurations. The data for the 3Z-configuration was estimated for the operation with three PC-I columns.

Process mode	**Target**	Outlet	$\mathbf{c_{RS,feed}}$	$\mathbf{m_{II}}$	$\mathbf{m_{III}}$	$\mathbf{Pr_{target}}$ kg/L_c/day	$\mathbf{SC_{target}}$ L/kg
4Z-TMB	*S*-MA	Raff.	15	0.45	0.61	0.25	797
	R-MA	Extr.	15	0.60	0.73	0.41	508
	S-MA	Raff.	40	0.30	0.61	2.78	40
	R-MA	Extr.	40	0.60	0.73	1.1	189
3Z-TMB	*S*-MA	Raff.	15	0.45	0.61	0.30	1290
	R-MA	Extr.	15	0.60	0.73	0.48	508
	S-MA	Raff.	40	0.30	0.61	3.30	92
	R-MA	Extr.	40	0.60	0.73	1.27	189

Besides lifting the constraints of the separation zones II and III, the constraints on the regeneration zones I and IV can be reconsidered. As already introduced in Sec. 2.1.7 and 2.3, the closed-loop 4Z-SMB unit can be simplified and run in an open-loop 3Z-SMB configuration by removing the fourth zone. This can be realized in two ways.

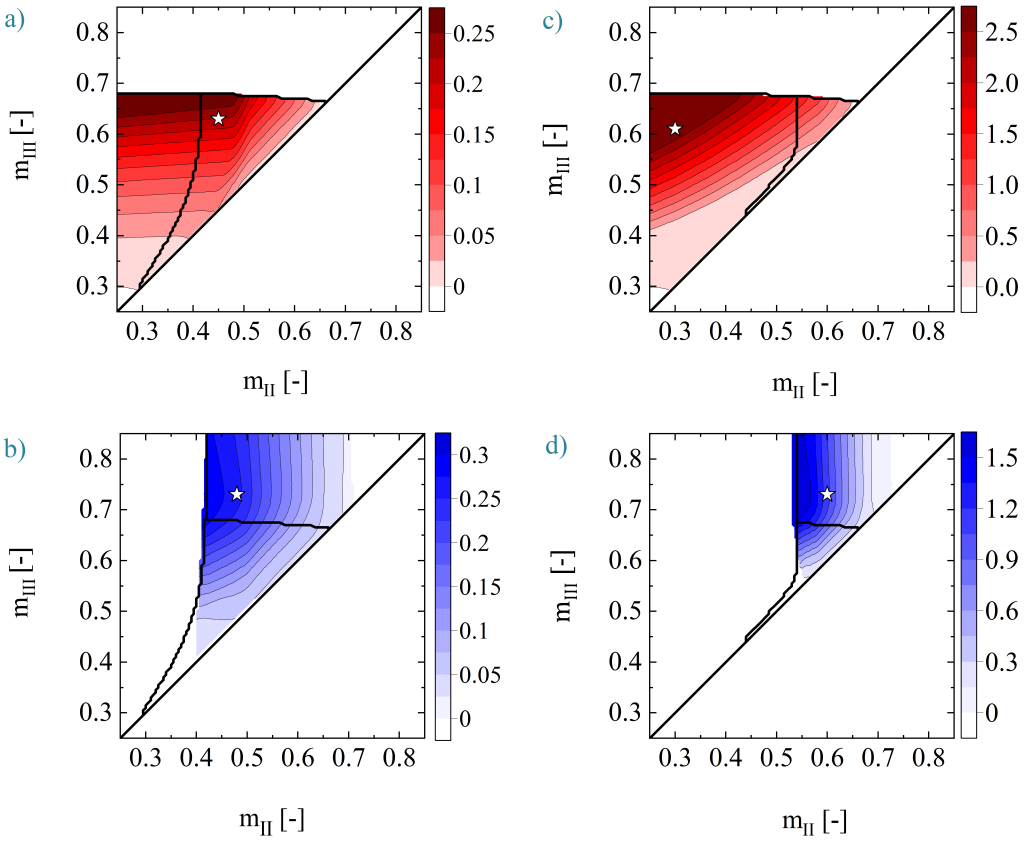

Fig. 5.11: Achievable productivities in kg/L_c/day in the m_{II}-m_{III}-plane for a 4Z-TMB for the provision of *R*- or *S*-MA with a purity of 99 % and a total flow rate of 45 mL/min (Eq. (2.96)): (a) $c_{RS,\,feed}$ = 4 g/L, target = *S*-MA in raffinate, (b) $c_{RS,\,feed}$ = 4 g/L, target = *R*-MA in extract, (c) $c_{RS,\,feed}$ = 40 g/L, target = *S*-MA in raffinate, (d) $c_{RS,\,feed}$ = 40 g/L, target = *R*-MA in extract.

One option is the removal of one column in a one-column-per-zone setup, which spares 25 % of the stationary phase. Thus, for a 3Z open-loop process the productivity increases by 33 % in a trade-off for a higher dilution of the raffinate stream. This seems acceptable for targeting either enantiomer for two reasons: When targeting *S*-MA, even for a feed concentration of 40 g/L and the operating point with the highest possible productivity, the raffinate is already diluted to $c_{R\text{-MA}} < 0.7$ g/L and the flow rate of $\dot{V}_{raff}$ = 10 mL/min is close to the feed flow rate of 11 mL/min. Therefore, a concentration of the raffinate is probably necessary for targeting either enantiomer. When targeting the raffinate, it will be beneficial for further processing of the product stream and when targeting the extract, it is even necessary, to avoid a dilution of the feed of the chromatographic unit. Hence, concentration units will be integrated into a coupled process anyways and can be exploited to perform a more cost efficient separation than with expensive chiral stationary phases. Furthermore, due the fronting behaviour of *S*-MA, the flow rate in zone IV was already low,

resulting in a comparably small extra dilution. Additionally, a significant advantage of this configuration for producing highly pure *R*-MA is the beneficial effect that *S*-MA can no longer contaminate the product extract stream via zone I.

A second option is a shifting of the column from zone IV to zone II or III and operating the TMB unit in a 1-2-1 mode when targeting the extract and in a 1-1-2 mode when targeting the raffinate. This will increase the separation efficiency of a SMB unit and allow an operation closer to the ideal operating window of a TMB unit. This also benefits the productivity, as visualized in Fig. 5.8 and 5.9.

It can therefore be concluded that relaxing the constraints on the flow rates benefits the chromatographic separation in a coupled setup with racemization with negligible disadvantages. While the concentration of the recyclate is operating properly, the EFBR is not affected by it. Whether it is more efficient to operate the unit with three columns in a 1-1-1 mode or with an additional column in zone II or III will be case specific.

5.3.3 Simulated performance of a coupled process for case study II

Like for CS-I, the chromatographic separation (Tab. 5.1) was simulated as an ideal 4Z-TMB with the method of lines (see Sec. C.2) and the adsorption isotherm parameters for the bi-Langmuir model in Tab. 5.5. The code was implemented with Python (Python 3.8, Rossum, CWI, Netherlands). The steady-state solutions were used for further analysis. For a better comparability of the two case studies, the data was evaluated for the column PC-I and for the design of the SMB unit in Chapter 6 for column PC-II.

In Fig. 5.12 (a) and (b) the achievable purities when targeting *L*-Met in the raffinate or *D*-Met in the extract are plotted in the m_{II}-m_{III}-plane in color code along with the explicit solution with the Langmuir model for the borders of the separation regions. The simulation results agree well with the explicit Langmuir solution, confirming the decision of exploiting the short-cut solution for the design of the separation. In Fig. 5.12 (c) and (d) the productivities with respect to a column volume of 4x11.78 mL are shown for the four PC-I columns with a total flow rate of $\dot{V}_{\mathrm{I}} = 47.8$ mL/min. The productivities achievable with PC-I, which will be used in the SMB system in chapter 6 are shown in Fig. C.9. In contrast to CS-I, here the productivity of the raffinate is unaffected by the relaxed constraints and also for the extract the benefits from operating outside the triangle are marginally. They mainly bring the benefit that the safety margin only needs to be applied to the upper side

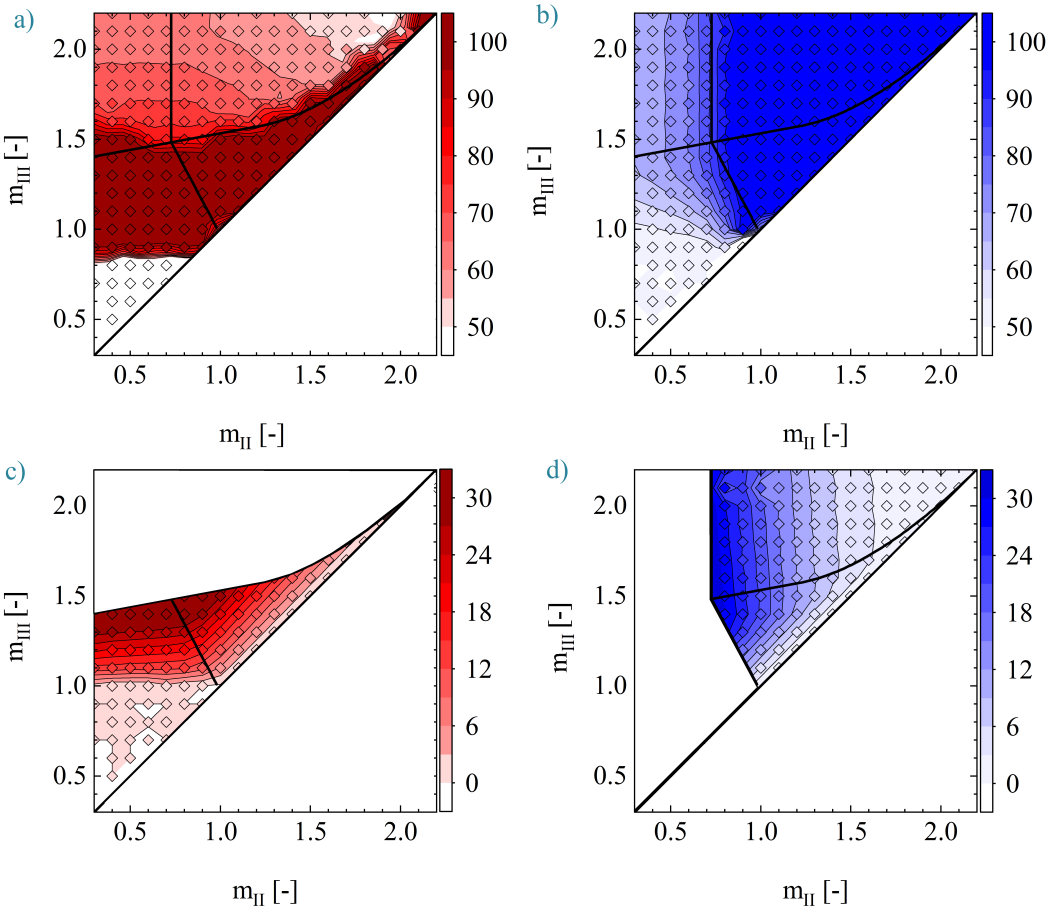

Fig. 5.12: Purities (a) and (b) and productivities in kg/L/day (c) and (d) in the m_{II}-m_{III}-plane of a TMB unit with four columns of the type PC-I with a feed concentration of 10 g/L *DL*-Met, targeting extract or raffinate and constant flow rate ratios zone m_I and m_{IV} of 2.5 and 0.65, respectively. The black lines mark the separation regions for the Langmuir model, while the rectangles show simulation results which were the grid to create the colored fit.

of the triangle when targeting the raffinate and to the left side, when targeting the extract. Hence, the unit should be operated in or close to the triangle.

So far, in this chapter, the chromatographic separation has only been studied in case of a racemic feed. However, when coupling the separation and racemization, the degree of racemization is an equally important design parameter, especially in case of a slow racemization kinetic. As shown in Fig. 4.6, the productivity of the EFBR is highly dependent on the exiting conversion at the reactor outlet. Therefore, the impact of an asymmetric feed on the chromatographic separation should also be studied. The correlation of the enantiomeric excess in the feed with the conversion at the EFBR outlet was presented in Eq. (5.9). In case of a perfect separation of both enantiomers, the enantiomeric excess at the EFBR outlet will be lowered by

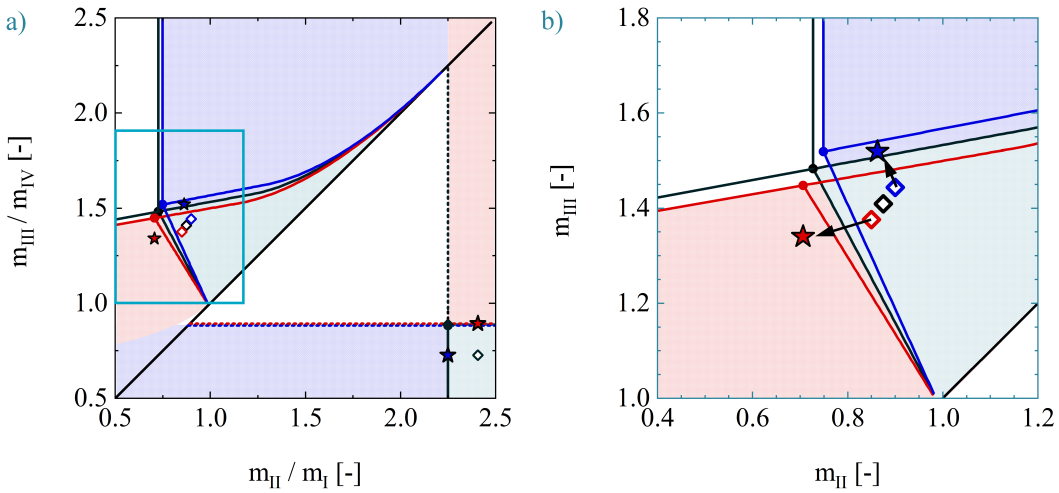

Fig. 5.13: Visualization of the impact of an enantiomeric excess in the chromatography feed, due to incomplete racemization for CS-II. If the TMB unit is operated with the m_{II} and m_{II} within the gray shaded area in the triangle and m_{I} and m_{IV} in the gray rectangle, pure *L*-Met is obtained at the raffinate port, pure *D*-Met at the extract port and zone I and IV are fully regenerated (see Fig. 2.6). In the blue zone, only pure extract is obtained and in the red zone only pure raffinate. The blue and red lines show the shift of the triangle for a feed with 4.5:5.5 *D*:*L*-Met (blue) and 5.5:4.5 *D*:*L*-Met (red).

50 % by the fresh feed. Thus, in case of an extremely high enantiomeric excess of 20 % at the EFBR outlet, the feed of the TMB unit would have 10 % ee. In Fig. 5.13 three scenarios of the operating window with a total feed concentration of 10 g/L are shown:

1. Complete racemization with 5:5 g/L *D*:*L*-Met (black line).
2. Incomplete raffinate racemization 4.5:5.5 g/L *D*:*L*-Met (blue line).
3. Incomplete extract racemization 5.5:4.5 g/L *D*:*L*-Met (red line).

The diamonds present the operating points, which should be chosen when operating with safety margins and complete separation of both enantiomers. The blue and red stars visualize the opportunities arising from the coupled setup, when targeting *D*-Met in the extract or *L*-Met in the raffinate, respectively.

According to the short-cut model with safety margins, with the racemic feed a productivity of 0.72 kg/L_c/day can be reached. For asymmetric feeds this productivity is lowered to 0.65 kg/L_c/day when targeting the extract (blue diamond) and 0.64 kg/L_c/day when targeting the raffinate (red diamond). This productivity loss of 10 % mainly results from the lowered concentration of the target compound in the feed and not the shifted operating window. Also, according to Fig. 5.12, moving

to the operating points marked by the stars, the productivity of both enantiomers can be improved and partially compensate for the productivity loss.

The reduction of the conversion from 99 % or even 99.9 % to 80 % at the EFBR outlet would therefore reduce the productivity of the TMB unit by 10 % while improving the productivity of EFBR by 130 % or 240 %, respectively and is highly recommended.

5.3.4 Performance evaluation: Impact of process specific parameters

For a comparison of the performance of the two case studies in a coupled setup, the productivity of the chromatographic separation in a 3Z-TMB unit with three columns and the racemization in an EFBR is provided in Fig. 5.14 for the following four scenarios:

1. Perfect separation and racemization: $Pu_{dist} > 99$ %, $X_{EFBR} = 99$ %
2. Perfect separation: $Pu_{dist} > 99$ %, $X_{EFBR} = 80$ %
3. Perfect racemization: $Pu_{dist} < 99$ %, $X_{EFBR} = 99$ %
4. Relaxed constraints for both units: $Pu_{dist} < 99$ %, $X_{EFBR} = 80$ %

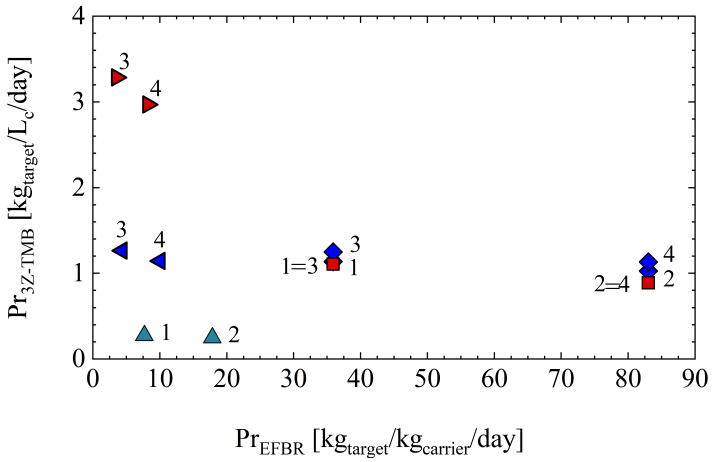

Fig. 5.14: Comparison of the productivity of the separation and racemization unit in a couple setup for both case studies. The symbols are color coded with the targeted enantiomer of CS-I: ◀ = *R*-MA, ▶ = *S*-MA ▲ = *R* and *S*-MA; and CS-II: ◆ = *D*-Met, ■ = *L*-Met.

For the relaxed purity constraints on the separation, the producivities from Tab. 5.10 were used for CS-I and were estimated from Fig. 5.12 for CS-II. For the maximum

processable feed concentration of $c_{DL,\text{feed}}$ = 10 g/L, the productions of both Met enantiomers (CS-II) exceed the productivities of MA enantiomers (CS-I) at the same feed concentration. However, when exploiting the potential of using a higher feed concentration of $c_{RS,\text{feed}}$ = 40 g/L and the anti-Langmuir behaviour of *S*-MA of CS-I in a coupled setup, a productivity for *S*-MA of more than 3 $\text{kg}_{S\text{-MA}}/\text{L}_\text{c}$/day can be achieved, which is much higher than the productivity for CS-II. On the other hand the mandelate racemase of CS-I has a much slower kinetic than the AAR of CS-II. In combination with the high throughput in the scenarios 3 and 4, the EFBR has a productivity of only 4 and 8 $\text{kg}_{D\text{-}/L\text{-Met}}/\text{kg}_\text{carrier}$/day, respectively, compared to over 80 $\text{kg}_{D\text{-}/L\text{-Met}}/\text{kg}_\text{carrier}$/day for CS-II in scenario 2 and 4.

This comparison visualizes that the optimal process configuration must be determined individually for each chiral system and racemase, considering the costs of the individual process units. Furthermore, it shall be highlighted again, that the productivities above are estimated under the assumption that a safety margin of 10 % from the operating lines of a TMB system are sufficient for pure enantiomer provision. Depending on the amount of available columns, their dimensions and packing, as well as the operation mode of the chromatographic system, it is likely that this margin will not be sufficient. Should this be the case, CS-I would be stronger affected by the increased margin than CS-II, due to its smaller operating window. Finally, it should be considered, that due to the unavailability of the Chirobiotic T columns with 20 μm particles, the SMB system in the following chapter will be operated with 5 μm particles and therefore with much lower flow rates and thus particles. These shifts will widen the gap between the productivitiy of the separation and racemization.

5.4 Conclusions from the theoretical study on the investigated chromatographic separation and process coupling

In this chapter, two case studies were used for theoretical investigations on favourable conditions under which enantioselective chromatography can be coupled with enzymatic racemisation. For this purpose, the adsorption behaviour of the two case studies, *R*-/*S*-mandelic acid and *D*-/*L*-methionine, was characterized experimentally. The adsorption isotherms of the mandelic acid enantiomers, with the rare anti-Langmuir behaviour of *S*-mandelic acid, were estimated by peak fitting of point injections. For *D*-/*L*-methionine, different solvent compositions were compared using Henry coefficients. Then, the adsorption isotherms for three solvent compositions were determined using the perturbation method and were fitted to the bi-Langmuir model. While the low Henry coefficients of *R*-/*S*-mandelic acid are favorable for high productivities at low feed concentrations, the anti-Langmuir behaviour of *S*-mandelic acid narrows the operation window at high concentrations. The separation of *D*-/*L*-methionine, on the other hand, benefits from the strong adsorption of *D*-methionine at the chiral site of the stationary phase and is only limited by the low solubility of methionine in water.

In the next section, the operating windows and productivities of a classical four zone true moving bed (TMB) chromatographic process and an open-loop three zone TMB process were designed based on the experimental data. While the triangular operating window of *D*-/*L*-methionine could be predicted analytically, the window for *R*-/*S*-mandelic acid needed to be determined by screening the window with a dynamic model of the TMB process. This screening was performed for both components and provided further information about the purity and productivity of the raffinate and extract stream outside the operation window for perfect separation. Subsequently, the feasible productivities, assuming a safety margin of the flow rates of 10 %, were estimated and compared for both case studies.

A comparison of two chiral systems reveals two important aspects to achieve high productivities: Firstly, highly selective stationary phases with sufficiently large particles to avoid a high pressure drop and secondly, exploitable high feed concentrations, which are limited by solubilities in the mobile phase. If both conditions are met, the TMB units and corresponding simulated moving bed (SMB) units could provide high productivities for *S*-mandelic of up to 3 kg/L_c/day at > 99 % purities and acceptable solvent consumptions, while the low solubilities of *D*-/*L*-methionine limit

the productivity to 1 kg/L_c/day. Considering the rather expensive chiral stationary phases and the possibility of recovering the eluent by evaporation or nanofiltration, it is recommended to remove the solvent regeneration zone in the TMB and to operate it as a three zone TMB unit.

In a next step, the TMB process was studied in a coupled setup with recycling of the distomer by racemization and subsequent feed-back into the TMB process. Recycling of the distomer after performing racemization and solvent removal steps alters and expands the operating region of the chromatographic separation process. Thus, the effect of operating the TMB process outside the triangular window of complete separation was studied. It had no negative effect on *D-/L*-methionine and, due to their adsorption characteristics, even enhanced the separation productivity of *R-/S*-mandelic acid, without affecting the yield. Furthermore, it was shown enantiomeric excess of the feed had disproportionate effect on the feed and can therefore be well tolerated.

In coupled setup, the three zone SMB option becomes even more attractive. For both case studies, the dilution of the enantiomers in the outlet stream of the TMB requires a concentration of the distomer steam, before it can be recycled to the SMB feed. Therefore, when recycling the raffinate, unlike in a non-integrated SMB unit, the three zone TMB unit with racemization already comprises a concentration unit. The extra dilution due to the missing fourth zone, can therefore be covered without the integration of an additional unit.

Finally, the productivities of the separation and racemization unit were estimated for different coupling scenarios. In case of fast enzyme kinetics, the chiral stationary phase is the main cost driving factor for the process operation. For further work on the optimization of the whole flowsheet, a focus should therefore be set on the chiral separation. Potential improvements of the process model could thus be the extension of the code, developed in the courses of this thesis, to simulate the different TMB and SMB variations. Also, the solvent components could be added to the model, along with a simulation of the evaporation unit. This would expand the parameter space for further fine tuning of the coupled process.

6 Experimental implementation of coupling simulate moving bed chromatography with enzymatic racemization in an enzymatic fixed bed reactor

With the conclusions drawn from Chapters 4 and 5 for case study II (CS-II), the simulated moving bed (SMB) system and the coupled setup with by-product recycling were experimentally implemented in a mini-plant. The results of operating the SMB unit and the coupled process are presented in this chapter. The setup of the SMB unit was realized with the guidance of Ju Weon Lee and the evaporation unit was implemented with the help of María Gutiérrez Sánchez, Peter Schulze and Vico Tennberg. The fast assembly and launch of the plant was managed thanks to the help and experience of the mechanical and electrical workshop.

In this chapter, first the results from the operating of the stand-alone SMB unit are presented, before the steps for the implementation of the racemization reactor and the evaporation unit are explained. In the last section, the results from experiments with increasing degree of process coupling are presented and the stability and robustness of the coupled process is demonstrated.

6.1 Performance of the simulated moving bed chromatography unit

The SMB unit for the separation for *DL*-methionine (Met) was set up based on the conclusions from Sec. 5.2.2. The validity of the predicted triangle regions, shown in Fig. 5.7 was tested with three runs, followed by a long fourth run in order to characterize the SMB chromatography system. The process monitoring was done manually for Run 1-3 and then automatized by installation of the on-site analysis (OA) unit.

6.1.1 Setup and characterization of the simulated moving bed chromatography system and the on-site analytic system

The SMB chromatography unit was built with four Chirobiotic T columns (PC-II, 150x10 mm, 5 μm) and one column per zone, according to Fig. 3.7. Before the assembly, the retention times of *D*- and *L*-Met in all columns was studied with small pulse injections. All retention times were in a sufficiently narrow range (Fig. C.6). The SMB system was assembled with capillaries with a total length of 6.85 m and an inner diameter of 0.5 mm. This results in a plant volume of V_{sys}= 1.3 mL. Furthermore, each pump head is expected to have a volume of approx. 1.0 mL. Since the pump in Zone I is within the column cycle, it needs to be added to the overall dead volume, resulting in an estimated total dead volume of V_{plant} = (1.3+1) mL = 2.3 mL.

The small particle size of the stationary phase, results in a high pressure drop in the columns. In combination with a maximum pressure limit of the system of first 60 bar and later on 80 bar, the column could only be operated for 20/80 EtOH/H_2O (E2080) up to 0.9-1.0 mL/min and for 20/80 MeOH/H_2O (M2080) up to a flow rate of 1.5-1.7 mL/min in zone I, which is typically the zone with the highest flow rate. When trying to maximize the productivity of a given system with regard to the flow rate, two aspects should be considered: High flow rates allow high throughput and the separation efficiency depends on the height equivalent of a theoretical plate (HETP), which is flow rate dependent. The columns used in the SMB reach their minimum HETP at around 1 mL/min. However, the HETP in the entire range of 0.5-3.0 mL/min is still excellent and with plate numbers > 1.000 far above the recommended 100-200 plates. Thus, for high productivities, the system should be operated at the highest possible flow rates.

The shifting times, $\Delta t_{\mathrm{shift}}$, for a given separation problem depend on multiple factors (Eq. (2.57)). For CS-I and its in Tab. 6.1 provided characteristics, in combination with $m_{I,min}$ = 2.3 (Fig. 5.7), the lowest possible shifting times were estimated and added to Tab. 6.1. Afterwards, the flow rates of the slower flow rates $\dot{V}_{\mathrm{II}}$, $\dot{V}_{\mathrm{III}}$, and $\dot{V}_{\mathrm{IV}}$ were determined from the flow rate ratios, m_{II}, m_{III}, and m_{IV}, by rearranging Eq. (2.57) for the actual zone flow rates $\dot{V}_{\mathrm{z}}$.

The initial runs of the SMB system were performed with the less toxic E2080 eluent. Once the system worked properly, the eluent was changed to M2080 with which, as shown in Sec. 5.2.2, shorter shifting times and therefore higher productivities could be realized. After three runs, the OA unit was connected to the SMB system at the outlet of the UV/VIS at the raffinate and extract port. For the OA unit, 1 mL

Tab. 6.1: Characteristics of the Knauer SMB Pilot Unit CSEP C9 with the configuration presented in Fig. 3.7.

V_{sys} mL	V_{pump} mL	$V_{overall}$ mL	Max. pressure bar	$\dot{V}_{I,max}$ mL/min	ε_t -	Δt_{shift} min
1.34	1.0	2.3	60	1.5/1.6/1.7	0.78	10.9/9.99/ 9.71

per cycle are drawn into a 1.8 mL mixing vial from which 0.1 μL are injected onto the 100x2.1 mm Chirobiotic T column and analyzed with the method described in Sec. 3.5.3.

6.1.2 Validation of the operating window determined with frontal analysis

The first operating parameters for the separation of *DL*-Met with the 4Z-SMB unit were chosen based on the triangle method with the adsorption and column parameters given in Tab. 5.1 and Tab. 5.4. The first separation (Run 1) was done with a racemic feed of 10 g/L *DL*-Met. The settings targeted pure extract in the first six cycles (24 shifts) and then pure raffinate for 4.5 cycles (18 shifts). Next, two runs with an asymmetric feed were performed: In Run 2a, a feed with 4.5:5.5 g/L *D*:*L*-Met was separated to purify *D*-Met in the extract and in Run 3, *L*-Met was purified at the raffinate port from a feed with 5.5:4.5 g/L *D*:*L*-Met. The chosen flow rates are visualized as dimensionless flow rates in Fig. 6.1 and are summarized in Tab. 6.2. All three runs were performed in a closed-loop operation. During each shifting time the eluate at the raffinate and extract port were collected and analyzed with HPLC (Sec. 3.4.3).

In Fig. 6.2 the actual flow rates during Run 2 and the resulting UV-signals at 230 nm at the raffinate and extract port are shown. Besides the initial build up of the profiles, the profiles of each shift resemble each other and show no unusual pattern. After around 20-24 shifts, a steady state is reached with the typical sawtooth profiles of *D*- and *L*-Met at the extract and raffinate port. The extract port signal rapidly increases after each shift, before the concentration decreases again until it reaches almost zero. The raffinate port signal shows the inverse behaviour. Especially during the first shifts the profile starts at almost zero and then gradually increases. After around five shifts, the raffinate signal no longer decreases to zero. Instead, a second sharp peak is formed at the end of each cycle. The first eluting peak reaches a signal

Tab. 6.2: Overview of settings for the SMB Runs 1-3.

Run		c_{feed} (*D*:*L*) g/L	Shifts	$\dot{V}_{feed}$ mL/min	$\dot{V}_{I}$ mL/min	$\dot{V}_{extr}$ mL/min	$\dot{V}_{raff}$ mL/min	Δt_{shift} min
1	a	5.0:5.0	1-24	0.19	1.70	0.45	0.24	9.71
	b		25-44	0.19	1.70	0.51	0.19	9.71
2	a	4.5:5.5	1-24	0.19	1.60	0.38	0.23	9.99
	b		25-32	0.19	1.60	0.40	0.21	9.99
	c		33-44	0.20	1.70	0.44	0.24	9.71
3	a	5.5:4.5	1-24	0.16	1.70	0.51	0.13	9.71
	b		25-36	0.16	1.70	0.49	0.15	9.71
	c		37-46	0.16	1.70	0.48	0.16	9.71

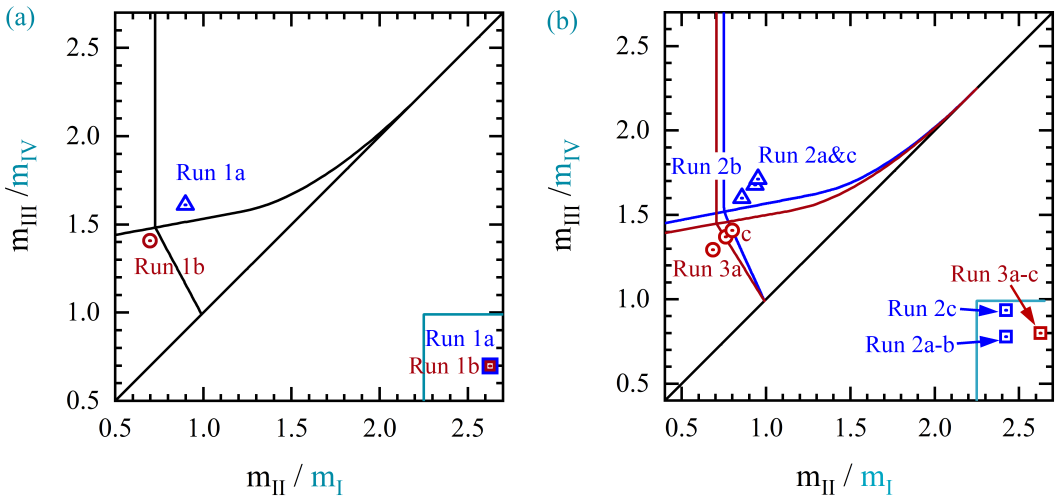

Fig. 6.1: Chosen flow rate ratios for the SMB Runs 1-3: (a) Run 1a: targeting pure extract (m_{II}/m_{III}: ▲, m_{I}/m_{IV}: ■), Run 1b: targeting pure raffinate (m_{II}/m_{III}: ●, m_{I}/m_{IV}: ■) with a racemic feed of 10 g/L *DL*-Met. (b) Run 2a-c: targeting pure extract (m_{II}/m_{III}: ▲, m_{I}/m_{IV}: ■) with a feed of 4.5:5.5 g/L *D*:*L*-Met and Run 3a-c, targeting pure raffinate (m_{II}/m_{III}: ●, m_{I}/m_{IV}: ■) with a feed of 5.5:4.5 g/L *D*:*L*-Met.

strength of around 0.7 AU for Run 2a and Run 2c and 0.65 AU for Run 2b. The size of the overshoot on top of it reaches around 0.9-0.95 AU.

The fact that the profiles show no irregularities, which are repeated every four shifts, confirms that the SMB operates properly. All four columns seem to have a similar porosity and adsorption behaviour and are suitable for further investigations. Furthermore, the increase of the UV signal half way through each shift at the raffinate port in Fig. 6.2 (b) and (e) indicates a contamination with *D*-Met. It adsorbs stronger than *L*-Met and therefore requires more time to mitigate through zone III. For the given flow rate, it elutes at the raffinate port half way through a shift. This *D*-Met

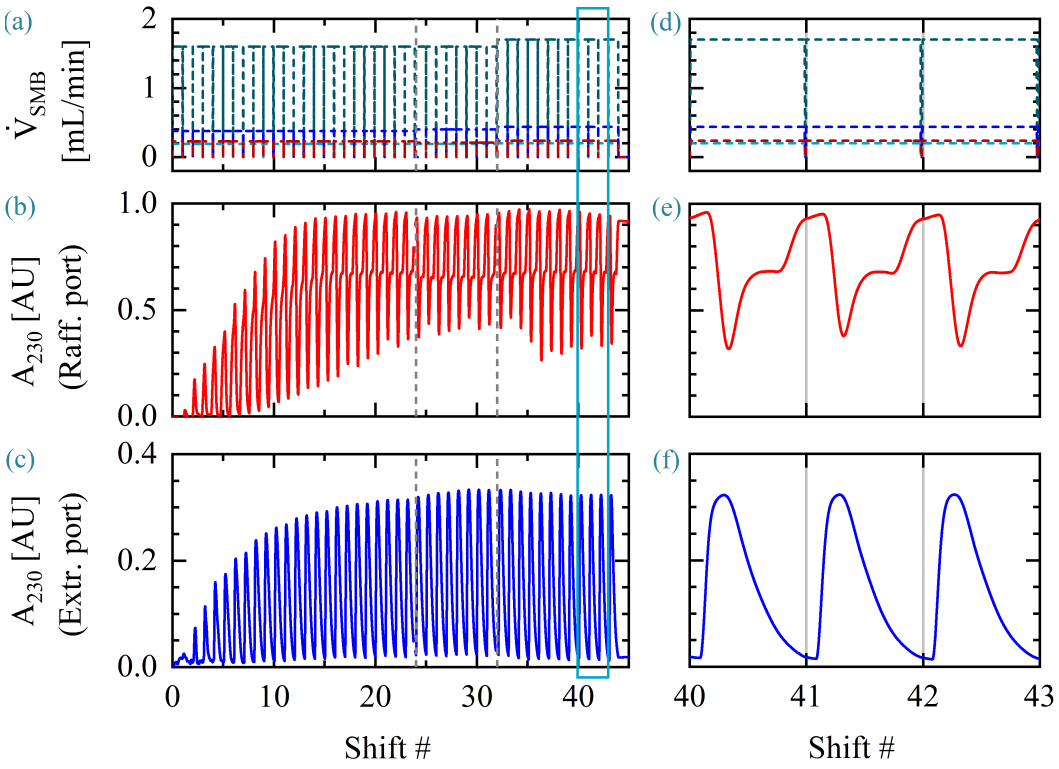

Fig. 6.2: Set flow rates and resulting SMB elution profiles of Run 2 at the raffinate and extract port: (a) Flow rates in zone I (■), at the raffinate (■) and extract port (■), and the feed (■), and UV-signals at 230 nm at (b) the raffinate and (c) the extract port. The gray dotted lines mark a switching of the settings (see Fig. 6.1). Subfigures (d)-(f) zoom into shift 41-43 from (a)-(c).

overshoot has an area of around 12 % in shift 40. In combination with the signal not going down to 0 anymore, this indicates a contamination of over 15 %. In order to avoid this contamination, the flow in zone III needs to be lowered to the point where the flow rate is weaker than the retention of *D*-Met on the stationary phase. This way, *D*-Met does not reach the raffinate port and is shifted into zone II.

A contamination of the extract port would be identified by a sharp increase of the UV-signal at the start of each shift, followed by a signal drop with an inflection point as seen in the raffinate signal. Since the profile at the extract port in Fig. 6.2 (c) and (f) is smooth, the extract seems to be pure. Therefore, the flows in zone II and IV are sufficiently low.

At the outlet of the UV-detector, the raffinate and extract are collected over the length of each cycle and their average concentration is determined with HPLC (see Sec. 3.4.3). These average concentrations of *D*- and *L*-Met are show for the racemic feed in Run 1 in Fig. 6.3 and for the asymmetric feeds in Run 2 and Run 3 in Fig. 6.4 along with the chosen dimensionless flow rates. Furthermore, for the last 3-4 shifts

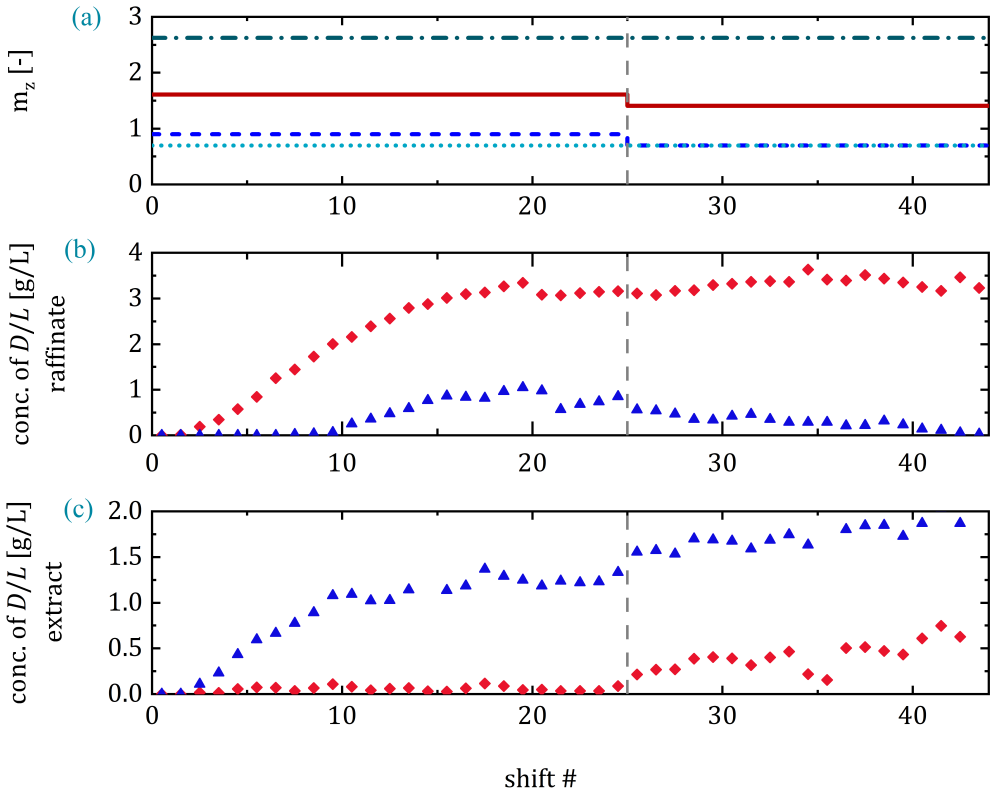

Fig. 6.3: Run 1: Chromatographic SMB separation of 10 g/L racemic feed *DL*-Met with the flow rates as visualized in Fig. 6.1 (a): (a) dimensionless flow rates in zone I (■), zone II (■), zone III (■), and zone IV (■); average concentration of *D*-Met (▲) and *L*-Met (◆) at (b) the raffinate and (c) the extract port.

of each setting, the the purity (Eq. (2.84)), productivity (Eq. (2.88)) and solvent consumption (Eq. (2.91)) of the setting was determined under the assumption of a steady-state-operation. As no reliable information about the porosity and density of the stationary phase was provided by the manufacturer, the productivity is determined with respect to the total column volume of 4x11.78 mL. The results are summarized in Tab. 6.3. For estimations of solid volume or mass related productivities (Eq. (2.89) or Eq. (2.90)), a total porosity of 0.78 or an interstitial porosity of $\varepsilon_e = 0.37$ and a density of $\delta = 2.2$ g/cm^3 can be used. For flow rate settings where no true steady state was reached, the numbers are written in gray.

In Run 1a, 98 % pure extract was collected with a productivity of 17 g/L$_c$/day. After lowering the flow rate in zone III and increasing the flow rate in zone II, raffinate was collected in Run 1b with a purity of 99 % and a productivity of 19 g/L$_c$/day. The solvent consumption was 0.91 and 0.83 L$_{eluent}$/g, respectively. In Run 2, the feed composition was 4.5:5.5 g/L *D*:*L*-Met and extract purities of 99 % *D*-Met in Run 2a-b and ≤ 99 % *D*-Met in Run 2c were obtained. The productivities were 13,

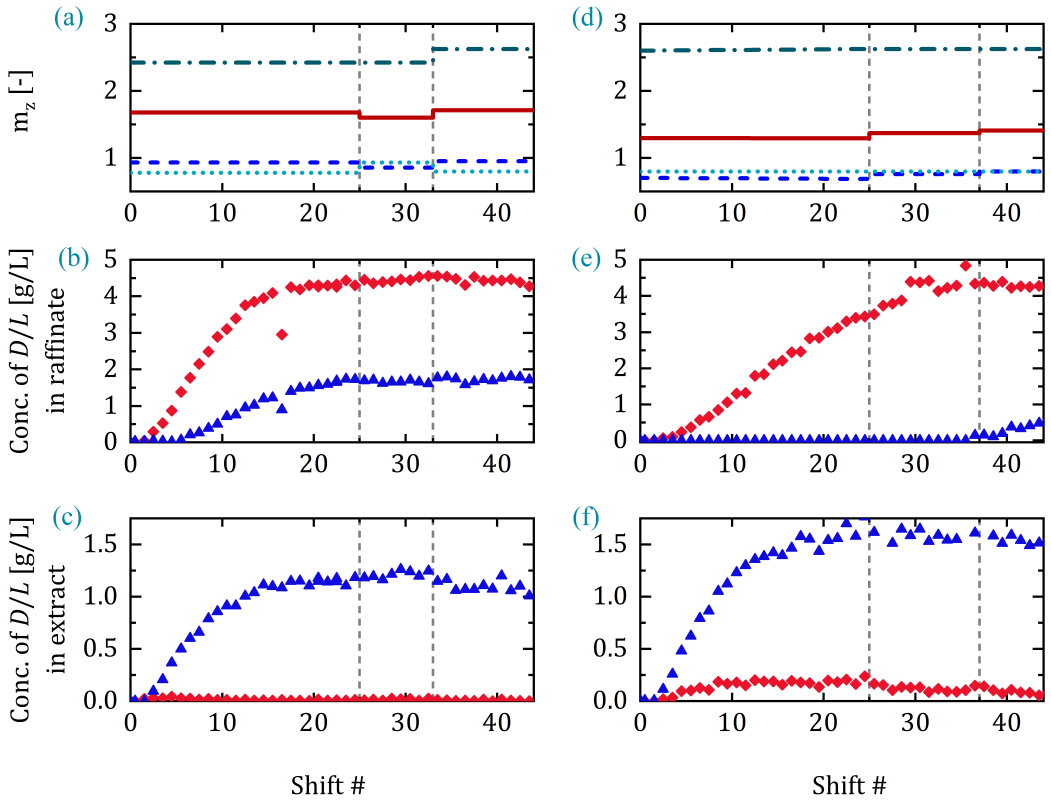

Fig. 6.4: Run 2&3: Chromatographic SMB separation of (a-c) 4.5:5.5 g/L *D*:*L*-Met and (d-f) 5.5:4.5 g/L *D*:*L*-Met with the flow rates as visualized in Fig. 6.1 (b): (a) dimensionless flow rates in zone I (■), zone II (■), zone III (■), and zone IV (■); average concentration of *D*-Met (▲) and *L*-Met (◆) at (b)+(e) the raffinate and (c)+(f) the extract port.

15 and 14 g/L_c/day, even though two cycles with the flow rates of Run 2b were not sufficient to reach steady state. For Run 3 with a feed composition of 5.5:4.5 g/L, *D*:*L*-Met the *L*-enantiomer was collected at the raffinate port with purities of 99.8 % and 99.9 % for Run 3a-b. A further lowering of the flow rate in zone III in Run 3c contaminated the outlet with *D*-Met and resulted in a purity drop to 95 % and potentially less, since the run was stopped after 10 shifts, which were again not sufficient to reach a steady-state. While the purities in Run 3a and Run 3b were very similar, the productivity could be increased by >50 % from 13 to 20 g/L_c/day. This trend was accompanied by a drop in the solvent consumption from 1.09 to 0.74 $L_{eluent}/g_{L\text{-Met}}$.

In all three runs, the targeted enantiomer could be obtained with a sufficient purity of 98 - 99.9 % and the results matched with the optical analysis of the chainsaw tooth profiles. The TMB operating window predicted in Sec. 5.2.2 based on the parameters in Tab. 5.4 described the plant sufficiently well. This means the perturbation method

Tab. 6.3: Purities, productivities and solvent consumption of SMB Runs 1-3 (parameters given in Tab. 6.2).

Run		Pu Raff %	Pu Extr. %	Prod. Raff. $g/L_c/day$	Prod. Extr. $g/L_c/day$	SC Raff. L_{eluent}/g	SC Extr. L_{eluent}/g
1	a	80	98	23	17	0.68	0.91
	b	97	75	19	29	0.83	0.52
2	a	72	99	30	13	0.42	0.97
	b	71	99	29	15	0.5	0.97
	c	71	>99	32	14	0.45	0.99
3	a	99.8	90	13	26	1.09	0.55
	b	99.9	94	20	23	0.74	0.63
	c	85	95	21	22	0.7	0.64

was well suited to characterize the adsorption behaviour and predict the right settings of all four zones for pure enantiomer provision. Furthermore, a comparison of Run 2a and Run 2c shows that reducing the time between two shifts and increasing the flow rates by the same factor, did increase the productivity for *L*-Met from 13 to 14 $g/L_c/day$ by increasing the throughput. The incremental changes of the flow rates in zone II and zone III in Run 3c from the operating region of pure extract into the triangle showed that operating outside the region of pure extract and raffinate can lead to higher productivities and purities. The low productivity observed in Run 3a may be attributed to not reaching steady state at the raffinate port. This theory was confirmed in the next section, when a more detailed study was performed.

In comparison to the simulation results of the TMB process in the previous chapter, the achieved productivities for a racemic feed of 17 and 19 $g/L_c/day$ are over 50 % lower than what could theoretically be achieved with OA-II. A reason for this is that the assumed safety factor of 10 % was not sufficient to achieve 99 % purity in a one-column-per-zone setup and mixing within the capillaries and the pumps. This led to more back-mixing and therefore a lower resolution in the experiments in comparison to the simulations. This meant that the plant could not be operated as close to the vertex as expected. Also, a lower overall flow rate was chosen, while the flow rate ratio m_I was increased. Consequently, the solvent consumption of over 600 L_{eluent}/kg_{Met} was twice as high as expected. However, this problem will be tackled partially by coupling the SMB to the evaporation and racemization unit, avoiding the solvent loss at the by-product port.

Even though high flow rates improve productivity, the following experiments were performed using a flow rate of 1.5 mL/min in zone I and a shifting time of 654 s

(10.9 min) to operate at lower pressure. This will increase the lifespan of the columns and moving parts in the SMB system.

6.1.3 Experimental screening of the operation window

After the preliminary Runs 1-3, the OA was calibrated and connected to the SMB system. Therefore, no manual sample collection was necessary anymore. In the following, all concentrations were automatically obtained from the OA unit. Manual sample collection was only done occasionally for validation. Furthermore, some capillaries were shortened, resulting in a total plant volume of $t_{plant} = 2.0$ mL.

In Run 4, the SMB was operated for 38 h and 209 shifts in order to scan the operating region and identify the operating points for achieving high purities and their corresponding productivities. At the same time the stability of the SMB system and OA system could be investigated. During the run the flow rates in the regeneration zones were kept constant at $\dot{V}_{I} = 1.5$ mL/min and $\dot{V}_{VI} = 1.0$ mL/min, which corresponds to $m_{I} = 2.6$ and $m_{VI} = 0.5$. This was sufficient in order to ensure complete regeneration of the stationary phase and the eluent. Zone II and III, regulating the separation were started at $\dot{V}_{II} = 1.080$ mL/min and $\dot{V}_{III} = 1.205$ mL/min ($m_{II} = 0.85$ and $m_{III} = 1.23$).

The UV-signals at the raffinate and extract outlet are shown in Fig. 6.5. Like in Fig. 6.2 the profiles confirm an indistinguishable porosity and adsorption behaviour of all four columns. The zoom into the profiles of shifts #24-28 in Fig. 6.2 (d)-(f) show an even sharper saw-tooth profile at both ports than before. In comparison to Run 2, in shifts #24-28, pure *L*-Met is eluting at the raffinate port. This is shown by the lack of the overshoot, which occurred in Fig. 6.2. Only during the last shift a small upward deflection indicates the breakthrough of a small amount of *D*-Met. This small deflection increased during the following shifts, as shown in Fig. 6.5 (b), and only started to decrease after shift #110. The extract port profile shows a similar behaviour as in Run 2. However, during shifts #26 and #27 small peaks can be seen at the front of the elution main peak of each shift. As already explained in the previous chapter, this indicates the elution of *L*-Met, which had not fully left zone II during the prior shifting time and had therefore been shifted to zone I. From there it eluted during the start of the new shifting period into the extract port.

In Fig. 6.6, the *D*- and *L*-Met concentration at (b) the raffinate and (c) the extract ports are presented along with (a) the changes of the flow rate ratios m_{II} and m_{III}. The small continuous symbols present the values determined with the OA, while the

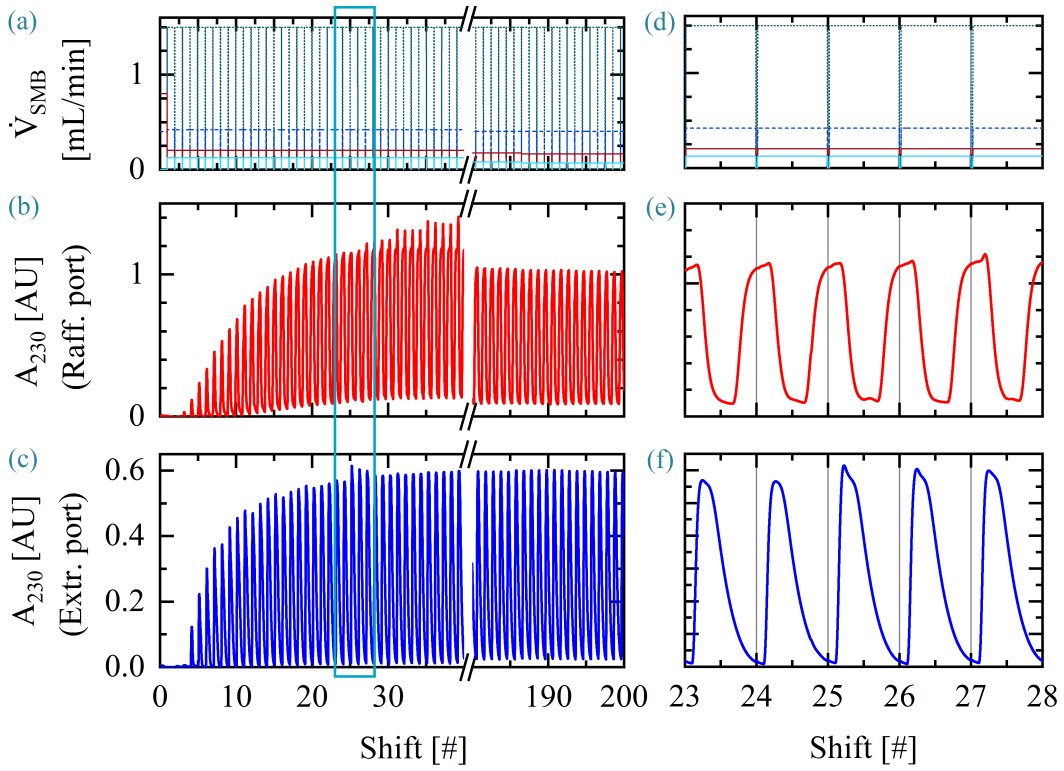

Fig. 6.5: Set flow rates and resulting SMB elution profiles of Run 4 at the raffinate and extract port: (a) Flow rates in zone I (■), at the raffinate (■) and extract port (■), and the feed (■), and UV-signals at 230 nm at (b) the raffinate and (c) the extract port. The gray dotted lines mark a switching of the settings (see Fig. 6.1). Subfigures (d)-(f) zoom into shift 24-28 from (a)-(c).

larger symbols present the results from manual samples, analyzed in an off-site HPLC. The volume of sample drawn with the OA was 1 mL/shift over the whole operating range, except for shift #86-100, where the volume was reduced to 0.5 mL/shift.

The initial configuration let to a *L*-Met purity of 90 % at the raffinate port and a 98 % purity of *D*-Met at the extract port. Next, the flow rate of zone II was gradually increased up to a flow rate of $\dot{V}_{II}$ = 1.10 mL/min, for which an extract purity of $Pu_{D\text{-Met}}$ = 99.99 % was reached with a productivity of $Pr_{D\text{-Met}}$ 12-13 g/L/day. Then, from shift # 109 on, the flow rate of zone II was kept constant at 1.095 mL/min and the flow rate of zone III was gradually lowered from 1.20 mL/min to 1.165 mL/min. For $\dot{V}_{III}$ = 1.185 mL/min and $\dot{V}_{II}$ = 1.095 mL/min a raffinate purity of $Pu_{L\text{-Met}}$ = 99.99 % was reached with a productivity of $Pr_{L\text{-Met}}$ 13 g/L/day. The purity and productivity of each configuration is shown in Fig. 6.7. A detailed list of the tested flow rates, corresponding flow rate ratios, m_I-m_{IV}, and resulting purities and productivities is given in Tab. C.4. The productivities for the conditions

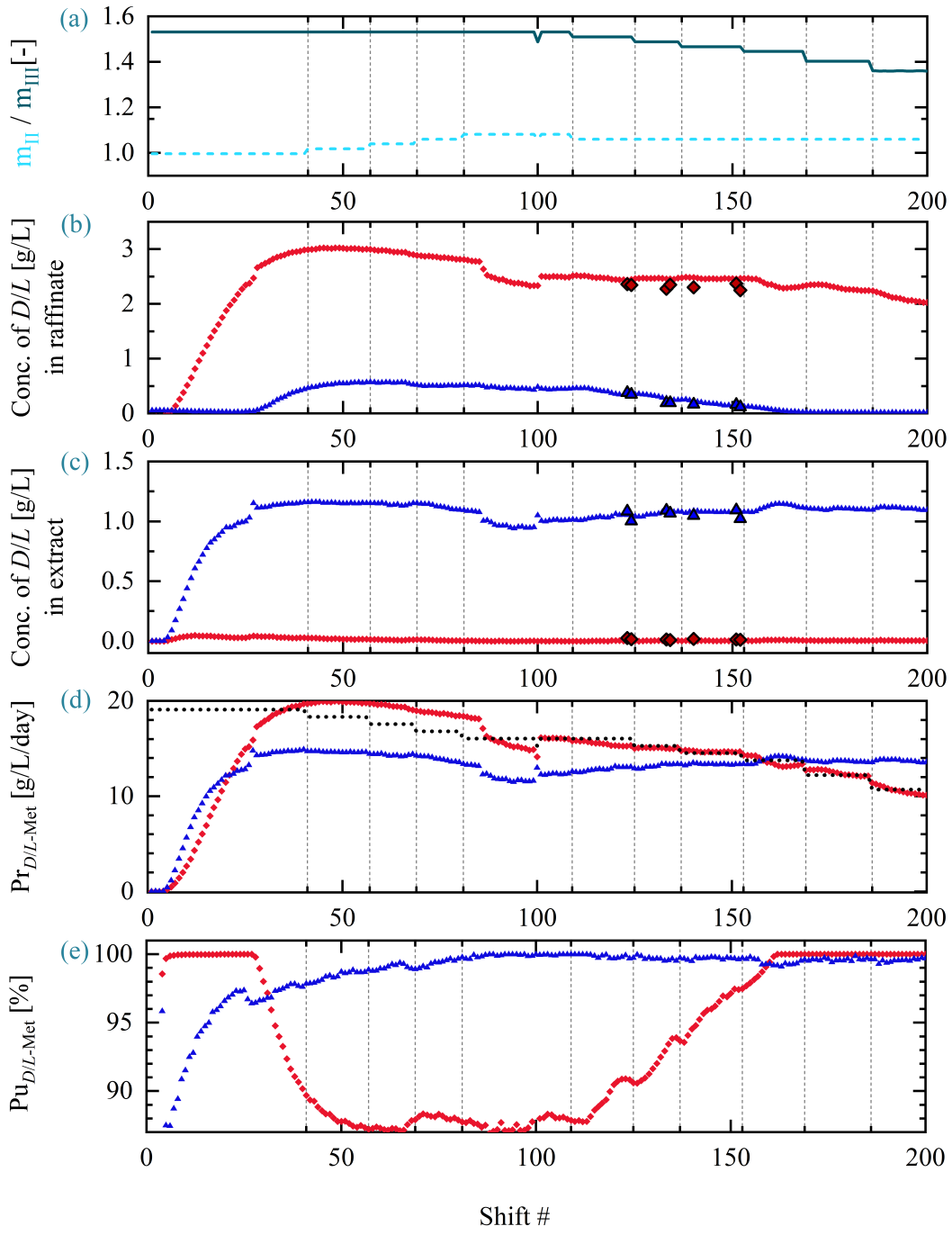

Fig. 6.6: Run 4: 200 shifting times of an SMB run with a constant flow in zone I and IV of 1.5 and 1.0 mL/min, respectively, while the flow in zone II and III was slightly varied. (a) flow rate ratios in zone II (▬) and zone III (▬); average concentration of *D*-Met (▲) and *L*-Met (◆) at (b) the raffinate and (c) the extract port and the corresponding (d) productivities and (e) purities of *D*-Met at the extract port and *L*-Met at the raffinate port.

under which both enantiomers elute with a purity > 99.5 % match well with the predictions using Eq. (2.89) with the assumption

$$\dot{m}_{\text{target}} = c_{\text{target,feed}} \cdot (\dot{V}_{\text{III}} - \dot{V}_{\text{II}}) \tag{6.1}$$

This confirms the proper calibration of the SMB system and the online analytic system. However, the productivities lay far below the predictions made in Sec. 5.2.2. The deviation originates from the assumption that the 10 % safety margin is sufficient for pure enantiomer provision. While this might be the case for well optimized systems with two or more columns in the separation zones II and III, it is not sufficient for this SMB system. Yet, the lower productivity of the given system does not affect its applicability in a coupled setup.

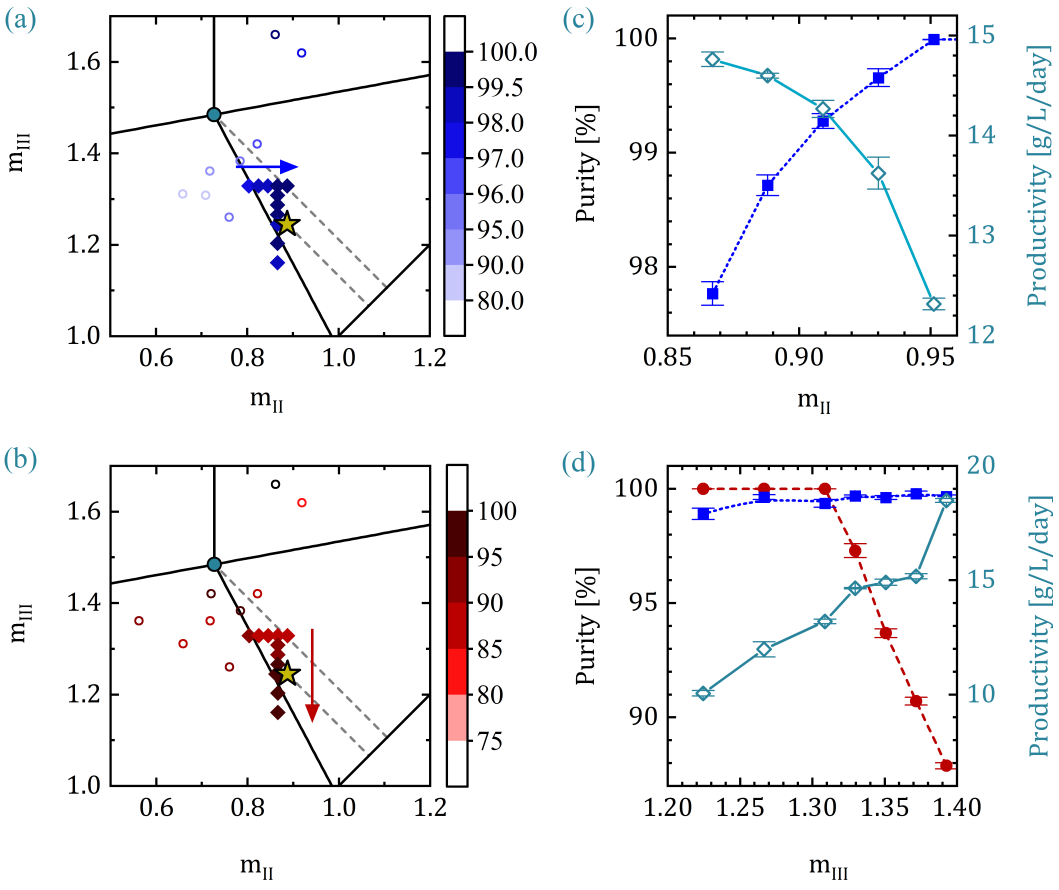

Fig. 6.7: Impact of different flow rates in the SMB chromatography system on the purity of the product and the process productivity, measured in Run 4 (V_{plant} = 2 mL). The light blue dot marks the vertex and therefore optimum operating condition of a TMB system.

6.2 Design of the coupled setup for case study II

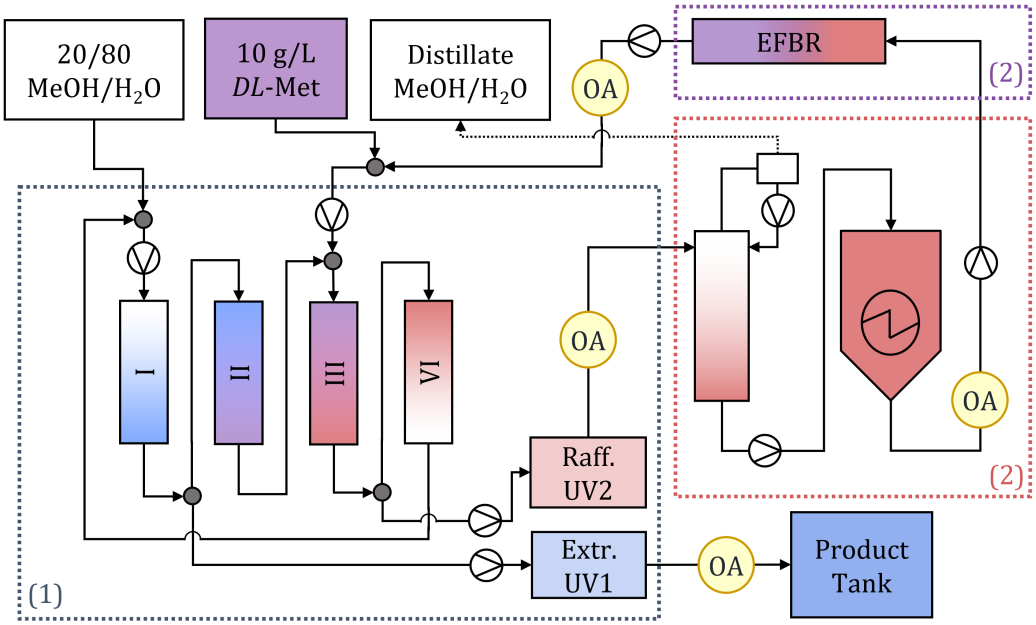

Fig. 6.8: Simplified process scheme of the mini-plant setup for coupling SMB chromatography (1) with evaporation (2) and enzymatic racemization (3).

Coupling chromatographic resolution, subsequent racemization and recycling removes constraints for both units, offering two significant advantages. The resolution step can be operated with a relaxed purity constraint regarding the by-product, which allows higher productivities. At the same time, since the separation unit can be operated with an excess of the by-product, a lower degree of racemization is needed. Thus, the EFBR can be operated with shorter retention times and less amount of racemase. The effect of these benefits have already been discussed in Sec. 5.3. Yet, the simulation study assumed ideal concentration and alcohol removal, as well as a stable racemase activity. Now, the design aspects of the concentration by distillation and fluctuations during the process operation need to be considered. The complete process scheme is shown in Fig. 6.8 and the design aspects for the evaporation and racemization units are discussed below.

6.2.1 Implementation of the evaporation unit

Evaporation offers the advantage of simultaneously increasing the concentration of *DL*-Met, while changing the solvent composition in favour of this process. An evaporation unit at the outlet of the by-product stream of the SMB unit can remove

most of the excess alcohol, since the boiling points of ethanol and methanol are below the one of water (EtOH: 78.4 °C, 58.7 hPa (20 °C); MeOH: 65 °C, 129 hPa (20 °C)). In addition, the evaporation of alcohols is more energy efficient than the concentration of a solvent without alcohol. This provides the opportunity to design a process in which the chromatographic separation operates with ≤ 20 vol% alcohol and therefore with a large separation factor (Sec. 5.1.3). The recycling by-product stream can then be sent to an evaporation unit, in which the alcohol (and some water) is withdrawn. The resulting concentrated stream with < 5 vol% alcohol is subsequently injected into the EFBR. This can significantly enhance the performance of both units and is therefore identified as the more favorable coupling option for CS-II.

The evaporation unit was integrated into the process setup, as shown in the flow scheme in Fig. 3.9. Goal of the evaporation was a concentration of the recycling stream back to the feed concentration of the SMB unit $c_{tot,feed\ SMB} = c_{tot,bottom} =$ 10 g/L and a reduction of MeOH from 20 % in the evaporator feed to < 5 % in the bottom product. The concentration of the extract streams is in the range of 1.0-1.3 g/L and the raffinate stream is in the range of 2-3 g/L. The resulting required parameters for the bottom-to-distillate-ratio and the MeOH-fractions in the distillate are given in Tab. 6.4.

Tab. 6.4: Overview of the evaporation requirements for the concentration of expected recycling streams from the raffinate and extract of the SMB.

$c_{tot,in}$ g/L	$c_{tot,b}$ g/L	$\dot{V}_b/\dot{V}_f$ -	$\dot{V}_f$ mL/min	$\dot{V}_b$ mL/min	$\tilde{x}_{MeOH,\ IN}$ -	$\tilde{x}_{MeOH,\ b}$ -	$\tilde{x}_{MeOH,\ d}$ -
1.0	10	0.1	0.4	0.040	0.2	0.05	0.28
1.3	10	0.13	0.43	0.056	0.2	0.05	0.29
2.0	10	0.2	0.19	0.038	0.2	0.05	0.31
3.0	10	0.3	0.16	0.056	0.2	0.05	0.39

b = bottom product in the sump, f = feed in to evaporation unit,
d = distillate at column head

Preliminary experiments had shown that *DL*-Met was stable at 50 °C for multiple days. Therefore, the evaporation was designed at a pressure of 100 and later 110 mbar, for which a temperature of < 50 °C in the sump can be ensured. Further lowering of the pressure increases the energy consumption and makes it more difficult to pump the bottom product back to ambient pressure. Next, the McCabe-Thiele diagram for the binary MeOH/H_2O mixture, shown in Fig. 6.9, was designed based on the data given in Tab. 6.4. Here, the assumption was made that Met will not effect the

separation, since its concentration is low enough and its evaporation temperature is high enough. Also, it was assumed that the reflux ratio is R = 1. The Mc-Cabe-Thiele diagram showed that only one or two theoretical steps were needed in order to reduce the alcohol fraction to < 5 %.

The same diagram was designed for a 20/80 and 40/60 EtOH/H_2O-mixture. With these less toxic mixtures, the preliminary tests of the evaporation unit were done. They showed that the rectification column had sufficient theoretical steps and achieved a reduction of EtOH for both mixtures and the given flow rates to 1-3 % EtOH. Since the separation factor for MeOH/H_2O mixtures is very comparable for low alcohol concentrations, it was save to assume that the separation is as good as with EtOH.

Even though a recycling of the distillate back into the rectification column was installed, it was not needed most of the time because the insufficiently insulated tube, connecting the column head with the distillate tank, caused sufficient condensation of the distillate and reflux. Furthermore, the feed was installed at the column head, allowing a fast wetting of the glass packing of the column.

According to the T-x-y-diagram at 110 mbar, the bottom should have a temperature of 46.5-47 °C. This matched well with the temperatures of 47.7-48.3 °C, which were measured in the bottom during the preliminary experiments and the runs presented in the following section. The slightly higher values probably resulted from a small pressure drop within the column. This indicated that the vacuum pump was working properly and the system was air tight. In order to reach the temperature in the sump and provide sufficient evaporation for the concentration, the temperature of the thermostat needed to be in the range of 54-64 °C.

Based on this knowledge, the evaporation unit could be operated as desired. In the following the pressure was set to either 100 or 110 mbar and the liquid level as well as the concentration of *DL*-Met in the bottom were controlled by adjusting the temperature of its double-vessel and the reflux.

6.2.2 Implementation of the racemization unit

After a successful operation of the evaporation unit, ensuring a MeOH fraction smaller 5 %, the racemization unit was also integrated into the process. The flow through the reactor is equal to the flow out of the evaporation bottom and therefore in the range of 0.04-0.09 mL/min. The temperature of the EFBR is controlled by the heated double vessel and was adjusted within the range of 22-40 °C.

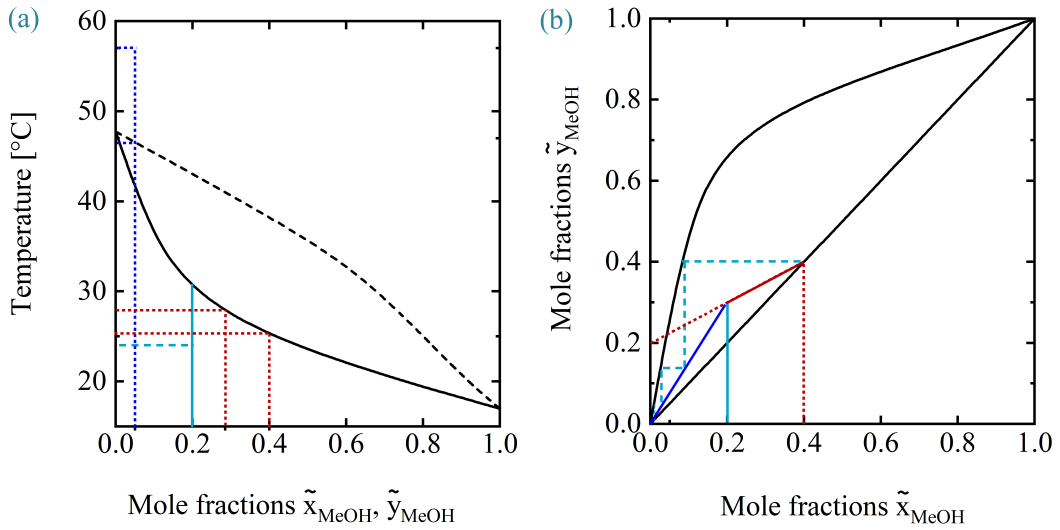

Fig. 6.9: (a) T-x-y and (b) liquid-vapor-phase diagram for MeOH/H_2O at 110 mbar. The red vertical lines mark the feed compositions, while the blue vertical lines mark the outlet requirements.

Based on the given parameters and the necessary degree of conversion, the amount of required mass of immobilized resin can be determined from Fig. 4.6 or the parameters from Tab. 4.2 and Eq. (2.104). According to the data, a recycling of the by-product stream with a conversion of 98 % at a flow rate of 0.1 mL/min should be possible with only 12-15 $g_{carrier}$. This volume is only 25 % of the EFBRs used for characterization. In order to put the focus on the separation, for Run 5-7 an old EFBR with 58 $mg_{carrier}$ (2 mg_{AAR}) was used. For Run 8 a and Run 9, fresh columns with again 58 $mg_{carrier}$ were packed, even though a much smaller EFBRs should also achieve sufficient racemization.

6.3 Operation of the coupled SMB-EFBR process

Due to the relatively large volume of the evaporation tank (40 mL) and the low flow rates at the extract and especially raffinate port, the coupled system had a long start-up phase. Therefore, the experiments were splitted: during the first runs the start-up behaviour was tested and later on the evaporation tank was prefilled with a *DL*-Met mixture, prepared in the expected composition. Run 8, with an involuntary outage at the SMB unit and overregulation in the evporation unit, was used to observe the robustness of the coupled setup. Finally, the stability of the coupled process with by-product recycling was tested in Run 9.

In all experiments, the OA analyzed four streams of the coupled process. The first two streams are the raffinate and extract. Here, the average concentration was measured as described in Sec. 6.1. Additionally, the outlets of the evaporation tank and the EFBR were analyzed with a bypass, allowing momentary snapshots of each shifting time (see Sec. 3.5.3). Also, in all start-up experiments the recyclate was not fed back to the feed tank and, like in Sec. 6.1.3, a plant dead volume of 2 mL was assumed for the determination of the flow rate ratios.

Tab. 6.5: Summary of the operating regimes of the Runs 4-9 of the coupled process with information about the shifts during which the different units were coupled.

Run	Cycles	Target	Recycled dist.*	Filling of EFBR	Dist.* to evap.	Evap. to EFBR	EFBR to SMB
4	40	*D*-Met	*L*-Met	H_2O	#0	#0	-**
5	50	*L*-Met	*D*-Met	H_2O	#0	#0	-**
6	40	*D*-Met	*L*-Met	H_2O	#0	#0	-**
7	40	*D*-Met	*L*-Met	empty	#21	#21	-**
8	65	*D*-Met	*L*-Met	4.5:1.5 *D*:*L*	#31	#0	-**
9	120	*D*-Met	*L*-Met	4.5:1.5 *D*:*L*	#32	#0	#32

*dist. = distomer; **the Runs were not operated with a recycling of the racemized distomer to the feed of the SMB unit.

6.3.1 Start-up of the coupled process

The start-up phase of the process was tested for two settings: In Run 5, the raffinate was collected and the extract was sent to the evaporation and the EFBR unit. In Run 6, the extract was collected while the raffinate was recycled. In both runs the evaporation tank was prefilled with 50 mL pure water. The concentrations of the analyzed streams are shown in Fig. 6.10. With both experiments the targeted enantiomers were collected with high purities in the product tank. The distomer stream was sent to the evaporation reactor and slowly build up its concentration. By the time the experiments were stopped, the concentration of bottom product had increased to > 5 g/L *DL*-Met in Run 5 and to 5 g/L in Run 6. Also, the concentration slopes from both runs indicated that the concentrations could have increased further. At a temperature of 17 °C in the thermostat of the EFBR, almost full conversion was reached for Run 5 with a remaining enantiomeric excess of $ee_{D\text{-Met}} < 1$ %, while the conversion seemed to be incomplete for Run 6 with a remaining $ee_{L\text{-Met}} = 2\text{-}3$ %, even when increasing the temperature to 40 °C.

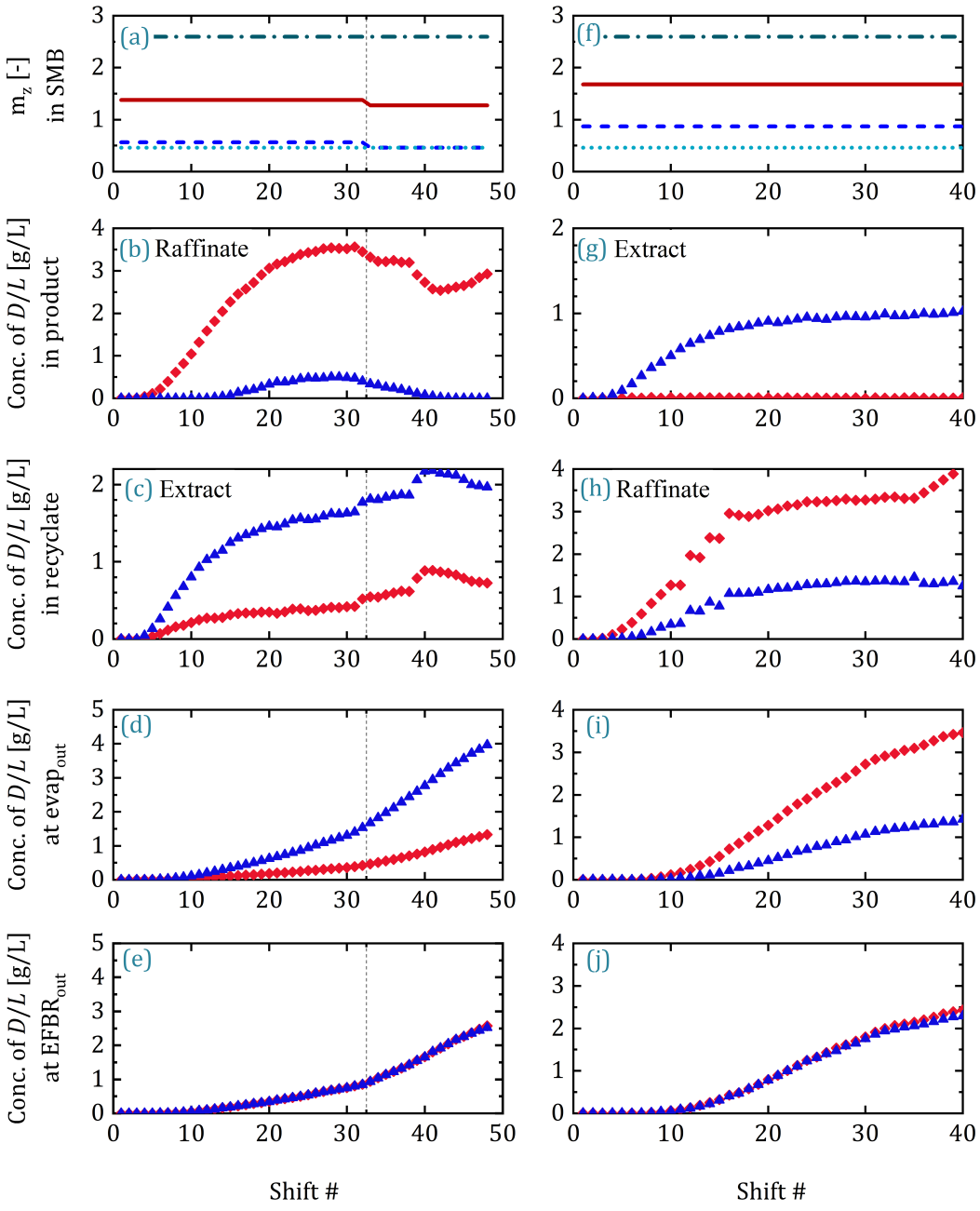

Fig. 6.10: Run 5 (a)-(e) and Run 6 (f)-(j): Start-up behaviour of the SMB unit coupled with evaporation and racemization targeting in Run 5 the *L*-Met (◆) at the raffinate port (b) and in Run 6 *D*-Met (▲) at the extract port (g). (a) and (f) show the flow rate ratios: m_z-values: I (- - -), II (—), III (– –), and IV (· · ·), (b) and (h) the raffinate port, (c) and (g) the extract port, (d) and (i) the concentration in the evaporation tank, and (e) and (j) the concentrations at the outlet of the EFBR.

For Run 7, a different start-up approach was used. The SMB unit was started with a high raffinate flow and an empty evaporation tank. In Fig. 6.11 (a) the flow rate

ratios are shown along with (b) the targeted extract and (c) the raffinate, which was fed into the head of the evaporation unit. The evaporation unit was set to a pressure of 110 mbar and a bottom thermostat temperature of 60 °C. After 20 shifts sufficient raffinate had accumulated in the bottom product and the vacuum was shortly lifted in order to start the pumping of the bottom product of the evaporator to the EFBR and the collection tank. Then the vacuum pump was restarted, set to 110 mbar and the flow through the capillaries allowed an OA measurement of the evaporation tank and the EFBR, shown in Fig. 6.11 (d) and (e), respectively.

The flow set of $V_{I\text{-}IV}$ = [1.5, 1.084, 1.191, 1.072] mL/min with t_{shift} = 10.9 min allowed collection of *D*-Met with 97 % purity in the extract and also seems to result in only small contamination of the raffinate. As a result, with a feed of 1.05 $mg_{DL\text{-}Met}$/min, a productivity of 15.5 $g_{D\text{-}Met}/L_c$/day was obtained. Furthermore, the high flow rate of zone III led to a quick build up of the profile in the SMB unit and faster increase of the concentration in the evaporation unit. In combination with the empty evaporation tank, this allowed a more efficient start-up with no unnecessary heat consumption for evaporation of water during this period. Towards the end of the experiment, the evaporation reached a total *DL*-Met concentration of close to 8 g/L in the bottom product and would have reached higher concentrations if continued. The EFBR was heated to 24 °C and started with a conversion of 99 % and before dropping to 96 % with increasing inlet concentration. This was surprising, since the reactor should be packed with sufficient racemase.

Initially it was assumed, that the racemase was already too old, since it had been used for over two weeks at various temperatures and MeOH containing eluents. However, an offline analysis of drawn samples at the end of the run indicated that the expected conversion of > 99 % was indeed achieved. It can therefore be assumed that the discrepancy derived from the automized peak analysis of the OA system.

The on-site system had been designed for rapid analysis and needed to cover the entire range from measuring 1 % impurities at low concentrations of 1 g/L up to racemic mixtures of up to 10 g/L. However, the focus has been set on the detection of small impurities. As a trade-off, broad peaks from samples with high concentrations of both, *D*- and *L*-Met, eluted from the OA column with a small overlap. The fixed times defining the integrals for the peak analysis were not optimized for analysis of these peaks and therefore have a measuring error for these samples.

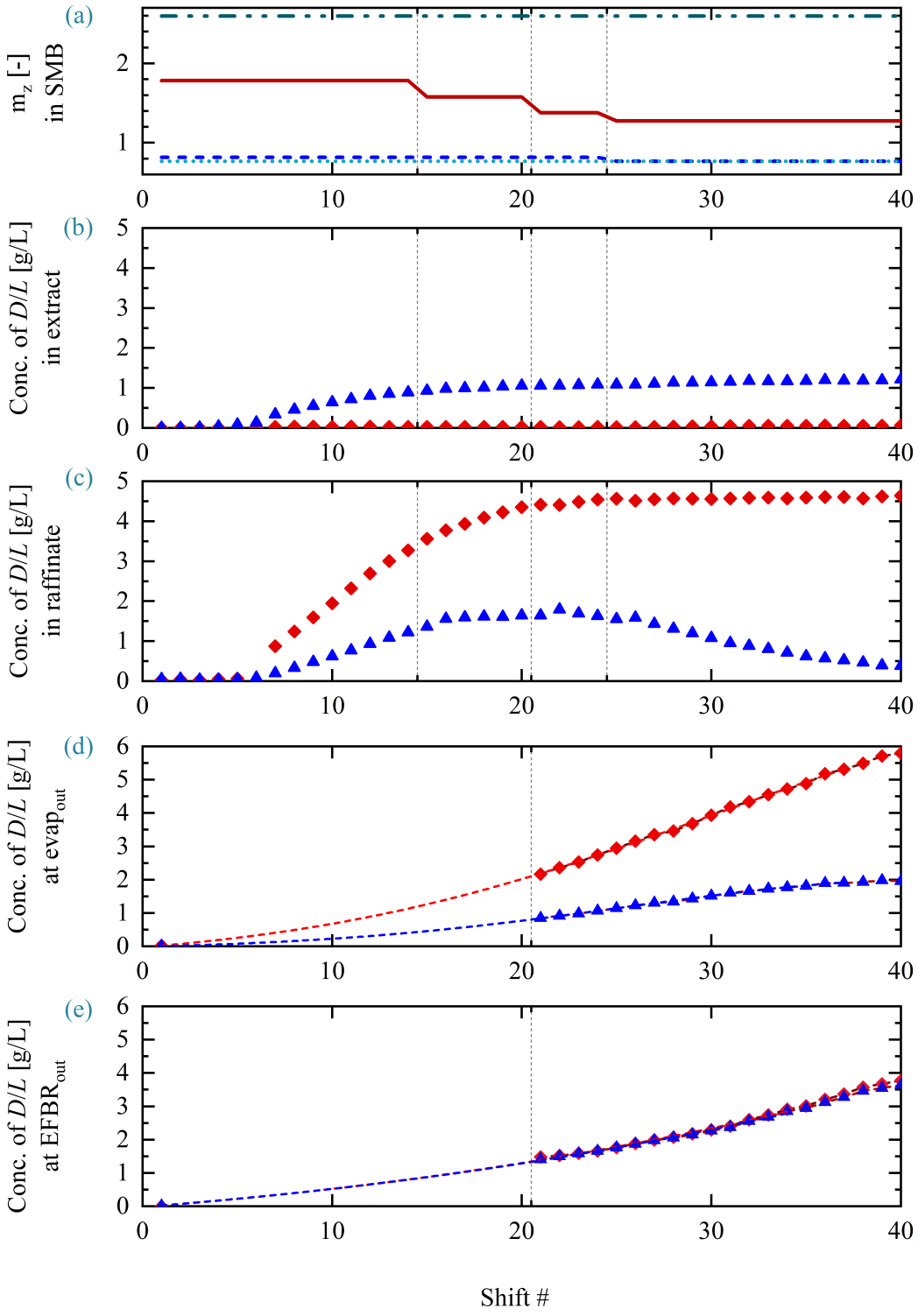

Fig. 6.11: Run 7: Start-up profiles of the SMB-EFBR plant: (a) m_z-values: I (▬·▬·▬), II (▬), III (▬ ▬), and IV (▪▪▪), (b) extract and (c) raffinate concentration at the outlet of the SMB chromatography unit over the course of 40 shifts. The raffinate was collected in the bottom of the evaporation unit. After 20 shifts the flow from the evaporation unit (d) to the EFBR (e) was started. Color code: *L*-Met = ◆ and *D*-Met = ▲.

6.3.2 Robustness test: Impact of disturbances on the process performance

For better process understanding and in order to test the robustness of the process, in Run 8 first the flow rates and afterwards the reaction temperature were changed. Also, due to a mistake in shift # 40 of not opening a lever for the eluent after refilling the feed tank, even greater disruption of the system could be tested.

The run was started with the goal of obtaining pure extract from 10 g/L *DL*-Met, recycling the raffinate and quickly reaching steady state. This was again approached by starting with a high flow rate in zone III, followed by a gradual decrease of this flow rate. The chosen flow rates in all zones are shown in Fig. 6.12. After shift #20 the system was switched from an open-loop configuration to a closed-loop. At the start of the run, the evaporation bottom was filled with 50 mL 1.5:4.5 g/L *DL*-Met in H_2O and fed with 1.5:4.5 g/L *DL*-Met in 20/80 MeOH/H_2O. The pumps transporting the bottom product to the EFBR were set to $\dot{V} = 0.08$ mL/min and the thermostat of the EFBR was set to 23 °C and was increased to 31 °C after shift #12. However, the concentration in the evaporator stagnated. Therefore, the temperature of the thermostat was increased to 63 °C and then 64 °C after shift #20 and #27, respectively. This led to a slow rise of the bottom concentration and the raffinate port of the SMB unit was connected to it after shift #31.

Since the concentration in the evaporator started to stagnate again despite a thermostat temperature for the bottom of $T_{therm,bottom} = 64$ °C, the low pressure section of the plant was checked and a leakage was closed at shift #37. On top of that the flow rate of the pump in the thermostat was increased, to enhance the heat exchange. After closing the leakage, the signal at the vacuum pump stabilized, the bottom temperature dropped from 54 °C to 48 °C and the concentration of the bottom product started to rise from 6 to > 11 g/L within 5 shifts, before the temperature of the thermostat was lowered to ≈ 56 °C after shift #42. Also, the EFBR thermostat was set to 40 °C after shift #40.

Once the concentration in the evaporator had started to increase after shift #37, the feed was switched from 10 g/L *DL*-Met in 20/80 MeOH/H_2O to 10 g/L *DL*-Met in 40/60 MeOH/H_2O. Unfortunately, here a mistake was made and the lever, connecting the eluent tank to the SMB unit, was not switched back to its open position after changing the feed and stayed closed for around 10-15 min. As a consequence, the eluent flow in the system was abruptly decreased to a minimum. This stopped the flow in the columns and the mitigation of the profiles through the columns. At the end of the shifting time, the profiles were therefore shifted before

being able to elute at the proper port. As a result, high concentrations of *L*- and *D*-Met eluted at the extract port, while zone III was drained and the concentrations at the raffinate port dropped from 6 g/L to 1 g/L. Once the lever was opened again, the flow rates were restored and the concentration profile in the SMB unit and at its outlets slowly recovered. At the end of the run, the concentration profiles in the entire plant were shifted back to their expected levels.

6.3.3 Steady-state operation of the coupled process

With the knowledge gained from Run 8, a final Run 9 was planned to study the performance of a process when recycling the racemized distomer back into the feed. Like in the previous runs, *D*-Met was targeted at the extract port and the raffinate was sent to the evaporation unit and EFBR. The run started with a setting for pure extract and contaminated raffinate while keeping the flow rates in Zone I and IV sufficiently high and low, respectively, to exclude a contamination from the regeneration zones. After 12 and 64 shifts, flow rate $\dot{V}_{\mathrm{III}}$ was lowered and after 24 shifts the SMB was switched to a closed-loop configuration.

The racemization was performed with a fresh EFBR with 57 $\mathrm{mg_{carrier}}$ (2 $\mathrm{mg_{AAR}}$) and changing reactor temperatures (see Fig. D.3).

The distillation column was operated at 110 mbar and the temperature of the thermostat of the bottom was varied between 54 and 58 °C in order to maintain a constant bottom volume of around 50 mL. After a slightly warmer start-up period and except for small fluctuations, the bottom-product kept a temperature of 48.1-48.3 °C. The head thermometer showed a temperature range of 43-47 °C, except for one instance during shifts 20-35, when it temporarily dropped to 32 °C, which was due to a temporary lowering of the bottom thermostat temperature to 54 °C. At shift #32 the raffinate was connected to the distillation column and the outlet of the EFBR was connected to the SMB feed.

The resulting concentration profiles and the flow rate ratios of the SMB unit are shown in Fig. 6.13. Based on these concentration profiles, the purity and productivity of the SMB unit, assuming remaining steady state of the current concentration, are determined and shown in Fig. 6.14. Furthermore, the enantiomeric excess in the bottom product of the distillation and after the EFBR are shown along with the resulting conversion.

The concentration profile at the extract port build up during the first 20 shifts and after increasing the flow rate in zone II from 1.084 mL/min to 1.090 mL/min and

1.096 mL/min, the extract could be collected with >99 % and >99.5 % purity, respectively, 14.5-15.5 g/L/day. These purities and productivities remained stable for over 22 h and were not affected by closing the feed-back loop for the recycling of the raffinate outlet. The concentration profile at the raffinate port was subject to stronger fluctuations. Due to the high initial flow rate in zone III the *L*-Met at the outlet was strongly contaminated with *D*-Met. Lowering the flow rate to 1.215 mL/min improved the purity to 80 %. Finally, after further lowering the flow in zone III to 1.191 g/L the purity of *L*-Met increase to 97 % at shift #100. At the same time the productivity decreases from 18.5 g/L/day to 15 g/L/day.

The concentration of the bottom product of the distillation column shows only small fluctuations and even the switch from the prepared 4.5:1.5 *L*:*D*-Met feed to the raffinate outlet at the distillation head did not strongly affect the concentration. The fluctuations at the raffinate port were buffered and an average overall concentration of 9-10 g/L was held. However, no matter how much the temperature in the EFBR was raised, an enantiomeric excess of up to 1.5 % was measured by the OA at the reactor outlet. Since the EFBR showed a strong temperature dependency during its characterization, it was concluded, that this remaining excess is a measurement error, since the OA unit works with fixed integration boarders and its calibration can not cover the entire range from 0 to 10 g/L *DL*-Met. This was confirmed by off-site HPLC measurements of samples taken at the end of the run, with which an ee < 0.5 % was measured. Taking the temperature dependency into account, it can therefore be concluded from the seemingly full racemization at 12 °C, that at least 50 % or less of the used carrier are sufficient for full racemization.

Overall, it can be concluded that SMB chromatography was successfully coupled with an EFBR and a distillation unit and operated for over 22 h. During this time more than 500 mL of 1 g/L *D*-Met were collected with an average purity of almost 99 %, a productivity of 15-16 g/L/day and a yield during the process coupling of 99 %. The greatest challenges were the proper operation of the distillation unit in the recycling loop due to the extremely low flow rates. Operating the SMB unit with columns with larger particle sizes could eliminate this problem and further increase the process stability. Operating the EFBR with 2 mg AAR decreased the enantiomeric excess of the recyclate to below the detection limit and the temperature fluctuations showed that the EFBR could also compensate for fluctuations of the recyclate concentration.

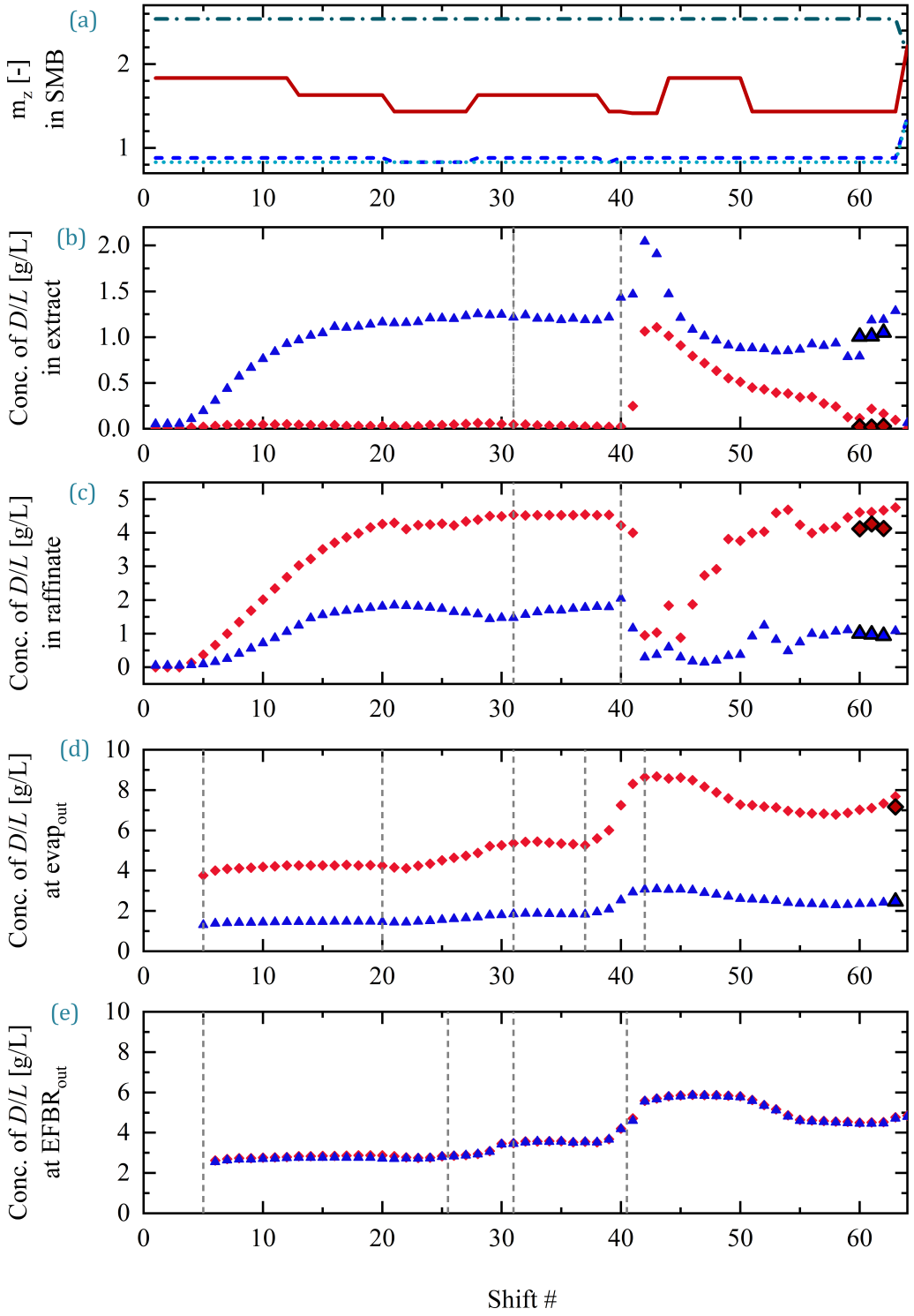

Fig. 6.12: Run 8: Concentration profiles in the SMB-EFBR plant: (a) m_z-values: I (■), II (■), III (■), and IV (■), (b) extract and (c) raffinate concentration at the outlet of the SMB chromatography unit over the course of 70 shifts. At shift #31, the raffinate outlet was connected to (d) the distillation unit and (e) the EFBR unit. Color code: *L*-Met = ◆ and *D*-Met = ▲.

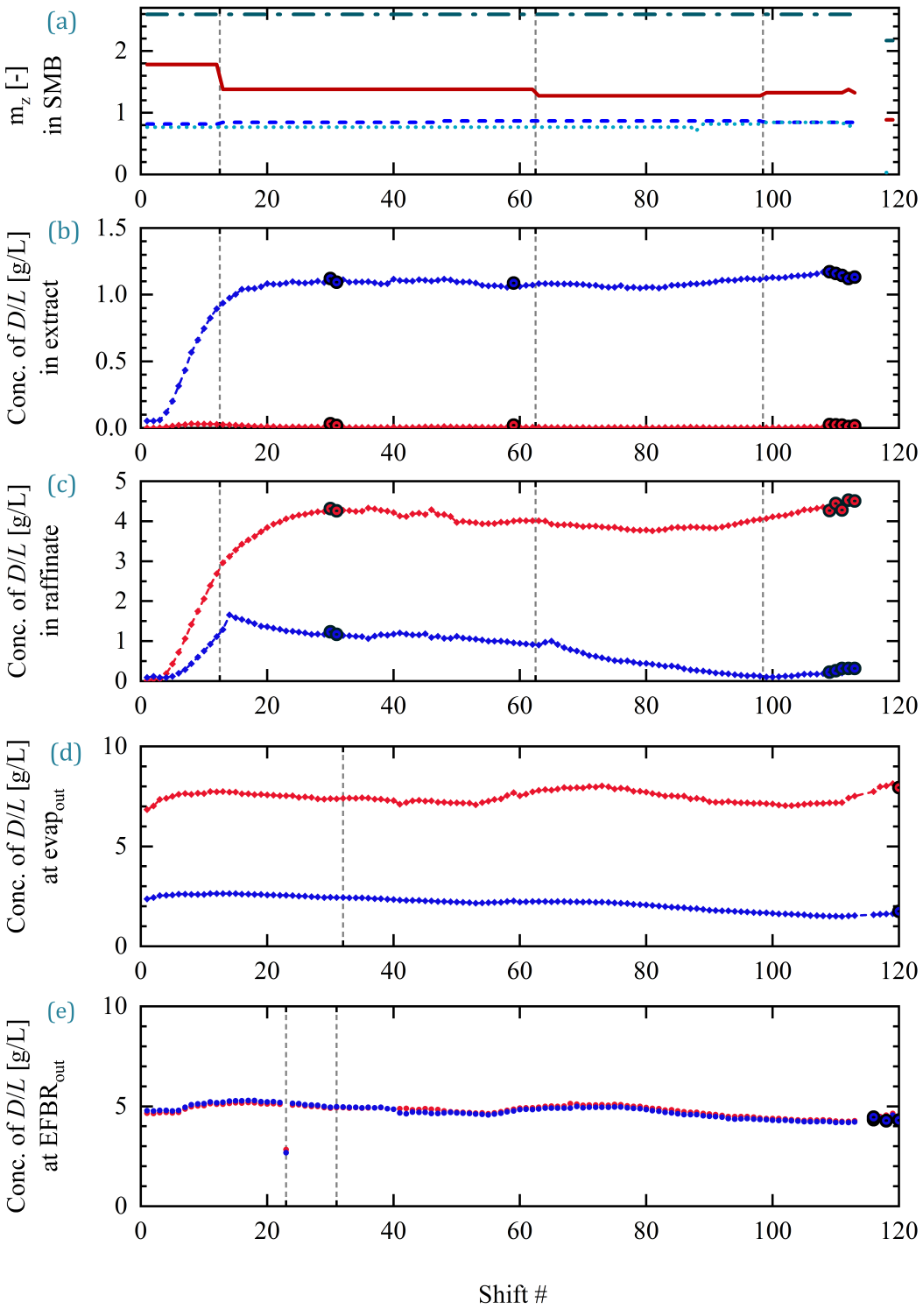

Fig. 6.13: Run 9: Concentration profiles in the SMB-EFBR plant: (a) m_z-values: I (▬·▬·▬), II (▬), III (▬ ▬), and IV (▪▪▪), (b) extract and (c) raffinate concentration at the outlet of the SMB chromatography unit over the course of 70 shifts. At shift #31, the raffinate outlet was connected to (d) the distillation unit and (e) the EFBR unit. After 32 shifts the SMB unit was coupled with the evaporation and the EFBR unit and operated for another 80 shifts while recycling the Met at the raffinate outlet. Color code: *L*-Met = ◆ and *D*-Met = ▲.

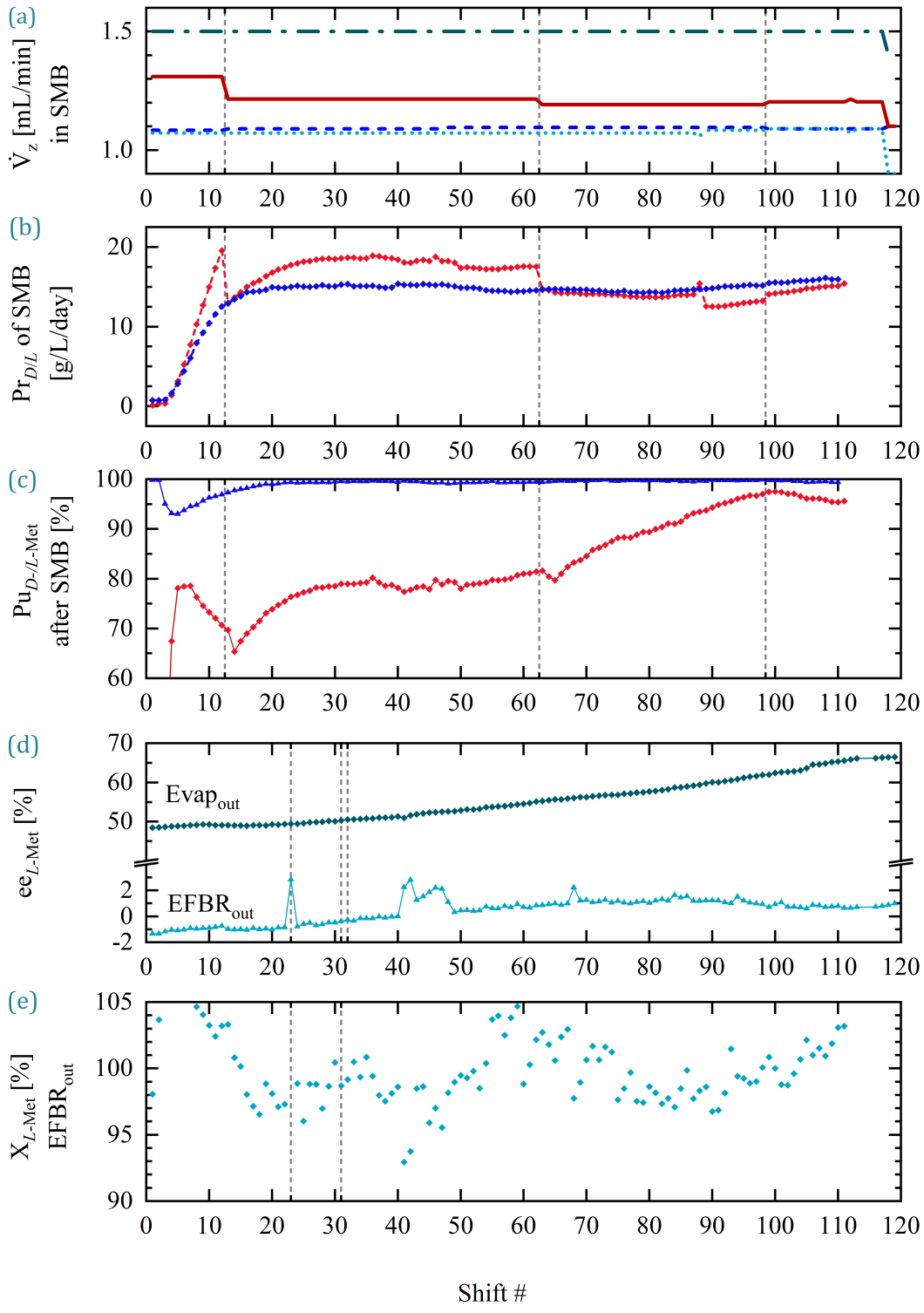

Fig. 6.14: Run 9: Performance of the SMB-EFBR plant: (a) Flow rates in zones I (▬ ▪ ▬), II (▬), III (▬ ▬), and IV (▪ ▪), (b) and (c) productivity and purity at the raffinate and extract port for *L*- (◆) and *D*- (◆) Met, (d) enantiomeric excess of the bottom product of the distillation unit (■) and at the EFBR outlet (■), (e) the resulting conversion of *L*-Met to *D*-Met within the EFBR.

6.4 Performance of the coupled process and outlook

A classical four zone simulated moving bed (SMB) chromatography process for the separation of *D*-/*L*-methionine (Met) was designed based on single component adsorption behaviour. The process was successfully operated in a four column setup for 36 h with a racemic feed of 10 g/L *DL*-Met. The process reached purities of up to 99.98 % for both enantiomers and a productivity of around 14 g/L/day. For lower purity requirements higher productivities were obtained and it was found beneficial to operate accepting a small contamination of the distomer enantiomer. Furthermore, the separation was tested for asymmetric feed mixtures with 4.5:5.5 and 5.5:4.5 g/L *D*:*L*-Met, simulating an incomplete racemization. Again a successful separation was achieved and the preliminary tests showed only small reduction of the productivity. However, it seems worth mentioning, that the optimal operation zone seemed to shift towards lower flow rates, indicating that the adsorption behaviour might have changed and some adsorption sites might have been blocked. The productivity of the SMB process was far below the predicted optimal true moving bed (TMB) process, due to using the simple four column setup, which shifted the optimal operating point from the vertex of the SMB triangle towards the diagonal line.

In a next step, the recycling loop was installed, by integrating the SMB unit with an enzymatic fixed bed reactor (EFBR) and rectification column. After preliminary evaporation tests and with the results reported in Sec. 4.5, the coupled setup was tested in different runs. In these experiments, the robustness of the setup towards disturbances was shown and a run over two days showed the stability of the system and its ability to provide 0.5 L of *D*-Met with a concentration of 1 g/L and purity of almost 99 %, combined with full recycling of *L*-Met. For this process, four chiral columns with a total column volume of 47 mL and an EFBR with 57 mg carrier (V_{EFBR} = 0.08 mL) were required. The experiments show the further potential of coupling the chiral separation to enzymatic racemization. The EFBR could be operated without visible decline of activity. In combination with the results from Sec. 4.2.3 it can be assumed that an EFBR with a reactor volume of 0.14 mL would be sufficient to operate successfully for 60 days. This reactor volume would be just 0.3 % of the volume of the chiral stationary phase. Also, the implementation of the evaporation did not create significant operating costs and operated reliably, after applying the proper equipment (see Sec. 3.5.2). In summary, in order to increase the efficiency of the given process, the focus of further studies should be on improving the chiral separation.

Options to increase the productivity of the SMB are using columns with larger particle diameters, allowing higher flow rates and replacing the four columns with eight shorter columns with half the length and the same diameter. With both options, higher productivities would be achievable with the same amount of stationary phase. However, while neither option was available for this case study, another possible approach for improvement considered would be an operation with incomplete regeneration. When targeting the extract, the safety margin for the flow of zone I can be ignored, to allow higher overall flow rates and a higher throughput, since a contamination of the raffinate would not effect the process yield. Alternatively, when targeting the raffinate, the safety margin on zone IV could be removed, for the benefit of a lower solvent consumption.

Furthermore, to improve the separation efficiency, the four zone SMB process could be changed into a 1-2-1 or 1-1-2 three zone open-loop configuration, as shown in the simulations in Sec. 5.3. When targeting the extract, the resulting dilution of the raffinate stream could be compensated in the evaporation unit, or when targeting the raffinate, the product fraction could be concentrated in a second evaporation unit. Alternatively, many other SMB process options, like a Varicol, PowerFeed, ModiCon or Intermittent SMB [103, 104, 167, 105, 106], could be implemented. While these operation modes all will increase the separation complexity, they offer potential to further increase the productivity.

A reliable solution for stable operation of complex processes is automated process control. Unfortunately, since the monitoring and control system used in this work was still under development, in this work the on-site analytic system was only used for monitoring. Yet, its accuracy was excellent for a wide detection range of 0.01-3 g/L *D-/L*-methionine (Met) and still sufficient for higher concentrations. Thus, it is highly recommended to extend the application of the on-site analytic system for automated process control. With the application of the on-site analytics system in a control system, as described in Sec. 2.3.3, the overall process robustness could be guaranteed for complex operation modes and a long-term steady process operation and distomer recycling appear to be feasible.

7 Conclusions

Chiral resolution is of great importance for the life-science industry. One approach for the provision of pure enantiomers is the combination of enantioselective chromatography with racemization. Recycling of the distomer by integrating racemization and solvent removal efficiently exploits the unwanted enantiomer of a racemic feed mixture and expands the operating region of the separation process.

The main objectives of this work were the theoretical and practical evaluation of chiral chromatographic separation and enzymatic racemization individually and in an integrated setup. The goal of this investigation was the identification of key parameters for process intensification and the provision of insights for a benchmark problem.

The application of racemases to improve enantioselective separation processes is a rarely studied option. In this thesis, the wide applicability and high stability of an immobilized amino acid racemase (AAR) is shown. An immobilized AAR was studied as an enzymatic fixed bed reactor (EFBR) regarding its activity for racemizing *L*- and *D*-methionine (Met). The activity increased with temperature in the range of 10-30 °C. It was maximized in a phosphate buffered system at pH 7-8, as well as in pure water. When targeting a moderate conversion rate of X_L = 90 % with a feed of $c_{L\text{-Met},0}$ = 20 g/L at 20 °C, the EFBR reached a productivity of $Pr_{D\text{-Met}}$ = 106 $g_{D\text{-Met}}/g_{carrier}$/day. Furthermore, significant AAR activities were confirmed for a range of other amino acids and a high stability of immobilized AAR in comparison to free AAR was demonstrated. After operating for one month with water at 20 °C, the AAR still had an activity of 80 %. These encouraging results promote the application of the AAR in an EFBR as a process intensification tool in coupled processes. The EFBR can easily be integrated into an enantio-separation process for different amino acids, if the separation is performed in a water-based non-toxic solvent.

With the knowledge of the benefits of racemization, conventional closed-loop four zone and an open-loop three zone simulated moving bed (SMB) chromatography processes were investigated theoretically and experimentally. The SMB chromatographic separation was investigated in two case studies: *R*-/S-mandelic acid and *D*-/L-Met. For both cases, the adsorption behaviour was determined and the enantioseparation using TMB and SMB chromatography was modelled. The comparisons

demonstrated that the key characteristics for high productivities are high selectivities of the binary mixture for the applied stationary phases and exploitable high feed concentrations in combination with the process configuration. In case the system can operate sufficiently close to the optimal operating point, *R*-/S-mandelic acid benefits from its high solubility, while the larger operating window of *D*-/L-Met would perform better in a less optimized configuration with e.g. low plate numbers and only one column per zone.

Furthermore, in a coupled setup with racemization, three zone SMB chromatography without a solvent regeneration zone outperformed the conventional four zone setup. This configuration is not only less complex, but it also opens the option of saving 25 % of the stationary phase without reducing throughput and yield. Alternatively, the configuration increased the process productivity by shifting the column from the former fourth zone to the critical separation zones.

In the mini-plant setup, four zone SMB chromatography in a one-column-per-zone-mode was coupled to a distillation column for eluent evaporation and an EFBR for racemization. The distillation provided the possibility to concentrate the recyclate in combination with a solvent change between the SMB and EFBR unit. It removed the 20 vol% MeOH in the eluent, which was needed to achieve sufficient chromatographic resolution in the SMB unit, but reduced the racemization rate of the EFBR unit compared to pure water. After preliminary screening experiments, the plant was connected to recycle the *L*-Met from the raffinate port, while the extract outlet was collected for the provision of *D*-Met with high productivity and yield. With this setup, 99 % pure *D*-Met could be collected with a productivity of 16 $g_{D\text{-Met}}/L_c/day$. The process required 48 mL of chiral stationary phase. The integration of less < 0.1 mL immobilized AAR doubled the yield.

The significant difference in the size required for the two units allows the conclusion that, for the given system, a further improvement of the chiral separation would yield the higher overall benefit. The results achieved also show the synergy between the two process units. In comparison to stand-alone preferential crystallization, chromatography can provide the distomer with high enantiomeric excesses and can tolerate moderate excesses of the distomer in the feed. This enables the racemase to operate at a high driving force and thus with its full potential. Therefore, while it is encouraged to integrate the immobilized AAR into other chiral resolution processes, these processes should be adapted to operate the racemase in a feed with high enantiomeric excess. In this case, the AAR used in this study and immobilized racemases in general, have a great potential to increase the overall performance of chiral resolution processes for pure enantiomer provision.

Bibliography

[1] R. A. Sheldon. *Chirotechnology: industrial synthesis of optically active compounds*. CRC press, 1993.

[2] A. M. Rouhi. "Chiral business". In: *Chemical & engineering news* 81.18 (2003), pp. 45–45.

[3] N. M. Maier, P. Franco and W. Lindner. "Separation of enantiomers: needs, challenges, perspectives". In: *Journal of chromatography A* 906.1-2 (2001), pp. 3–33.

[4] I. Wainer. *Drug stereochemistry: analytical methods and pharmacology*. Vol. 18. CRC Press, 1993.

[5] J. Caldwell. "Stereochemical determinants of the nature and consequences of drug metabolism". In: *Journal of Chromatography A* 694.1 (1995), pp. 39–48.

[6] H. Lorenz and A. Seidel-Morgenstern. "Processes to separate enantiomers". In: *Angewandte Chemie International Edition* 53.5 (2014), pp. 1218–1250. DOI: 10.1002/anie.201302823.

[7] J. Jacques, A. Collet and S. H. Wilen. *Enantiomers, racemates, and resolutions*. Wiley, 1981.

[8] *Chirality induction*. 2022. URL: https://www.chemie.uni-halle.de/bereiche_der_chemie/physikalische_chemie/ak_sebastiani/research/chirality_induction.

[9] R. Breslow and Z.-L. Cheng. "On the origin of terrestrial homochirality for nucleosides and amino acids". In: *Proceedings of the National Academy of Sciences* 106.23 (2009), pp. 9144–9146.

[10] E. Fischer. "Ueber die Configuration des Traubenzuckers und seiner Isomeren. II". In: *European Journal of Inorganic Chemistry* 24.2 (1891), pp. 2683–2687.

[11] L. A. Nguyen, H. He and C. Pham-Huy. "Chiral drugs: an overview". In: *International journal of biomedical science: IJBS* 2.2 (2006), p. 85.

[12] R. S. Cahn, C. K. Ingold and V. Prelog. "The specification of asymmetric configuration in organic chemistry". In: *Cellular and Molecular Life Sciences* 12.3 (1956), pp. 81–94.

[13] S. W. Smith. "Chiral toxicology: it's the same thing... only different". In: *Toxicological sciences* 110.1 (2009), pp. 4–30.

[14] A. Calcaterra and I. D'Acquarica. "The market of chiral drugs: Chiral switches versus de novo enantiomerically pure compounds". In: *Journal of pharmaceutical and biomedical analysis* 147 (2018), pp. 323–340.

[15] J. Gal. *Chiral drugs from a historical point of view*. Vol. 33. WILEY-VCH: Weinheim, 2006.

[16] T. Bach. "Katalytische Varianten enantioselektiver C-C-Verknüpfungen: Allylübertragung und Mukaiyama-Aldolreaktion". In: *Angewandte Chemie* 106.4 (1994), pp. 433–435.

[17] B. List. "Proline-catalyzed asymmetric reactions". In: *Tetrahedron* 58.28 (2002), pp. 5573–5590.

[18] *The Nobel Prize in Chemistry 2021*. 2021. URL: https://www.nobelprize.org/prizes/chemistry/2021/summary/ (visited on 26th Jan. 2022).

[19] Z. Feng and B. Xu. "Inspiration from the mirror: D-amino acid containing peptides in biomedical approaches". In: *Biomolecular concepts* 7.3 (2016), pp. 179–187.

[20] D. Grishin, D. Zhdanov, M. Pokrovskaya et al. "D-amino acids in nature, agriculture and biomedicine". In: *All Life* 13.1 (2020), pp. 11–22.

[21] S. Ahuja. *Chiral separation methods for pharmaceutical and biotechnological products*. John Wiley & Sons, 2011.

[22] P. Franco, A. Senso, L. Oliveros et al. "Covalently bonded polysaccharide derivatives as chiral stationary phases in high-performance liquid chromatography". In: *Journal of chromatography A* 906.1-2 (2001), pp. 155–170.

[23] B. Martín-Matute and J.-E. Bäckvall. "Dynamic kinetic resolution catalyzed by enzymes and metals". In: *Current opinion in chemical biology* 11.2 (2007), pp. 226–232. DOI: 10.1016/j.cbpa.2007.01.724.

[24] W. Marckwald and A. McKenzie. "Ueber eine principiell neue Methode zur Spaltung racemischer Verbindungen in die activen Bestandtheile". In: *Berichte der deutschen chemischen Gesellschaft* 32.2 (1899), pp. 2130–2136.

[25] D. W. Armstrong and H. L. Jin. "Enrichment of enantiomers and other isomers with aqueous liquid membranes containing cyclodextrin carriers". In: *Analytical chemistry* 59.18 (1987), pp. 2237–2241.

[26] C. A. Afonso and J. G. Crespo. "Recent advances in chiral resolution through membrane-based approaches". In: *Angewandte Chemie International Edition* 43.40 (2004), pp. 5293–5295.

[27] M. Lämmerhofer. "Chiral recognition by enantioselective liquid chromatography: mechanisms and modern chiral stationary phases". In: *Journal of Chromatography A* 1217.6 (2010), pp. 814–856.

[28] I. Ilisz, A. Aranyi, Z. Pataj et al. "Enantiomeric separation of nonproteinogenic amino acids by high-performance liquid chromatography". In: *Journal of Chromatography A* 1269 (2012), pp. 94–121.

[29] A. Péter, A. Árki, D. Tourwé et al. "Comparison of the separation efficiencies of Chirobiotic T and TAG columns in the separation of unusual amino acids". In: *Journal of Chromatography A* 1031.1-2 (2004), pp. 159–170.

[30] A Arki, D Tourwe, M Solymar et al. “High-performance liquid chromatographic separation of stereoisomers of β-amino acids and a comparison of separation efficiencies on CHIROBIOTIC T and TAG columns”. In: *Chromatographia* 60.1 (2004), S43–S54.

[31] E. R. Francotte. “Enantioselective chromatography as a powerful alternative for the preparation of drug enantiomers”. In: *Journal of chromatography A* 906.1-2 (2001), pp. 379–397.

[32] U. Strauss, U Felfer and K Faber. “Biocatalytic transformation of racemates into chiral building blocks in 100% chemical yield and 100% enantiomeric excess”. In: *Tetrahedron: Asymmetry* 10.1 (1999), pp. 107–117.

[33] M. Kaspereit, S. Swernath and A. Kienle. “Evaluation of competing process concepts for the production of pure enantiomers”. In: *Organic Process Research & Development* 16.2 (2012), pp. 353–363.

[34] J. von Langermann, M. Kaspereit, M. Shakeri et al. “Design of an integrated process of chromatography, crystallization and racemization for the resolution of 2, 6-pipecoloxylidide (PPX)”. In: *Organic Process Research & Development* 16.2 (2012), pp. 343–352. DOI: 10.1021/op200268h.

[35] J. G. Palacios, M. Kaspereit and A. Kienle. “Integrated simulated moving bed processes for production of single enantiomers”. In: *Chemical Engineering & Technology* 34.5 (2011), pp. 688–698.

[36] S. Swernath, M. Kaspereit and A. Kienle. “Coupled continuous chromatography and racemization processes for the production of pure enantiomers”. In: *Chemical Engineering & Technology* 37.4 (2014), pp. 643–651. DOI: 10.1002/ceat.201300597.

[37] M. Fuereder, C. Femmer, G. Storti et al. “Integration of simulated moving bed chromatography and enzymatic racemization for the production of single enantiomers”. In: *Chemical Engineering Science* 152 (2016), pp. 649–662. DOI: 10.1016/j.ces.2016.05.033.

[38] E. J. Ebbers, G. J. Ariaans, J. P. Houbiers et al. “Controlled racemization of optically active organic compounds: prospects for asymmetric transformation”. In: *Tetrahedron* 53.28 (1997), pp. 9417–9476.

[39] L. K. Thalén, D. Zhao, J.-B. Sortais et al. “A chemoenzymatic approach to enantiomerically pure amines using dynamic kinetic resolution: application to the synthesis of norsertraline”. In: *Chemistry–A European Journal* 15.14 (2009), pp. 3403–3410.

[40] *EU project: INTENANT*. 2022. URL: https://cordis.europa.eu/project/id/214129 (visited on 28th Jan. 2022).

[41] K. Petruševska-Seebach, K. Wuerges, A. Seidel-Morgenstern et al. “Enzyme-assisted physicochemical enantioseparation processes—Part II: Solid–liquid equilibria, preferential crystallization, chromatography and racemization reaction”. In: *Chemical Engineering Science* 64.10 (2009), pp. 2473–2482.

[42] K. Wrzosek, M. A. García Rivera, K. Bettenbrock et al. “Racemization of undesired enantiomers: Immobilization of mandelate racemase and application in a fixed bed reactor”. In: *Biotechnology journal* 11.4 (2016), pp. 453–463.

[43] T. Carneiro, K. Wrzosek, K. Bettenbrock et al. “Immobilization of an amino acid racemase for application in crystallization-based chiral resolutions of asparagine monohydrate”. In: *Engineering in Life Sciences* 20.12 (2020), pp. 550–561. DOI: 10.1002/elsc.202000029.

[44] L. R. Snyder, J. J. Kirkland and J. W. Dolan. *Introduction to modern liquid chromatography*. John Wiley & Sons, 2011.

[45] J. G. Kirchner. “Thin-layer chromatography”. In: XIV (1978).

[46] C. G. Horvath and S. Lipsky. “Use of liquid ion exchange chromatography for the separation of organic compounds”. In: *Nature* 211.5050 (1966), pp. 748–749.

[47] S. Hober, K. Nord and M. Linhult. “Protein A chromatography for antibody purification”. In: *Journal of Chromatography B* 848.1 (2007), pp. 40–47.

[48] E. Hochuli, W. Bannwarth, H. Döbeli et al. “Genetic approach to facilitate purification of recombinant proteins with a novel metal chelate adsorbent”. In: *Bio/technology* 6.11 (1988), pp. 1321–1325.

[49] J. Porath. “Immobilized metal ion affinity chromatography”. In: *Protein expression and purification* 3.4 (1992), pp. 263–281.

[50] D. Graham. “The characterization of physical adsorption systems. I. The equilibrium function and standard free energy of adsorption”. In: *The journal of physical chemistry* 57.7 (1953), pp. 665–669.

[51] H. Schmidt-Traub, M. Schulte and A. Seidel-Morgenstern. *Preparative chromatography: of fine chemicals and pharmaceutical agents*. 3rd ed. Weinheim, Germany: Wiley–VCH Verlag GmbH & Co. KGaA, 2020. DOI: 10.1002/9783527816347.

[52] S. Jacobson, S. Golshan-Shirazi and G. Guiochon. “Chromatographic band profiles and band separation of enantiomers at high concentration”. In: *Journal of the American Chemical Society* 112.18 (1990), pp. 6492–6498.

[53] A. Gentilini, C. Migliorini, M. Mazzotti et al. “Optimal operation of simulated moving-bed units for non-linear chromatographic separations: II. Bi-Langmuir isotherm”. In: *Journal of Chromatography A* 805.1-2 (1998), pp. 37–44.

[54] O Lisec, P Hugo and A Seidel-Morgenstern. “Frontal analysis method to determine competitive adsorption isotherms”. In: *Journal of Chromatography A* 908.1-2 (2001), pp. 19–34.

[55] A. Seidel-Morgenstern. “Rapid Estimation of the Breakthrough Behavior of Competing Adsorbing Components”. In: *Chemie Ingenieur Technik* 92.4 (2020), pp. 323–330.

[56] A. Kremser. “Theoretical analysis of absorption process”. In: *National Petroleum News* 22 (1930), p. 42.

[57] W. E. Schiesser. *The numerical method of lines: integration of partial differential equations*. Elsevier, 2012.

[58] M. Fechtner and A. Kienle. “Efficient simulation and equilibrium theory for adsorption processes with implicit adsorption isotherms–mass action equilibria”. In: *Chemical Engineering Science* 171 (2017), pp. 471–480.

[59] P. Rouchon, M. Schonauer, P. Valentin et al. “Numerical simulation of band propagation in nonlinear chromatography”. In: *Separation Science and Technology* 22.8-10 (1987), pp. 1793–1833.

[60] A Seidel-Morgenstern, C Blümel and H Kniep. “Fundamentals Of Adsorption 6, chapter Efficient design of the SMB process based on a perturbation method to measure adsorption isotherms and on a rapid solution of the dispersion model”. In: (1998).

[61] H. Kniep, G. Mann, C. Vogel et al. “Separation of Enantiomers through Simulated Moving-Bed Chromatography”. In: *Chemical Engineering & Technology: Industrial Chemistry-Plant Equipment-Process Engineering-Biotechnology* 23.10 (2000), pp. 853–857.

[62] R. J. LeVeque and R. J. Leveque. *Numerical methods for conservation laws*. Vol. 214. Springer, 1992.

[63] V. Zahn. “Herleitung des TMB Modells, Diskussion der Randbedingungen und Analyse numerischer Fehler”. Zusammenschrift. Max-Planck-Institut Magdeburg, 2010.

[64] J. Nowak, D. Antos and A. Seidel-Morgenstern. “Theoretical study of using simulated moving bed chromatography to separate intermediately eluting target compounds”. In: *Journal of chromatography A* 1253 (2012), pp. 58–70.

[65] D. B. Broughton and C. G. Gerhold. *Continuous sorption process employing fixed bed of sorbent and moving inlets and outlets*. 1961.

[66] G Storti, M Mazzotti, L. Furlan et al. “Continuous adsorption separation of vapor mixtures in simulated moving bed pilot plant.[Mixtures of alkylaromatic C8 fraction and isopropylbenzene]”. In: *Chimica e l’Industria (Milan);(Italy)* 74.11 (1992).

[67] D. M. Ruthven and C. Ching. “Counter-current and simulated counter-current adsorption separation processes”. In: *Chemical Engineering Science* 44.5 (1989), pp. 1011–1038.

[68] M. Negawa and F. Shoji. “Optical resolution by simulated moving-bed adsorption technology”. In: *Journal of Chromatography A* 590.1 (1992), pp. 113–117.

[69] R.-M. Nicoud, G. Fuchs, P. Adam et al. “Preparative scale enantioseparation of a chiral epoxide: comparison of liquid chromatography and simulated moving bed adsorption technology”. In: *Chirality* 5.4 (1993), pp. 267–271.

[70] E. R. Francotte and P. Richert. “Applications of simulated moving-bed chromatography to the separation of the enantiomers of chiral drugs”. In: *Journal of Chromatography A* 769.1 (1997), pp. 101–107.

[71] G. Zhong and G. Guiochon. “Analytical solution for the linear ideal model of simulated moving bed chromatography”. In: *Chemical Engineering Science* 51.18 (1996), pp. 4307–4319. DOI: https://doi.org/10.1016/0009-2509(96)00262-X.

[72] A. Rodrigues. *Simulated moving bed technology: principles, design and process applications*. Butterworth-Heinemann, 2015.

[73] G. Storti, M. Mazzotti, M. Morbidelli et al. "Robust design of binary countercurrent adsorption separation processes". In: *AIChE Journal* 39.3 (1993), pp. 471–492.

[74] M. Mazzotti, G. Storti and M. Morbidelli. "Optimal operation of simulated moving bed units for nonlinear chromatographic separations". In: *Journal of chromatography A* 769.1 (1997), pp. 3–24.

[75] D. Beltscheva, P. Hugo and A. Seidel-Morgenstern. "Linear two-step gradient countercurrent chromatography: Analysis based on a recursive solution of an equilibrium stage model". In: *Journal of chromatography A* 989.1 (2003), pp. 31–45.

[76] M. Kaspereit and B. Neupert. "Vereinfachte Auslegung der simulierten Gegenstromchromatographie mittels des Hodographenraums". In: *Chemie Ingenieur Technik* 11.88 (2016), pp. 1628–1642.

[77] H. Amos. "A racemase for threonine in Escherichia coli". In: *Journal of the American Chemical Society* 76.14 (1954), pp. 3858–3858.

[78] C. T. Walsh. "Enzymes in the D-alanine branch of bacterial cell wall peptidoglycan assembly". In: *Journal of biological chemistry* 264.5 (1989), pp. 2393–2396.

[79] Y.-H. Lim, K Yokoigawa, N Esaki et al. "A new amino acid racemase with threonine alpha-epimerase activity from Pseudomonas putida: purification and characterization". In: *Journal of bacteriology* 175.13 (1993), pp. 4213–4217.

[80] R. Kourist, Y. Miyauchi, D. Uemura et al. "Engineering the promiscuous racemase activity of an arylmalonate decarboxylase". In: *Chemistry–A European Journal* 17.2 (2011), pp. 557–563.

[81] T. Yoshimura and N. Esak. "Amino acid racemases: functions and mechanisms". In: *Journal of bioscience and bioengineering* 96.2 (2003), pp. 103–109.

[82] U. T. Strauss, A. Kandelbauer and K. Faber. "Stabilization and activity-enhancement of mandelate racemase from Pseudomonas putida ATCC 12336 by immobilization". In: *Biotechnology letters* 22.6 (2000), pp. 515–520.

[83] F. F. Huerta, A. B. E. Minidis and J.-E. Bäckvall. "Racemisation in asymmetric synthesis. Dynamic kinetic resolution and related processes in enzyme and metal catalysis". In: *Chemical Society Reviews* 30.6 (2001), pp. 321–331. DOI: 10.1039/B105464N.

[84] R. A. Sheldon. "Enzyme immobilization: the quest for optimum performance". In: *Advanced Synthesis & Catalysis* 349.8–9 (2007), pp. 1289–1307. DOI: 10.1002/adsc.200700082.

[85] E. Katchalski-Katzir and D. M. Kraemer. "Eupergit® C, a carrier for immobilization of enzymes of industrial potential". In: *Journal of molecular catalysis B: enzymatic* 10.1-3 (2000), pp. 157–176.

[86] B. M. Brena and F. Batista-Viera. "Immobilization of enzymes". In: *Immobilization of enzymes and cells*. Springer, 2006, pp. 15–30.

[87] C. Garcia-Galan, Á. Berenguer-Murcia, R. Fernandez-Lafuente et al. “Potential of different enzyme immobilization strategies to improve enzyme performance”. In: *Advanced Synthesis & Catalysis* 353.16 (2011), pp. 2885–2904.

[88] R. A. Sheldon and S. van Pelt. “Enzyme immobilisation in biocatalysis: why, what and how”. In: *Chemical Society Reviews* 42.15 (2013), pp. 6223–6235.

[89] U. Bornscheuer and K Buchholz. “Highlights in biocatalysis–historical landmarks and current trends”. In: *Engineering in Life Sciences* 5.4 (2005), pp. 309–323.

[90] *Application guide: Lifetech ECR Enzyme, Immobilization Procedure*. 2015.

[91] R. M. da Silva, P. M. P. Souza, F. A. Fernandes et al. “Co-immobilization of dextransucrase and dextranase in epoxy-agarose-tailoring oligosaccharides synthesis”. In: *Process Biochemistry* 78 (2019), pp. 71–81.

[92] J. N. Talbert and J. M. Goddard. “Enzymes on material surfaces”. In: *Colloids and Surfaces B: Biointerfaces* 93 (2012), pp. 8–19.

[93] G. E. Briggs and J. B. S. Haldane. “A Note on the Kinetics of Enzyme Action”. In: *Biochemical Journal* 19.2 (1925), pp. 338–339. DOI: 10.1042/bj0190338.

[94] A. Seidel-Morgenstern and G. Guiochon. “Theoretical study of recycling in preparative chromatography”. In: *AIChE journal* 39.5 (1993), pp. 809–819.

[95] I. Quiñones, C. M. Grill, L. Miller et al. “Modeling of separations by closed-loop steady-state recycling chromatography of a racemic pharmaceutical intermediate”. In: *Journal of chromatography A* 867.1-2 (2000), pp. 1–21.

[96] M. Kaspereit and T. Sainio. “Simplified design of steady-state recycling chromatography under ideal and nonideal conditions”. In: *Chemical Engineering Science* 66.21 (2011), pp. 5428–5438. DOI: 10.1016/j.ces.2011.07.058.

[97] J. Siitonen, M. Mänttäri, A. Seidel-Morgenstern et al. “Robustness of steady state recycling chromatography with an integrated solvent removal unit”. In: *Journal of chromatography A* 1391 (2015), pp. 31–39.

[98] A. E. Kostanyan. “Theoretical study of separation and concentration of solutes by closed-loop recycling liquid-liquid chromatography with multiple sample injection”. In: *Journal of chromatography A* 1506 (2017), pp. 82–92.

[99] Z. Zhang, M. Mazzotti and M. Morbidelli. “Continuous chromatographic processes with a small number of columns: comparison of simulated moving bed with Varicol, PowerFeed, and ModiCon”. In: *Korean Journal of Chemical Engineering* 21.2 (2004), pp. 454–464.

[100] A. Seidel-Morgenstern, L. C. Kessler and M. Kaspereit. “New developments in simulated moving bed chromatography”. In: *Chemical Engineering & Technology: Industrial Chemistry-Plant Equipment-Process Engineering-Biotechnology* 31.6 (2008), pp. 826–837.

[101] P. Sá Gomes and A. E. Rodrigues. “Simulated moving bed chromatography: from concept to proof-of-concept”. In: *Chemical engineering & technology* 35.1 (2012), pp. 17–34.

[102] K.-M. Kim, J. W. Lee, S. Kim et al. “Advanced Operating Strategies to Extend the Applications of Simulated Moving Bed Chromatography”. In: *Chemical Engineering & Technology* 40.12 (2017), pp. 2163–2178.

[103] O Ludemann-Hombourger, R. Nicoud and M Bailly. “The “VARICOL” process: a new multicolumn continuous chromatographic process”. In: *Separation science and technology* 35.12 (2000), pp. 1829–1862.

[104] Y. Kawajiri and L. T. Biegler. “Optimization strategies for simulated moving bed and PowerFeed processes”. In: *AIChE journal* 52.4 (2006), pp. 1343–1350.

[105] H Schramm, A Kienle, M Kaspereit et al. “Improved operation of simulated moving bed processes through cyclic modulation of feed flow and feed concentration”. In: *Chemical Engineering Science* 58.23-24 (2003), pp. 5217–5227.

[106] M Tanimura, M Tamura and T Teshima. “Chromatographic separation method”. In: *Japanese Patent JP-B-H07–046097* (1995).

[107] Y. Kawajiri. “Model-based optimization strategies for chromatographic processes: a review”. In: *Adsorption* 27.1 (2021), pp. 1–26.

[108] G. Paredes, S. Abel, M. Mazzotti et al. “Analysis of a simulated moving bed operation for three-fraction separations (3F-SMB)”. In: *Industrial & engineering chemistry research* 43.19 (2004), pp. 6157–6167.

[109] B. Sreedhar and Y. Kawajiri. “Multi-column chromatographic process development using simulated moving bed superstructure and simultaneous optimization–Model correction framework”. In: *Chemical Engineering Science* 116 (2014), pp. 428–441.

[110] P. Tangpromphan, H. Budman and A. Jaree. “A simplified strategy to reduce the desorbent consumption and equipment installed in a three-zone simulated moving bed process for the separation of glucose and fructose”. In: *Chemical Engineering and Processing-Process Intensification* 126 (2018), pp. 23–37.

[111] J Blehaut and R.-M. Nicoud. “Recent aspects in simulated moving bed”. In: *Analusis* 26.7 (1998), pp. 60–70.

[112] K. Hashimoto, S. Adachi, H. Noujima et al. “A new process combining adsorption and enzyme reaction for producing higher-fructose syrup”. In: *Biotechnology and bioengineering* 25.10 (1983), pp. 2371–2393. DOI: 10.1002/bit.260251008.

[113] T. Borren and H. Schmidt-Traub. “Vergleich chromatographischer reaktorkonzepte”. In: *Chemie Ingenieur Technik* 76.6 (2004), pp. 805–814.

[114] M. Bechtold, S. Makart, M. Heinemann et al. “Integrated operation of continuous chromatography and biotransformations for the generic high yield production of fine chemicals”. In: *Journal of biotechnology* 124.1 (2006), pp. 146–162.

[115] J. G. Palacios, M. Kaspereit and A. Kienle. “Conceptual Design of Integrated Chromatographic Processes for the Production of Single (Stereo-) Isomers”. In: *Chemical Engineering & Technology: Industrial Chemistry-Plant Equipment-Process Engineering-Biotechnology* 32.9 (2009), pp. 1392–1402. DOI: 10.1002/ceat.200900231.

[116] N. Wagner, M. Fuereder, A. Bosshart et al. “Practical aspects of integrated operation of biotransformation and SMB separation for fine chemical synthesis”. In: *Organic Process Research & Development* 16.2 (2012), pp. 323–330.

[117] J. W. Lee, Z. Horváth, A. G. O’Brien et al. “Design and optimization of coupling a continuously operated reactor with simulated moving bed chromatography”. In: *Chemical Engineering Journal* 251 (2014), pp. 355–370.

[118] S. Nimmig and M. Kaspereit. “Continuous production of single enantiomers at high yields by coupling single column chromatography, racemization, and nanofiltration”. In: *Chemical Engineering and Processing: Process Intensification* 67 (2013), pp. 89–98.

[119] K. E. Cassimjee, M. Trummer, C. Branneby et al. “Silica-immobilized His6-tagged enzyme: Alanine racemase in hydrophobic solvent”. In: *Biotechnology and bioengineering* 99.3 (2008), pp. 712–716.

[120] P. Soriano-Maldonado, L. Heras-Vazquez, F. Javier et al. “Enzymatic dynamic kinetic resolution of racemic N-formyl-and N-carbamoyl-amino acids using immobilized LN-carbamoylase and N-succinyl-amino acid racemase”. In: *Applied microbiology and biotechnology* 99.1 (2015), pp. 283–291.

[121] F. Breveglieri, T. Otgonbayar and M. Mazzotti. “Optimizing the Yield of a Pure Enantiomer by Integrating Chiral SMB Chromatography and Racemization. Part 1: Experiments”. In: *Industrial & Engineering Chemistry Research* 60.29 (2021), pp. 10710–10719.

[122] F. Breveglieri, T. Otgonbayar and M. Mazzotti. “Optimizing the Yield of a Pure Enantiomer by Integrating Chiral SMB Chromatography and Racemization. Part 2: Theory”. In: *Industrial & Engineering Chemistry Research* 60.29 (2021), pp. 10720–10735.

[123] J. W. Lee and A. Seidel-Morgenstern. “Model Predictive Control of Simulated Moving Bed Chromatography for Binary and Pseudo-binary Separations: Simulation Study”. In: *IFAC-PapersOnLine* 51.18 (2018). 10th IFAC Symposium on Advanced Control of Chemical Processes ADCHEM 2018, pp. 530–535. DOI: https://doi.org/10.1016/j.ifacol.2018.09.370.

[124] P. Suvarov, J.-W. Lee, A. V. Wouwer et al. “Online estimation of optimal operating conditions for simulated moving bed chromatographic processes”. In: *Journal of Chromatography A* 1602 (2019), pp. 266–272.

[125] M. Amanullah, C. Grossmann, M. Mazzotti et al. “Experimental implementation of automatic ‘cycle to cycle’control of a chiral simulated moving bed separation”. In: *Journal of Chromatography A* 1165.1-2 (2007), pp. 100–108.

[126] C. Langel, C. Grossmann, M. Morbidelli et al. “Implementation of an automated on-line high-performance liquid chromatography monitoring system for ‘cycle to cycle’control of simulated moving beds”. In: *Journal of Chromatography A* 1216.50 (2009), pp. 8806–8815.

[127] H. Brauer. *Grundlagen der Einphasen-und Mehrphasenströmungen*. Vol. 2. Sauerländer, 1971.

[128] S. Ergun and A. A. Orning. “Fluid flow through randomly packed columns and fluidized beds”. In: *Industrial & Engineering Chemistry* 41.6 (1949), pp. 1179–1184.

[129] G. M. Coppola, H. F. Schuster et al. *Alpha-hydroxy acids in enantioselective syntheses*. Wiley Online Library, 1997.

[130] J. Guo, X. Mu, C. Zheng et al. “A highly stable whole-cell biocatalyst for the enantioselective synthesis of optically active alpha-hydroxy acids”. In: *Journal of chemical technology and biotechnology* 84.12 (2009), pp. 1787–1792.

[131] H. Gröger. “Enzymatic routes to enantiomerically pure aromatic \alpha-hydroxy carboxylic acids: a further example for the diversity of biocatalysis”. In: *Advanced Synthesis & Catalysis* 343.6-7 (2001), pp. 547–558.

[132] R. D. Simoni, R. L. Hill and M. Vaughan. “A New Sulfur-containing Amino-Acid Isolated from the Hydrolytic Products of Protein (Mueller, JH (1923) J. Biol. Chem. 56, 157–169)”. In: *Journal of Biological Chemistry* 277.25 (2002), e1–e2.

[133] G. Barger and T. Weichselbaum. “Organic Syntheses”. In: *Biochem. J.* II.25 (1931), pp. 997–1000.

[134] T. Willke. “Methionine production—a critical review”. In: *Applied Microbiology and Biotechnology* 98.24 (2014), pp. 9893–9914.

[135] M Pack. “Aminosäuren in der Tierernährung”. In: *Elements-Degussa Science Newsletter* 6 (2004), pp. 30–33.

[136] Y.-J. Yuan, S.-h. Wang, Z.-x. Song et al. “Production of l-methionine by immobilized pellets of Aspergillus oryzae in a packed bed reactor”. In: *Journal of Chemical Technology & Biotechnology* 77.5 (2002), pp. 602–606.

[137] O. May, S. Verseck, A. Bommarius et al. “Development of dynamic kinetic resolution processes for biocatalytic production of natural and nonnatural L-amino acids”. In: *Organic Process Research & Development* 6.4 (2002), pp. 452–457.

[138] M. P. Ferla and W. M. Patrick. “Bacterial methionine biosynthesis”. In: *Microbiology* 160.8 (2014), pp. 1571–1584.

[139] D. Polenske and H. Lorenz. “Solubility and metastable zone width of the methionine enantiomers and their mixtures in water”. In: *Journal of Chemical and Engineering Data* 54.8 (2009), pp. 2277–2280.

[140] M. Fuereder, I. N. Majeed, S. Panke et al. “Model-based identification of optimal operating conditions for amino acid simulated moving bed enantioseparation using a macrocyclic glycopeptide stationary phase”. In: *Journal of chromatography A* 1346 (2014), pp. 34–42.

[141] K. Petrusevska, M. A. Kuznetsov, K. Gedicke et al. “Chromatographic enantioseparation of amino acids using a new chiral stationary phase based on a macrocyclic glycopeptide antibiotic”. In: *Journal of separation science* 29.10 (2006), pp. 1447–1457. DOI: 10.1002/jssc.200600036.

[142] D. Binev, A. Seidel-Morgenstern and H. Lorenz. “Continuous separation of isomers in fluidized bed crystallizers”. In: *Crystal Growth & Design* 16.3 (2016), pp. 1409–1419.

[143] G. D. Hegeman, E. Y. Rosenberg and G. L. Kenyon. “Mandelic acid racemase from Pseudomonas putida. Purification and properties of the enzyme”. In: *Biochemistry* 9.21 (1970), pp. 4029–4036.

[144] G. L. Kenyon, J. A. Gerlt, G. A. Petsko et al. “Mandelate racemase: structure-function studies of a pseudosymmetric enzyme”. In: *Accounts of chemical research* 28.4 (1995), pp. 178–186.

[145] A. Narmandakh and S. L. Bearne. “Purification of recombinant mandelate racemase: improved catalytic activity”. In: *Protein expression and purification* 69.1 (2010), pp. 39–46.

[146] K. E. Nelson. “The complete genome sequence of Pseudomonas putida KT2440 is finally available”. In: *Environmental Microbiology* 4.12 (2002), pp. 777–778. DOI: 10.1046/j.1462-2920.2002.00367.x.

[147] M. Ikeda. “Amino acid production processes”. In: *Microbial production of l-amino acids* (2003), pp. 1–35.

[148] K. Wuerges, K. Petruševska-Seebach, M. P. Elsner et al. “Enzyme-assisted physico-chemical enantioseparation processes—Part III: Overcoming yield limitations by dynamic kinetic resolution of asparagine via preferential crystallization and enzymatic racemization”. In: *Biotechnology and bioengineering* 104.6 (2009), pp. 1235–1239.

[149] A. D. Radkov and L. A. Moe. “Amino acid racemization in Pseudomonas putida KT2440”. In: *Journal of bacteriology* 195.22 (2013), pp. 5016–5024. DOI: 10.1128/JB.00761-13.

[150] A. C. Eliot and J. F. Kirsch. “Pyridoxal phosphate enzymes: mechanistic, structural, and evolutionary considerations”. In: *Annual review of biochemistry* 73.1 (2004), pp. 383–415.

[151] U. K. Laemmli. “Cleavage of structural proteins during the assembly of the head of bacteriophage T4”. In: *nature* 227.5259 (1970), pp. 680–685.

[152] *FAQ Chirobiotic T*. 2023. URL: https://www.sigmaaldrich.com/DE/de/technical-documents/technical-article/analytical-chemistry/purification/faq#chirobiotic (visited on 25th Mar. 2023).

[153] X. Becker and A. Seidel-Morgenstern. “Experimentelle Entwicklung der On-line-Analytik für eine SMB-Anlage mittels HPLC und Inbetriebnahme der Anlage”. Bachelor Thesis. Otto-von-Guericke University, 2021.

[154] I. Harriehausen, J. Bollmann, T. Carneiro et al. “Characterization of an Immobilized Amino Acid Racemase for Potential Application in Enantioselective Chromatographic Resolution Processes”. In: *Catalysts* 11.6 (2021), p. 726.

[155] K. Intaraboonrod, I. Harriehausen, T. Carneiro et al. “Temperature Cycling Induced Deracemization of DL-Asparagine with Immobilized Amino Acid Racemase”. In: *Crystal Growth & Design* 2020 (2020). DOI: 10.1021/acs.cgd.0c01140.

[156] A. Bhatwa, W. Wang, Y. I. Hassan et al. “Challenges associated with the formation of recombinant protein inclusion bodies in Escherichia coli and strategies to address them for industrial applications”. In: *Frontiers in Bioengineering and Biotechnology* 9 (2021), p. 630551.

[157] A. K. Upadhyay, A. Murmu, A. Singh et al. “Kinetics of inclusion body formation and its correlation with the characteristics of protein aggregates in Escherichia coli”. In: *PloS one* 7.3 (2012), e33951.

[158] K. Tsumoto, D. Ejima, I. Kumagai et al. “Practical considerations in refolding proteins from inclusion bodies”. In: *Protein Expression and Purification* 28.1 (2003), pp. 1–8. DOI: https://doi.org/10.1016/S1046-5928(02)00641-1.

[159] H. Yamaguchi and M. Miyazaki. “Refolding techniques for recovering biologically active recombinant proteins from inclusion bodies”. In: *Biomolecules* 4.1 (2014), pp. 235–251.

[160] A. Basso, M. S. Brown, A. Cruz-Izquierdo et al. “Optimization of Metal Affinity Ketoreductase Immobilization for Application in Batch and Flow Processes”. In: *Organic Process Research & Development* 26.7 (2022), pp. 2075–2084.

[161] A. M. Knight, A. Nobili, T. van den Bergh et al. “Bioinformatic analysis of fold-type III PLP-dependent enzymes discovers multimeric racemases”. In: *Applied microbiology and biotechnology* 101 (2017), pp. 1499–1507.

[162] I. Harriehausen, K. Wrzosek, H. Lorenz et al. “Assessment of process configurations to combine enantioselective chromatography with enzymatic racemization”. In: *Adsorption* 26 (2020), pp. 1199–1213. DOI: 10.1007/s10450-020-00231-6.

[163] K. Wrzosek, I. Harriehausen and A. Seidel-Morgenstern. “Combination of Enantioselective Preparative Chromatography and Racemization: Experimental Demonstration and Model-Based Process Optimization”. In: *Organic Process Research & Development* 22.12 (2018), pp. 1761–1771.

[164] J. Bollmann and A. Seidel-Morgenstern. “Experimentelle Untersuchung der Aktivität einer Aminosäuren-Racemase für neue Substrate unter geeigneten Kopplungsbedingungen mit einem vorgeschalteten enantioselektiven chromatographischen Trennprozess”. Masters Thesis. Otto-von-Guericke University, 2020.

[165] A. Berthod, Y. Liu, C. Bagwill et al. “Facile liquid chromatographic enantioresolution of native amino acids and peptides using a teicoplanin chiral stationary phase”. In: *Journal of Chromatography A* 731.1-2 (1996), pp. 123–137.

[166] T. Fornstedt, P. Sajonz and G. Guiochon. “A closer study of chiral retention mechanisms”. In: *Chirality* 10.5 (1998), pp. 375–381.

[167] Y. Kawajiri and L. T. Biegler. “Comparison of configurations of a four-column simulated moving bed process by multi-objective optimization”. In: *Adsorption* 14 (2008), pp. 433–442.

[168] D. Klein-Marcuschamer, P. Oleskowicz-Popiel, B. A. Simmons et al. “The challenge of enzyme cost in the production of lignocellulosic biofuels”. In: *Biotechnology and bioengineering* 109.4 (2012), pp. 1083–1087.

[169] J. B. van Beilen and Z. Li. “Enzyme technology: an overview”. In: *Current opinion in biotechnology* 13.4 (2002), pp. 338–344.

[170] *Vapor-Liquid-Equilibria determination by CheCalc*. 2023. URL: https://checalc.com/solved/binary_vle.html (visited on 22nd Apr. 2023).

[171] *Distillation*. 2023. URL: https://www.thermopedia.com/content/703/ (visited on 22nd Apr. 2023).

[172] *McCabe–Thiele method*. 2023. URL: https://www.wikiwand.com/en/McCabe%E2%80%93Thiele_method (visited on 22nd Apr. 2023).

Appendix

A

Chemicals, materials and devices used in this work

Tab. A.1 summarizes all chemicals used in this work. All devices and components used in this work and installed in the SMB-EFBR mini plant are listed in Tab. A.2 and Tab. A.3.

Tab. A.1: Chemicals used in this work

Compound	Manufacturer/Supplier	Purity
Ampicillin	VWR life Science	
Bacto Tryptone (211705)	Gibco	
Bacto Yeast Extract (212750)	Gibco	
$CaCl_2 \cdot 2\ H_2O$	Sigma-Aldrich	
DL-methionine	Sigma-Aldrich,	≥ 99 %
D-methioine	TCI,	≥ 99 %
L-methioine	fisher bioreagents	98.5 - 100 %
DNase 1	Roche Diagnostics GmbH	
Ethanol absolute, HiPerSolv CHROMANORM for HPLC - Gradient Grade	VWR Chemicals	>99.7 %
Glucose	Carl Roth GmbH	
Isopropyl-β-D-thiogalactopyranosid (IPTG)	Carl Roth GmbH	
Methanol HiPerSolv CHROMANORM	VWR Chemicals	
NaCl	Sigma Aldrich	
NaH_2PO_4	Carl Roth GmbH	
Na_2HPO_4	Carl Roth GmbH	
Protease Inhibitor cocktail set VII	Calbiochem, Merck KGaA	
pyridoxal-5'-phosphate (PLP)	Sigma-Aldrich	
R-/S-mandelic acid	Sigma-Aldrich	
R-mandelic acid	Sigma-Aldrich	
S-mandelic acid	Sigma-Aldrich	
Ultrapure water	Millipore Q-Pod	

Tab. A.2: Devices used in this work (besides the mini-plant)

Device	Specification	Manufacturer
12 L bio reactor	Biostat C	B. Braun Biotech
Äkta system	Purifier 25	GE Healthcare
Centrifuge	Avanti JXN-26	Beckman Coulter
French Press	EmulsiFlex-C5	Avestin
LC System	1260 Series	Agilent
LC System	1200 Series	Agilent
LC System	1100 Series	Agilent
Polarimeter	Modular Circular Polarimeter (MCP) 500	Anton Paar

Tab. A.3: Devices and components of the SMB-EFBR plant

Type and model	Manufacturer	Model specification
SMB chromatography		
Pump: Smartline Pump 100 V.5010	Knauer	Extrakt (Extr.)
Pump: Smartline Pump 100 V.5010	Knauer	Raffinat (Raff.)
Pump: Smartline Pump 100 V.5010	Knauer	Zone 1 (Z1)
Pump: Smartline Pump 100 V.5010	Knauer	Feed
SMB-Control unit and valve: CSEP C9 Series Simulated Moving Bed Chromatography Systems V0499, 12/2000	Knauer	
chiral column: Astec Chirociotic T, (15 cm x 10 mm), 5 μm	Astec, Merk	
UV-Detector: K-2501	Knauer	
UV-Detector: K-2501	Knauer	
EFBR		
packing material	immobilized AAR	
Surrounding plant		
Pump 0.03-18 mL/min: mzr-2921X1-hs-vb M2.1 ND	HNP Mikrosysteme	big pump
Pump 0,015-9 mL/min: mzr-2521X1-hs-vb M2.1 ND	HNP Mikrosysteme	small pump
Balances: Präzisions- und Analysewaage MT-TS	Mettler Toledo	
Magnetrührer MR Hei-Standard	heidolph	
Software		
SMB-Steuerung	LabView	
Anlagen-Steuerung	PLS	

Enzymatic fixed bed reactor

B

Detailed fermentation, purification and packing protocol

In the following the preparation of the AAR as well as the method for the determination of the initial reaction rates are explained in detail. The AAR production was based on the protocol described in Carneiro et al. 2020. All solutions have been prepared with Milli Q water (Millipore Q-Pod MilliQ).

B.1 Preparation of required fermentation media and solutions for AAR purification

For the fermentations and purification of the AAR, different media were required as well as additional solutions.The required media are

- Fermentation media: LB-media or 2TY-media with small variations, as listed in Tab. B.1.
- 120 mL ampicillin solution: 10 mg/mL ampicillin in 50/50 ethanol/water
- 120 mL IPTG solution: 0.1 M Isopropyl-β-D-thiogalactopyranosid (IPTG)

The 12-L fermentation media were prepared in 2x5 L and 1x3L beakers, the 0.5-L media in 1-L beakers . All components, except for the Ampicillin were weighted in and then stirred in MilliQ-water until they were dissolved. The media was then sterilized in an autoclave and cooled down. It is then pumped into the fermentor with a sterilized filter and the ampicillin is added.

For the cell harvest, and enzyme purification additional buffers are required:

The solutions S1 and S2 are prepared with 20 mM NaH_2PO_4 (pH 4.6) and 20 mM Na_2HPO_4 (pH 9.1), respectively. They are then used as stock solutions for the preparation of the lysis, washing and elution buffers. All buffers were filtered to remove possible contaminations.

Tab. B.1: Fermentation media of the performed 0.5-L and 12-L-fermentations.

Media	Ampicillin mg/L	Tryptone g/L	Yeast g/L	Glucose g/L	IPTG mM	NaCl g/L	NaCl mM
B-1/B-3	100	10	5	10	100	5	2.5
FB-1	100	10	5	10	10	5	2.5
FB-2	100	10	5	20	10	5	2.5
FB-3	100	10	5	20	100	5	2.5
FB-4	100	20	10	20	100	5	2.5
FB-5	100	10	5	20	100	5	2.5
FB-6	100	10	5	20	100	5	2.5

Tab. B.2: Solutions for the purification of the AAR by cell disruption and affinity chromatography

Solution	Buffer		Salt	Displacer	pH
	NaH_2PO_4	Na_2HPO_4	NaCl	Imidazole	pH
Standard solution 1 (S1)	20 mM	-	500 mM	0	4.6
Standard solution 2 (S2)	-	20 mM	500 mM	0	9.1
Lysis buffer	20 mM		500 mM	0	7.4
Washing buffer	20 mM		500 mM	15	7.4
Elution buffer	20 mM		500 mM	300	7.4

B.2 Existing racemase fermentation method, utilized during the racemase characterization

The AAR (45 kDa, pI = 7.03) was produced by overexpression in *E. coli* BL21 (DE3) in three fermentations. Each were performed in a 12 L LB-medium (B. Braun Biotech International GmbH), containing 100 mg/L ampicillin, 10 g/L glucose, 2.5 mM $CaCl_2$ (see FB-5 and FB-6 in Tab. B.2). The expression was induced by adding 0.1 M IPTG and decreasing the temperature from 30 °C to 22 °C at an optical density (OD) at 650 nm of OD_{650nm} = 1.5. At an OD_{650nm} = 2.5, the cells were harvested by centrifugation of the cell suspension (5000 g, 50 min, 4 °C, Avanti JXN-26, Beckman Coulter) and stored at -20 °C. In both batches used for this work, the overexpression produced 5.4 mg_{pellet}/L_{ferm} (Carneiro et al. (2020)).

B.3 New implemented fermentation method for the production of racemase in fed-batch mode

In the following the fermentation method with the highest achieved racemase yield is explained.

B.3.1 Preparations for the fermentation

Solutions

- LB media
  - 10 g/L Bacto Tryptone (~200€/kg)
  - 5 g/L Bacto Yeast Extract (~240€/kg)
  - 5 g/L Sodium chloride (~12€/kg)
  - 20 g/L Glucose (~15€/kg)
  - 100 mg/L ampicillin (~15,000€/kg)
- 1-2 drops/L Pluronic 8100 (1-2 drops/L)
- IPTG-Solution (Isopropyl-β-D-thiogalactopyranosid (IPTG), 100 mM or 23.83 g/L) (~12,000€/kg)
- Glucose-feed: 15 vol% or 150 g/L *D*-glucose in water
- 1 M NaOH for pH control (~19€/L)

Harvest-Buffer (see Table B.2)

- Standard solution 1 (S1): 20 mM $NaH_2PO_4 \cdot H_2O$ (~14€/kg), 500 mM NaCl
- Standard solution 1 (S2): 20 mM $Na_2HPO_4 \cdot 2\,H_2O$ (~22€/kg), 500 mM NaCl
- Harvest-buffer: mix S2 and S1 until pH 7.4 is reached (at 4 °C)

B.3.2 Cultivation of the pre-culture

- Distribute E. coli-cells on a LB-plate, grow mono cultures over night at 37 °C
- 1st Pre-culture: Inoculate a volume of 5 ml LB-media with one single mono culture in 15 mL flasks and shake it at 140 rpm and 37 °C for 8 hours.
- 2nd Pre-culture: Mix 5 mL of the first pre-culture with 5x120 mL LB-media in a 1 L shaking flask and incubate it at 130 rpm at 37 °C for 16 hours. (Afterwards the OD should be $OD_{650nm} > 8.5$; Reference = LB-Media)

- Concentrate 2nd pre-culture by centrifugation (10 min at 4°C, 5000 rpm, Themo Scientific Heraeus Biofuge stratos Centrifuge)

B.3.3 Production of *E. coli*-cell-culture

- pO_2-probe calibration:
- 0-point: with Zeroing Gel (last time was some time ago)
- 100-point: once stationary point was reached at 37 °C with 10 mL/min air
- Fill 12 L sterilized LB-media in the sterilized fermenter.
- Before inoculation: Heat media to T = 37 °C and stir it (at 250 rpm on 12 L scale)
- Fermentation (control pH with 5 N NaOH to pH = 7):
  1. Start: $OD_{650nm} \simeq 0.22$
  2. At $OD_{650nm} > 4$ (after ca. 4 h): decrease reactor temperature from 37 °C to 22 °C.
  3. At T ≃ 22 °C Induction with 1 mM IPTG, start glucose feed with 1.5 $g_{D\text{-}Glu}/h/L_{ferm}$ or 10 $mL_{D\text{-}Glu}/h/L_{ferm}$ of 15 vol% Glucose-solution (120 mL/h for our 12 L fermenter)

B.3.4 Cell harvest

- Harvest: 24 h after induction or once steady-state is reached ($OD_{650nm} \simeq 8$, $V_{ferm} = 15$ L):
- 1st centrifugation: (for 15 L: 400 mL for 50 min at 4 °C with 4,300 rpm, Avanti JXN-26 Beckman Coulter)
- Resuspend in Harvest-buffer
- 2nd centrifugation: 20 min at 4 °C at 5,000 gz
- Storage of the biomass at -20 °C

B.4 500-L-fermentation

Here, the report of the toller, the monitored process parameters (Fig. B.2) and SDS-pages are shown.

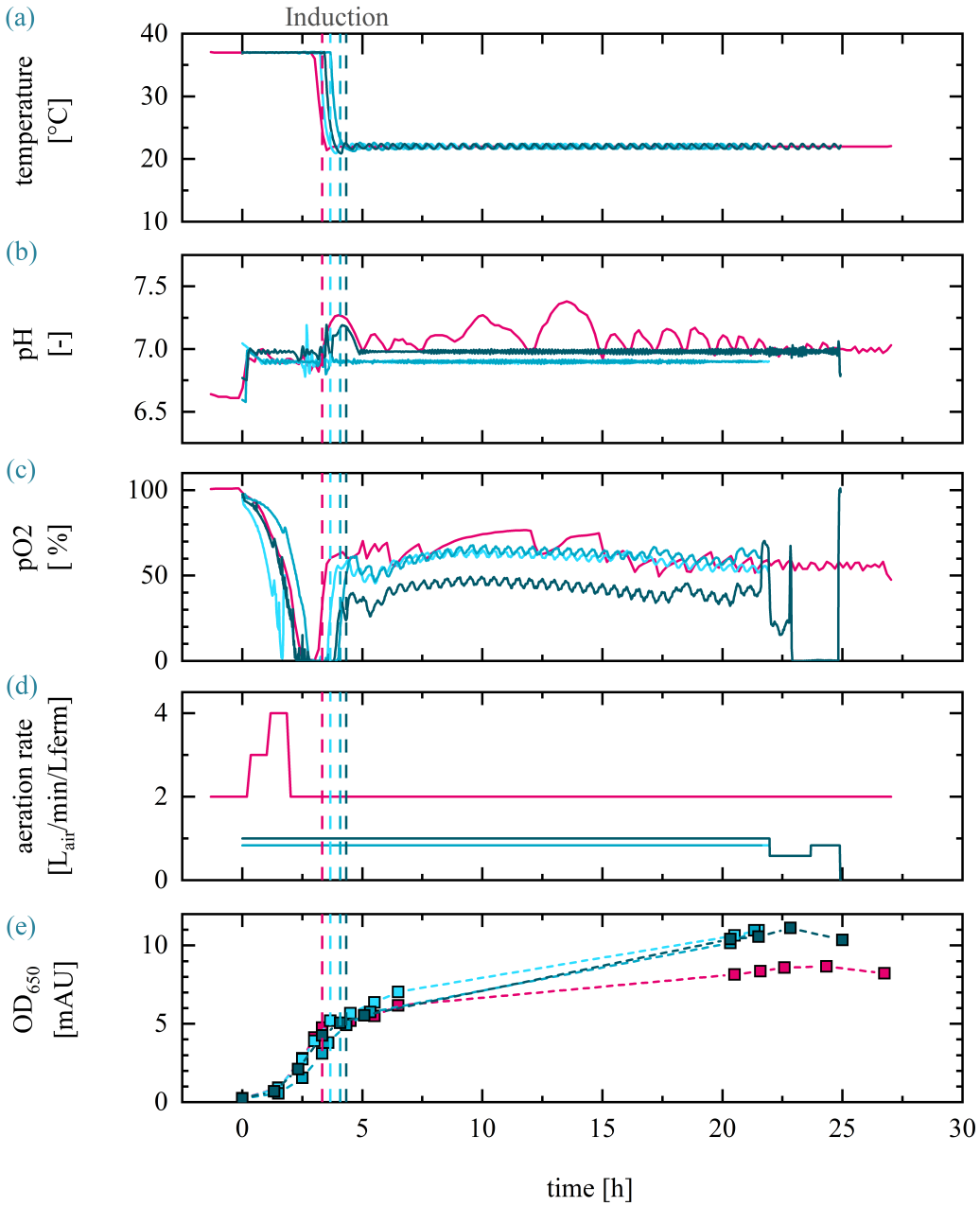

Fig. B.1: Monitored process parameters during the 0.5-L-fermentation FB-3 (–) and 12-L-fermentations FB-5, FB-6 and FB-7 (– , –, –), which were performed according to the new fermentation protocol.

B.4.1 Report from the toller about the 500 L fermentation

"We finished the AAR fermentation. Since we used a bioreactor instead of the second step in flasks, the cultivation time in this step shortened form 16 h to 8. After that, we led the main cultivation starting 500 L in the with induction and feeding according

to the protocol supplied. The batch phase finished earlier, we overstepped OD 4. The production phase took 15 hours only, because of OD started to stagnate and decrease slightly. According to the protocol, we finished it due to a reaching of a "steady state" and it did not look that OD 8 can be achieved (OD measurement is device dependent). Subsequently we centrifuged the broth yielded 6.49 kg of the very "dry" cell paste (CDW 46.2 %). For the buffer washing we used 20 L of the buffer (if use 10 L only, if would be hardly centrifugable by our pilot centrifuge). A lysis occurred during the washing, as expected, so we had a loss of the cell paste, yielded 5.87 kg within two-step centrifugation and the second supernatant sill contained 3.52 g/l of the dry non-centrifugable material.
We have 5.87 kg of the washed cells in our freezer.
Media changes: Sensient Produkte Amberferm 7020 and Tastone 900-A instead of Bacto Yeast and Bacto Typtone."

B.4.2 Qualitative comparison of the amount of racemase from the 12-L and the 500-L fermentation

The SDS-PAGE of FB-4 and the 500-L-fermentation, shown in Fig. B.3 confirm that in the latter one inclusion bodies were formed, which can be seen in the wet biomass, but are removed with the cell debris after the cell disruption and can therefore not be found in the crude extract or the eluting fractions.

B.5 Cell disruption and racemase purification using a packed or gravity-flow columns

In the following section a detailed protocol of the cell disruption method and two approaches for the racemase purification is given.

B.5.1 Cell disruption

For protein purification the cell pellets were resuspended in the 3.5 mL lysis buffer per gram pellet (20 mM sodium phosphate, 500 mM NaCl, pH 7.4 at 4 °C) with protease inhibitor (0.1 mL/g-wet pellet, EMD Millipore) and Deoxyribonuclease I (1 scoop/g-wet pellet, DNAase 1, Roche Diagnostics GmbH). The cells were disrupted by high-pressure homogenization (EmulsiFlex-C5, Avestin Inc.), followed

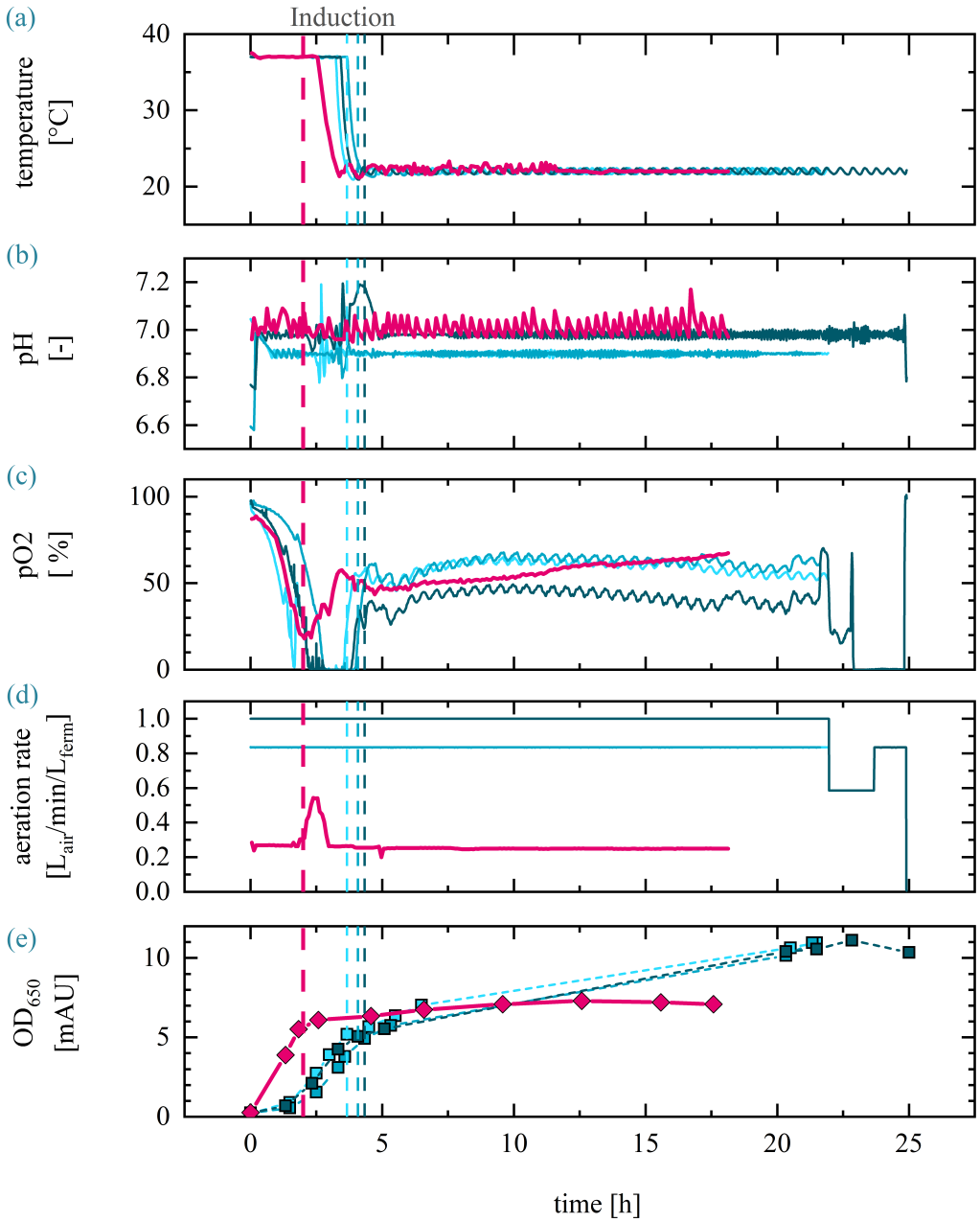

Fig. B.2: Monitored process parameters during the 500-L-fermentation (—) and the 12-L-fermentations FB-5, FB-6 and FB-7 (—, —, —), which were performed according to the new fermentation protocol.

by centrifugation (25 000 g, 4 °C, 25 min, Sartorius Sigma 3K30). Being a PLP-dependent enzyme, PLP was added to a final concentration of 100 μM (Eliot und Kirsch 2004).

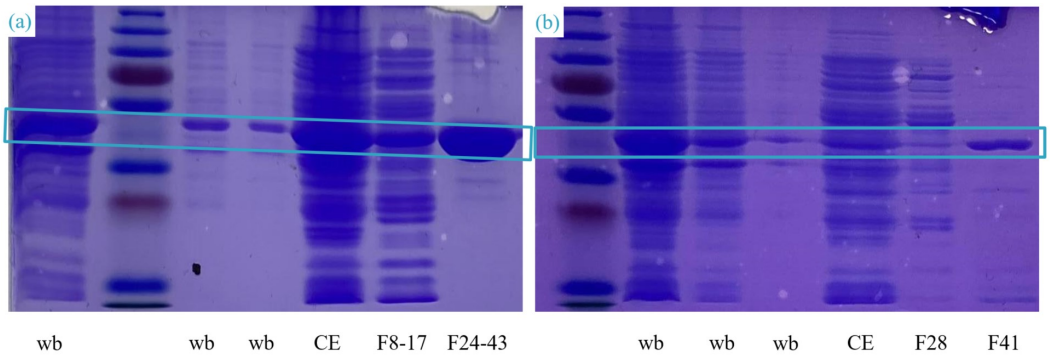

Fig. B.3: SDS-PAGE of different samples from (a) FB-4 and (b): wb = wet biomass, CE = crude extract (after cell disruption), F = fractions see Fig. 4.9; blue rectangle marks region of 45 kDa, which is the size of the AAR.

Tab. B.3: Purification protocol for the HisTrap FF curde cartridge with the solutions from Tab. B.2

Step	**Solution**	**imidazole** mM	**CV** -	**Flow rate** mL/min
Cleaning	distilled H_2O	0	3	5.0
Equilibration	lysis buffer	0	5	3.0
Loading	cell extract	0	5	3.0
Washing	washing buffer	15	15	1.5
Elution (1-3)	elution buffer	0-300	8	1.0

B.5.2 Racemase purification with a HisTrap FF crude column

The His-Tagged AAR was purified using a HisTrap FF crude 5 mL (GE Healthcare, 5 mL) in an Äkta system (Purifier 25, GE Healthcare, 4 °C). The amount of loaded crude extract (CE) varied. For the material from the batch fermentations B-1 and B-2 12.8 column volumes (CV) and 13.8 CV were purified, respectively. Non-specific bindings were washed with a washing buffer (lysis buffer with 15 mM imidazole) and the AAR eluted by stepwise increasing the elution buffer (lysis buffer with 300 mM imidazole). The detailed procedure and the variations tested in Sec. 4.4.3 are shown in Tab. B.3 and Tab. B.4. The purity of the relevant fractions was checked by SDS-PAGE. The purification of the first batch (B-1) resulted in 2.5 mg_{AAR}/g_{wb} and the two purifications of the second batch in 2.4 mg_{AAR}/g_{wb}.

Tab. B.4: Standard elution and modifications of the bed volumes (BV) and elution buffer gradient (100 % elution buffer = 300 mM imidazole) concentrations with the HisTrap FF curde cartridge

	Std.		Mod. 1		Mod. 2		Mod. 3	
	CV	%	CV	mM	CV	mM	CV	mM
Lysis	-	0	-	0	-	0	-	40
Washing	15	0	15	0	15	0	15	0
Elution 1	2	0-65	2	0-50	3	0-40	2	4-65
Elution 2	2	65	2	65	1.5	65	2	65
Elution 3	2	65-100	2	50-100	1.5	40-100	2	4-65

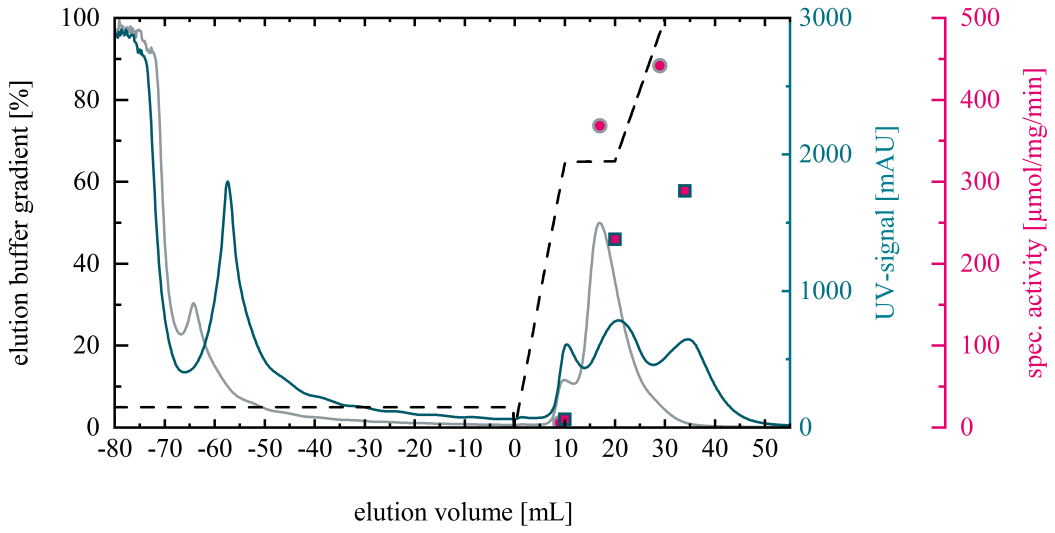

Fig. B.4: Effect of imidazole in the lysis buffer on the purity of the collected active AAR fraction: (a) 0 mM imidazole, 65-%-plateau -■-■; (b) 12 mM imidazole, 65-%-plateau -●-●. The dashed lines represent the elution buffer gradient from 0 to 300 mM imidazole, the solid line is the calibrated signal at A280 nm in g/L while the solid points present individual concentration measurements. The relative activity is plotted with pink centers.

Fig. B.5: Purification of AAR with different resins with the "slurry-method" on gravity-flow columns

B.5.3 Racemase purification with gravity-flow columns and different IMAC slurries

Below is the protocol with which the different resins were tested in the gravity-flow columns.

1. Transfer 1 mL resin into a gravity-flow column (slurries are 50:50 mixture of resin and ethanol).
2. Remove supernatant by opening the gravity-flow column at the bottom and let it drain (never let it run dry).
3. Equilibrate resin with 10 CV lysis buffer on ice (apply buffer from top and let it drain).
4. Transfer resin with defined amount of crude extract into a centrifuge tube and let it incubate for 1 h at 4 °C on a rotating shaker.
5. Centrifuge the mixture for 2 min at 4 °C.
6. collect the supernatant and transfer the rest back onto the GF column. If necessary, use lysis buffer to transfer remaining resin.

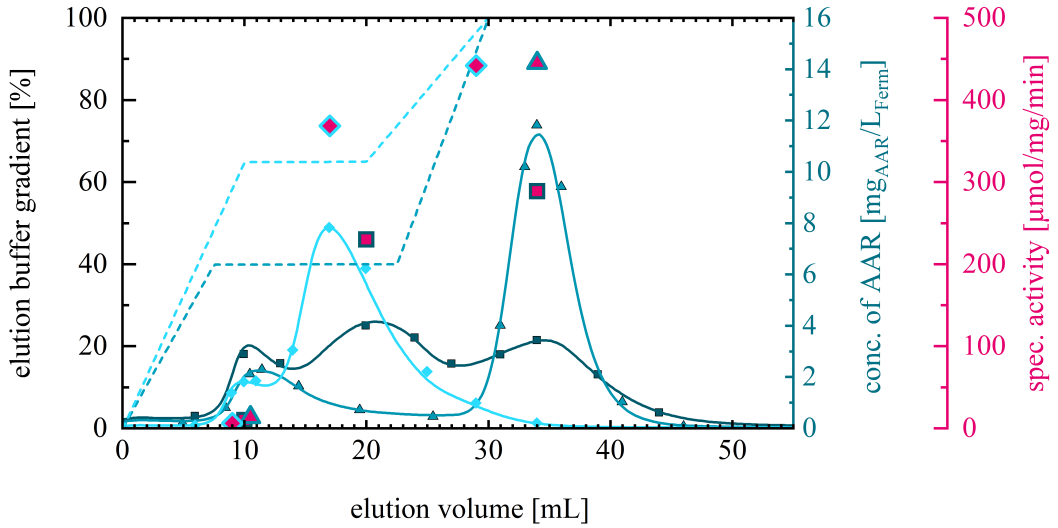

Fig. B.6: Effect of the elution buffer gradient on the separation of the active and inactive AAR fraction: (a) 65-%-plateau -■- ■, (b) 50-%-plateau -●-● and (c) 40-%-plateau -▲-▲. The dashed lines represent the imidazole concentration in % from 0 to 300 mM, the solid line is the calibrated signal at A280 nm in g/L while the solid points present individual concentration measurements. The relative activity is plotted with pink centers.

7. let the remaining supernatant drain from the column until almost all is gone (never let it run dry).
8. place a fresh tube below the column and wash the resin with 5 BV wash buffer (repeat it four times).
9. place a fresh tube below the column and start the elution process with:
   either a single step elution:

   - 5 CV elution buffer (500 mM imidazole; repeat 5x)

   or a gradient elution:

   - 2 CV elution buffer (150 mM imidazole; repeat 2x)
   - 2 CV elution buffer (300 mM imidazole; repeat 3x)
   - 2 CV elution buffer (500 mM imidazole; repeat 4x)

10. analyze all collected fractions regarding the AAR concentration and activity.

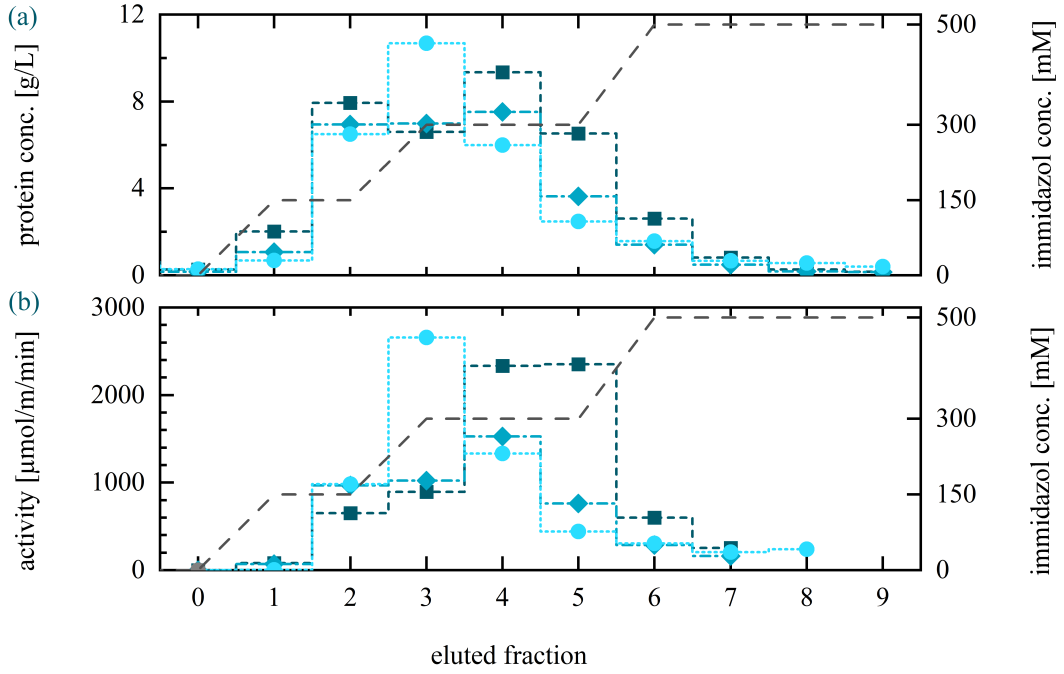

Fig. B.7: (a) Concentration and (b) activity of the fractions eluting from the gravity-flow column for the gradient elution method described in the protocol above for Ni-Sepharose 6 FF (···), HisPur Ni-NTA (-··-), and Pierce High Capacity Ni-IMAC (--).

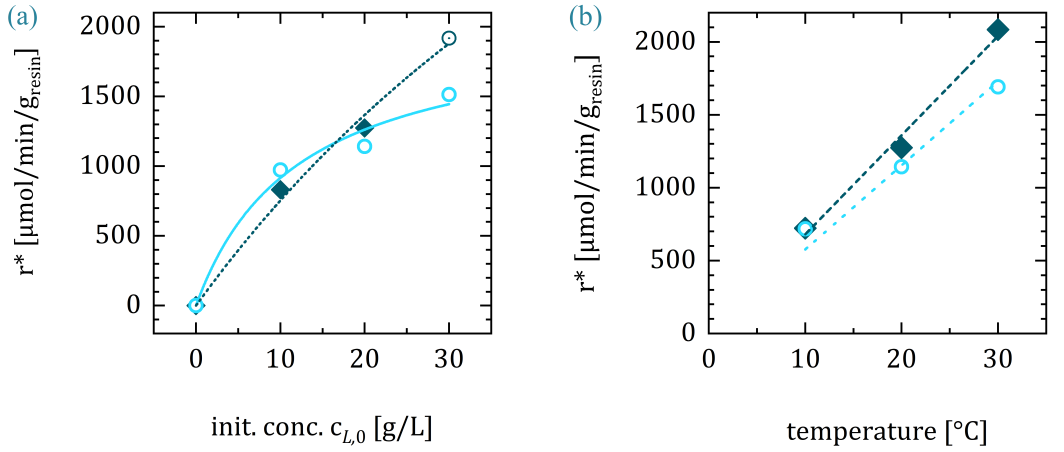

Fig. B.8: Comparison of the activity of immobilized AAR with (◆···) and without (○–) prior buffer exchange and concentration (a) initial reaction rates at different concentrations and 20 °C (b) initial reaction rates for 20 g/L at different temperatures.

B.6 Cost estimation for the production of immobilized racemase

In the following a brief cost estimation was made for the production of 14 g soluble AAR or 0.4 kg immobilized racemase, which is required for one experiment with the before mentioned enantioselective crystallization process. No acquisition costs or working hours were taken into account and the prices looked up in 2022.

The operation cost for the **fermentation** can be estimated from the fermentation results of the 12-L fermentations FB-5 and FB-6. The costs of all currently used media components are listed in the new protocol (see. Appendix B.3). They sum up to about 8.3 €/L_{media}, excluding the cost of the anti foam agent. When taken the pre-cultures (≈ 6 vol%) and the anti foam agent into account, about 9 €/L_{ferm} can be assumed in lab scale. For industrial applications the economy of scale would need to be taken into account and cheaper tryptone and yeast sources could be found. Furthermore, it can be extracted from Tab. 4.4, that 240-270 mg AAR can be obtained from each liter fermentation broth. Therefore, we can assume 35-40 €/g_{AAR} when using our standard media.

Main factor for the **cell disruption and purification** is the cost of the IMAC. The Ni-Sepharose 6 Fast Flow could be purchased from VWR 5300€/250 mL. Being able to purify 5x40 mg/mL with one charge would result in 106 €/g_{AAR} for the material. Adding the costs for the buffers (lysis, washing and elution buffer, PLP) this step could cost around 120€/g_{AAR}.

The **immobilization** on the carrier ECR8309F (Purolite), with a price of 1,350 €/$kg_{carrier}$ and an optimal loading capacity of 35 mg/g, results in 38.6 €/g_{AAR} and around 40 €/g_{AAR}, when adding the cost of the glutaraldehyde (≈ 3 €/L).

This results in **overall costs** of 200 €/g_{AAR} or 7 €/$g_{carrier}$. With these assumptions 14 g AAR immobilized on 0.4 kg carrier, would require material costs of 2.800 €. A summary of the costs items and a cost estimation for the production of 0.4 kg immobilized AAR is given in Tab. B.5.

Even the 40 €/kg_{AAR} for soluble racemase is far above the in 2012 published baseline production cost of enzymes of 10 €/kg_{enz} [168]. However, this number was most likely assumed for extracellular enzymes [169]. It still shows how much more improvement can be done in the optimization of all production steps, especially the expensive purification step and how the economy of scale is able to reduce production cost.

Tab. B.5: Material cost estimation for the production of immobilized AAR.

Step	Specific cost €/g_{AAR}	Required volume 0.4 kg immob. AAR	Material expenses for for 0.4 kg immob. AAR €
Fermentation	35-40	Broth: 52-58 L	500-560
Purification	120	IMAC: 70 mL	1500
Immobilization	40	carrier: 0.4 kg	560
Overall	≈ 200		2.800

B.7 Initial reaction rate determination

For the determination of the initial racemization rates the conversion rate was measured for different flow rates within the pressure limits of the HPLCs system. Depending on the solvent and temperature, the maximal flow rate was equivalent to a retention time of around 0.02 min. The length of each flow rate step was 6-30 min and was anti-proportional to the flow rate. The advanced laser polarimeter ensured that the reaction equilibrium was reached, before samples were taken. The samples were analysed with HPLC and the ratio of the peaks correlated directly to the ratio of the two enantiomers and thus the conversion rate (Fig. B.9). Next, a MM-curve was fitted through the obtained 5-7 data points and the data pair at a conversion rate of 20 % (x,y)= (τ(X=0.2),0.2) was determined for all tested concentrations. They were then converted into initial concentration rates with Eq. (3.2). It is worth mentioning, that in other work the conversion rate chosen for the initial reaction rate was sometimes only 5 %, which of course would have led to higher initial reaction rates. However, since the reaction rate could not be measured at lower conversion rates, the conversion rate of X = 0.1 was chosen in this work.

To ensure the constant activity of a packed bet the conversion rates were tested at a concentration of 10 g/L *L*-Met for each given solvent at 2.5 mL/min before and after each performed experiment. After two days of performance or once degeneration effects were measured, the AAR was discarded and fresh AAR was used. However, only the presence of 10 vol% alcohol and at a reaction temperature of 30 °C, measurable activity decrease occurred. In all other cases the conversion rates fluctuated stronger due to the slightly varying amount of packed resin (56 ± 2 mg) than due to deactivation. A higher reproducibility of the packed resin was not possible in this small scale due to the changing moisture content of the resin and its electrostatic charge.

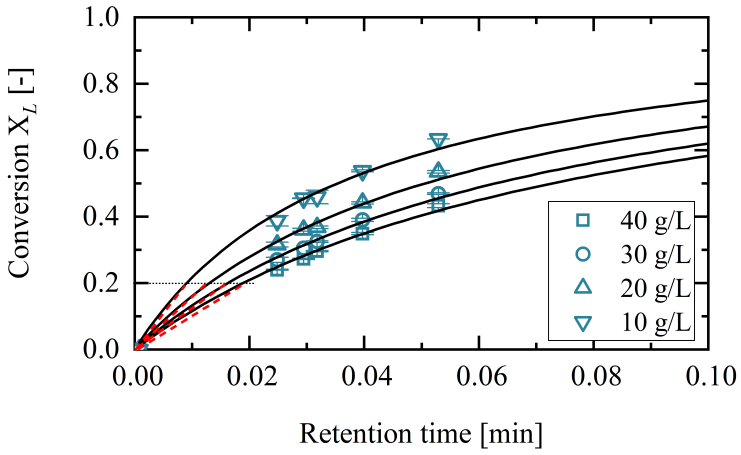

Fig. B.9: Conversion rates of the AAR for pure *L*-Met from Batch FB-1 for samples taken at different flow rates for 10 g/L (downwards pointing triangle), 20 g/L (upwards pointing triangle), 30 g/L (circle), 40 g/L (square) *L*-Met. The red dotted lines indicate the reaction slopes taken for the calculation of the initial reaction rate.

B.8 Temperature effects on kinetics of immobilized racemase

The temperature dependency of K_M and r_{max} in the range between 10-30 °C is shown in Fig. B.10. The dependencies were described with Eqs. (2.66)-(2.66) and a least-square parameter fitting resulted in the parameters of Tab. 4.3:

$$r_{\max}(T) = 2.72x10^{6}\mathrm{U/g_{carrier}} \cdot \exp\left(-\frac{16.6\mathrm{kJ/mol}}{R \cdot T}\right) \tag{B.1}$$

$$K_{\mathrm{M}}(T) = 150.6\mathrm{mM} + 3.7x10^{18}\mathrm{mM}\exp\left(-T/(7.5\mathrm{mM})\right) \tag{B.2}$$

B.9 Stability test of the immobilized amino acid racemase

To ensure the constant activity of a packed bed, the conversion rates were tested at a concentration of 10 g/L *L*-Met for each given solvent at 2.5 mL/min before and after each performed experiment. After two days of performance or once degeneration effects were measured, the AAR was discarded and fresh AAR was used. However, only the presence of 10 vol% alcohol and at a reaction temperature

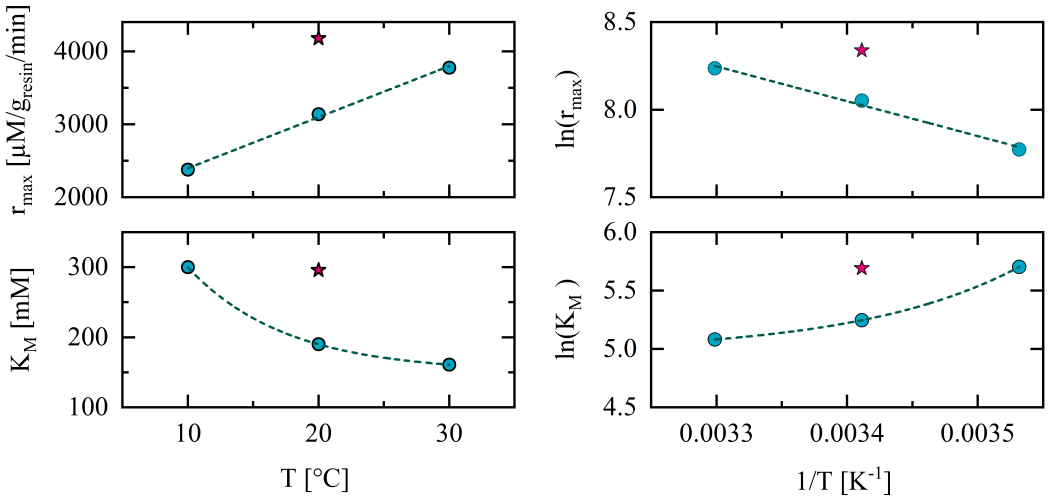

Fig. B.10: Temperature dependency of the two MM-parameters K_M and r_{max}.

of 30 °C, measurable activity decrease occurred. In all other cases the conversion rates fluctuated stronger due to the varying amount of packed resin (56 ± 2 mg) than due to deactivation. A higher reproducibility of the packed resin was not possible in this small scale due to the varying moisture content of the resin and its electrostatic charge.

Furthermore, the activity decline of the AAR in different solutions was tested at 30 °C for 20 h. The remaining activities in comparison to fresh resin are plotted in Fig. B.11(b). All activites were in a narrow range of 77 to 91 % remaining activity with a standard deviation of up to 16 % for 10 vol% MeOH. The highest remaining activities were 91-92 % for resin in pure water and at pH 8. Unexpected was that 30 % MeOH in the solvent seemed to result in less activity loss than 10% MeOH. However, the standard error for 10 % was relatively high, so additional experiments would be necessary to confirm this vage trend.

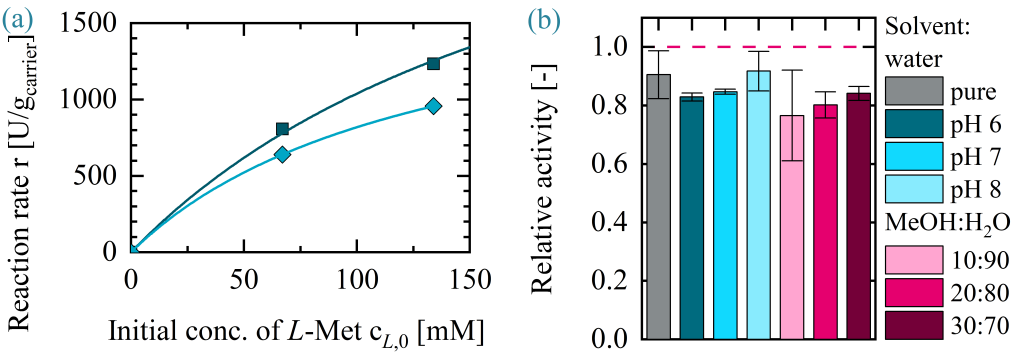

Fig. B.11: Activity decline of the AAR in an EFBR (a) for 6 month at 4 °C as a packed bed under moist conditions and (b) for 20 h at 30 °C in a vial with different solvents. The solutions with a specific pH were adjusted with 20 mM NaH_2PO_4/Na_2HPO_4.

C Chromatography related topics

This chapter is a collection of all chromatography related topics and contains unpublished work, which were only a subsidiary topics, as well as supplementary data and info of the performed experiments.

C.1 Method for determination of Langmuir adsorption isotherm parameters of ternary mixtures from breakthrough curves

The characteristic features of elution profiles is directly related to the corresponding adsorption isotherms (AI) and can be predicted by equilibrium theory. An exploitation of this relation is the determination of adsorption isotherm parameters from breakthrough curves. In this section, an approach for the extraction of the Langmuir adsorption isotherm parameters for binary and ternary mixtures is presented.

C.1.1 Binary mixtures

The retention time of a shock wave of component i is defined as

$$t_{R,\mathrm{shock},i} = \frac{L}{u_{i,c_i^*}} = t_0 \left(1 + F \frac{\Delta q_i}{\Delta c_i}\bigg|_{\bar{c}}\right) \tag{C.1}$$

$$= t_0 \left(1 + F \frac{q_{i,\mathrm{II}} - q_{i,\mathrm{I}}}{c_{i,\mathrm{II}} - c_{i,\mathrm{I}}}\bigg|_{\bar{c}}\right) \tag{C.2}$$

and can be rearranged with a normalized retention time $\hat{k}_n$:

$$\hat{k}_n = \frac{t_{R,n} - t_0}{t_0 F} = \frac{\Delta q_{i,n}}{\Delta c_{i,n}}\bigg|_{\bar{c}} = \frac{q_{i,n+1} - q_{i,n}}{c_{i,n+1} - c_{i,n}}\bigg|_{\bar{c}} \tag{C.3}$$

where $t_{R,n}$ is the n-th breakthrough with $n = \mathrm{I}, N_c + \mathrm{I}$ from state n to state $n + \mathrm{I}$.

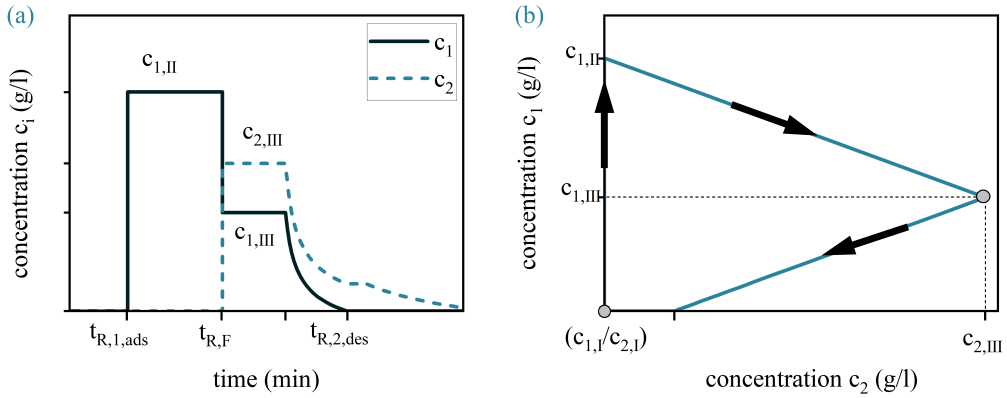

Fig. C.1: Prediction of adsorption isotherms from breakthrough curve characteristics.

The breakthrough behavior of a binary system for an unloaded column ($q_{i,\mathrm{I}} = c_{i,\mathrm{I}}$=0 with i = 1,2) is shown in Fig. C.1. Here, the first component breaks through at the time $t_{\mathrm{R},1}$:

$$t_{\mathrm{R},1} = t_0\left(1 + F\frac{q_{1,\mathrm{II}}(\bar{c}_{\mathrm{II}}) - 0}{c_{1,\mathrm{II}} - 0}\right) = t_0(1 + F\frac{q_{s,1}H_1}{q_{s,1} + H_1 c_{1,\mathrm{II}}}) \tag{C.4}$$

With Eq. C.3 it can be normalized to

$$\hat{k}_1 = \frac{t_{\mathrm{R},1} - t_0}{t_0 F} = \frac{q_{1,\mathrm{II}}(\bar{c}_{\mathrm{II}}) - q_{1,\mathrm{I}}(\bar{c}_{\mathrm{I}})}{c_{1,\mathrm{II}} - c_{1,\mathrm{I}}} = \frac{q_{s,1}H_1}{q_{s,1} + H_1 c_{1,\mathrm{II}}} \tag{C.5}$$

Next, due to the before mentioned coherence of propagating fronts, the second component breaks through with the feed concentration $c_{2,\mathrm{III}}$ and in a simultaneous shock, the first component drops from the plateau concentration $c_{1,\mathrm{II}}$ to the feed concentration $c_{1,\mathrm{III}}$ at the retention time $t_{R,2}$:

$$\hat{k}_2 = \frac{t_{R,2} - t_0}{t_0 F} = \frac{q_{1,\mathrm{III}}(\bar{c}_{\mathrm{III}}) - q_{1,\mathrm{II}}(\bar{c}_{\mathrm{II}})}{c_{1,\mathrm{III}} - c_{1,\mathrm{II}}} = \frac{\frac{q_{s,1}H_1 c_{1,\mathrm{III}}}{q_{s,1}+H_1 c_{1,\mathrm{III}}+H_2/q_{s,2}q_{s,1}c_{2,\mathrm{III}}} - \frac{q_s H_1 c_{1,\mathrm{II}}}{q_s+H_1 c_{1,\mathrm{II}}}}{c_{1,\mathrm{III}} - c_{1,\mathrm{II}}} \tag{C.6}$$

$$\hat{k}_2 = \frac{t_{R,2} - t_0}{t_0 F} = \frac{q_{2,\mathrm{III}}(\bar{c}_{\mathrm{III}}) - 0}{c_{2,\mathrm{III}} - 0} = \frac{q_{s,2}H_2}{q_{s,2} + H_1 c_{1,\mathrm{III}}/q_{s,1}q_{s,2} + H_2 c_{2,\mathrm{III}}} \tag{C.7}$$

This set of equations (Eqs. (C.5)-(C.7)) can now be used for the characterization of a binary mixture. In case the saturation capacity of both components is assumed to be similar

$$q_s = q_{s,i} = q_{s,1} = q_{s,2} \tag{C.8}$$

the three Langmuir AI parameters q_s, H_1 and H_2 need to be determined. One solution for this case has already been described by Seidel-Morgenstern (2020). In this paper a slightly different solution is provided. The Langmuir AI parameters

requires the same amount of independent equations. This is given by the shock fronts of Eqs. (C.5)-(C.7). In order to obtain the AI parameters from the information of these three shocks, first Eq. (C.5) is rearranged with Eq. (2.2) to define H_1 as a function of q_s, the plateau concentration $c_{1,\mathrm{II}}$ and the first breakthrough time coefficient $\hat{k}_1$:

$$H_1 = \frac{\hat{k}_1 q_s}{q_s - c_{1,\mathrm{II}}\hat{k}_1} \tag{C.9}$$

With Eqs. (C.8)-(C.9), Eq. (C.7) can analogously be rearranged to define H_2 as a function of q_s, the plateau concentration $c_{1,\mathrm{II}}$ and the first breakthrough time coefficient $\hat{k}_2$:

$$H_2 = \frac{\hat{k}_2(q_s(q_s - c_{1,\mathrm{II}}\hat{k}_1 + c_{1,\mathrm{III}}\hat{k}_1))}{(q_s - c_{2,\mathrm{III}}\hat{k}_2)(q_s - c_{1,\mathrm{II}}\hat{k}_1)} \tag{C.10}$$

Finally, Eq. (C.6) is rearranged with Eq. (C.9) and Eq. (C.10) for q_s.

$$q_s = \frac{\hat{k}_1((c_{1,\mathrm{III}})^2\hat{k}_2 - (c_{1,\mathrm{II}})^2\hat{k}_1 + (c_{1,\mathrm{II}})^2\hat{k}_2 + c_{1,\mathrm{III}}c_{2,\mathrm{III}}\hat{k}_2 + c_{1,\mathrm{III}}c_{1,\mathrm{II}}\hat{k}_1 - 2c_{1,\mathrm{III}}c_{1,\mathrm{II}}\hat{k}_2)}{(c_{1,\mathrm{III}} - c_{1,\mathrm{II}})(\hat{k}_1 - \hat{k}_2)} \tag{C.11}$$

The equation can be simplified with α and β:

$$\alpha = (c_{1,\mathrm{III}} - c_{1,\mathrm{II}})(\hat{k}_1 - \hat{k}_2) \tag{C.12}$$

$$\beta = (c_{1,\mathrm{III}} - c_{1,\mathrm{II}} + c_{2,\mathrm{III}}) \tag{C.13}$$

to

$$q_s = \frac{\hat{k}_1(\beta c_{1,\mathrm{III}}\hat{k}_2 + \alpha c_{1,\mathrm{II}})}{\alpha} \tag{C.14}$$

Based on the Eqs. (C.12)-(C.14), the Henry coefficients from Eq. (C.9) and Eq. (C.10) can be determined with:

$$H_1 = \frac{\hat{k}_1(\beta c_{1,\mathrm{III}}\hat{k}_2 + \alpha c_{1,\mathrm{II}})}{\beta c_{1,\mathrm{III}}\hat{k}_2} \tag{C.15}$$

$$H_2 = \frac{\hat{k}_1(\beta c_{1,\mathrm{III}}\hat{k}_2 + \alpha c_{1,\mathrm{II}})}{\beta(\hat{k}_2(c_{1,\mathrm{III}} - c_{1,\mathrm{II}}) + c_{1,\mathrm{II}}\hat{k}_1)} \tag{C.16}$$

In another scenario the two components might have different saturation capacities $q_{s,1} \neq q_{s,2}$. Thus, in total four AI parameter needs to be determined, even though only three independent breakthrough characteristics can be measured with one breakthrough time. The system is underdetermined.

To compensate this, additionally to experiment A, another breakthrough experiment B must be performed. It provides three additional shock fronts with characteristic information. From the six available shock fronts, only four need to be used for the AI parameter estimation. In the previous example Eq. (C.9) was derived from the first break through front (Eq. (C.4)). For individual $q_{s,i}$ and $q_{s,i}$>0 the Eq. (C.9) can be rewritten for the two experiments A and B as

$$H_1 = \frac{\hat{k}_{1,A} q_{s,1}}{q_{s,1} - c_{1,II,A}\hat{k}_{1,A}} = \frac{\hat{k}_{1,B} q_{s,1}}{q_{s,1} - c_{1,\mathrm{II},B}\hat{k}_{1,B}} \tag{C.17}$$

And solved for $q_{s,1}$:

$$q_{s,1} = \frac{\hat{k}_{1,A}\hat{k}_{1,B}(c_{1,\mathrm{II},B} - c_{1,\mathrm{II},A})}{\hat{k}_{1,A} - \hat{k}_{1,B}} \tag{C.18}$$

After estimating $q_{s,1}$ from Eq. (C.18) and then H_1 from Eq. (C.17), H_2 can be defined from Eq. (C.7) as:

$$H_2 = \frac{\hat{k}_{2,A} q_{s,2}(q_{s,1} + H_1 c_{1,\mathrm{III},A})}{q_{s,1}(q_{s,2} - c_{2,\mathrm{III},A}\hat{k}_{2,A})} = \frac{\hat{k}_{2,B} q_{s,2}(q_{s,1} + H_1 c_{1,\mathrm{III},B})}{q_{s,1}(q_{s,2} - c_(2,III,B)\hat{k}_{2,B})} \tag{C.19}$$

Finally, Eq. (C.19) can then be solved, using the characteristics from two shocks A and B, for $q_{s,2}$:

$$q_{s,2} = -\frac{\hat{k}_{2,A}\hat{k}_{2,B}(q_{s,1}(c_{2,\mathrm{III},A} - c_(2,III,B)) - H_1(c_{1,\mathrm{III},A}c_{2,III,B} - c_{1,\mathrm{III},B}c_{2,\mathrm{III},A}))}{q_{s,1}(\hat{k}_{2,A} - \hat{k}_{2,B}) + H_1(c_{1,\mathrm{III},A}\hat{k}_{2,A} - c_{1,\mathrm{III},B}\hat{k}_{2,B})} \tag{C.20}$$

Alternatively, in case the Henry coefficients have already been determined from other experiments, the same approach as for the single component AI (Eq. (C.5)) can be chosen: the Henry coefficients can be determined from pulse injections and then be used in Eq. (C.17) and (C.19) to estimate the saturation capacities. This allows an estimation of all four AI parameters from e.g. one pulse injection and one breakthrough experiment.

C.1.2 Ternary mixtures

The first three shocks can be described by Eqs. (C.5)-(C.7), even though now state III is not the feed composition, but the plateau concentrations of component 1 and 2 before the breakthrough of the third component. The mass balances (Eqs. (C.21)-

(C.23)) describe the shocks around the third breakthrough time, $t_{R,3}$, before reaching the feed concentrations (c_{IV}):

$$t_{R,3} = t_0\left(1 + F\frac{q_(1,F)(\bar{c}_{\mathrm{IV}}) - q_{1,\mathrm{III}}(\bar{c}_{\mathrm{III}})}{c_{1,\mathrm{IV}} - c_{1,\mathrm{III}}}\right) \tag{C.21}$$

$$t_{R,3} = t_0\left(1 + F\frac{q_{2,IV}(\bar{c}_{\mathrm{IV}}) - q_{2,\mathrm{III}}(\bar{c}_{\mathrm{III}})}{c_{2,\mathrm{IV}} - c_{2,\mathrm{III}}}\right) \tag{C.22}$$

$$t_{R,3} = t_0\left(1 + F\frac{q_{3,IV}(\bar{c}_{\mathrm{IV}}) - q_{3,\mathrm{III}}(\bar{c}_{\mathrm{III}})}{c_{3,\mathrm{IV}} - c_{3,\mathrm{III}}}\right) = t_0\left(1 + F\frac{q_{3,IV}(\bar{c}_{\mathrm{IV}}) - 0}{c_{3,\mathrm{IV}} - 0}\right) \tag{C.23}$$

With these six shocks theoretically either the four parameters H_1,H_2,H_3 and q_s from Eq. (2.2) with Eq. (C.8) or the six parameters H_1,H_2,H_3 and $q_{s,1}$, $q_{s,2}$, $q_{s,3}$ from Eq. (2.5) with individual saturation capacities can be estimated from a single experiment. However, the solution for individual saturation capacities results in large definitions for each parameter. Thus, in this paper we only present the first case with identical saturation capacities. Due to the resemblance of the first three shocks with the binary behaviour, the parameters H_1,H_2, and q_s can be estimated with Eqs. (C.14)-(C.16). Now, three more shocks (Eqs. (C.21)-(C.23)) are available for the estimation of H_3. Since Eq. (C.23) has the easiest shape, and avoids intermediate plateau concentrations, it is rearranged with Eqs.(C.14)-(C.16) to define H_3 with the coefficients $\hat{k}_i$, α and β:

$$H_3 = \frac{\hat{k}_1(\beta c_{1,\mathrm{III}}\hat{k}_2 + \alpha c_{1,\mathrm{II}})\hat{k}_3\left(1 + \frac{\alpha c_{1,\mathrm{IV}}}{K_2 c_{1,\mathrm{III}}\hat{k}_2} + \frac{\alpha c_{2,\mathrm{IV}}}{\beta(\hat{k}_2(c_{1,\mathrm{III}} - c_{1,\mathrm{II}}) + c_{1,\mathrm{II}}\hat{k}_1)}\right)}{\hat{k}_1(\beta c_{1,\mathrm{III}}\hat{k}_2 + K_1 c_{1,\mathrm{II}}) - c_{3,\mathrm{IV}}\hat{k}_3\alpha} \tag{C.24}$$

Eqs. (C.14)-(C.16), and Eq. (C.24) can now be exploited for a rapid AI estimation.

C.2 Method of lines for the simulation of a multi component simulated moving bed chromatography process

The mass balance equation for one component with the ideal model:

$$\frac{\partial c_i}{\partial t} + F \cdot \frac{\partial q_i(c_{1\ldots N})}{\partial t} + \frac{\partial(c_i \cdot u_{\mathrm{int}})}{\partial z} - F \cdot \frac{\partial(q_i \cdot u_s)}{\partial z} = 0 \tag{C.25}$$

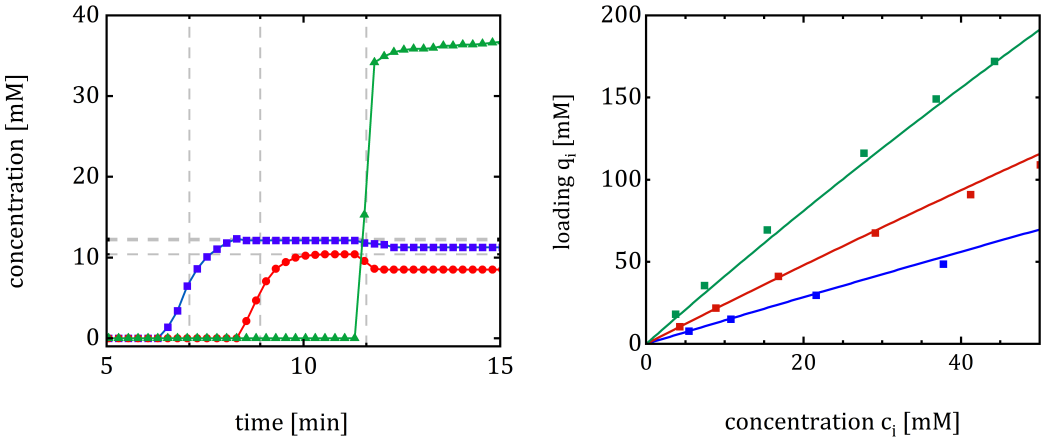

Fig. C.2: Prediction of adsorption isotherms from breakthrough curve characteristics.

For a mixture with N_c components the system of equations is defined with $q : U \subset R^{N_c} \rightarrow R^{N_c}$ where $q := (q_1, \ldots, q_{N_c})$ and $c := (c_1, \ldots, c_{N_c})$. The Jacobian matrix has the following structure:

$$J_q = Dq := \left(\frac{\partial q_i(c_{1\ldots N_c})}{\partial c} \right)_{i=1,\ldots,N_c;\, j=1,\ldots,N_c} = \begin{pmatrix} \frac{\partial q_1}{\partial c_1} & \cdots & \frac{\partial q_1}{\partial c_{N_c}} \\ \vdots & \ddots & \vdots \\ \frac{\partial q_{N_c}}{\partial c_1} & \cdots & \frac{\partial q_{N_c}}{\partial c_{N_c}} \end{pmatrix} \tag{C.26}$$

Vector set:

$$\bar{c} = \begin{pmatrix} c_1 \\ \vdots \\ c_{N_c} \end{pmatrix}; \quad \bar{q} = \begin{pmatrix} q_1 \\ \vdots \\ q_{N_c} \end{pmatrix} \tag{C.27}$$

In case of a binary mixture $N_c = 2$ a 2x2-Jacobian matrix is created. Furthermore, the phase ratio, F, is introduced and neglection of the dispersion term, which will later be replaced by numerical diffusion.

$$F = \frac{1 - \varepsilon_t}{\varepsilon_t} \tag{C.28}$$

$$\frac{\partial \bar{c}}{\partial t} + F \cdot J_q \frac{\partial \bar{c}}{\partial t} + \frac{\partial (\bar{c} \cdot u_{\text{int}})}{\partial z} - F \cdot \frac{\partial (\bar{q} \cdot u_s)}{\partial z} = 0 \tag{C.29}$$

1. Reformation for explicit $\frac{\partial}{\partial t}$ operator.

$$\frac{\partial \bar{c}}{\partial t} + F \cdot J_q \frac{\partial \bar{c}}{\partial t} + \frac{\partial (\bar{c} \cdot u_{\text{int}})}{\partial z} - F \cdot u_s \cdot \frac{\partial \bar{q}}{\partial z} = 0 \tag{C.30}$$

$$\left(\mathbb{I} + F \cdot J_q\right) \frac{\partial \bar{c}}{\partial t} + \frac{\partial (\bar{c} \cdot u_c)}{\partial z} - F \cdot u_s \cdot \frac{\partial \bar{q}}{\partial z} = 0 \tag{C.31}$$

$$\frac{\partial \bar{c}}{\partial t} = \left(\mathbb{I} + F \cdot J_q\right)^{-1} \left[-\frac{\partial (\bar{c} \cdot u_{\text{int}})}{\partial z} + F \cdot u_s \cdot \frac{\partial \bar{q}}{\partial z} \right] \tag{C.32}$$

2. If $q = q(c)$ is explicit, the Jacobian J_q can be calculated directly. Otherwise it can be determined from implicit differentiation:

$$J_q = -\left(\frac{\partial f}{\partial q_i}\right)^{-1} \cdot \frac{\partial f}{\partial c_i} \tag{C.33}$$

3. A discretization in time is applied (e.g. central or backward differences) to obtain a system of ODEs.

$$\frac{\partial \bar{c}}{\partial t} = \left(\mathbb{I} + F \cdot J_q\right)^{-1} \left[-u_{\text{int}} \cdot \frac{\partial \bar{c}}{\partial z} - \bar{c} \cdot \frac{\partial u_{\text{int}}}{\partial z} + F \cdot u_s \cdot \frac{\partial \bar{q}}{\partial z} \right] \tag{C.34}$$

$$\frac{\partial \bar{c}}{\partial t} = \left(\mathbb{I} + F \cdot J_q\right)^{-1} \left[-u_{\text{int}} \cdot \frac{\Delta \bar{c}}{\Delta z} - \bar{c}_{ext} \cdot \frac{\Delta u_{ext}}{\Delta z} + F \cdot u_s \cdot \frac{\Delta \bar{q}}{\Delta z} \right] \tag{C.35}$$

The system can be solved via any ODE solver.

4. The convection term in the brackets [*] can be further simplified with the following assumptions:

$$u_{\text{int}} = \frac{\dot{V}_z \cdot L_c}{V_c \cdot \varepsilon_t} \tag{C.36}$$

$$u_s = \frac{\dot{V}_s \cdot L_c}{V_c \cdot (1 - \varepsilon_t)} \tag{C.37}$$

$$\Delta z = \frac{L_c}{N_{\text{P}}} \tag{C.38}$$

$$V_{cell} = \frac{V_c}{N_{\text{P}}} \tag{C.39}$$

Resulting in:

$$u_{\text{int}} \cdot \frac{\Delta c}{\Delta z} = \frac{\dot{V}_z \cdot L_c}{V_c \cdot \varepsilon_t} \cdot \frac{N_p}{L_c} \cdot \Delta c = \frac{\dot{V}_z}{V_{cell} \cdot \varepsilon_t} \cdot \Delta c \tag{C.40}$$

$$c_{ext} \cdot \frac{\Delta u_{ext}}{\Delta z} = c_{ext} \cdot \frac{L_c}{V_c \cdot \varepsilon_t} \cdot \frac{N_p}{L_c} \cdot \Delta \dot{V}_{ext} \overset{?}{=} \frac{\dot{V}_{ext}}{V_{cell} \cdot \varepsilon_t} \cdot c_{ext} \tag{C.41}$$

$$F \cdot u_s \cdot \frac{\Delta q}{\Delta z} = \frac{\dot{V}_s \cdot L_c}{V_c \cdot (1 - \varepsilon_t)} \cdot \frac{1 - \varepsilon_t}{\varepsilon_t} \cdot \frac{N_p}{L_c} \cdot \Delta q = \frac{\dot{V}_s}{V_{cell} \cdot \varepsilon_t} \cdot \Delta q \tag{C.42}$$

with

$$\dot{V}_z = \left\{ \dot{V}_I, \dot{V}_{II}, \dot{V}_{III}, \dot{V}_{IV} \right\} \tag{C.43}$$

$$\dot{V}_{ext} = \{-\dot{V}_F,\ \dot{V}_R,\ -\dot{V}_D,\ \dot{V}_E\} \tag{C.44}$$

$$\bar{c}_{ext} = \{\bar{c}_F,\ \bar{c}_R,\ \bar{c}_D,\ \bar{c}_E\} \tag{C.45}$$

5. The equations (C.40), (C.41) and (C.42) are integrated into equation (C.35):

$$\frac{\partial \bar{c}}{\partial t} = \left(\mathbb{I} + F \cdot J_q\right)^{-1} \left[-\frac{\dot{V}_z}{V_{cell} \cdot \varepsilon_t} \cdot \Delta\bar{c} - \frac{\dot{V}_{ext}}{V_{cell} \cdot \varepsilon_t} \cdot \bar{c}_{ext} + \frac{\dot{V}_s}{V_{cell} \cdot \varepsilon_t} \cdot \Delta\bar{q} \right] \tag{C.46}$$

Final form:

$$\frac{\partial \bar{c}}{\partial t} = \frac{1}{V_{cell} \cdot \varepsilon_t} \cdot \left(\mathbb{I} + F \cdot J_q\right)^{-1} \left[-\dot{V}_z \cdot (\bar{c}_n - \bar{c}_{n-1}) - \dot{V}_{ext} \cdot \bar{c}_{ext} + \dot{V}_s \cdot (\bar{q}_{n+1} - \bar{q}_n) \right] \tag{C.47}$$

C.3 Optimal operation of simulated moving bed units for chromatographic separations with Langmuir adsorption isotherms

The following method for determination of optimal operation of simulated moving bed units for chromatographic separations with Langmuir adsorption isotherms has been proposed by Mazzotti et al. (1997):

- Straight $\overline{wh}$:

$$\left[H_B - H_A(1 + b_B c_B^{\mathrm{F}})\right] m_{\mathrm{II}} + b_B c_B^{\mathrm{F}} H_A m_{\mathrm{III}} = H_A(H_B - H_A) \tag{C.48}$$

- Straight $\overline{wf}$:

$$\left[H_B - \omega_G(1 + b_B c_B^{\mathrm{F}})\right] m_{\mathrm{II}} + b_B c_B^{\mathrm{F}} \omega_G m_{\mathrm{III}} = \omega_G(H_B - \omega_G) \tag{C.49}$$

- Curve rg:

$$m_{\mathrm{III}} = m_{\mathrm{II}} + \frac{\left(\sqrt{H_B} - \sqrt{m_{\mathrm{II}}}\right)^2}{b_B c_B^{\mathrm{F}}} \tag{C.50}$$

- Intersections g, h, f:

$$(H_B; H_B), \qquad (H_A; H_A), \qquad (\omega_G; \omega_G) \tag{C.51}$$

- Point r:

$$\left(\frac{\omega_G^2}{H_B}; \frac{\omega_G\left[\omega_F(H_B-\omega_G)(H_B-H_A)+H_A\omega_G(H_B-\omega_F)\right]}{H_B a_A(H_B-\omega_F)} \right) \tag{C.52}$$

- Point w (optimal operating point):

$$\left(\frac{H_A\omega_G}{H_B}; \frac{\omega_G\left[\omega_F(H_B-H_A)+H_A(H_A-\omega_F)\right]}{H_A(H_B-\omega_F)} \right) \tag{C.53}$$

The auxiliary variables ω_G and ω_F used above, are dependent from the feed concentration and fulfill the following quadratic equation where $\omega_G > \omega_F > 0$ applies:

$$0 = (1 + b_A c_A^{\mathrm{F}} + b_B c_B^{\mathrm{F}})\omega^2 - \left[H_A(1 + b_B c_B^{\mathrm{F}}) + H_B(1 + b_A c_A^{\mathrm{F}})\right]\omega + H_A H_B. \tag{C.54}$$

Furthermore, optimal operating points for zone I and IV are defined:

$$m_{\mathrm{I,opt}} = m_{\mathrm{I,min}} = H_A \tag{C.55}$$

and

$$m_{\mathrm{IV,opt}} = m_{\mathrm{IV,max}} = 0.5\left((H_A + m_{\mathrm{III}} + b_A c_A^{\mathrm{F}}(m_{\mathrm{III}} - m_{\mathrm{II}}) - \sqrt{\left(H_A + m_{\mathrm{III}} + b_A c_A^{\mathrm{F}}(m_{\mathrm{III}} - m_{\mathrm{II}})\right)^2 - 4H_A m_{\mathrm{III}}}\right) \tag{C.56}$$

C.4 Additional data for the experimental characterization of the adsorption behaviour and simulation results from modeling true and simulated moving bed chromatographic separation

In this section various elution profiles, measured retention times and resulting derivatives dqdc, used for the characterization of the adsorption behaviour are summarized.

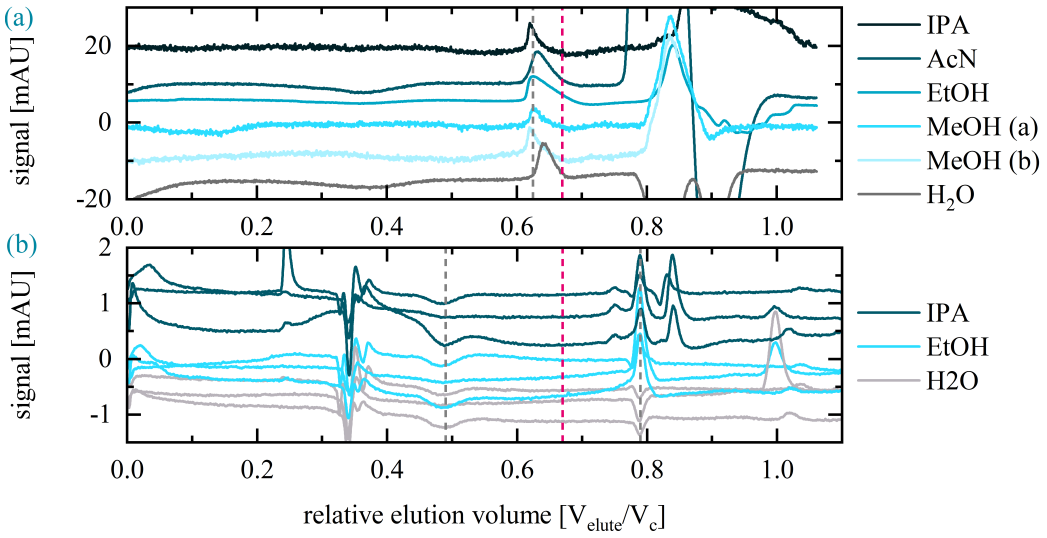

Fig. C.3: Elution profiles from small injections of different eluents plotted over a normalized elution time or volume ($V_{\mathrm{elute}}/V_c = (t - t_{\mathrm{plant}}) \cdot \dot{V}/V_c$) for (a) PC-I and (b) PC-II. The pink line marks the porosity of 0.7, assumed by the manufacturer.

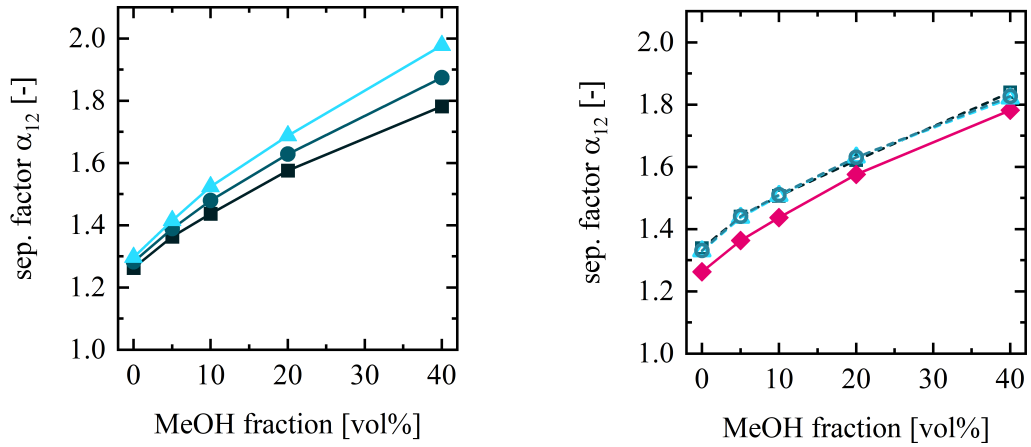

Fig. C.4: Separation factor of *D*- and *L*-Met on a Chirobiotic T column (250x4.6 mm, 5 μm), determined from small pulse injections of *DL*-Met with an aqueous eluent with 0-40 vol% MeOH. (a) at 10 °C (▲), 15 °C (●) and 20 °C (■) and (b) at 20 °C in pure water (◆) and in buffer 20 mM NaH_2PO_4/Na_2HPO_4 with pH 6.0 (▲), 6.5 (●) and 7.0 (■). The separation factor was determined from the Henry coefficients of *D*- and *L*-Met, using the column porosity of $\varepsilon_t = 0.6$ and a system dead volume of $V_{\mathrm{plant}} = 0.075$ min.

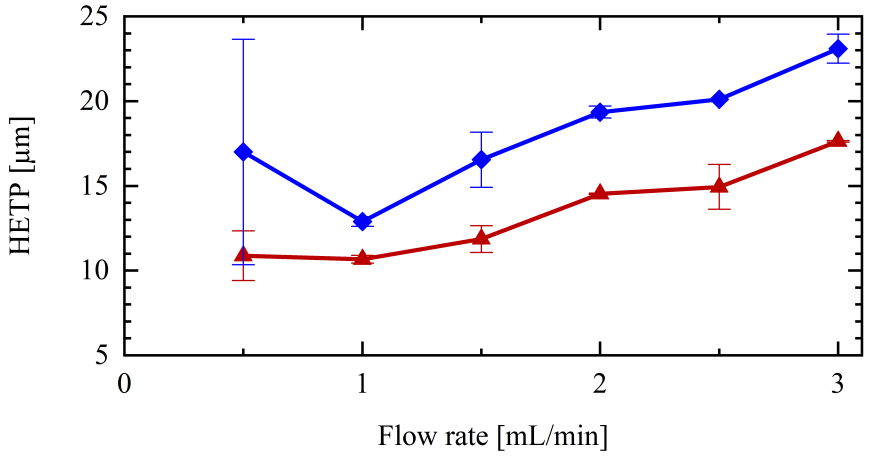

Fig. C.5: HETP over the flow rate of *D*- (◆) and *L*-Met (▲) in the Chirobiotic T column PC-II (150x10 mm, 5 μm).

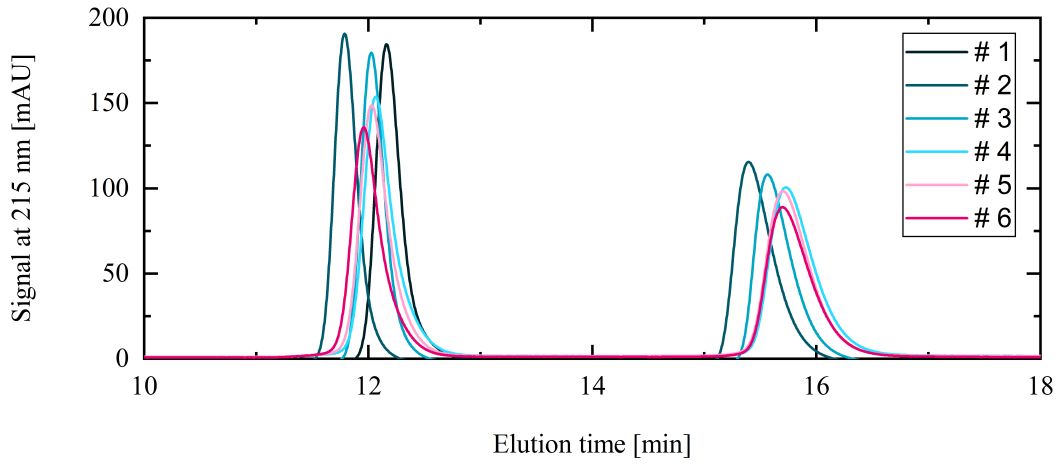

Fig. C.6: Comparison of the elution profiles of all six preparative columns in M2080 used for the characterization experiments. The most alike columns #3-6 were used in the SMB unit.

Tab. C.1: Experimental data of pulse injections for a solvent screening for CS-II. All experiments were carried out with a flow rate of 1 mL/min and the 1 μL pulses were injected onto column OA-b (250x4.6 mm, 5μm). Assumed parameters: V_c = 4.155, t_{sys} = 0.06 min, ε = 0.72

Org. fraction %	MeOH				EtOH			
	$t_{R,L\text{-Met}}$ min	$t_{R,D\text{-Met}}$ min	H_L -	$H_{D\text{-Met}}$ -	$t_{R,L\text{-Met}}$ min	$t_{R,D\text{-Met}}$ min	$H_{L\text{-Met}}$ -	$H_{D\text{-Met}}$ -
0	4.83	5.32	1.53	1.95	4.72	5.21	1.43	1.85
10	4.41	5.04	1.17	1.71	4.38	5.00	1.14	1.68
20	4.33	5.24	1.10	1.88	4.38	5.19	1.14	1.84
30	4.40	5.59	1.16	2.18	4.44	5.45	1.19	2.06
40	4.49	5.93	1.24	2.47	4.51	5.72	1.26	2.29
50	4.66	6.47	1.38	2.94	4.61	6.04	1.34	2.57
60	-	-	-	-	4.77	6.49	1.47	2.96
70	-	-	-	-	5.05	7.27	1.72	3.62

Tab. C.2: Estimated AI parameters from the results of the perturbation method in Tab. 5.3 for the bi-Langmuir model for identical saturation capacities.

Eluent	$q_{s,I}$	$b_{I,L\text{-Met}}$	$b_{I,D\text{-Met}}$	$q_{s,II}$	$b_{II,L\text{-Met}}$	$b_{II,D\text{-Met}}$	$H_{L\text{-Met}}$	$H_{D\text{-Met}}$
M2080	57.7	0.0169	0.0179	3.90	0.0025	0.387	0.98	2.30
E2080	32.7	0.0341	0.0382	2.18	0.0347	0.849	1.19	2.54
E4060	24.9	0.0244	0.0409	3.0	0.182	1.0	1.15	3.41

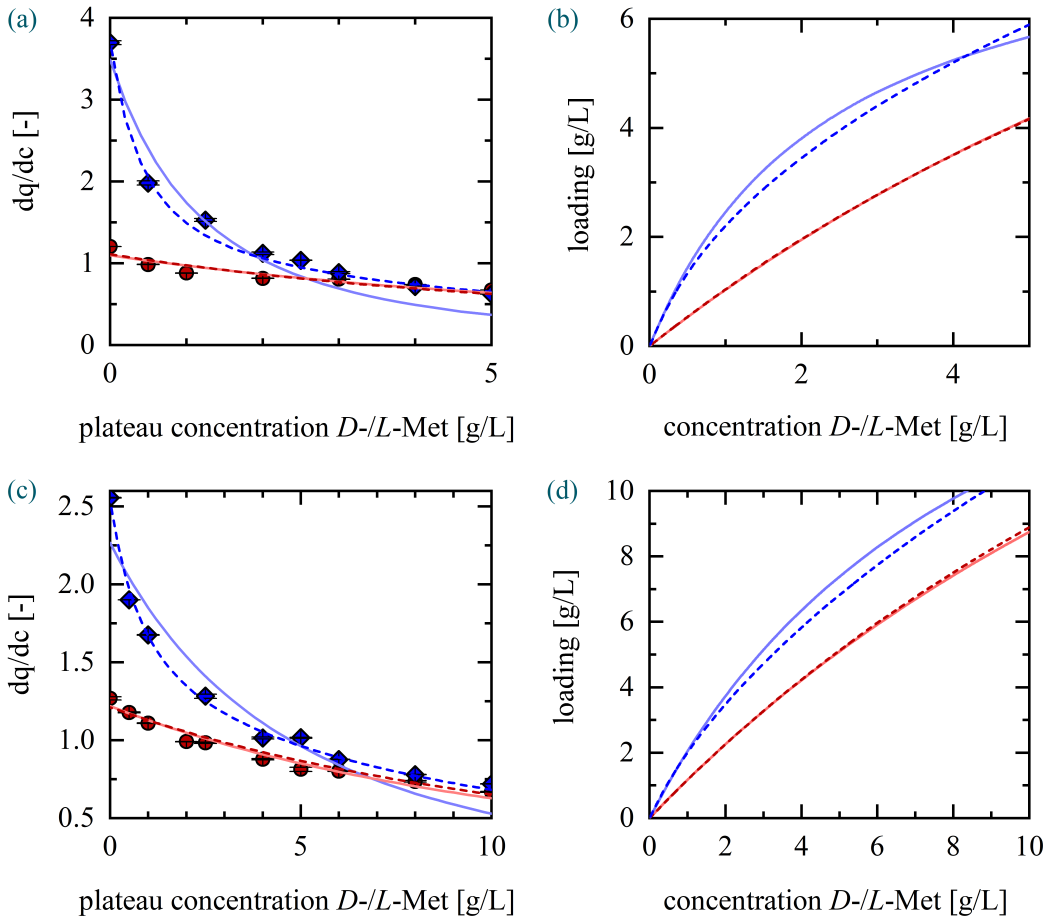

Fig. C.7: Total derivative dqdc from perturbation method (see Tab. C.3) and the resulting adsorption isotherms for *D*- and *L*-Met in EtOH-water mixtures. (a)&(b) in E2080 and (c)&(d) in E4060.

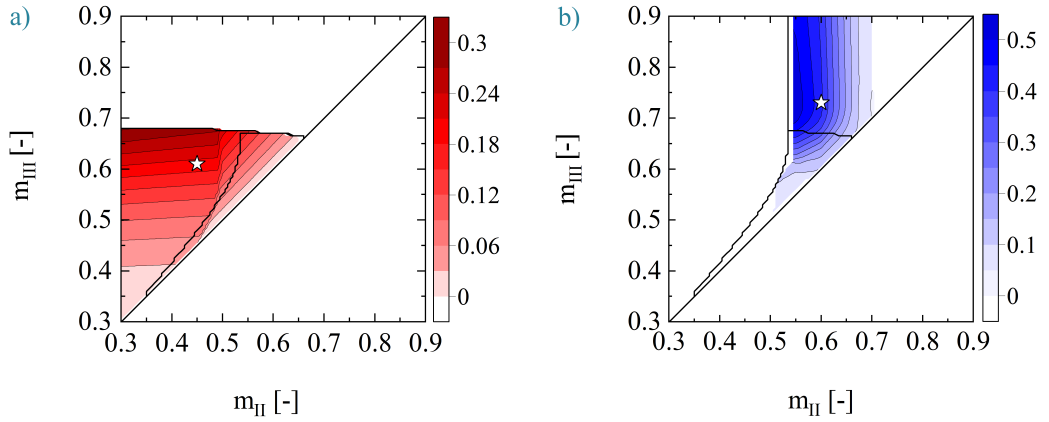

Fig. C.8: Productivities in kg/L_c/day in the m_{II}-m_{III}-plane for a 4Z-TMB unit (type PC-I) for the provision of *R*- or *S*-MA with Pu = 99 %. Conditions: $c_{RS,\,feed}$ = 15 g/L, $\dot{V}_{tot}$ = 45 mL/min (Eq. (2.96)). (a) target = *S*-MA in raffinate, (b) target = *R*-MA in extract.

Tab. C.3: Experimental data of perturbation method for the adsorption isotherm determination of CS-II. All experiments were carried out with a flow rate of 1 mL/min and the 1 μL pulses were injected onto constant loading conditions on PC-I. Assumed parameters: t_0 = 9.23, t_{dead} = 0.05 min, F = 0.27

Eluent	$c_{D/L}$	$t_{R,L}$	$dq/dc_{R,L}$	$t_{R,D}$	$dq/dc_{R,D}$
E2080	10.0	11.00± 0.01	0.696 ± 0.003	11.13± 0.02	0.727 ± 0.007
	8.0	11.18± 0.01	0.764 ± 0.005	11.29± 0.01	0.787 ± 0.005
	6.0	11.34± 0.01	0.829 ± 0.002	11.53± 0.02	0.884 ± 0.006
	4.0	11.54± 0.01	0.905 ± 0.004	11.88± 0.07	1.022 ± 0.028
	2.0	11.83± 0.00	1.019 ± 0.000	-	-
	1.0	12.13± 0.00	1.137 ± 0.002	13.57 ± 0.02	1.684 ± 0.006
	0.0	12.53± 0.03	1.296 ± 0.011	15.81± 0.01	2.564 ± 0.003
E4060	5	11.00± 0.01	0.67 ± 0.016	10.88± 0.03	0.62 ± 0.016
	4	11.18± 0.01	0.74 ± 0.003	11.12± 0.05	0.72 ± 0.003
	3	11.34± 0.01	0.81 ± 0.010	11.55± 0.13	0.89 ± 0.01
	2.5	-	-	11.94± 0.04	1.04 ± 0.003
	2	11.37± 0.03	0.82 ± 0.017	12.16± 0.19	1.12 ± 0.017
	1.25	-	-	13.20± 0.16	1.53 ± 0.019
	1.0	11.54± 0.01	0.88 ± 0.019	-	-
	0.5	11.81± 0.01	0.99 ± 0.025	14.36± 0.18	1.98 ± 0.025
	0	12.37± 0.00	1.2 ± 0.024	18.75± 0.12	3.70 ± 0.024

Tab. C.4: Flow rates in Zone II and III of Run 4 and the resulting purities and productivities

Shifts	$\dot{V}_{II}$	$\dot{V}_{III}$	m_{II}	m_{III}	Pur R	Pur E	Prod R	Prod E
1-40	1.5	1.08	1.205	1	89.7	97.8	-	14.7
41-56	1.5	1.085	1.205	1	87.3	98.7	-	14.6
57-68	1.5	1.09	1.205	1	87.8	99.3	-	14.3
69-80	1.5	1.095	1.205	1	87.9	99.7	18.5	13.6
81-108	1.5	1.1	1.205	1	88	99.99	-	12.3
109-123	1.5	1.095	1.2	1	90.7	99.8	15.2	-
124-136	1.5	1.095	1.195	1	93.7	99.7	14.9	-
137-152	1.5	1.095	1.19	1	97.3	99.7	14.7	-
153-168	1.5	1.095	1.185	1	> 99.99	99.4	13.2	-
169-185	1.5	1.095	1.175	1	> 99.99	99.6	12.0	-
186-204	1.5	1.095	1.165	1	> 99.99	98.9	10.1	-

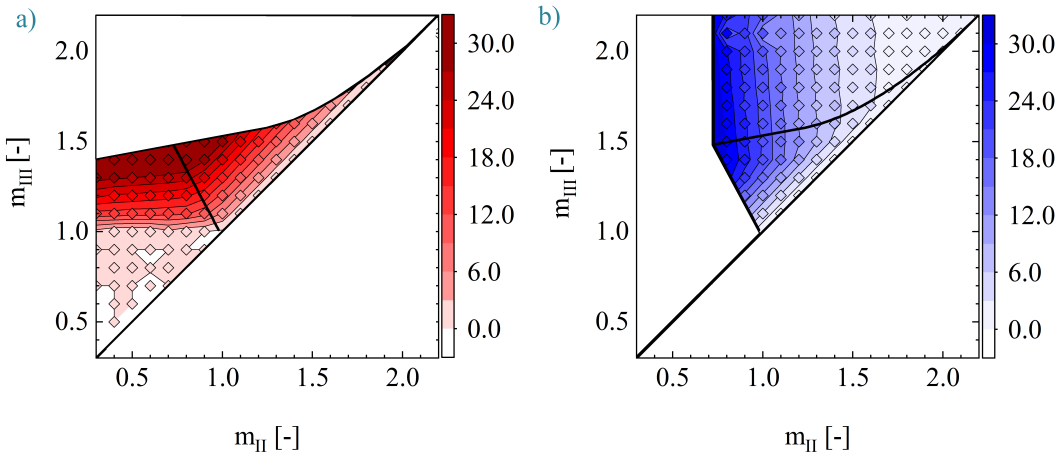

Fig. C.9: Productivities in g/L_c/day in the m_{II}-m_{III}-plane of a 4Z-TMB unit (type PC-II) for the provision of *D*- or *L*-Met with Pu = 99 %. Conditions: $c_{DL,\,feed}$ = 10 g/L, m_I = 2.5, m_{IV} = 0.65. The black lines mark the separation regions for the Langmuir model, the rectangles show simulation results which were the grid to create the colored fit. (a) target = *L*-Met in raffinate, (b) target = *D*-Met in extract.

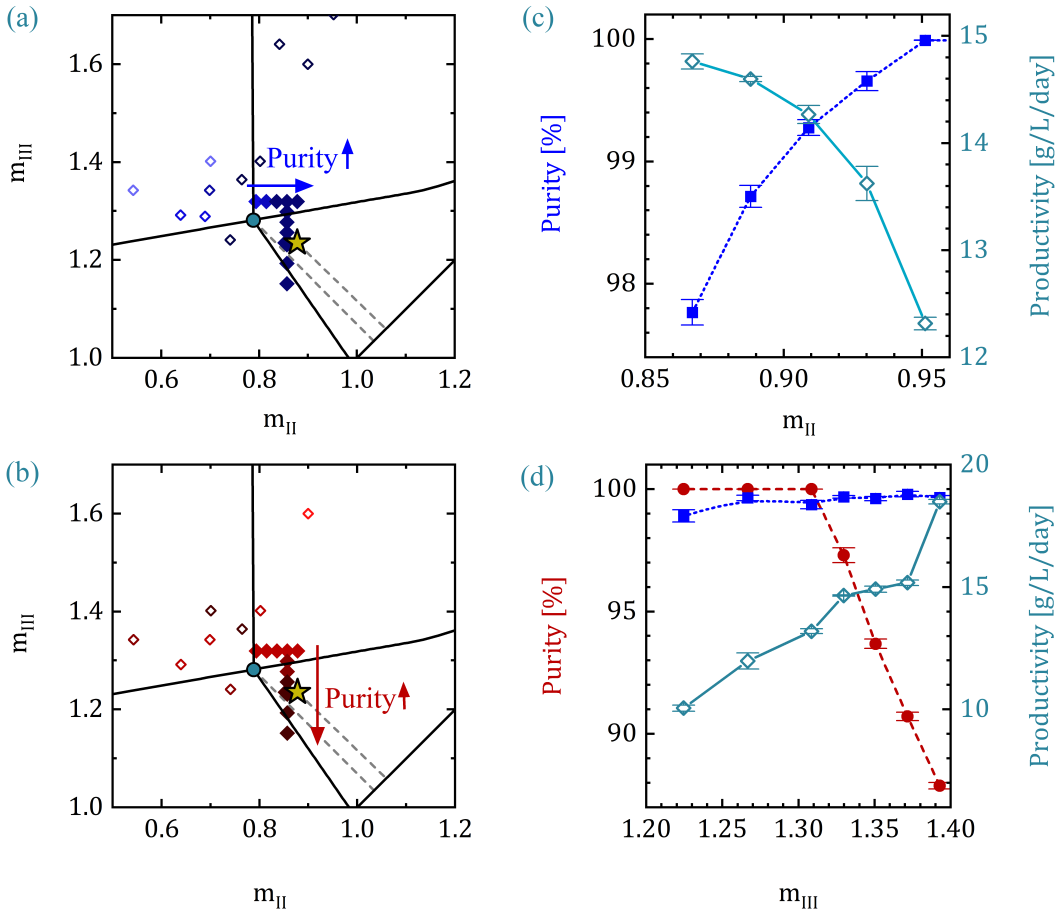

Fig. C.10: Impact of different flow rates in the SMB on the purity of the product and the process productivity during Run 4 based on the isotherms from Tab. 5.5.

D Coupling of simulated fixed bed chromatography and enzymatic racemization in a fixed bed reactor

D.1 Design of an evaporation unit with a rectification column

In the following, the design of an evaporation unit for a binary mixture is briefly presented and assumed parameters for EtOH, MeOH and water are provided.

D.1.1 Derivation of the vapor and liquid equilibria

For generating phase diagrams, a combination of Raoult's and Dalton's law

$$x_i \cdot p_i^*(T) = y_i \cdot p_{sys} \tag{D.1}$$

and the Antoine-equation

$$log_{10}p = A - \frac{B}{C+T} \tag{D.2}$$

with T in °C and p in mmHg, can be used. For this work, the vapor and liquid equilibria of the binary mixtures of ethanol, methanol with water for a constant pressure were obtained from CheCalc [170] with the Wilson model and the Antoine-parameter set given in Table D.1.

D.1.2 Design of a liquid-vapor-phase diagram for McCabe-Thiele

With the T-x- and T-y-data of the binary mixtures at 100 and 110 mbar, the x-y-diagram can be plotted with data points over the given temperature range ($x(T_1)/y(T_1)$) and constant pressure [171, 172].

Tab. D.1: Antoine-parameters for ethanol-water and methanol-water mixtures for T in °C and p in mmHg

Name	Ethanol	Methanol	Water
A	18.9119	18.5875	18.3036
B	38303.98	3626.55	3816.44
C	-41.68	-34.29	-46.13

The balance line of the rectification section can be described as:

$$y = \frac{R}{R+1}\tilde{x} + \frac{x_D}{R+1} \tag{D.3}$$

starting at the point (x_D/y_D) and ending when crossing the q-line, starting at (x_F/y_F) and a slope q/(q-1). In case of a completely liquid feed, the slope of the q-line is a vertical line.

D.2 Prior work on coupling chiral chromatographic resolution with racemization

Author	Model/exp.	Comp.	Separation	Racem.	Filtr.	Dyn. effects	Y [%]	PR [g/L/d]	SC [L/g]	Cost ana.
Langermann, 2012 ([34] ASM)	both but Chr+Cry	PPX	SSR	Shvo's Cat	–	steady s. after 3 c	54%	270 g/day	–	–
Nimmig, 2013 ([118] Kaspereit)	both	CTD	batch CSTR	chemically	0.92	steady s.	68-77%	1.31 g/L/h	12-23 L/g	–
Swernath, 2014 ([36] Kaspereit)	model	???	4Z-SMB	–	–	–	?	?	?	–
Fuereder, 2016 ([37] Panke)	both P.o.C.: 33 h	Met	1-2-1-1 c. l.	EMR, AAR r = 4.2 g/L	0.985	–	93.5%	3.6 g/day	0.97 L	simple
Wrzosek, 2018 ([42] ASM)	model + P.o.C.	MA	batch	FBR, MR	–	–	?	0.68 g/day	0.94 L	–

Y = yield, PR = productivity, SC = solvent consumption, c. l. = closed loop, MR = mandelate racemase

CSTR = Continuous stirred tank reactor

D.3 Operation of the coupled plant

The following section provides further information about the plant.

Start-up and operating guidelines

- When installing a new eluent or feed, 5 mL of solvent can be removed with a syringe in order to remove air and fasten the solvent switching time.
- When starting the SMB, the pump of ZI (P-31) always needs to be started first.
- The other flow rate requirement is: $\dot{V}_{\mathrm{ZI}} > (\dot{V}_{\mathrm{Feed}}\text{-}\dot{V}_{\mathrm{Raff}})$
- The plant should be flushed in *open loop* configuration. A flushing method is described in Tab. D.2.
- A mixing of water and EtOH or MeOH with the pumps, let to gas formation. Therefore, the eluents were pre-mixed. A degasser could solve this issue.
- Usage of two pumps (HNP Microsysteme GmbH), connected with Check Valve Outlet Assembly, 1/4-28, (Perfluor), 1pc/PAK (Upchurch Scientific) in Series: By connecting two or even three pumps with the correct fittings in series and setting the pumps closer to the evaporation tank to a high flow rate of e.g. 3 mL/min, increased the pressure for the next pump sufficiently to allow it to provide the expected flow rate. Whether two or three pumps in series were necessary, depended on the chosen vacuum and the height difference between the first and second tank.

Tab. D.2: Flushing method for the SMB plant

Eluent	$\dot{V}_{\mathrm{Z1}}$ [mL/min]	$\dot{V}_{\mathrm{extr}}$ [mL/min]	$\dot{V}_{\mathrm{feed}}$ [mL/min]	$\dot{V}_{\mathrm{raff}}$ [mL/min]	length [min]
Eluent used in run	1.0	0.5	0.25	0.25	60
Methanol	1.5	0.0	0.25	0.25	120

The process control system from Siemens in Fig. D.1 is used to operate all parts of the plant except for the SMB unit, which is controlled via the interface of the software "LabView". Finally, Fig. D.4 and Fig. D.5 show the detailed flow sheet of the plant.

Fig. D.1 shows the user interface of the PLS system with which everything, except for the SMB process and the OA were controlled. In Fig. D.2 and Fig. D.3 the flow rates and temperatures of Run 8 and Run 9 are shown.

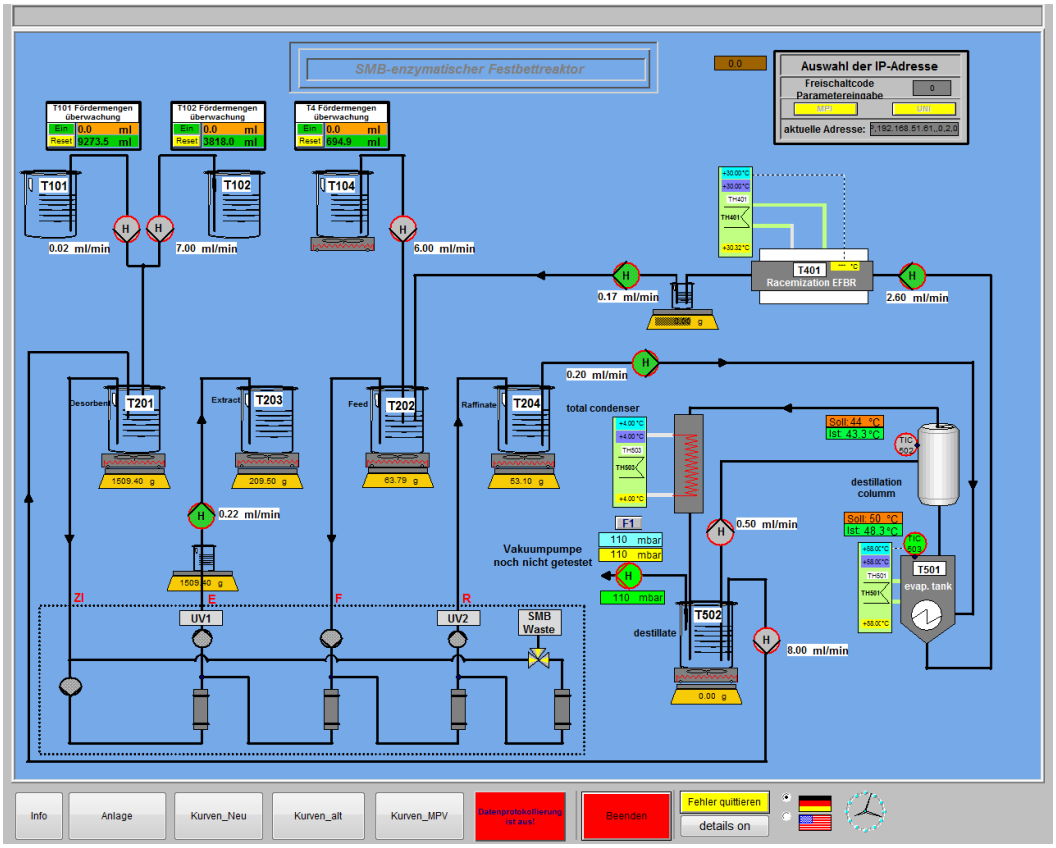

Fig. D.1: User interface of the process control system "WinCC" (Siemens) with which all pumps, balances and thermostats of the mini plant could be monitored and controlled, except for the pumps belonging to the SMB unit.

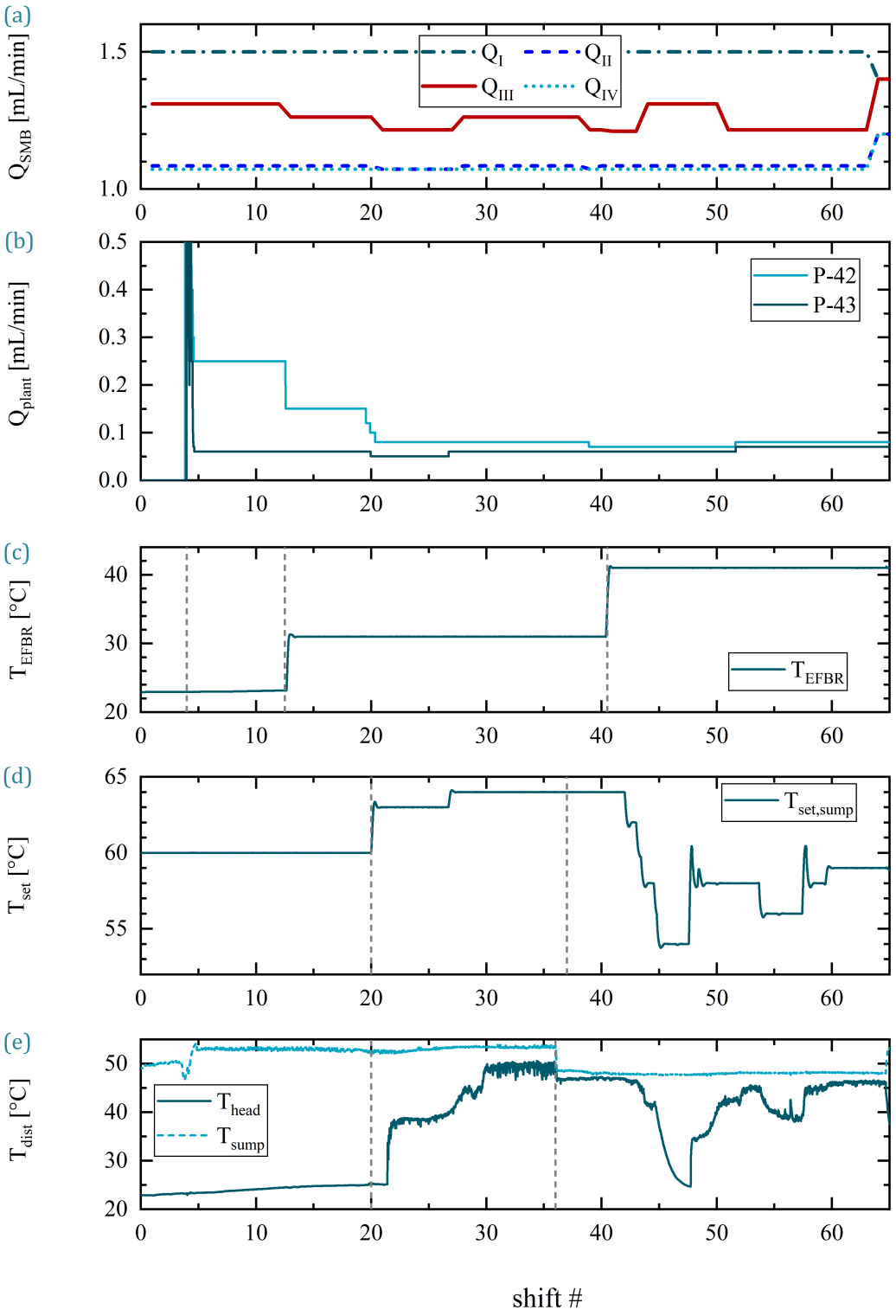

Fig. D.2: Run 8: (a) flow rates of the SMB, (b) set flow rates for the pumps P-42 (dashed, blue) and P-43 (solid, red), (c) temperature of the thermostate for the EFBR, (d) temperature of the thermostat for the distillation sump and (e) the resulting temperature at the sump and measured temperature at the distillation head.

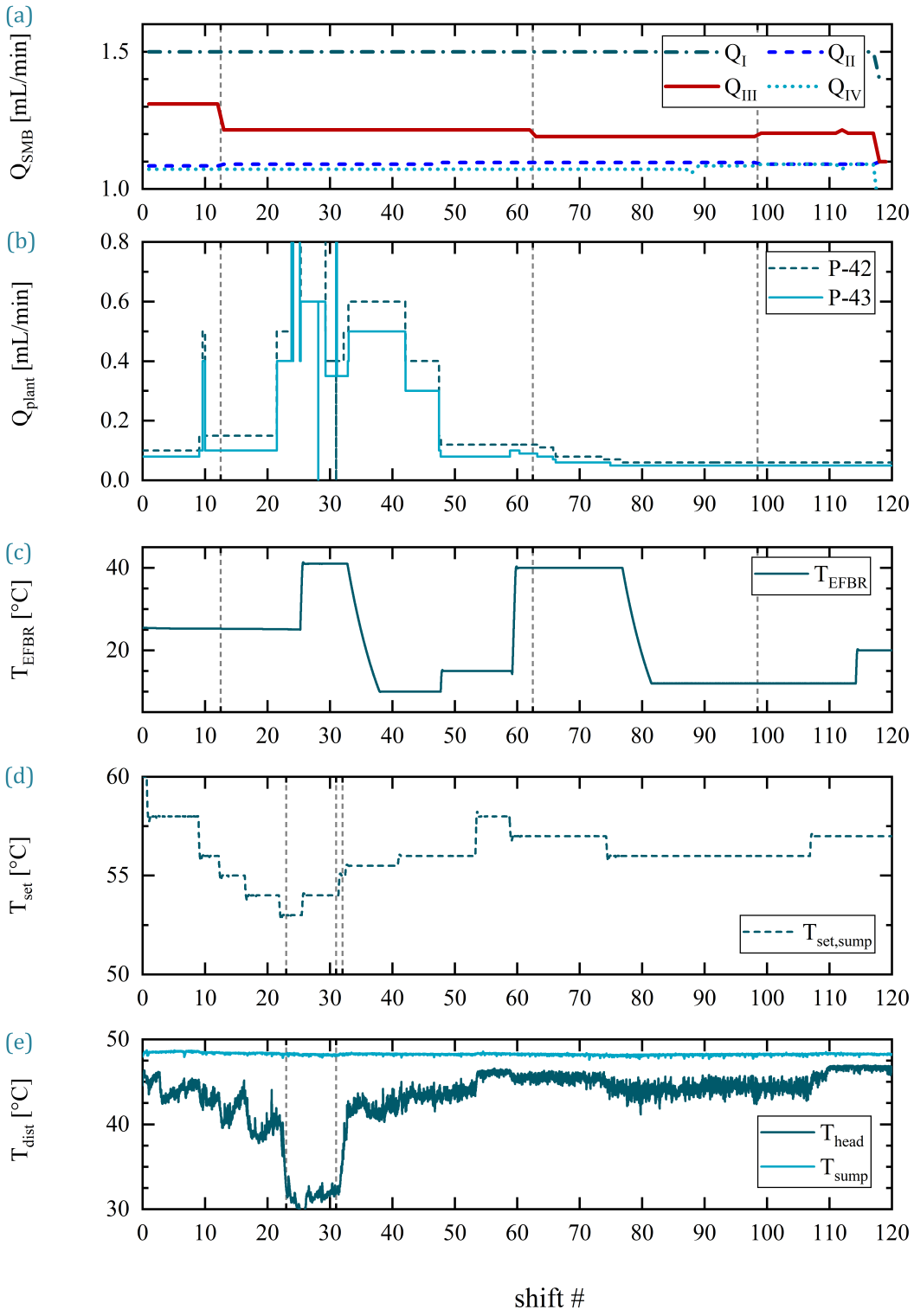

Fig. D.3: Run 9: (a) flow rates of the SMB, (b) set flow rates for the pumps P-42 (dashed, blue) and P-43 (solid, red), (c) temperature of the thermostate for the EFBR, (d) temperature of the thermostat for the distillation sump and (e) the resulting temperature at the sump and measured temperature at the distillation head.

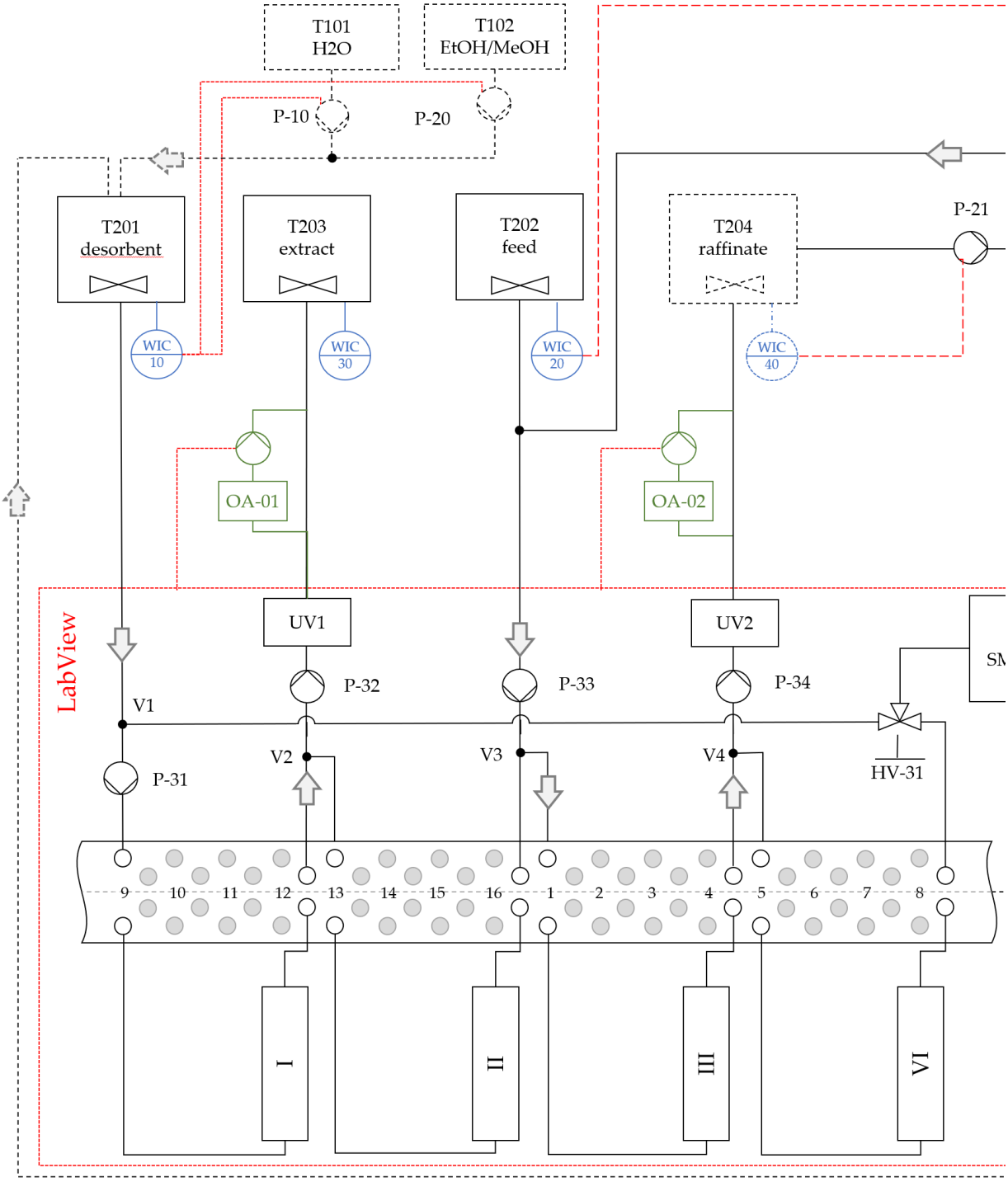

Fig. D.4: Left hand side of the flow scheme of the SMB-EFBR-plant.

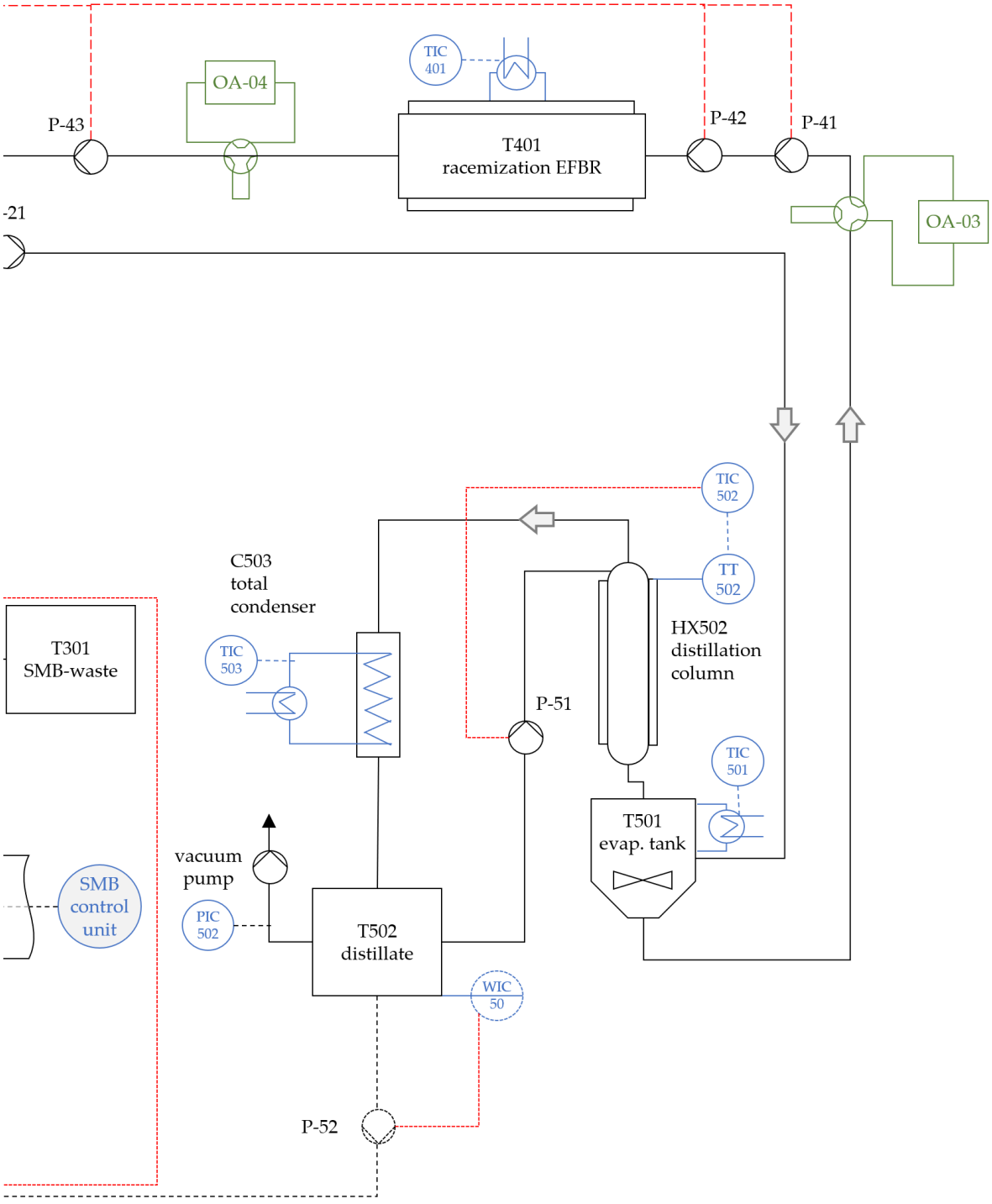

Fig. D.5: Right hand side of the flow scheme of the SMB-EFBR-plant.